THE UNIVERSITY OF ADELAIDE

DEPARTMENT OF MECHANICAL ENGINEERING

STRUCTURES AND TURBULENCE CHARACTERISTICS IN A PRECESSING JET FLOW

submitted by

Gerald Manfred Schneider

for the Degree of Doctor of Philosophy

September 1996

SUMMARY

The precessing jet (PJ) flow phenomenon can occur as a natural fluid mechanical instability in a 'fluidic' nozzle. In that nozzle an axisymmetric jet passes through a large abrubt expansion into a cylindrical chamber of suitable length. When the dimensions of the chamber are appropriate, the jet attaches asymmetrically to the inside wall, is deflected at the chamber exit, leaves at an angle relative to the geometric axis and precesses about that axis. The jet precesses with a characteristic frequency which is a function of the chamber length and diameter and of the flowrate. If, in addition, a lip is placed at the exit of the chamber, the exit angle of the jet can be increased to 45° or more. The exit angle, the jet diameter and the frequency of precession all fluctuate wildly about the characteristic values from cycle to cycle. To simplify the collection of phase–averaged experimental data and so to allow the effect of precession on the external flow field to be investigated, it is necessary to have control of the characteristic variables. This is not possible with the 'fluidic nozzle' described above.

The present thesis reports on a fundamental investigation of a precessing jet flow which is analogous to that which emanates from the fluidic nozzle. A 'mechanical nozzle' is used to generate a well defined PJ flow. A circular jet is located on, and inclined relative to, an axis about which the nozzle is mechanically rotated. In this mechanical analogue of the fluidic nozzle flow field, the precessional frequency can be varied independently of the exit velocity. Thus, unlike the fluidic nozzle, the precessional Strouhal number is decoupled from the Reynolds number ($Re = u_e \cdot d_e/\nu$).

Nathan (1988) proposed that the key parameters which control the flow in a fluidic nozzle of a fixed length to diameter ratio could be characterised by a non–dimensional Strouhal number of precession, $St_p = f_p \cdot d_e/u_e$, where f_p is the frequency of precession, d_e is the exit diameter and u_e the exit velocity of the jet. The exit angle was recognised as a significant parameter in the PJ flow. One exit angle only, $\alpha_e = 45^o$, is examined in depth in the present thesis. For this particular angle the influence of the precessional Strouhal number and of the Reynolds number on the flow field are each explored systematically and independently. For the fully turbulent flows investigated here the Reynolds number has negligible effect on the structure of the flow.

Qualitative images of the changes which occur in the flow field as the Strouhal number is varied, based on conditional smoke pulses and on a laser sheet visualisation technique, are reported for a precessing jet of air issuing into air. For a precessing water jet issuing into water, the field is imaged by use of laser induced fluorescence (LIF). Quantitative velocity and pressure data obtained from hot-wire anemometry, from a high frequency response pitot–type 'Cobra' pressure probe and from a three dimensional Laser Doppler Anemometer system are reported. Mean velocity, static pressure and turbulence intensities in both the time–averaged and the phase–averaged domains in all three dimensions are documented and related to the flow visualisations. Reynolds stresses are presented in the phase–averaged domain only where the phase–averaging is tied to the frequency of precession. In addition, frequency spectra and the skewness and flatness have been obtained from the time–averaged velocity data.

Large differences have been identified in the character of a precessing jet flow as the precessional Strouhal number is varied. Using the Strouhal number definition for the precessing jet flow examined by Nathan (1988), as described above, a 'low' Strouhal number regime has been found to occur below $St_p = 5 \times 10^{-3}$ and a 'high' Strouhal number regime has been identified above $St_p = 9 \times 10^{-3}$, although the transition between these regimes appears to be gradual.

The flow field identified here as the low Strouhal number regime displays characteristics which are almost identical to those of a simple turbulent jet. Each vortex structure follows a straight line path from its origin, resulting in an overall flow which is described well by a projected Archimedian spiral of low curvature. Negligible asymmetry is found in the pressure gradients.

The flow in the high Strouhal number regime is dramatically different. A low pressure region and a recirculation zone are established in the near field and the path of the jet is changed significantly. The jet spirals out from the nozzle around the recirculating flow zone. The streamlines of the jet are curved, both radially towards the spinning axis, and tangentially in the direction opposite from that of the precession. Meanwhile flow is drawn toward the recirculation zone from the region which is not instantaneously occupied by the jet. The path of the 'individual' vortex structures in the jet, which appear to be very similar to vortex puffs, assumes a helical (spiral) shape whose radial extent seems to asymptote to a well defined radius within the near field examined here . The jet velocity decays much more rapidly and Reynolds stresses are much higher than in a simple turbulent jet. In the flow field downstream from the recirculation zone the flow

becomes axisymmetric in the mean. The vortex puff structures cannot be found when phase–averaging at the frequency of precession and the frequency spectra in this flow region do not carry any obvious information from which the frequency of precession, or any other dominant frequency, can be identified.

The thesis is the first fundamental work on precessing jet flows and will built an important basis for further research. To perform this work a novel experimental methodology has been developed and refined. Through this it has been established that the Strouhal number of precession is the dominant parameter in a precessing jet, while the Reynolds number has been shown to have only a second order effect on the flow. The fundamental parameters which remain to be investigated are the exit angle, the shape of the exiting jet and the significance of 'jitter' in the frequency. Each of these parameters has been found to influence the behaviour of the fluidic precessing jet and an improved understanding will facilitate the optimisation of these flows for the practical applications. Use of the mechanical nozzle concept and measurement methods has been shown to contribute to a greater understanding of precessing jet flows.

Contents

1 INTRODUCTION **1**

1.1 Precessing Jet Nozzles and their Applications 3

1.1.1 The Abell Nozzle 3

1.1.2 The Fluidic Precessing Jet Nozzle 4

1.1.3 Industrial Applications of Precessing Jet Flows 5

1.1.4 The Mechanical Precessing Jet Nozzle 7

1.2 Related Flow Fields 9

1.2.1 Simple Turbulent Jets 10

1.2.2 Vortex Puffs 15

1.2.3 Flapping Jets 17

1.2.4 Pulsed Jets 19

1.2.5 Jets in a Cross Flow 20

1.2.6 Swirling Flows 22

1.2.7 Jets in Rotating Systems 24

2 EXPERIMENTAL TECHNIQUES AND APPARATUS **26**

2.1 The Mechanical Precessing Jet Nozzle 26

2.1.1 The Exit Parameters of the Jet 28

2.1.2 External Influences: A Boundary Layer Study 30
2.1.3 Internal Influences: The Jet Issuing from the Nozzle 32
2.2 The Low Velocity Wind Tunnel 36
2.2.1 Design and Layout 36
2.2.2 Calibration and Velocity Distribution in the Wind Tunnel 41
2.3 Flow Visualisation Techniques 47
2.3.1 Smoke Visualisation 47
2.3.2 Laser Sheet Flow Visualisation 49
2.3.3 Laser Induced Fluorescence (LIF) 53
2.4 Measurement Techniques 54
2.4.1 Hot-Wire Anemometers 54
2.4.2 The Cobra Probe 56
2.4.3 Laser Doppler Anemometer System 64

3 THE DEPENDENCY OF THE PRECESSING JET ON THE STROUHAL NUMBER 72

3.1 The Non–Rotating Jet 72
3.2 The Low Strouhal Number Jet 81
3.2.1 The Overall Flow Field 81
3.2.2 The Axial Velocity Component 84
3.2.3 The Radial and Tangential Velocity Components 90
3.2.4 The Turbulence Intensities 95
3.2.5 The Reynolds stresses 105
3.2.6 The Skewness and Flatness 110
3.3 The High Strouhal Number Jet 119

3.3.1 The Overall Flow Field 119
3.3.2 The Axial Velocity Component 122
3.3.3 The Radial and Tangential Velocity Components 127
3.3.4 The Turbulence Intensities 132
3.3.5 Reynolds stresses 141
3.3.6 Skewness and Flatness 145
3.4 Discussion 153

4 VORTEX STRUCTURES AND MOTION IN A PRECESSING JET FLOW 163

4.1 Characteristic Regions in a Precessing Jet 164
4.1.1 Region I: the Potential Core Region 164
4.1.2 Region II: the Precession Dominated Region 165
4.1.3 Region III: the Region of no Dominant Frequency 166
4.2 An Overview of the Behaviour of Precessing Jet Flows 167
4.2.1 The Formation of Vortical Structures in the Potential Core Region 167
4.2.2 The Model of an Archimedian Spiral 169
4.3 Structures in the Low Strouhal Number Regime 172
4.3.1 Asymmetry in the Evolution of the Vortical Structures 172
4.3.2 The Pressure Distribution 174
4.3.3 The Deflection of the Low Strouhal Number Jet 178
4.3.4 Frequency Spectra in a Low Strouhal Number Jet 182
4.4 Structures in the High Strouhal Number Regime 184
4.4.1 Asymmetry in the Evolution of the Vortical Structures 184
4.4.2 The Pressure Distribution 186

4.4.3 The Deflection of the High Strouhal Number Jet 189

4.4.4 Frequency Spectra in the High Strouhal Number Jet 193

4.5 Conclusions 195

5 Analytical Evaluation of the Strouhal number Influence **196**

5.1 The Turbulent, Time–Dependent, Three–Dimensional Navier–Stokes Equations 197

5.1.1 The Laminar Equations of Motion 197

5.1.2 The fully turbulent three-dimensional Equations of Motion 198

5.1.3 Normalisation 200

5.2 The Reynolds Number Effects 201

5.2.1 Phase–Averaged Results 204

5.2.2 Time–Averaged Results 209

5.3 Conclusion 218

6 Conclusions **219**

6.1 Measurements in the Precessing Jet Flow 220

6.2 Identified Flow Structures 223

6.3 Future Work 225

6.3.1 Further Research 225

6.3.2 Existing and Potential Industrial Applications 226

A Further Visualisation: St_p=0.002 and Re=26,600 **I**

B Further Visualisation: St_p=0.015 and Re=26,600 **III**

C Further Results: St_p=0.0058, Re=26,600 **V**

D Further Results: St_p=0.0098, Re=26,600 XIV

E Further Results: St_p=0.0098, Re=6,600 XXIII

F Technical Drawings of the Mechanical Nozzle XXV

List of Figures

1.1 A schematic diagram of the Fluidic Precessing Jet Nozzle 4

1.2 A 100 MW Gyro–Therm burner for a cement kiln in Geelong, Australia . 5

1.3 The bulbous, luminous flame of the Gyro–Therm burner in the Geelong cement plant 6

1.4 The precessing jet generated by the mechanical nozzle 9

1.5 Turbulent Vortex Puff (after: Glezer and Coles, 1990; Richards 1965) . . . 15

2.1 Mechanically Rotated Precessing Jet Nozzle 28

2.2 The nozzle tip with $\alpha_e = 45^o$, nozzle exit diameter d_e=10mm 29

2.3 The influence of the external boundary layer produced by rotation of the mechanical nozzle. Smoke visualisation, no external sleeve, $u_e = 0$m/s, $f_p = 60$Hz 30

2.4 Reduced external boundary layer effects produced by rotation of the mechanical nozzle. With external sleeve, $u_e = 0$m/s, $f_p = 60$Hz 31

2.5 Self–similarity of the jet produced by the spinning nozzle for $\alpha_e = 0^o$, co–flow velocity = 0.03m/s, Re=15,550, St_p=0.015 33

2.6 Induced tangential velocity of the jet produced by the spinning nozzle for $\alpha_e = 0^o$, co–flow velocity = 0.03m/s, Re=15,550, St_p=0.015 34

2.7 Turbulence Intensity of the jet produced by the spinning nozzle with $\alpha_e = 0^o$, Re=15,550 and St_p=0.015 35

2.8 The low speed wind tunnel 42

2.9 Inside the low speed wind tunnel showing the robust vortex shedding anemometer, consisting of two 75.5mm spheres on an approx. 19mm cylinder and a hot wire (suspended from the right wind tunnel wall). 44

2.10 'Calibration' of the vortex shedding anemometer in the low speed wind tunnel plotted as Roshko number $= f \cdot d^2/\nu$ as a function of Reynolds number $= u \cdot d/\nu$ 44

2.11 A calibration curve showing the mean co–flow velocity in the tunnel as a function of the fan–power supply setting 45

2.12 Velocity distributions in the wind tunnel. Note that the data for x/d_e=0 defined by the triangle was taken in a poorly sealed tunnel. Data defined by the white square was obtained after the tunnel was sealed. 46

2.13 The smoke visualisation system mounted beside the nozzle and its variable speed drive. NH_3 and SO_2 are pulsed through two thin tubes to the right of the nozzle. 48

2.14 Vertical laser sheet generated from the Copper Vapour laser 51

2.15 The arrangement of cameras and object 52

2.16 Arrangement for the Laser Induced Fluorescence experiments 54

2.17 A typical hot-wire calibration curve, showing data collected before and after an experimental run. 55

2.18 A photograph and sketch of the Cobra probe 56

2.19 Phase shift and frequency response of a pressure signal taken with the Cobra probe in a turbulent jet flow. 58

2.20 Corrected and uncorrected pressure signal taken with the Cobra probe in a precessing jet flow. 58

2.21 Calibration Surface cut at pitch of: a) 0^o; and b) -42^o. 60

2.22 A typical pressure signal from the Cobra probe showing one cycle of precession in the precessing jet flow. 61

2.23 Apparatus and coordinate system used in the Cobra probe measurements. 63

2.24 The 3-D LDA system and the mechanical nozzle 64

2.25 The apparatus used for the LDA measurements 66

3.1 The x–y–z coordinate system for the non–rotating jet *only* 73

3.2 Image of the non–rotating water jet issuing from the 45^o mechanical nozzle. LIF technique, Re=26,000. 74

3.3 Velocity profiles, traversed in y-direction, in the non–rotating jet issuing from the $\alpha_e = 45^o$ mechanical nozzle. Re=26,000 75

3.4 Velocity profiles, traversed in z-direction, in the non–rotating jet issuing from the $\alpha_e = 45^o$ mechanical nozzle. Re=26,000. 75

3.5 Velocity profiles at x/d_e=1.0 and a symmetric line of best fit in the non–rotating jet issuing from the $\alpha_e = 45^o$ mechanical nozzle obtained by LDA. Re=26,000 76

3.6 Centerline velocity decay of the non–rotating jet. Re=26,000. 77

3.7 Spreading angle of the non–rotating jet. Re=26,000 77

3.8 Self–similarity of the non–rotating jet in y-direction. Re=26,000 79

3.9 Self–similarity of the non–rotating jet in z-direction. Re=26,000 79

3.10 Axial turbulence intensities at x/d_e=1.0 in the non–rotating jet obtained by LDA. Re=26,000 80

3.11 Two consecutive cycles of precession in the low Strouhal number jet (here St_p=0.002). The beginning of each cycle is marked by a smoke pulse. Re=26,600 82

3.12 Vertical Light Sheet from $0<x/d_e<12$ through the r–x Plane in the low Strouhal number Jet marked with glass beads. St_p=0.002. 83

3.13 Instantaneous particle images and phase-averaged axial velocity $\tilde{u}_x$ contours at x/d_e=2, 4, 6. St_p=0.002, Re=26,600. 86

3.14 Instantaneous particle images and phase-averaged axial velocity $\tilde{u}_x$ contours at x/d_e=8, 10, 12. St_p=0.002, Re=26,600. 87

3.15 Time–averaged axial velocity $\overline{u}_x$ at x/d_e=2 to 12. St_p=0.002, Re=26,600. 89

3.16 Phase-averaged radial $\tilde{u}_r$ and phase–averaged tangential $\tilde{u}_\Phi$ velocities combined to form vectors, x/d_e=2, 4, 6, 8, 10, 12, St_p=0.002, Re=26,600. . . 92

3.17 Time–averaged radial velocity $\overline{u}_r$ at x/d_e=2 to 12. St_p=0.002, Re=26,600. 93

3.18 Time–averaged tangential velocity $\overline{u}_\Phi$ at x/d_e=2 to 12. St_p=0.002, Re=26,600. 94

3.19 Phase-averaged axial turbulence intensity at x/d_e=2, 4, 6, 8, 10, 12. St_p=0.002, Re=26,600. 97

3.20 Time–averaged axial turbulence at x/d_e=2 to 12. St_p=0.002, Re=26,600. . 98

3.21 Phase-averaged radial turbulence intensity at x/d_e=2, 4, 6, 8, 10, 12. St_p=0.002, Re=26,600. 100

3.22 Time–averaged radial turbulence at x/d_e=2 to 12. St_p=0.002, Re=26,600. 101

3.23 Phase-averaged tangential turbulence intensity at x/d_e=2, 4, 6, 8, 10, 12. St_p=0.002, Re=26,600. 103

3.24 Time–averaged tangential turbulence at x/d_e=2 to 12. St_p=0.002, Re=26,600. 104

3.25 Normalised phase-averaged $\widetilde{u_x u_r}$ Reynolds stress component at x/d_e=2, 4, 6, 8, 10, 12. St_p=0.002, Re=26,600. 106

3.26 Normalised phase-averaged $\widetilde{u_x u_\Phi}$ Reynolds stress component at x/d_e=2, 4, 6, 8, 10, 12. St_p=0.002, Re=26,600. 108

3.27 Normalised phase-averaged $\widetilde{u_r u_\Phi}$ Reynolds stress component at x/d_e=2, 4, 6, 8, 10, 12. St_p=0.002, Re=26,600. 109

3.28 Time–averaged axial skewness at x/d_e=2 to 12. St_p=0.002, Re=26,600. . . 113

3.29 Time–averaged axial flatness at x/d_e=2 to 12. St_p=0.002, Re=26,600. . . 114

3.30 Time–averaged radial skewness at x/d_e=2 to 12. St_p=0.002, Re=26,600. . 115

3.31 Time–averaged radial flatness at x/d_e=2 to 12. St_p=0.002, Re=26,600. . . 116

3.32 Time–averaged tangential skewness at x/d_e=2 to 12. St_p=0.002, Re=26,600. 117

3.33 Time–averaged tangential flatness at x/d_e=2 to 12. St_p=0.002, Re=26,600. 118

3.34 Two consecutive cycles of precession in the high Strouhal number jet (here St_p=0.015). The beginning of each cycle is marked by a smoke pulse. Re=26,600. 120

3.35 Vertical laser sheet from $0< x/d_e <12$ through the r–x plane in the high Strouhal number jet marked with glass beads (multiple exposure). St_p=0.015, Re=26,600. 121

3.36 Instantaneous particle images and phase-averaged axial velocity $\tilde{u}_x$ contours at x/d_e=2, 4, 6. St_p=0.015, Re=26,600. 123

3.37 Instantaneous particle images and phase-averaged axial velocity $\tilde{u}_x$ contours at x/d_e=8, 10, 12. St_p=0.015, Re=26,600. 124

3.38 Time–averaged axial velocity $\overline{u}_x$ at x/d_e=2 to 12. St_p=0.015, Re=26,600. 126

3.39 Phase-averaged radial $\tilde{u}_r$ and phase–averaged tangential $\tilde{u}_\Phi$ velocities combined to form vectors, x/d_e=2, 4, 6, 8, 10, 12, St_p=0.015, Re=26,600. . . 129

3.40 Time–averaged radial velocity $\overline{u}_r$ at x/d_e=2 to 12. St_p=0.015, Re=26,600. 130

3.41 Time–averaged tangential velocity $\overline{u}_\Phi$ at x/d_e=2 to 12. St_p=0.015, Re=26,600.131

3.42 Phase-averaged axial turbulence intensity at x/d_e=2, 4, 6, 8, 10, 12. St_p=0.015, Re=26,600. 135

3.43 Time–averaged axial turbulence at x/d_e=2 to 12. St_p=0.015, Re=26,600. . 136

3.44 Phase-averaged radial turbulence intensity at x/d_e=2, 4, 6, 8, 10, 12. St_p=0.015, Re=26,600. 137

3.45 Time–averaged radial turbulence at x/d_e=2 to 12. St_p=0.015, Re=26,600. 138

3.46 Phase-averaged tangential turbulence intensity at x/d_e=2, 4, 6, 8, 10, 12. St_p=0.015, Re=26,600. 139

3.47 Time–averaged tangential turbulence intensity at x/d_e=2 to 12. St_p=0.015, Re=26,600. 140

3.48 Normalised phase-averaged $\frac{\widetilde{u'_x u'_r}}{u_x u_r}$ Reynolds stress component at x/d_e=2, 4, 6, 8, 10, 12. St_p=0.015, Re=26,600. 143

3.49 Normalised phase-averaged $\frac{\widetilde{u'_x u'_\Phi}}{u_x u_\Phi}$ Reynolds stress component at x/d_e=2, 4, 6, 8, 10, 12. St_p=0.015, Re=26,600. 144

3.50 Normalised phase-averaged $\frac{\widetilde{u'_r u'_\Phi}}{u_r u_\Phi}$ Reynolds stress component at x/d_e=2, 4, 6, 8, 10, 12. St_p=0.015, Re=26,600. 144

3.51 Time–averaged axial skewness at x/d_e=2 to 12. St_p=0.015, Re=26,600. . . 147

3.52 Time–averaged axial flatness at x/d_e=2 to 12. St_p=0.015, Re=26,600. . . 148

3.53 Time–averaged radial skewness at x/d_e=2 to 12. St_p=0.015, Re=26,600. . 149

3.54 Time–averaged radial flatness at x/d_e=2 to 12. St_p=0.015, Re=26,600. . . 150

3.55 Time–averaged tangential skewness at x/d_e=2 to 12. St_p=0.015, Re=26,600. 151

3.56 Time–averaged tangential flatness at x/d_e=2 to 12. St_p=0.015, Re=26,600. 152

3.57 The influence of the jet precession on the deflection in the x–r plane of the jet 'centreline'. The plot shows the axial and radial location of the point of maximum phase–averaged velocity as a function of the Strouhal number of precession. 154

3.58 The influence of the jet precession on the deflection in the x–Φ plane of the jet 'centreline'. The plot shows the axial and tangential location of the point of maximum phase–averaged velocity as a function of the Strouhal number of precession. 155

3.59 The axial velocity decay along the locus of maximum velocity in the phase–averaged jet. Re=26,600. 156

3.60 The spreading of the phase–averaged precessing jet in radial direction. Body fitted coordinate system x', r', Φ'; Re=26,600. 158

3.61 The spreading of the phase–averaged precessing jet in tangential direction. Body fitted coordinate system x', r', Φ'; Re=26,600. 158

3.62 The maximum negative axial phase–averaged velocity in the recirculation zone. Re=26,600. 159

3.63 The maximum time–averaged axial turbulence, skewness and flatness. Re=26,600. 161

3.64 The maximum time–averaged radial turbulence, skewness and flatness. Re=26,600. 162

4.1 Characteristic flow regions which have been identified in the phase–averaged domain for: a) the low Strouhal number jet; b) the high Strouhal number jet 166

4.2 Evidence of Kelvin–Helmholtz instabilities in the potential core region of the precessing jet flow 168

4.3 Curvature, $\frac{1}{R} = \frac{2\pi f}{\tilde{u}_c} \cdot \frac{\Phi^2+2}{(\Phi^3+1)^{3/2}}$, of an Archimedian spiral 171

4.4 Evolution of vortices in the low Strouhal number flow projected in the r–Φ plane (simplified sketch ignoring vortex pairing and growth) 173

4.5 The phase–averaged pressure field $p_s - p_{atmos}$ <-50Pa at x/d_e=3. St_p=0.004, Re=30,000. Colour scale: blue(-50Pa) < green < yellow < red(-80Pa) . . 175

4.6 The phase–averaged pressure field $p_s - p_{atmos}$ <-50Pa at x/d_e=7 (velocity contour overlayed). St_p=0.004, Re=30,000. Colour scale: blue(-50Pa) < green < yellow < red(-80Pa) 176

4.7 The phase–averaged pressure field $p_s - p_{atmos}$ <-50Pa at x/d_e=10 (velocity contour overlayed). St_p=0.004, Re=30,000. Colour scale: blue(-50Pa) < green < yellow < red(-80Pa) 177

4.8 The time–averaged pressure field in the high Strouhal number flow at x/d_e=3, 7 and 10. St_p=0.004, Re=30,000 178

4.9 Deviation of the locus of the points of maximum phase–averaged velocity in the precessing jet relative to the path of a projected Archimedian spiral in two low Strouhal number flows 179

4.10 Laser sheet flow visualisation of a low Strouhal number jet, using Glycol vapour to mark the jet. The light sheet is in the x–r plane and the exit conditions are: Re=26,600, St_p=0.002 180

4.11 A time–sequence of vortex structures through a quarter of a cycle of precession for a low Strouhal number flow. The light sheet is in the r–Φ plane at x/d_e=4. St_p=0.002, Re=26,600 181

4.12 Frequency spectrum on the jet centreline at x/d_e=10, 20 and 40 183

4.13 Evolution of vortices in the high Strouhal number flow projected in the r–Φ plane (simplified sketch ignoring vortex pairing and growth) 186

4.14 The phase–averaged pressure field in the high Strouhal number flow at x/d_e=2 (overlayed contour of the jet). St_p=0.015, Re=26,600 187

4.15 The time–averaged pressure field in the high Strouhal number flow at x/d_e=2, 4 and 6. St_p=0.015, Re=26,600 188

4.16 Deviation of the locus of the points of maximum phase–averaged velocity in the precessing jet relative to the path of a projected Archimedian spiral in two high Strouhal number flows 190

4.17 Laser induced fluorescence in a water tank showing vortical structures generated with a high Strouhal number precessing jet flow: Note 'isolated' vortex structures (1) and (2). St_p=0.015, Re=26,600 191

4.18 A time–sequence of vortex structures through half a cycle of precession for a high Strouhal number flow. The light sheet is in the r–Φ plane at x/d_e=4. St_p=0.015, Re=26,600 192

4.19 Frequency spectrum on the jet centreline at x/d_e=10, 20 and 40 194

5.1 Phase–averaged axial velocity contours at x/d_e=2, 6 and 10 for Reynolds numbers of a) 26,600 b) 6,600 205

5.2 The influence of the Reynolds number on the jet deflection in r–direction. St_p=0.0098. 207

5.3 The influence of the Reynolds number on the jet deflection in Φ–direction. St_p=0.0098. 207

5.4 The influence of the Reynolds number on the velocity decay. St_p=0.0098 . 208

5.5 **Maximum reverse flow in the central recirculation** 209

5.6 **Time–averaged axial velocity profiles normalised by its maximum value at the x/d_e location for Reynolds numbers of 26,600 and 6,600. St_p=0.0098.** 210

5.7 **Time–averaged radial velocity profiles normalised by its maximum value at the x/d_e location for Reynolds numbers of 26,600 and 6,600. St_p=0.0098.** 211

5.8 **Time–averaged tangential velocity profiles normalised by its maximum value at the x/d_e location for Reynolds numbers of 26,600 and 6,600. St_p=0.0098.** 212

5.9 **Time–averaged axial turbulence intensity for Reynolds numbers of 26,600 and 6,600. St_p=0.0098** 215

5.10 **Time–averaged radial turbulence intensity for Reynolds numbers of 26,600 and 6,600. St_p=0.0098** 216

5.11 **Time–averaged tangential turbulence intensity for Reynolds numbers of 26,600 and 6,600. St_p=0.0098** 217

A.1 **Conditional smoke visualisation. St_p=0.002, Re=26,600.** II

A.2 **Laser illuminated flow field of the precessing jet. St_p=0.002, Re=26,600.** . II

B.1 **Laser sheet visualisation. Multiple exposure, St_p=0.015, Re=26,600.** . . . IV

B.2 **Laser sheet visualisation. Multiple exposure, St_p=0.015, Re=26,600.** . . . IV

C.1 **Phase-averaged axial velocity $\tilde{u}_x$ contour at x/d_e=2, 4, 6, 8, 10, 12** VI

C.2 **Phase-averaged radial–tangential velocity $\tilde{u}_r - \tilde{u}_\Phi$ at x/d_e=2, 4, 6, 8, 10, 12** VII

C.3 **Phase-Averaged Axial Turbulence Intensity at x/d_e=2, 4, 6, 8, 10, 12** . . . VIII

C.4 **Phase-Averaged Radial Turbulence Intensity at x/d_e=2, 4, 6, 8, 10, 12** . . IX

C.5 **Phase-Averaged Tangential Turbulence Intensity at x/d_e=2, 4, 6, 8, 10, 12** X

C.6 **Phase-Averaged Reynolds stress $\widetilde{u_x' \cdot u_r'}$ at x/d_e=2, 4, 6, 8, 10, 12** XI

C.7 **Phase-Averaged Reynolds stress $\widetilde{u_x' \cdot u_\Phi'}$ at x/d_e=2, 4, 6, 8, 10, 12** XII

C.8 **Phase-Averaged Reynolds stress $\widetilde{u_\Phi' \cdot u_r'}$ at x/d_e=2, 4, 6, 8, 10, 12** XIII

D.1 **Phase-averaged axial velocity $\tilde{u}_x$ contour at x/d_e=2, 4, 6, 8, 10, 12** XV

D.2 **Radial-Tangential Velocity $\tilde{u}_r - \tilde{u}_\Phi$ vectors at x/d_e=2, 4, 6, 8, 10, 12** . . . XVI

D.3 **Phase-Averaged Axial Turbulence Intensity at x/d_e=2, 4, 6, 8, 10, 12** . . . XVII

D.4 **Phase-Averaged Radial Turbulence Intensity at x/d_e=2, 4, 6, 8, 10, 12** . . XVIII

D.5 **Phase-Averaged Tangential Turbulence Intensity at x/d_e=2, 4, 6, 8, 10, 12** XIX

D.6 **Phase-Averaged Reynolds stress $\widetilde{u_x' \cdot u_r'}$ at x/d_e=2, 4, 6, 8, 10, 12** XX

D.7 **Phase-Averaged Reynolds stress $\widetilde{u_x' \cdot u_\Phi'}$ at x/d_e=2, 4, 6, 8, 10, 12** XXI

D.8 **Phase-Averaged Reynolds stress $\widetilde{u_\Phi' \cdot u_r'}$ at x/d_e=2, 4, 6, 8, 10, 12** XXII

E.1 **Phase-averaged axial velocity $\tilde{u}_x$ contour at x/d_e=2, 4, 6, 8, 10, 12** XXIV

Statement of Originality

The material in this thesis is original and has not been submitted or accepted for the award of a degree or diploma at any other university. To the best of my knowledge and belief, the thesis contains no material previously published or written by another person except where due reference is made in the text of the thesis.

Gerald M. Schneider

(September 1996)

Permission to Copy

The author consents to the thesis being made available for loan and photocopying provided that the thesis is accepted for the award of the degree.

Gerald M. Schneider

(September 1996)

ACKNOWLEDGEMENTS

A PhD thesis is somewhat like building a pyramid: the postgraduate student puts only the top few stones on the edifice (although not even those can he lift by himself). A multitude of helpers participate in the design and in building the foundations and the bulk of the structure. There are many to whom I owe a debt of gratitude for this help. Without them this work wouldn't have been possible.

The first to mention have to be my supervisors Prof.R.E. Luxton (Sam) and Dr. Graham Nathan (Gus). The enthusiasm of Sam over the years of the project has always been most inspiring. His help, personal involvement and scientific input in this work has been beyond measure.

Gus' personal and scientific support have been beyond all I have known. Not only did he make my start in a new country most enjoyable, but also he has continued to encourage and guide my way through this investigation. He has always been available to answer questions and is the epitomy of patience and helpfulness.

Uncounted discussions, input and help from the members of the Combustion Group at the University of Adelaide have been greatly appreciated. Greg Newbold, Steve Hill, Neil Smith, David Nobes, Dr. J.Mi and Dr. Steve Vidakovic have not only contributed scientifically to this thesis, but have also been (and still are) friends who have made my studies very enjoyable.

No research would proceed past first base without technicians and workshop staff who are masters of equipment manufacture. My thanks to Ron Jager, Craig Price, An-

thony Sherry and Malcolm Bethune from the workshop and to the electronic technicians Silvio DeIeso, Herwig Bode, George Osborne, Alan Mittler and Jonathan May. The occasions on when they contributed not only technical expertise but also great patience in repairing yet another piece of equipment were far from few.

I also would like to thank Dr. John Hooper and Tony Musgrove, then of the CSIRO Division of Mineral and Process Engineering, Menai NSW, who supported the work reported herein which used the 'Cobra' probe both scientifically and with inputs of effort that went far beyond the normal call of duty.

For the time spent at the University of Wales in Cardiff I have many people to thank. Prof.Dr. Nick Syred and Dr. Tim O'Doherty have taken a personal interest in the research and have given much helpful and encouraging advice.
The financial support of the 'Euroflam' program and its capable administration at the hands of Dr. Tony Griffiths and Dr. Phil Bowen has been greatly appreciated. The care and efforts of Tony and Phil to make my time in Cardiff at the same time scientifically rewarding and pleasurable were immeasurable.
The technicians and workshop staff, in particular Paul Malpas, Alan Griffiths and Malcom Seybourne, were very helpful and patient.
Other postgraduates working in the Industrial Liasion Section were very generous with both their skills and advice (and with their computers). In particular I would like to thank Dr. Daniel Froud and Wolfgang Fick for their support.

And finally thanks to my wife, family and friends who have given practical assistance, sympathised, entertained and prayed !!

For The Lord gives wisdom, and from His mouth

come knowledge and understanding

Proverbs 2:6

To my wife Mary

NOTATION

d_e, D	exit diameter of the spinning nozzle (=10mm)
f_c	frequency of vortex ring formation in a turbulent jet
f_p	frequency of precession
p_{atmos}	atmospheric pressure
p_d	dynamic pressure
p_s	static pressure
p_t	total pressure
1/R	curvature = 1/ local radius of a curve
r_e	exit radius = $d_e/2$
$r_{0.5}$	radius, where the velocity is half of the local centreline velocity
Re	Reynolds Number = $u_e d_e/\nu$
St_c	Strouhal Number of vortex ring formation in a turbulent jet = $f_c d_e/u_e$
St_p	Strouhal Number of precession = $f_p d_e/u_e$
u	total velocity
u_c	total centreline velocity
u_e	exit velocity of the precessing jet
u_r	radial velocity component
u_x	axial velocity component
u_Φ	tangential velocity component
$u_{\Phi,max}$	maximum tangential velocity
$u_{r,e}$	radial velocity component at the exit
$u_{r,max}$	maximum radial velocity

$u_{x,cl}$	axial velocity component on the centreline
$u_{x,e}$	axial velocity component at the exit
$u_{x,max}$	maximum axial velocity
$u_{x,rec}$	maximum negative axial velocity in the recirculation zone
x_0	virtual origin of a jet
x,r,Φ	cylindrical coordinates
	(Φ positive anti–clockwise, precession clockwise)
	(Φ_0 tangential position of the jet in the exit plane)
x', r', Φ'	body–fitted coordinates
α_e	exit angle of the spinning nozzle
ν	kinematic viscosity
~	phase–averaged component
—	time–averaged component
'	fluctuating component

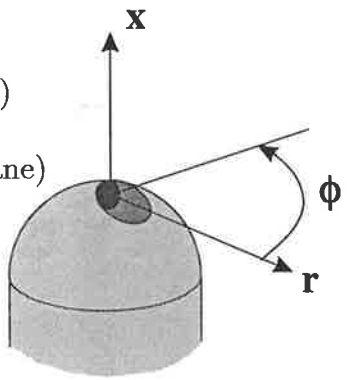

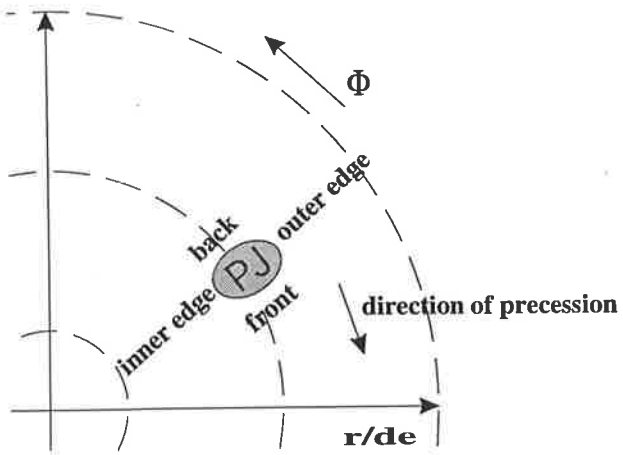

Nomenclature in the phase-averaged precessing jet

Chapter 1

INTRODUCTION

Increased levels of greenhouse gases in recent times have led to concerns about the potential changes of the world climate and the prospect of global warming. The Oxides of nitrogen and carbon dioxide are the principal contributors to the global greenhouse effect. The international community has recognised the potential danger and crafted an agreement to lower global greenhouse gas emissions. This was signed by over 150 countries at the Earth Summit in Brazil in 1992, and was reaffirmed in Berlin in March 1994 to become the *Framework Convention on Climate Change (FCCC)* (NIEIR 1994). Almost three quarters of the greenhouse gas emissions result from the burning of fossil fuels for power generation and for industrial process heating in smelters, kilns, furnaces, boilers etc. A taxation system based on carbon dioxide production is being discussed in many countries, but its implementations are politically controversial because, it is claimed, financial pressures on many industries could be crippling (Hirs 1992). Catalytic filters can provide a solution for the problem of increased emissions in many industrial processes, but they are costly and hard to control when loads vary (Valenti 1993). Industrial burners which produce less emissions and are easy to retrofit are vital

elements in any long term strategy to solve the emission problem. Research effort in the developed countries of the world has been strongly focussed on the development of low NO_x burners which can also maintain low CO emission levels. Valenti (1993) has described the situation in the USA, where companies have retrofitted low NO_x burners to meet new emission standards. Similar developments are now being seen all over the industrial world (Paleokrassas 1992).

The subject of the present investigation is motivated by an industrial burner project which targets the combined aims of increased efficiency and lower exhaust emissions. The GYRO–THERM burner (Section 1.1.3), has been developed in the University of Adelaide, Australia, and is being marketed by Fuel and Combustion Technology International (FCTI) in Adelaide/Australia, London/UK and in Pennsylvania/USA. The GYRO–THERM employs a novel precessing jet mixing nozzle to produce flow and mixing characteristics which reduce NO_x emissions by typically 30-60% while maintaining low CO emssions. As an additional bonus, typical fuel reductions of 5% or more have been measured in rotary kilns, and this provides, for the client company, a positive return on investment in less than 2 years. Similar benefits have been achieved in the Alumina Industry (Jenkins et al. 1995) and potential also exists to utilise the technology in power station applications (Ward et al. 1990). Further applications are in the course of development for metallurgical processes, glass and lime manufacturer, the steel industry etc. Experience shows that the GYRO–THERM burner has the potential to make a major contribution to more efficient and environmentally friendly production of vital products worldwide (Manias and Nathan,1994).

The present thesis describes an investigation of the cold, non–reacting flow field downstream from a precessing jet burner nozzle to determine the fluid mechanic phenomena that lead to the improved combustion characteristics.

1.1 Precessing Jet Nozzles and their Applications

1.1.1 The Abell Nozzle

Abell (1977) studied Brown-Roshko vortices in a mixing layer, using acoustic excitation in an attempt to investigate the pairing or amalgation of the structures. The acoustic excitation was found to change the flow field fundamentally and to increase the mixing characteristics of a jet dramatically. To apply this increased mixing to combustion, an orifice–cavity–orifice (OCO) configuration was developed, based on a 'fox whistle' (Abell and Luxton, 1979, 1980, 1981). The flame produced by this nozzle is stable at high throughput, but has poor turn–down capability. Nathan (1988) extended the studies of the OCO geometries and found a different range of geometries in which a new flow instability, termed jet precession, is generated. A natural gas flame produced by the precessing jet is very stable and can be turned up or down over a very large range without becoming unstable.

1.1.2 The Fluidic Precessing Jet Nozzle

Beginning with the investigation by Nathan (1988), the precessing jet (PJ) flow has been the subject of detailed investigations at the University of Adelaide, Australia, for more than a decade. A precessing jet flow has been demonstrated to be a naturally occuring instability which follows a large, abrupt axisymmetric expansion into a short chamber (Nathan, 1988; Hill et al. 1992). This phenomenon occurs over a wide range of nozzle dimensions and conditions (Nathan and Luxton, 1991; Nathan and Luxton,1992; Nathan et al. 1992). The effect of the unsteady, asymmetric reattachment of the jet-like flow within the 'fluidic' nozzle (Fig.1.1) is augmented by placing a lip at the exit of the short chamber. The exiting jet is then sharply deflected, leaving the cavity at an angle of about 45° from the nozzle axis. This deflected jet precesses about the nozzle axis as the reattachment point inside the cavity precesses. A simple form of the patented fluidic precessing jet nozzle is shown in Fig.1.1. A description of the flow field inside the nozzle is given by Hill (1997). While the above work has provided the stimulus for the investigation described in the present thesis, it is not specifically the subject of the thesis, as discussed in Section 1.1.4.

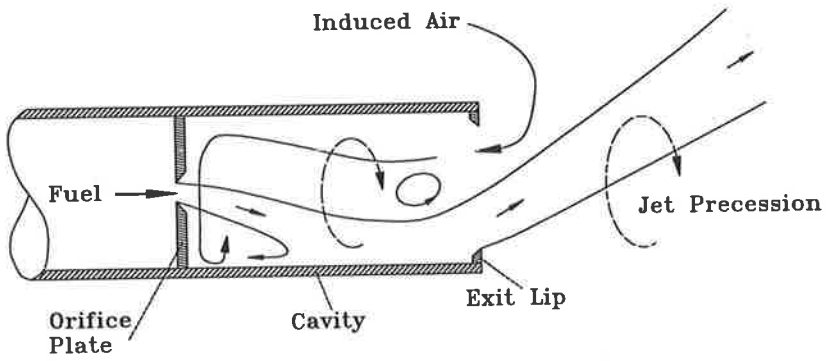

Figure 1.1: **A schematic diagram of the Fluidic Precessing Jet Nozzle**

1.1.3 Industrial Applications of Precessing Jet Flows

Mullinger (1984,1986) has described the importance of burner design in enabling a flame to meet the specific requirements of a given industrial process. Fuel costs can be reduced and product quality, e.g. in the cement industry (Manias and Nathan, 1993, 1994), can be improved, while the emissions are kept low. As noted in the previous section, the fluidic precessing jet nozzle has been patented (Luxton et al. 1988) and is now marketed commercially by FCTI as the GYRO–THERM burner. This burner can be tailored to suit a wide range of applications, in sizes from tens of kilo Watts to more than one hundred mega Watts, and enables the flame shape to be changed during operation. It can generate a bulbous flame with a stand–off distance which is an order of magnitude less than that of a flame from a simple jet burner at compatible throughput. Alternatively, the flame can be made progressively longer and less bulbous, depending on the needs of the product process.

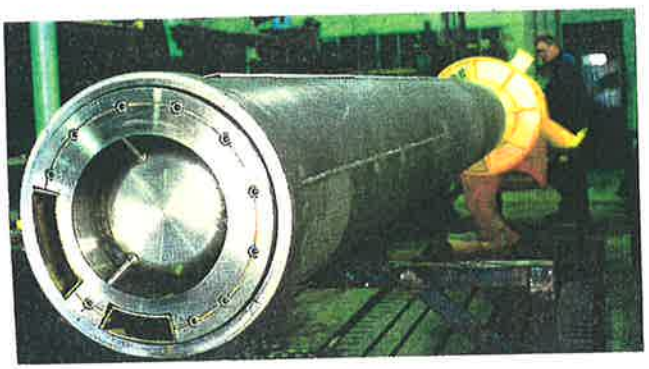

Figure 1.2: **A 100 MW Gyro–Therm burner for a cement kiln in Geelong, Australia**

Measurements in the PJ flame have shown that the maximum time-averaged flame temperature is typically 150°C lower than that of a comparable swirl burner, a result which is consistent with the observed reduction of NO_x emissions, while burn–out, as indicated by low flue CO, is virtually complete (Nathan and Luxton, 1991; Nathan et al.

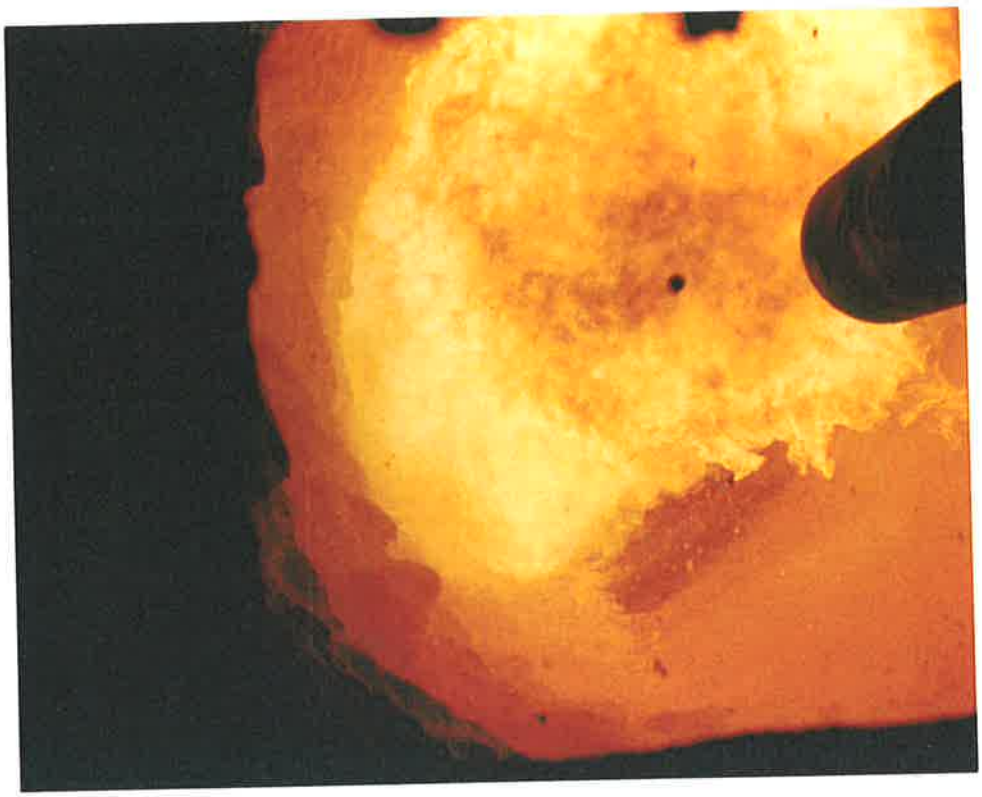

Figure 1.3: **The bulbous, luminous flame of the Gyro–Therm burner in the Geelong cement plant**

1992). In rotary kilns in the cement, lime and alumina industries, the GYRO–THERM burner has been shown to reduce both emissions and specific fuel consumption simultaneously. The burner operates stably over a wide range of driving pressures (0-700kPa) and thus allows exceptional turn–down during operation. Adelaide Brighton Ltd, the holding company of Australia's largest cement manufacturer, has facilitated the commercialisation of the precessing jet technology through the purchase of a substantial majority ownership of the 'Fuel and Combustion Technology' group, a leading international combustion consulting and specialist burner supply company. Information on in–service performance of GYRO–THERM burners operating in the cement industry both in Australia and overseas may be found in Manias and Nathan (1993), Manias and Nathan (1994) and Manias and Nathan (1995). These authors summarise, the major advantages of the burner cement production as being:

- reduction of NO_x emissions by 30–70% with low CO emissions;
- increased kiln output, typically 5%, through better control of heat transfer near the front of the kiln;
- reduced specific consumption, by up to 8%, through a more efficient thermal profile, which closely matches the needs of the process;
- significant improvement in product quality which surpasses existing best practice in the cement industry, also through achievement of a shorter and hotter 'burning' or clinkering zone;
- additional saving of fuel and electricity through reduction of the primary air requirements and improvement of the grinding characteristics of the clinker.

The above dramatic differences all derive from the combustion process and are solely the result of the modifications in the mixing characteristics of the fuel jet caused by the jet precession. While performance results may already be spectacular, the understanding of precessing jet flows is presently limited and design criteria are almost certainly not yet optimal. These limitations in the knowledge base have provided the motivation for the present fundamental study of the precession phenomena.

1.1.4 The Mechanical Precessing Jet Nozzle

To gain insight into the effect of precession on the mixing characteristics of a jet emerging from a nozzle, a mechanically rotated nozzle has been developed (described in detail in Sec.2.1 and Fig.2.1). This nozzle provides an approximate model of the flow field downstream from the fluidic nozzle by mechanically rotating a round jet which is inclined to the axis of rotation. It is this work which is the prime focus of the present

thesis. The mechanical nozzle produces a jet with known initial conditions and also facilitates the conditional phase-averaging of the data based on the phase angle of the precession cycle. In particular, the Reynolds number at the origin, $Re=\frac{u_e d_e}{\nu}$, can be decoupled from the Strouhal number of precession, $St=\frac{f_p d_e}{u_e}$, in a way that is not possible with the fluidic nozzle.

Previously reported measurements in precessing jet flows, generated by both the fluidic and the mechanical nozzles, have revealed the following features of the flow:

- the mixing is dominated by turbulent structures of a scale which is many times that of a free turbulent jet (Nathan and Luxton, 1992);
- the entrainment rate of the precessing jet (PJ) nozzle in the first five exit diameters (Nathan and Luxton, 1992) is approximately five times greater than that of a simple turbulent jet measured by the same absolute method (Ricou and Spalding, 1961);
- the initial spreading of the precessing jet is significantly greater than that of the simple jet (Nathan and Luxton, 1991).

For the mechanical PJ nozzle:

- in the Strouhal number regime $St_p \geq 5 \times 10^{-3}$, the Reynolds stress is increased significantly above that found in a free turbulent jet (Schneider et al. 1995; Schneider et.al. 1996);
- conditional measurements of velocity and pressure contours reveal a low pressure zone between the jet and its spinning axis (Schneider et al. 1993).

1.2 Related Flow Fields

To be able to compare the precessing jet with other jet–like flows, a basic description of the flow topology is necessary (Fig.1.4). The characteristics of the PJ flow field are strongly dependent on the Strouhal number of precession, $St_p = \frac{f_p d_e}{u_e}$, (Section 3). At the lower extremum, St_p=0, the jet flow is identical to a free turbulent jet, as demonstrated in Section 3.1. With a low Strouhal number of precession, e.g. St_p=0.002 as investigated here, the precessing jet characteristics show many of the characteristics of a simple turbulent jet, however the locus of the jet now follows an Archimedian spiral. With increasing Strouhal number of precession, e.g. St_p=0.015 as investigated here, the characteristics of the precessing jet change dramatically. Large deflections of the jet from the original 45^o exit angle are apparent and 'isolated' vortical structures are observed. In the range of precessional Strouhal numbers investigated, the precessing jet flow exhibits characteristics which seperately are associated with many different classes of jet flows. These 'component flows' are discussed in the following sections.

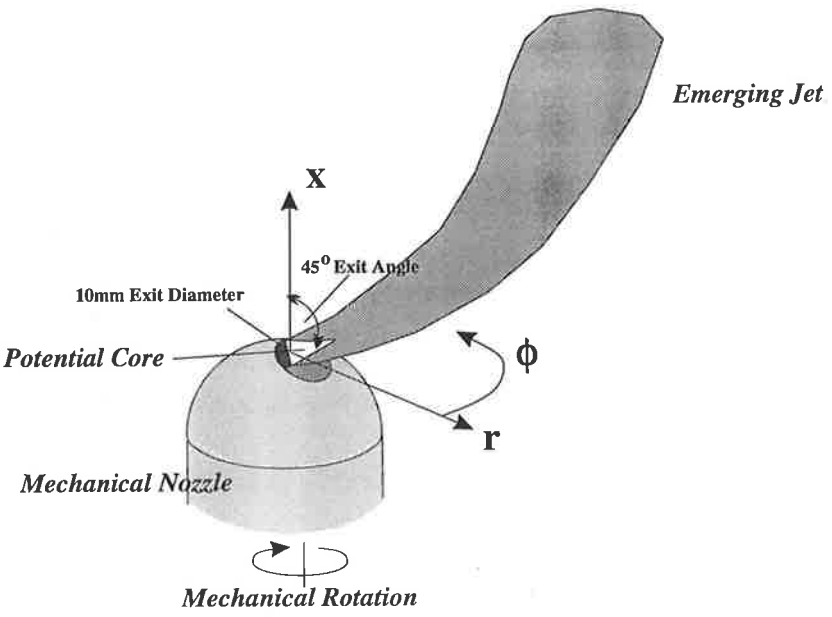

Figure 1.4: **The precessing jet generated by the mechanical nozzle**

1.2.1 Simple Turbulent Jets

The free turbulent jet is a fundamental component of a PJ flow and has been found to be most closely related to the PJ flow in the low Strouhal regime. Given the immense number of studies of free axisymmetric jets described in the literature, the aim of the present review is to establish a baseline for comparison with the PJ flow (of velocity, turbulence etc.). Present understanding of the role of coherent structures in free jets also facilitates the understanding of the precessing jet flow field, not only in the low Strouhal number regime, but also in the high Strouhal number range.

Velocity, Turbulence and Higher Order Statistics: Recorded investigations of jet flows date back to Leonardo Da Vinci in the fifteenth century who, in his seminal work 'Del Moto e Misura dell'Acqua', sketched and described the velocity distribution in a vortex and the velocity profiles of free liquid jets (Rouse and Ince, 1957). The first experimental results on circular turbulent air jets are attributed, by Rajaratnam (1976), to Trüpel. Trüpel measured velocity profiles in an axisymmetric jet with 87m/s exit velocity deriving from a nozzle with an exit diameter of 0.9m and established the well known velocity decay and spreading characteristics of a jet as it entrains fluid from its ambient surroundings.

In his book entitled 'The Theory of Turbulent Jets' Abramovich (1963) has described the character of free turbulent jets. He divided the jet into three parts. The first is the core or initial region, in which a core of potential flow exists. The velocity in that core is constant and entrainment is confined to the boundary of the region. The core ex-

tends from the jet exit to the end of that potential flow region ($x/d_e \approx 6$, Rajaratnam, 1976). The second region, named the transition region, starts where the potential core has been consumed and further entrainment of surrounding fluid causes the centerline velocity to decay. Mean velocity profiles are self–similar in this region, so that the mean profiles in the jet can be characterised by one length scale and one velocity scale. In the third, 'fully developed', region the jet, including its flow structures, becomes fully self–preserving. This third region usually starts some 50 nozzle diameters downstream from the exit (Wygnanski and Fiedler, 1969). Abramovich (1963) measured the half spreading angle of a jet to be 5.54^o, based on the $r_{0.5}$ radius, the radius at which the local jet velocity is half its centerline value. However, subsequent measurements by Wygnanski and Fiedler found the half–angle to be 4.9^o. The growth of the jet and its velocity decay were found by Ricou and Spalding (1961) and Townsend (1966) to be proportional to the entrainment rate. Schneider (1985) confirmed this with an analytical approach and found that the momentum flux in a jet vanishes when the axial distance goes to infinity. He also found the relation between velocity decay on the jet centreline and the axial distance from the origin to be $u_m \sim \frac{\text{const}}{x}$. Measurements of mean velocity profiles with Pitot pressure probes are documented by Hinze (1959). Additional measurements of turbulence in a jet conducted by Corrsin (1943), Corrsin and Uberoi (1949,1951), Corrsin and Kistler (1955), are described by Abramovich (1963) and Rajaratnam (1976). The most comprehensive work is that of Wygnanski and Fiedler (1969), which includes measurements of mean velocity, turbulence, intermittency, skewness, flatness, auto– and cross–correlations etc. Wygnanski and Fiedler also found that self–similarity of the mean velocity is evident a few nozzle diameters downstream from the exit, but true self–preservation of the turbulence intensity is only achieved beyond

50 nozzle diameters. Townsend (1976) found that this slower progress towards self–preservation is due to initial disturbances at the exit which attenuate very slowly.

The work of Tollmien, which is described in Schlichting (1960), investigated self–similarity and self–preservation of a turbulent free jet analytically based on Prandtl's mixing length hypothesis. Schlichting conducted a similar analysis but based it on the assumption of a constant eddy exchange coefficient across the flow. The experimental data in the investigations mentioned above display good agreement with the analytical solutions of Schlichting and Tollmien in parts of the flow. Schlichting's solution provides the best match with the experiments in the inner (high velocity) part of the jet, whereas Tollmien's curve fits better in the low velocity outer region.

Champagne et al. (1976) extended the experimental scope of the above studies to higher order statistics in a two–dimensional mixing region. Gibson (1963) and Antonia et al. (1982) obtained spectra in a jet down to the Kolmogorov scale. Champagne (1978) also examined the fine scale structures in a turbulent field and discovered universal normalised spectral functions which closely describe the fine-scale structures of all turbulent flow fields.

Vortical Structures: Many of the more recent studies of simple turbulent jets examine vortical structures in the jet flow. Perry (1986) states that the vorticity is the most succinct (although difficult to measure) quantity to use in the description of a flow pattern. In fact he calls it the 'genetic code' which leads to a complete understanding of the flow field via the Biot-Savart law. Morton (1984) provides proofs of the long

known but often overlooked fact that vorticity can only be generated at a boundary confining the flow of a viscous fluid. This implies that in a round free jet vorticity can only be generated in the boundary layer within the nozzle up to the nozzle exit. Vortical structures, i.e. the patterns into which the vorticity is confined, on the other hand, can be initiated as Kelvin–Helmholtz instabilities or waves in the shear layer around the jet core close to the nozzle walls. The shear layer starts to grow and rolls into a sequence of toroidal vortex structures (Liepmann and Gharib, 1992) of a preferred mode near the end of the potential core region (Hussain and Zaman, 1981). The characteristic dimensionless frequency, or Strouhal number, $St=\frac{f \cdot d_e}{u_e}$, is based on the exit velocity of the jet u_e, the exit diamater d_e and the frequency of the vortical structure. It has been found to be $St = 0.3$ by Crow and Champagne (1971). Values quoted in the literature vary from 0.2–0.85 and appear to depend on the experimental facility (Hussain 1986).

At the end of the potential core region evidence of coherent structures in the jet was found by Crow and Champagne (1971), Hussain (1983) and Hussain (1984). Crow and Champagne describe instabilities that lead to a pulsatile phenomenon or 'a train of axisymmetric puffs' at Reynolds numbers of the order 10^4, which is the same order of magnitude of the flows in the present investigation. Komori and Ueda (1985) found that flow structures exist both in the near field of the jet and in the self–preserving region, an observation which was also noted by Hussain and Zaman (1981), Dimotakis et al. (1983) and Mungal et al. (1992). These structures are generally understood to be vortices of different sizes which interact and cause the flow patterns to acquire a quasi–periodic motion which enhances turbulence and the entrainment of fluid (Dracos et al. 1992). The ring– or puff–like vortices grow as they move downstream and entrain

fluid. These vortical structures consist of both turbulent outflow of the jet fluid and inflow (entrainment) of ambient fluid.

Large scale turbulent structures have been found to contain the bulk of the momentum and to be responsible for most of the large scale mixing in a turbulent round jet (Chevray and Tutu, 1978). These observations were confirmed by Shlien (1987) who found large scale structures to be responsible for the entrainment in the self–preserving region of the jet (see also Dimotakis et al. 1983, Karasso and Mungal, 1992, Turner, 1986). Further work by Mungal et al. (1992) identified the large scale structures by applying the volume rendering technique. This work also suggests that at high Reynolds numbers, in the absence of solid boundaries, viscosity is not an important parameter in the dynamic behaviour of the dominant large structures, thus the Reynolds number is not a determining parameter in the flow. The spiralling motion in the core of vortical structures is, on the other hand, closely related to the Reynolds stress distribution (Handler et al. 1992; Chandrsuda and Bradshaw, 1981; Klewicki, 1989; Lu and Willmarth, 1973; Klewicki et al. 1993). The definition and results of measurements of Reynolds stresses in the precessing jet flow are presented in Sections 3.2.5 and 3.3.5. Bremhorst (1981) relates the increase in Reynolds stresses to increased entrainment. Structures convected downstream with different speeds interact and intensify the counter–rotating motion thus aiding the ejection and inflow of fluid particles and also increasing the Reynolds stresses (Bernard et al. 1995; Klewicki et al. 1993; Paschereit et al. 1992). Liepmann and Gharib (1992) have described a streamwise secondary vortex structure which folds around the upstream and downstream primary structures, enhances the vorticity and hence stimulates the entrainment and Reynolds stresses respectively.

1.2.2 Vortex Puffs

The vortical structures in a simple turbulent jet that were described in Section 1.2.1 are believed to be significant in the evolution of flow motions in precessing jet flows (Section 4.4). In the high Strouhal number regime of the precessing jet, e.g. at St_p = 0.0098 and 0.015 as investigated here, the motion of the vortex puffs, described by Crow and Champagne (1971) as a 'train' for a free turbulent jet, is dramatically altered. The puffs tend to group beside, rather than behind, each other and appear to coallesce to form much larger vortical structures.

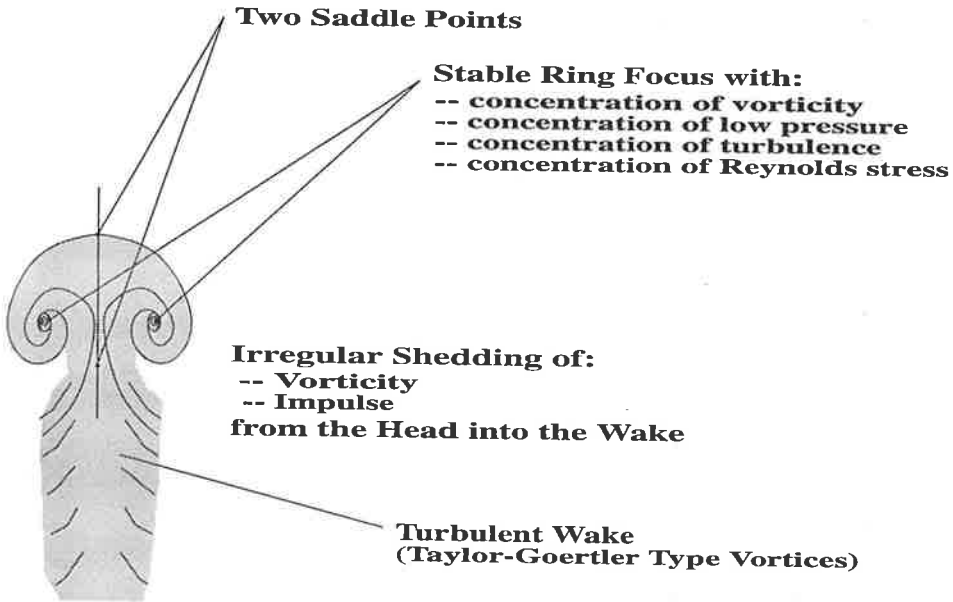

Figure 1.5: **Turbulent Vortex Puff (after: Glezer and Coles, 1990; Richards 1965)**

The flow field of a turbulent vortex puff or ring has been investigated by many authors, e.g. Maxworthy (1974 and 1977) and Glezer and Coles (1990). Although the

vorticity in a vortex ring is concentrated in the torroidal core, while that in a vortex puff is more uniformly distributed, in most applications this difference is insignificant(Glezer and Coles, 1990).

The dominant features of a turbulent puff (Fig.1.5) are the two stagnation points (and also saddle points), which are situated in front and on the lee side of the puff on the axis of symmetry. The other important characteristic is the stable ring focus, where the turbulence intensity is highest due to the largest velocity gradients. At the focus, the vorticity is concentrated and its vector lies in the azimuthal direction. The circulation for a vortex ring decreases as the structure is convected downstream, since irregular shedding (transfer) of vorticity occurs into the turbulent wake (Glezer and Coles, 1990), which entrains fluid constantly. In the near wake the radial component of the velocity is negligible and the vorticity, which is concentrated in Taylor-Görtler type structures is predominantly in the azimuthal direction.

Turner (1964) studied a series of vortex rings and puffs and defined them by two characteristic length scales (ring diameter and core thickness) and two characteristic velocity scales (propagation and circulation about the core), whereras more diffuse turbulent puffs possess only one characteristic length and velocity scale. Studying the dynamics of vortex rings and puffs, Richards (1965) found that the size of puffs grows in direct proportional to the distance travelled and that the distance travelled by a non–buoyant cylindrical puff is proportional to $t^{1/3}$. A puff grows along enveloping cones and is therefore asymptotically self–similar. The angles of the cones can vary significantly, depending on the source (Morton et al. 1994). High turbulence and Reynolds stresses

were found near the core of the vortex ring by Glezer and Coles (1990). This indicates large entrainment rates. They also suggest that secondary structures (Taylor–Görtler type) are wrapped around the core in azimuthal planes. Lee and Rodi (1994) presented a numerical study containing the pressure and velocity distribution in a turbulent puff. They found significant loss of initial impulse due to pressure influence and intense mixing in front of the puff.

In the precessing jet flow two features of the vortex puff are hypothesised to have an important influence on the overall flow field: the low pressure region which is concentrated in the toroidal core of the vortex ring and the negative axial velocity on the outer side of the ring focus. This leads to an asymmetry in the velocity and pressure field of the PJ flow, the degree of which is a function of the Strouhal number of precession. The phenomenon and its effect will be discussed in Chapter 4.

1.2.3 Flapping Jets

A planar analogue of the precessing jet flow is the oscillation or flapping of a planar (flip-flop) jet. However, there are also significant differences between the two flows. For example, no time–averaged recirculation flow zones or transverse pressure gradients are developed in the flapping jets investigated to date, while these features dominate the flow characteristics of precessing jet flows. At the same time, analogous structures can be expected in both flows since, in both cases, the momentum source is continuously re–directed from behind the flow structures, leaving them to be convected downstream in a somewhat 'isolated' fashion. This could be responsible for the high velocity decay and increased entrainment rates which have been found in both flows.

By detecting a negative correlation between the two sides of the planar turbulent jet Cervantes de Gortari and Goldschmidt (1981) showed that an inherent flapping instability exists in the shear layer region of a turbulent planar jet. This flapping motion was found to be related to the development of large scale coherent movement in the jet. The development of a planar jet and its structures can be altered significantly by exciting the jet using various means. Simmons et al. (1981) and Badri Narayanan and Raghu (1982) oscillated a vane placed in the potential core region of the jet, whereas Simmons et al. (1978) used an oscillating nozzle. A bi–vane system was studied by Badri Narayanan and Platzer (1987). For the jet resulting from separation in a two–dimensional wide angle diffuser, Viets (1975) had earlier found that a fluidic feedback loop could maintain a continuous flapping instability in the diffuser and Favre-Marinet et al. (1981) found the same result by alternate blowing from either side wall of the diffuser. The results of all these investigations show that the excitation of large–scale flapping motions in a planar jet results in increased spreading angles of the jet of up to a 33 degrees half angle in the study by Badri Narayanan and Raghu (1982) and increased entrainment rates of up to 50% in Galea and Simmons (1983). No similarity of the streamwise velocity profiles in the near field of the jet has been identified (Piatt and Viets, 1979) and significant fluctuation of the tranverse velocity component is observed, probably related to the large scale coherent structures in the jet. A substantial increase in turbulence energy in the near field of a flapping jet and a rapid decay in mean velocity has recently been found by Mi et al. (1995).

1.2.4 Pulsed Jets

When viewing the near field of precessing jet flows from a fixed (Eulerian) spatial position in the path of the jet, an observer will detect one pulse of jet flow with every precession cycle. The frequency of the arriving pulses is identical with the frequency of precession in the near field of the jet. This pulsatile behaviour of the precessing jet in a stationary coordinate system has strong similarities to the flow in an axisymmetric fully pulsed jet.

Studies of a pulsed round jet show higher spreading angles and more rapid velocity decay when compared with a simple turbulent jet (Hill and Green, 1977). Bremhorst and Harch (1978) and Bremhorst and Watson (1981) examined the increase in the entrainment rate in a pulsed jet relative to a free turbulent jet. Bremhorst (1979) measured higher rates of decay in mean velocity and a related increase in the spreading angles of a range of pulsed jets when compared with a simple turbulent jet. Bremhorst and Hollis (1990) have discussed the characteristics of a round pulsed jet and relate the higher entrainment rates in a pulsed jet to increased Reynolds stresses. They also found a 9% increase in the axial momentum decay in the first five nozzle diameters downstream from the exit. This was found to be equal to a static pressure decrease in the pulsed jet, as required by Newton's second law or 'conservation' of momentum.

Because the pulsed jets in the above experiments are generated by rapidly opening and closing a valve, a cyclic compression wave created by the opening and closing mechanism travels downstream with sonic speed. The jet fluid exhausts into the resultant pressure field. The phenomenon of the compression wave is not present in the precessing

jet, hence the puff structures do not experience a disturbed pressure field in each cycle. Therefore the opportunity for a direct comparison between the precessing jet flow and the pulsed jet flow is limited.

1.2.5 Jets in a Cross Flow

A jet in a cross flow may seem, at first sight, to be analogous to a precessing jet, if one assumes the relative 'cross flow' increases with radial distance as the precessing jet is rotated (i.e. solid body rotation of a jet). But this picture is inaccurate since the equation $u_t = 2\pi f_p \cdot$ r is only valid for a solid body rotation. Since the jet investigated here leaves on the axis of rotation it does not possess any inherent tangential velocity component. Also a Galiean transformation from a fixed x–y coordinate system to a rotating cylindrical coordinate system is not valid, since it does not allow the pressure field to be transformed. However, the jet may experience a small cross flow in some circumstances because the induced pressure field downstream from the potential core in the precessing jet creates secondary tangential velocity components. This phenomenon though, is only significant in the higher Strouhal number flows.

Comprehensive studies of jets deflected by cross flows have been published by Keffer and Baines (1963) and Pratte and Baines (1967). Crabb et al. (1981) and Catalano et al. (1989) measured mean velocity profiles and found the shear stress profiles were high. They have related the bending of the jet to the pressure gradient across the jet. Fric and Roshko (1994) identified **four types of structures in a jet in a cross flow**. The interaction of the crosswind with the emerging jet results in **horse–shoe vortex**

structures at the wall around the jets. In the wake–like region adjacent to the floor behind the jet, **wake vortices** develop and extend from the wall to the jet and a small momentum deficit exists which is smaller than that in the wake of a solid body. The cross flow boundary layer at the wall is the origin for the wake vortices shed into the wake–like region (Fric and Roshko, 1994). A third type of vortical structure develops in the **shear layer of the jet** (e.g. by Kelvin–Helmholtz instabilities). Andreopoulos (1985), Fric and Roshko (1989), Sykes et al. (1986), (Fric and Roshko 1994), demonstrate that the shear layer in the near field starts to roll into a **counter rotating vortex pair**. The work of Bousgarbies et al. (1993), Lim et al. (1992) and Bousgarbies et al. (1993) uses flow visualisation to show the influence of the ratio of the cross wind to the jet velocity on the vortical structures in the shear layer of the jet. The pair of counter rotating vortices which develop are responsible for an increase in the mixing (Kamotani and Greber, 1972; Birch et al. 1989).

In the precessing jet flow investigated here two of the above four structures found in jets in a cross flow can also be expected and these have been identified in flow visualisation experiments (Section 4). The shear layer around the jet (Fig.4.2) and the counter rotating vortex pair have both been identified in the precessing jet flow (Fig.4.13). The vortices related to the jet–wall interaction are insignificant here, since a stationary sleeve is used around the mechanical nozzle to reduce wall effects (Section 2.1.2).

Rajaratnam (1976) divided the jet in a cross flow into three distinct regions based on the counter rotating vortex pair. The first region is the potential core region where the vortex rings develop and the cross wind causes little deflection. In the second region the

vortex pair grows in size as it entrains fluid. In this region the jet experiences maximum curvature and maximum deflection. In the third region of the jet the vortical structures still grow in size while entraining fluid, but the curvature tends asymptotically to zero. Wu et al. (1988) have extended the investigation of the counter rotating vortex pairs to include jets from non–circular nozzles. Needham et al. (1988) has explained the jet deflection, the deformation of the vortex pairs and the axial vorticity using an inviscid analytical model. Catalano et al. (1991) examined the fine scale structures and higher order statistics of turbulence over a wide range of Reynolds numbers and found a range of different values of the integral scale in the flow field. Smith et al. (1993) and Lozano et al. (1993) have recently demonstrated, using instantaneous pictures of a jet in a cross flow, that the counter rotating vortex pairs are not symmetric relative to the centerline of the jet. This may be explained by a low frequency instability causing the vortices to oscillate (Fric and Roshko, 1994, Kelso et al. 1997). Low frequency oscillations have not yet been identified in the precesing jet, but observations indicate some similarities to the low frequency instabilities in a jet in a cross flow. However, that aspect of the flow is not subject of this investigation.

1.2.6 Swirling Flows

As emphasised in the previous section, the precessing jet investigated here exits on the axis of rotation and hence does not develop any direct tangential velocity. The tangential components measured are caused by secondary effects. In the high Strouhal number regime, examples of which investigated here are at St_p=0.0098 and 0.015, the jet is deflected towards the axis of rotation, due to a radial pressure gradient which is directed

towards the axis, until the flow becomes independent of Φ and can be represented wholly on the r–Φ plane. This result can be interpreted as a transfer of axial momentum into the tangential component which results in the generation of a centripetal pressure field. This phenomenon is the inverse of that observed in swirling jet flows where the intial tangential velocity causes a low pressure and recirculation zone to be established to due centripetal forces.

Kavsaoglu and Schetz (1989) induced swirl in a jet issuing into a cross flow and found a shortening of the potential core region and an increase in the turbulence levels in the jet. The characteristic feature of a swirling jet is the presence of a tangential velocity component, which produces a centripetal motion and establishes a low pressure core. If the swirl is high enough the low pressure core becomes strong enough and a core recirculation zone can develop which enhances mixing. High velocity gradients found near the edge of the recirculation zone result in higher Reynolds stresses and hence in enhanced turbulent entrainment and mixing.

Syred et al. (1973) and Syred and Beer (1974) discovered that the aerodynamic flow patterns in a swirling flow of sufficient strength to create recirculation, is dominated by a fluid mechanical instability which they termed a 'precessing vortex core' (PVC). The PVC is superimposed on the recirculation zone. It is an asymmetric and highly three–dimensional flow field which creates increased mixing (Syred et al. 1992). Syred and O'Doherty (1992) have found and quantified tangential velocity components by use of a three–dimensional LDA system which are in the opposite direction from the swirl. Froud et al. (1994) has expanded this study with measurements of phase–averaged velocity profiles at different distances above the exit.

1.2.7 Jets in Rotating Systems

Flow in a general rotational system has been documented by Greenspan (1968) and by Tritton (1988). Greenspan (1988) extended the earlier theoretical studies by considering the distribution of vorticity in a rotating, initially homogeneous, mixture of particles and fluid. The governing Navier Stokes equations for a rotating cylindrical coordinate system in a turbulent flow are derived by Hinze (1959). Gadgil (1970) found, in his investigation of the structures of jets in rotating systems, a strong dependence upon the rotation of the system. In the slowly rotating case, Rossby number Ro$\gg$ 1, the characteristics of the jet are essentially identical to those in a non–rotating system. The Rossby number is defined as $Ro = u/(\Omega d)$, where u is the velocity of the fluid, Ω is the angular velocity and d is a characteristic length scale (e.g. jet diameter).
The jet entrains fluid at its boundaries and the momentum flux is independent of the downstream distance. With an increase in the rate of rotation of the system, Ekman layer effects become important. The jets starts to eject fluid at its edges and the momentum flux decreases with the axial distance due to dissipation in the Ekman layer.

Gadgil (1970) also presented a similarity solution for a rapidly rotating case. Page and Earbry (1990) have studied the breakdown of jets in strongly rotating systems (Rossby number, Ro$\ll$ 1).

Savage and Sobey (1975) show that the length scale along the spiral path of a jet issuing into a rotating basin of deep water depends upon the rate of rotation. In shallow

water the confining effects of the upper free surface are observed and rotation has only a small effect on the velocity field (Taylor and Proudman; described in Tritton, 1988). The jet path remains straight as for no rotation.

As stated in Section 1.2.5 a Galiean transformation of the precessing jet to a rotating system is not valid. Hence, the precessing jet in an ambient environment cannot be compared directly to a turbulent jet in a rotating system. Nevertheless, jets in rotating sytems provide useful information of overall flow behaviour. The dependence of the structures of the jet on the rotation of the system (Gadgil, 1970; Savage and Sobey, 1975) reveals an especially close relationship to that of precessing jet flows.

Chapter 2

EXPERIMENTAL TECHNIQUES AND APPARATUS

The mechanical nozzle used to generate a jet which precesses under controlled conditions, its driving apparatus and the environment in which the measurements were conducted (e.g. low velocity windtunnel) are described in this chapter. Departures from this reported setup will be mentioned specifically in the appropriate sections. The flow visualisation and measurement techniques are also described and the accuracy of each is discussed.

2.1 The Mechanical Precessing Jet Nozzle

The fluidic precessing jet nozzle, described in Section 1.1, has been demonstrated to have mixing characteristics which are very different from conventional jets. Nathan (1988) has demonstrated that the fluidic PJ nozzle produces a precessing jet flow and has postulated that the precession is a major influence in causing the differences in the

mixing. But that nozzle does not provide conditions at its exit plane which are either uniform or constant. That is, the exit angle, exit velocity, frequency of precession, exit diameter and location of the exiting jet are neither uniform nor well defined. Furthermore the cross section of the exiting jet is not circular (Vidakovic 1995), so that comparison with other data in the literature is difficult. Ensemble–averaged measurements of flow structures in the flow outside the cavity are also difficult and are necessarily subjected to considerable smoothing. To minimise smoothing, to gain insight into the fluid mechanical processes generated by jet precession alone and to facilitate phase–controlled visualisation and measurement techniques, the present fundamental investigation of precessing jet flows was conceived and is the subject of the present thesis. A mechanical nozzle has been designed, termed the 'mechanical precessing jet' nozzle and is shown in Figure 2.1. Appendix F provides technical drawings with precise dimensions.

In contrast to the 'fluidic PJ' nozzle, where the jet precession is naturally induced, with the 'mechanical PJ' nozzle the jet precession is driven mechanically. The design enables precise control of the exit conditions of the precessing jet and the independent variation of each of the characteristic parameters. Figure 2.1 shows a schematic drawing of the nozzle used in the present investigation. The rotating outer nozzle pipe is connected with roller bearings to an inner stationary pipe. The air flow through the pipe passes through a mesh which assists in providing a uniform flow distribution into the rotating nozzle tip. A contraction ratio of *inner tip diameter/jet exit diameter* = *4.4* has been found to provide a low turbulence level with symmetric velocity profiles at the exit (see Sections 2.1.3 and 3.1).

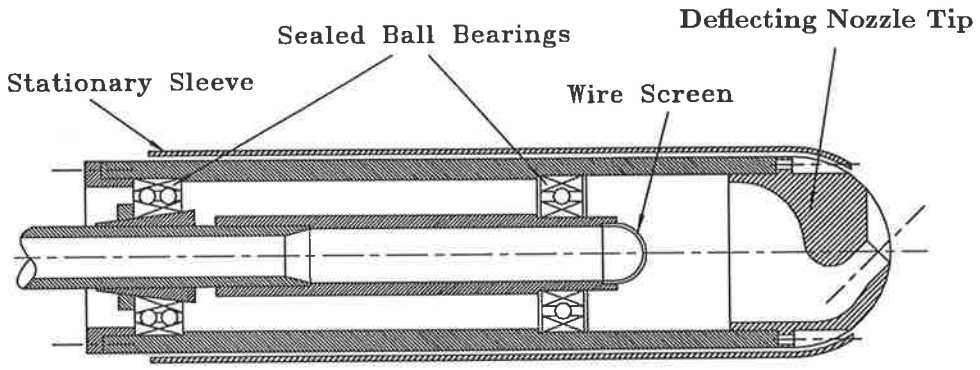

Figure 2.1: **Mechanically Rotated Precessing Jet Nozzle**

2.1.1 The Exit Parameters of the Jet

The significant parameters in a precessing jet flow are exit angle, exit velocity, frequency of precession, location of the jet exit relative to the nozzle axis and the exit diameter of the jet. The exit velocity is measured by means of a *FISHER & PORTER Extruded Body Indicating Flowrator* meter, which is accurate to within $\pm 1\%$ of full scale reading. The frequency of precession is controlled by a TASC Speedstar II (415 Volts, 50 Hz) speed control unit, modified in house to allow frequencies of precession of up to 100 Hz. The unit governs a 370 W electric motor which drives the mechanical nozzle through a tooth belt pulley drive. The chosen frequency of precession can be held constant to within ± 0.25 Hz at the maximum speed of 100 Hz. To obtain a reference signal for the angular position of the nozzle a Hall Effect magnetic sensor which operates at frequencies of up to 100Hz is attached to the lower end of the spinning nozzle. This sensor allows the data records to be conditionally averaged and facilitates accurate measurements of the frequency of precession. The remaining parameters (the location of the jet exit relative to the nozzle axis, the exit diameter and the exit angle) are varied by changing the rotating nozzle tips themselves. For all the cases discussed in this work the origin of the

jet is chosen to be on the spinning axis and the exit diameter of the jet is 10mm. Two exit angles for the nozzle, 0° and 45°, are used. The $\alpha_e = 45^o$ tip is shown in Figure 2.2. Both nozzle tips have been designed using the AUTOCAD drawing package to ensure that their critical dimensions, ie contraction ratio, exit diameter and curvature along the contraction, are kept constant as far as possible. The designs are loaded directly into the MASTERCAM program for a CNC mill. Good repeatability of the dimensions is ensured through a maximum deviation of the CNC mill of 0.02mm. Each of the nozzle tips were found to produce an exit velocity profile which conforms with that of a 'top hat' profile used in conventional jets when the nozzle is not rotating. Tests of the apparatus, with particular attention being paid to the exit condition of the nozzle, are described in Section 2.1.3 for the 0^o nozzle and in Section 3.1 for the 45^o nozzle.

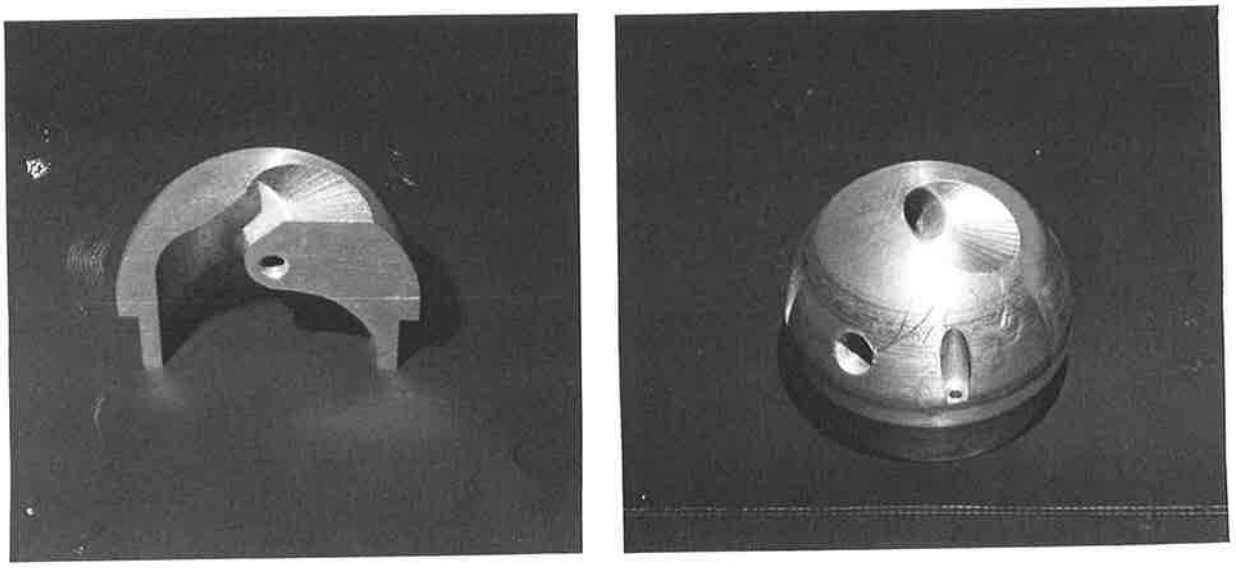

Figure 2.2: **The nozzle tip with $\alpha_e = 45^o$, nozzle exit diameter d_e=10mm**

2.1.2 External Influences: A Boundary Layer Study

A smoke visualisation technique (Section 2.3.1) has been utilised to assess the influence of the external boundary layer of the rotating nozzle on the general flow field. For this study the 45°, 10mm nozzle tip was used. Images were recorded with a KODAK EktaPro 1000 high speed video camera (Section 2.3.1) with a 1000W Halogen U-Lamp to illuminate the flow field. A dense cloud of smoke (Section 2.3.1) was produced around the unshielded nozzle (ie without the 'stationary sleeve' shown in Fig.2.1) which was rotated at a frequency $f_p = 60Hz$ (the maximum rotational frequency in this investigation), and with no jet flow ($u_e = 0m/s$). A small but noticable boundary layer effect was observed in the region close to the nozzle tip.

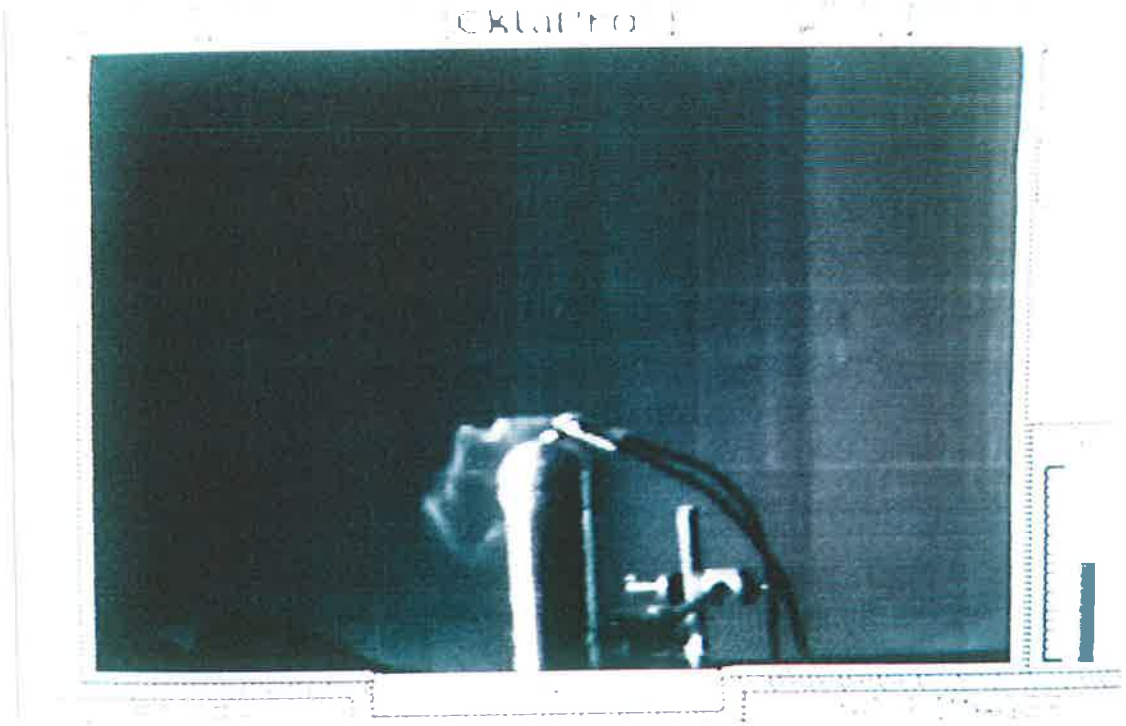

Figure 2.3: **The influence of the external boundary layer produced by rotation of the mechanical nozzle. Smoke visualisation, no external sleeve, $u_e = 0m/s$, $f_p = 60Hz$**

The smoke was drawn towards the nozzle tip (indicating a reduced pressure around the tip), spiralled in the direction of the rotation (negative Φ-direction) inwards (negative r-direction) and moved downwards (negative x-direction) along the outside of the mechanical nozzle (Fig. 2.3). Based on the framing rate of the camera the typical convection velocity of smoke structures was estimated to be 0.5m/s. While this is small compared with the typical exit velocity of the jet (39m/s), it can be eliminated almost completely by placing a stationary sleeve around the spinning nozzle (Fig.2.1). With such a sleeve no inward or downward motion is detectable using the above technique (Fig. 2.4). A very weak inconsequential swirl with a convection velocity of the order of 0.1m/s to 0.01m/s is detectable in the region immediately around the exit hole of the jet.

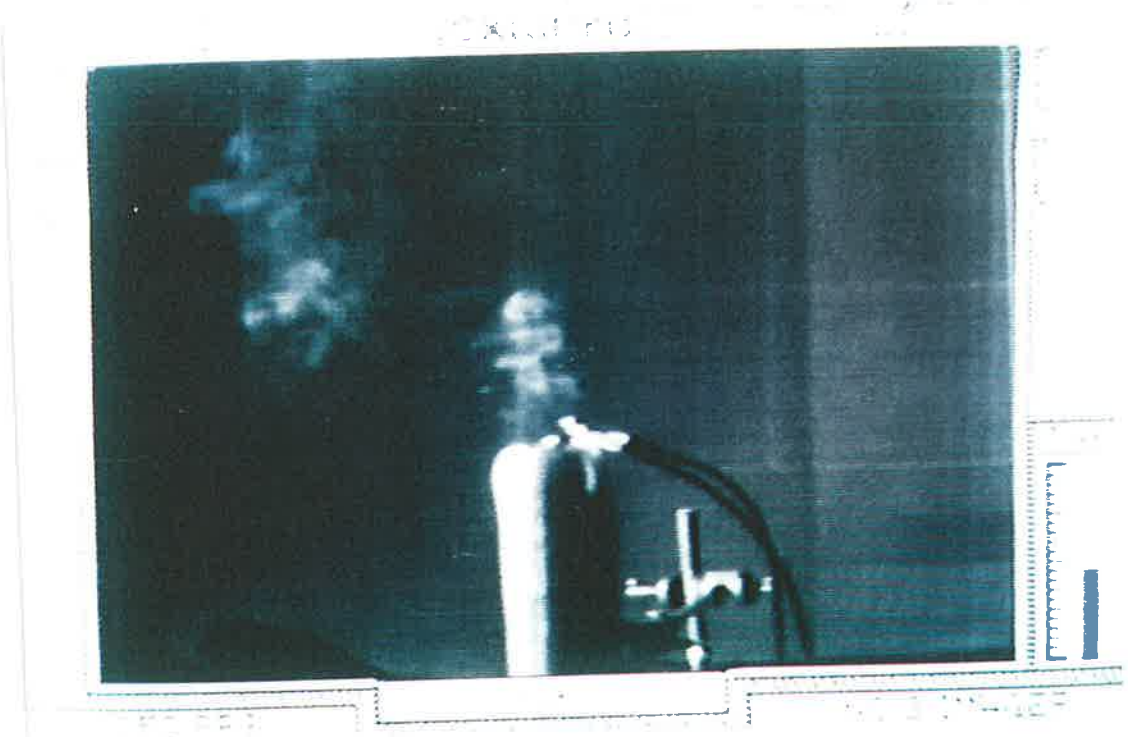

Figure 2.4: **Reduced external boundary layer effects produced by rotation of the mechanical nozzle. With external sleeve, $u_e = 0$m/s, $f_p = 60$Hz**

Overall the stationary sleeve reduces the spurious flows associated with the boundary layer on the spinning nozzle to at least two orders of magnitude less than any of the significant flows produced by the jet. It can be concluded therefore that the influence of the external detailed shape of the nozzle and the boundary layer around it is negligible when the stationary sleeve is placed around the mechanical nozzle. All results and examinations presented in this thesis have been conducted with the stationary sleeve in place.

2.1.3 Internal Influences: The Jet Issuing from the Nozzle

The influence of the internal assembly of the mechanical nozzle (meshes, contraction ratio etc.) on the issuing jet has been examined using the 0° nozzle tip. This enables a direct comparison with a simple turbulent jet to be made by measuring exit velocity profiles, self–similarity and turbulence intensity. To exclude all influences from surrounding ambient flows, these measurements were conducted in the low velocity wind tunnel described in Section 2.2. A small co–flow of 0.03m/s is provided to satisfy the entrainment appetite of the jet up to a distance of $x/d_e \approx 40$ from the nozzle exit, following Ricou and Spalding (1961). Measurements were only conducted up to $x/d_e=14$. By using the 0° nozzle tip it is possible to investigate the magnitude of the swirl in the jet induced from within the spinning nozzle tip. These effects were tested using an exit velocity of 23.33m/s (Re=15,553) and a rotational frequency of 35Hz (equivalent to $St_p = 15 \times 10^{-3}$), corresponding to the highest Strouhal number examined in this work. The exit conditions have been measured with the Cobra probe (see Section 2.4.2) which has the ability to detect the three components of velocity within an acceptance cone angle of 90°.

Measurements were taken from r/d_e=0 to r/d_e=4 in 5mm steps, in 7 different planes above the nozzle x/d_e=2 to x/d_e=14 in steps of 20mm. A statistically significant total of over 10,000 data samples was collected for each spatial position.

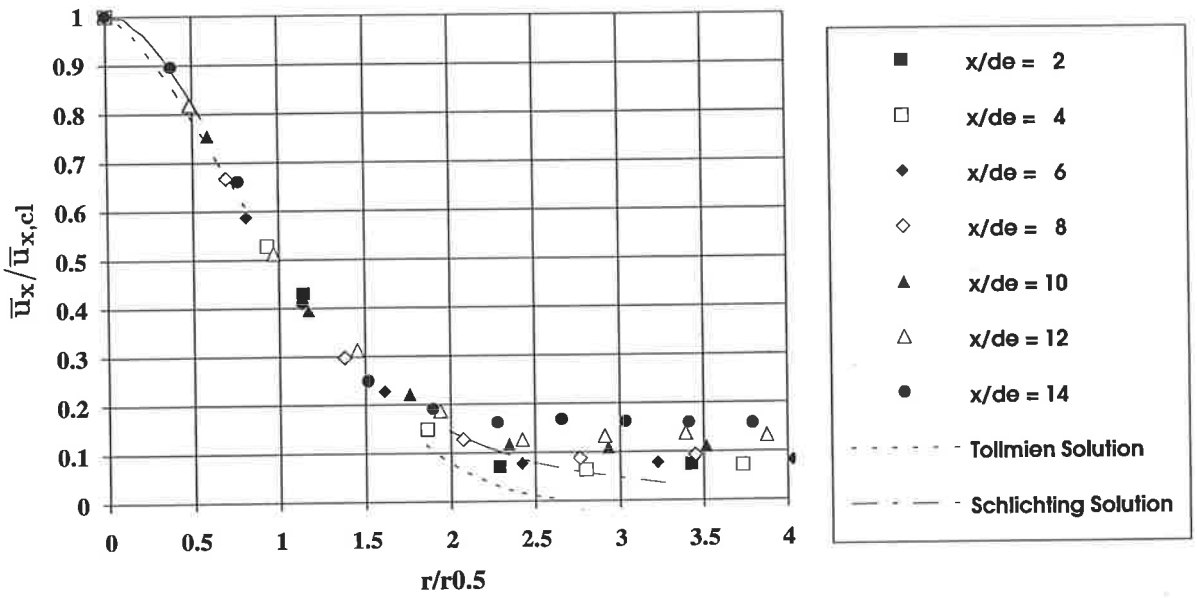

Figure 2.5: **Self–similarity of the jet produced by the spinning nozzle for $\alpha_e = 0^o$, co–flow velocity = 0.03m/s, Re=15,550, St_p=0.015**

The mean axial velocity profiles are presented in Figure 2.5 in normalised form. The local velocity is referred to the centreline velocity of the jet and the radial dimension is normalised on the half-width of the jet (i.e. the radial position at which the mean velocity is one half of its value on the axis). The results of the measurements are compared with two theoretical models predicting the shape of the velocity profiles in a simple turbulent jet with a uniform exit velocity profile. Tollmien's solution (1926) is based on the mixing length hypothesis, whereas Schlichting (1961) based his theory on constant eddy exchange coefficient across the flow. Both theories were found to be in good agreement with experimental investigations (Wygnanski and Fiedler, 1969; Rajaratnam, 1976). The experimental data for the 0° nozzle, obtained with the Cobra

probe, shows good agreement with the predicted values to about $r/r_{0.5} = 2.25$ (Fig.2.5). Beyond that point, the limitations of the Cobra probe and the pressure transducers respectively in low velocity regions become significant. Nevertheless, it confirms that the jet issuing from the 0^o mechanical PJ nozzle displays reasonable self–similarity and also conforms to the similarity expected of a simple turbulent jet, even when the mechanical PJ nozzle is rotated at a frequency equivalent to the highest Strouhal number regime used in the present work.

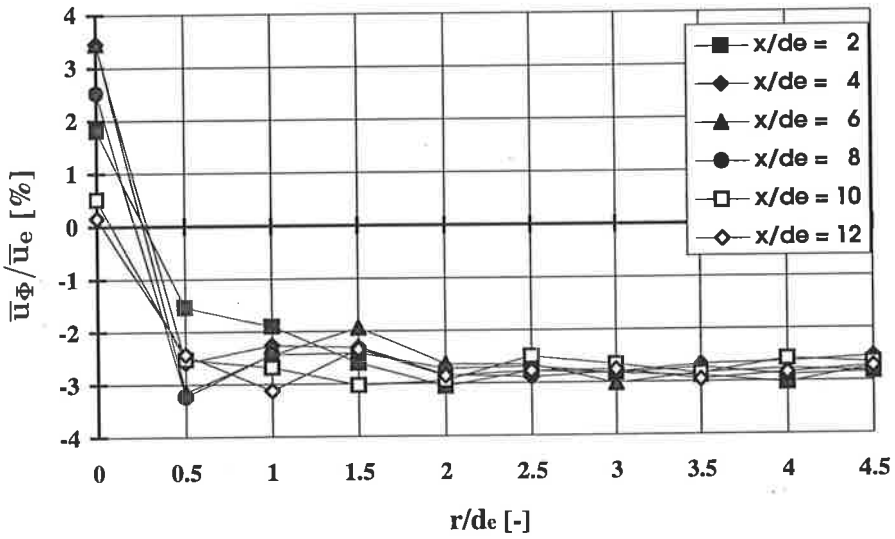

Figure 2.6: **Induced tangential velocity of the jet produced by the spinning nozzle for $\alpha_e = 0^o$, co–flow velocity = 0.03m/s, Re=15,550, St_p=0.015**

The tangential velocity components induced through the spinning motion are shown in Fig.2.6. The time–averaged tangential, or swirl, velocity component in the precessing jet flow is normalised on the exit velocity and the radius is divided by the exit diameter of the jet. The tangential velocity on the centreline of the jet is at its maximum only $\pm 3.4\%$ of the exit velocity, which can be regarded as insignificant. In the lower velocity regions of the jet, in the radial and axial directions, the values drop below the resolution of the Cobra probe.

Another important comparison of the jet produced by the spinning nozzle is the turbulence intensitiy. A comparison of the results of the spinning jet with a curve reproduced from Wygnanski and Fiedler (1969) is shown in Figure 2.7. The experiments show that turbulence increases with axial distance from x/d_e=2 so that at x/d_e=12 the data is approaching Wygnanski and Fiedlers's data measured at x/d_e=20 when allowance is made for the small co–flow velocity. This demonstrates that the turbulence levels in the spinning jet issuing from the present mechanical nozzle are comparable with those found in simple turbulent jets measured by others.

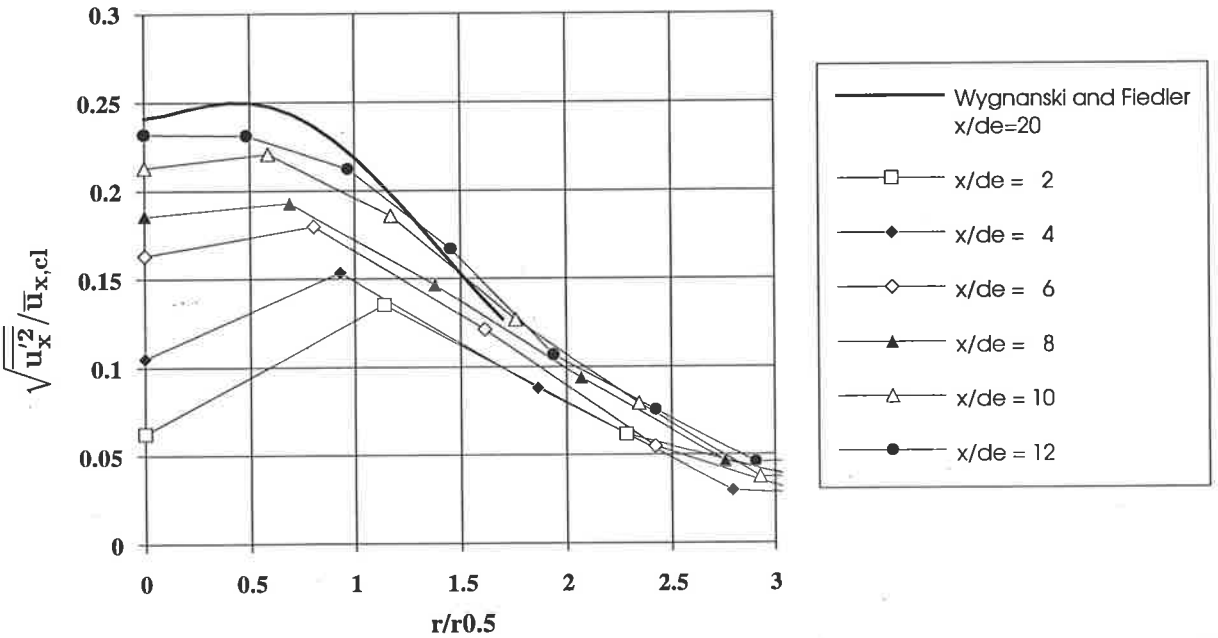

Figure 2.7: **Turbulence Intensity of the jet produced by the spinning nozzle with $\alpha_e = 0^o$, Re=15,550 and St_p=0.015**

Detailed data for the jet issuing from the 45° inclined mechanical nozzle is presented in Section 3.1.

It can be concluded that the jet which is produced by the present spinning mechanical PJ nozzle compares well with simple turbulent jets investigated elsewhere and that neither

the nozzle itself nor the spinning motion significantly influence the resulting flow field. Thus, the mechanical PJ nozzle is an appropriate tool for investigating the effect of precession on the mixing characteristics of a jet.

2.2 The Low Velocity Wind Tunnel

2.2.1 Design and Layout

A low speed wind tunnel has been designed, following Pankhurst and Holder (1952), Bradshaw (1968) and Bradshaw and Pankhurst (1964), to provide well defined boundary conditions and well known surrounding co–flow. The enclosure isolates the jet from variations in laboratory conditions, such as cross draughts and temperature, and provides a small co-flow, just sufficient to satisfy the entrainment of the precessing jets up to at least x/d_e=40 and to avoid attachment of the jet on the tunnel walls. An empirical equation for the entrainment of a simple turbulent jet is given by Ricou and Spalding (1961):

$$\dot{m}_{tunnel} = \dot{m}_{jet} \cdot 0.32 \cdot \frac{x}{d_e} - \dot{m}_{jet} \tag{2.1}$$

where $\dot{m}_{tunnel}$ is the mass flow rate in the wind tunnel (co-flow), $\dot{m}_{jet}$ is the mass flow rate through the (precessing) jet nozzle at the nozzle exit, x/d_e is the axial position downstream from the jet exit and 0.32 is an empirical constant found by Ricou and Spalding (1961). Nathan (1988), using a similar entrainment shroud to that used by Ricou and Spalding (1961), repeated their entrainment measurements for a simple turbulent jet and extended them to the precessing jet. He found the maximum entrainment for the precessing jet, which occurs over the first 5 diameters, to be

$$\dot{m}_{tunnel} \approx \dot{m}_{jet} \cdot 1.48 \cdot \frac{x}{d_e} - \dot{m}_{jet} \tag{2.2}$$

This is four to five times higher than the entrainment rate of a simple jet. These data were obtained using the fluidic PJ nozzle (Section 1.1). Applying both equations 2.1 and 2.2 and entering 'maximum flow scenarios' gives an estimate of the maximum co-flow for which the wind tunnel needs to be designed. The maximum axial distance at which measurements are taken is x/d_e=15, the maximum exit velocity of the jet in the present investigation is 45m/s and the exit diameter of the jet is always 10mm (see Section 2.1). Substituting these values into the continuity equation with $\rho = 1.22\text{kg/m}^3$ yields

$$\dot{m}_{\text{jet}} = 1.22\text{kg/m}^3 \cdot \pi \cdot 0.005^2\text{m}^2 \cdot 45\text{m/s} = 4.312 \times 10^{-3}\text{kg/s}. \tag{2.3}$$

Calculating the mass flow for the tunnel using equation 2.1 and rearranging the continuity equation gives a required co-flow velocity in the tunnel of $v_{\text{tunnel}} = 0.017\text{m/s}$ for a simple turbulent jet. Following the same procedure for the precessing jet but using equation 2.2 gives a maximum required co-flow velocity of 0.08 m/s. Note that this calculation is conservative, since the empirical constant of 1.48 only applies for the first five exit diamters of the PJ flow. To be more conservative, while still providing a low velocity such that its influence on the main flow is negligible, the wind tunnel was designed to have a maximum co–flow velocity of $\leq$0.12m/s.

The wind tunnel has been custom designed and built to suit the dimensions of both the mechanical nozzle and the laboratory in which it is housed. It provides a well defined boundary condition and this boundary condition is also being used in a collaborative numerical modelling program at the Pennsylvania State University (Manohar 1994). Hence data from the present experiments can be used to validate the numerical solutions. Figure 2.8 shows the overall design of the tunnel based on the above criteria.

The tunnel is cylindrical and operates under an induced draft. This arrangement allows access to the mechanical nozzle through the base and also eliminates disturbances in the test section which could have been produced by a fan. To eliminate flow separation at entry, thus to produce uniform inlet conditions and minimise pressure losses, the entry is in the form of a bellmouth (Mehta, 1977; Mehta and Bradshaw, 1978). Salter (1966) suggested in his review of 'Low speed wind tunnels for special purposes' that the radial thickness of a truncated bellmouth ring should be greater than 3/8 of the tunnel diameter. In our case, with a diameter of 1m, the optimal thickness of the ring should, by Salter's criterion, be 0.375m. However due to spatial restrictions and high manufacturing costs a diameter of only 0.080m could actually be accommodated. It was reasoned that if separation was apparent during commissioning, the bellmouth could be faired smoothly down to the outer surface of the cylindrical tunnel. However the velocity profiles, presented later, show that the additional fairing was not necessary to achieve the required uniformity of the flow in the test section. Since there was no special requirement to keep a low turbulence level in the tunnel, and also to minimise pressure losses, neither honeycomb flow straighteners nor a contraction section other than the bellmouth were required. Two screens were used to reduce the boundary layer thickness and reduce the effect of the rotating nozzle drive on the velocity profiles. The screens are placed 320mm downstream from the inlet to allow enough space to position the mechanical nozzle and its drive apparatus on the axis of the wind tunnel. Various sources (e.g. Bradshaw and Pankhurst, 1964; Mehta and Bradshaw, 1978; Engineering Science Data Unit, 1963) note that the total pressure drop coefficient, K, through the screens should be about 2.0. This is adequate to remove nearly all variations in the longitudinal mean

	Aperture [mm]	Diameter [mm]	Mesh size [mm]	β [-]	K [-]
Mesh1	0.5	0.32	0.815	0.37	1.67
Mesh2	2.0	0.45	2.450	0.67	0.29

Table 2.1: **Meshes used in the inlet of the low speed wind tunnel**

velocity, to provide uniform velocity profiles and to reduce the turbulence intensities. The equation used to calculate the coefficient K for a simple woven mesh screen is

$$K = 6.5 \cdot \frac{(1-\beta)}{\beta^{5/3}} \cdot \left(\frac{Ud}{\nu}\right)^{-1/3} \tag{2.4}$$

developed by Wieghardt (1953), where U is the tunnel velocity, d is the screen wire diameter, ν is the kinematic viscosity and β is the open area ratio. For a series of non–interacting screens the K values are additive. The equation for β is given by

$$\beta = (1 - d/M)^2 \tag{2.5}$$

where M is the mesh size. Mehta and Bradshaw (1978) note that screens with a value of β which is less than 0.57 tend to produce instabilities in the form of longitudinal vortices and coallescence of the jets from the holes in the screens. Therefore at least one screen should have a value greater than 0.57 and it should be located in the most downstream position. Taking the two main criteria into account (factor K$\approx$2 and $\beta > 0.57$) leads to choice of the two meshes defined in Table 2.1.

Mesh 2 fulfills the criteria of having a β-value greater than 0.57 and the sum of the pressure drop coefficients of the screens is K=1.96 (assuming a velocity of 0.1m/s). Mesh

1 with its low β-value and high pressure drop (high K value) was placed first, at the furthest possible upstream location from the tip of the mechanical nozzle, to minimise influences on the precessing jet flow field. By requiring that the static pressure is to recover from the pertubation caused by the first screen and that the minimum streamwise spacing is to be approximately equal to the scale of the large energy containing eddies from the first screen, thus to achieve maximum turbulence reduction, the minimum spacing between the two screens can be calculated. Three different criteria are applied in practice

- mesh size $\times$ 30 (Bradshaw 1968);
- section diameter $\times$ 0.2 (Mehta and Bradshaw, 1978);
- screen wire diameter $\times$ 500 (Bradshaw 1968).

In our case the first criterion leads to a value of $0.815 \times 30 = 24.45$, the second gives $1000 \times 0.2 = 200$mm and the third $0.37 \times 500 = 185$mm. The dimensions of the mechanical nozzle (Appendix F) allow only a total distance from the first screen to the nozzle tip of 185mm which has been divided in a distance between mesh 1 and mesh 2 of 100mm and a distance from mesh 2 to the tip of 85mm. The 100mm between mesh 1 and 2 fulfulls criterion one for minimum spacing of the screens and goes part of the way towards satisfying criteria two and three. Whilst it might not fully minimise pressure loss or provide maximum reduction in turbulence levels, the aim of the design was not principally to provide low turbulence intensity, but rather to provide well defined boundary conditions and to ensure that the co–flow influence is of second order. Thus, it is argued that the co–flow velocities are sufficiently low compared with the jet flow velocity to ensure that any turbulent disturbances which are introduced through the

co–flow are small, and further they will occur at lower frequencies than those of interest in the turbulent jet. The settling distance of 85mm after the second screen to the nozzle tip is conservative. Mehta (1977) suggests that only a very small settling distance, or none at all, is necessary. The test section has a length of 2m. However measurements were only performed in the near field of the nozzle (x/d_e <20) so the tests for uniformity of the velocity profiles and measurements of the turbulence intensities are conducted in that region only. At the end of the test section the tunnel diameter is reduced to match a standard pipe with a nominal diameter of 100mm to fit the inlet of the centrifugal suction fan (Engineering Science Data Unit, 1963). The fan is connected to the wind tunnel by rubber seals to avoid transmission of vibration into the flow.

The overall design of the wind tunnel is similar to the NPL Aero 18 inch tunnel described by Salter (1966) for use in very low speed experiments.

2.2.2 Calibration and Velocity Distribution in the Wind Tunnel

To measure the low co–flow velocity of approximately 0.12m/s in the low speed wind tunnel accurately, the technique of measuring the vortex shedding frequency behind a circular cylinder was utilised. Roshko (1954) found that a stable and well defined Karman Vortex–Street occurs in a small range of cylinder Reynolds numbers ($40 < Re < 150$). In his experiments, cylinder diameters of 0.235mm to 6.35mm were used. Roshko found the relationship between the Reynolds number ($Re = u \cdot d/\nu$) and the Roshko number ($Ro = f \cdot d^2/\nu$) to be

$$Ro = 0.212 \cdot Re - 4.5 \qquad \text{for} \quad 50 < Re < 150$$

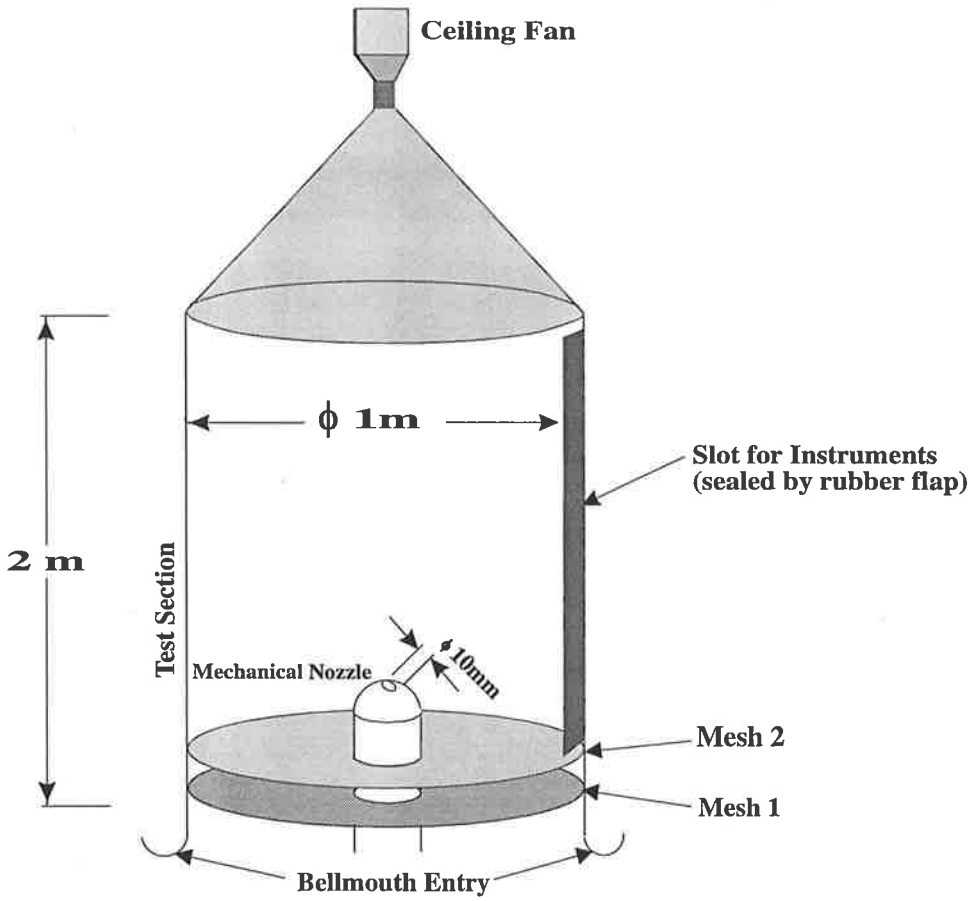

Figure 2.8: **The low speed wind tunnel**

where u is the velocity, f the frequency of the vortex shedding, d the diameter of the cylinder and ν the kinematic viscosity. Gerich and Eckelmann (1982) and Williamson (1989) respectively investigated vortex shedding for low length-to-diameter ratio cylinders, and the effects of the boundary conditions on the angle and the frequency of the shedding. The low speed measurement method derived from these previous investigations, and used here, was developed by Papangelou (1992). He produced a robust vortex shedding anemometer by placing two spheres at a defined distance apart on the cylinder to force the system into parallel shedding. In his investigation two different cylinders were used, one with a diameter of 1.59mm and the other 2.37mm, with spheres of four

times the respective cylinder diameters. The spheres were placed 19 cylinder diameters apart. He found the relation between the Roshko and Reynolds numbers to be

$$d = 1.59 \qquad Ro = 0.194 \cdot Re - 4.032 \qquad \text{for} \quad 60 < Re < 150$$

$$d = 2.37 \qquad Ro = 0.198 \cdot Re - 4.577 \qquad \text{for} \quad 60 < Re < 150$$

To set up the robust vortex shedding anemometer in the present facility for the velocity range of < 0.12 m/s a cylinder with a diameter of 18.895mm has been selected to achieve Reynolds numbers in the range necessary to achieve stable shedding (Re= 60 to 150). Two spheres with d=75.58mm, which is four times the cylinder diameter, were placed 359mm apart on the cylinder (Fig.2.9). A hot-wire anemometer was used to test the uniformity of the flow in the wind tunnel and to ensure the anemometer was positioned in a uniform flow field. The signal from the 1.2 μm Platinum-Silver-Coated (Wollaston) hot–wire with an active length of 0.5mm, located approximately 130mm downstream from the cylinder and slightly offset from the cylinder axis, was analysed on a HP 3582A spectrum analyser, following Williamson (1989). The results in Figure 2.10 show good agreement with the results found by Papangelou (1992) over the whole range of Reynolds numbers.

Since the vortex shedding behind the cylinder in the wind tunnel would be altered if it were to be used during experiments with the precessing jet, the variable power supply driving the suction fan was calibrated over the range of co–flow settings. Figure 2.11 shows the relationship between the Ampere settings and the mean co–flow velocity, assuming a uniform distribution across the wind tunnel.

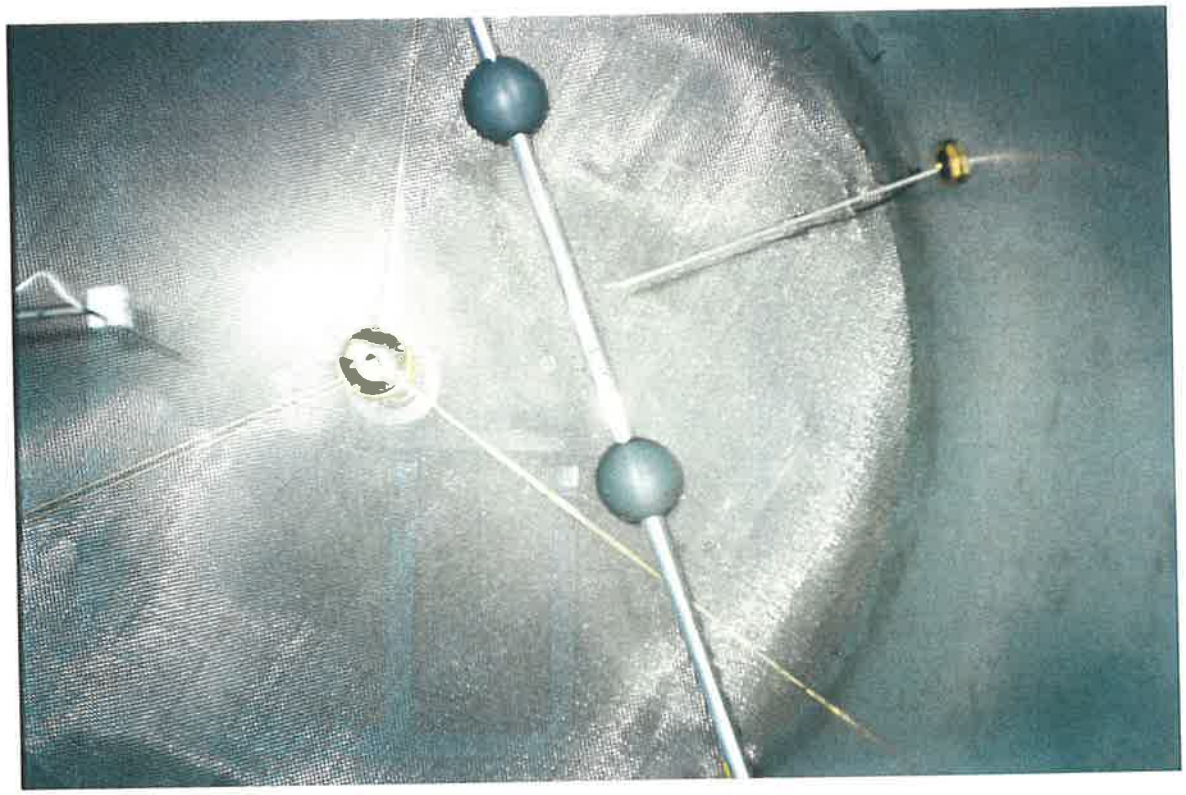

Figure 2.9: **Inside the low speed wind tunnel showing the robust vortex shedding anemometer, consisting of two 75.5mm spheres on an approx. 19mm cylinder and a hot wire (suspended from the right wind tunnel wall)**

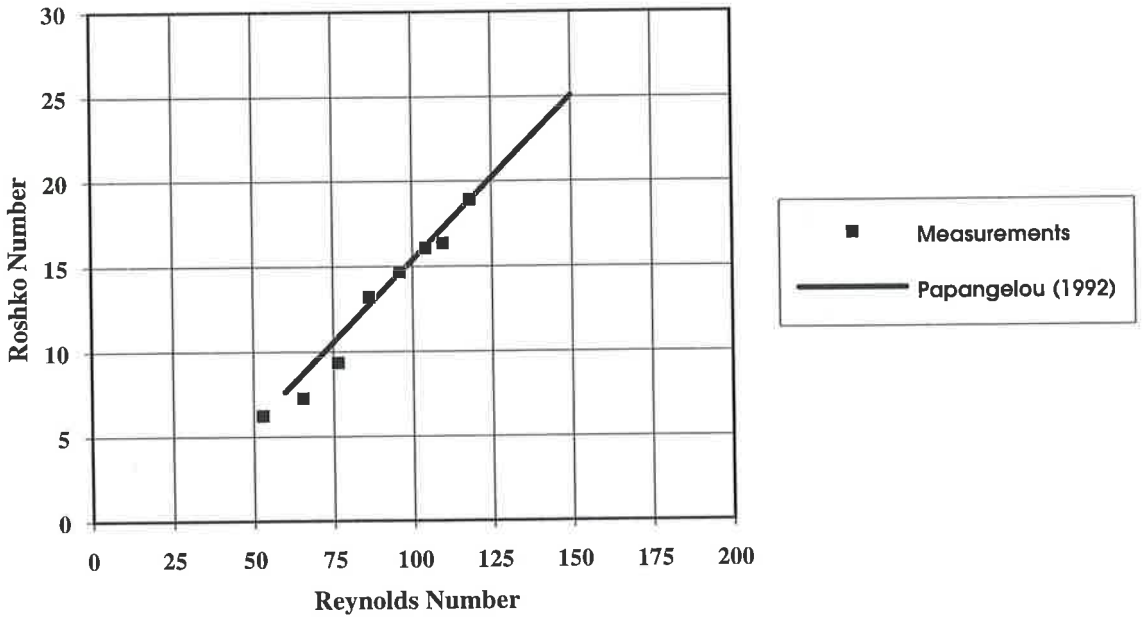

Figure 2.10: **'Calibration' of the vortex shedding anemometer in the low speed wind tunnel plotted as Roshko number** $= \mathrm{f} \cdot \mathrm{d}^2/\nu$ **as a function of Reynolds number** $= \mathrm{u} \cdot \mathrm{d}/\nu$

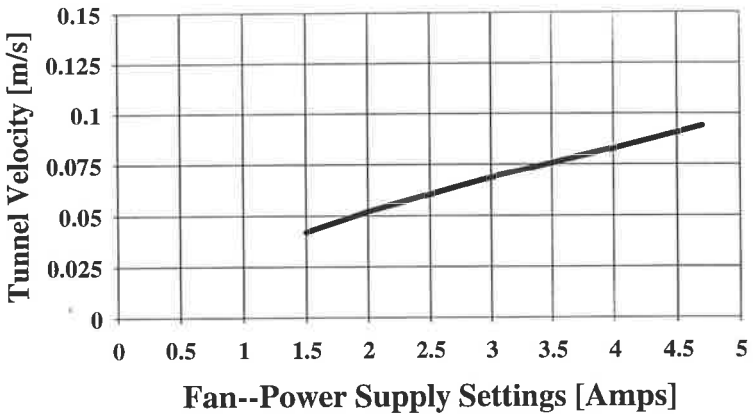

Figure 2.11: **A best fit curve of mean co–flow velocity data from Fig.2.10 as a function of the tunnel fan–power supply setting.**

Velocity measurements have been taken every 50mm across the 1000mm diameter of the cylindrical wind tunnel to define the co–flow velocity profiles over two planes: the exit plane of the mechanical nozzle $x/d_e=0$ and further downstream at $x/d_e=20$. The second plane is further downstream than the measurements domain for the precessing jet investigation. An identical hot-wire to that described above was calibrated using the robust vortex shedding method as a reference for the velocity magnitudes. A sampling frequency of 2Hz was used with a total of 1024 samples collected per position to ensure good statistical resolution. This corresponds to a very long sampling period of about 8.5 min for each radial position. Four different profiles were measured and are shown in Figure 2.12. The profiles display adequate uniformity when precautions are taken to seal the tunnel openings (compare set 2 repeated in set 5 with a better seal). The turbulence intensities found in the test section are less than 5%, which is deemed to be satisfactory and justifies the relatively simple design of the tunnel inlet.

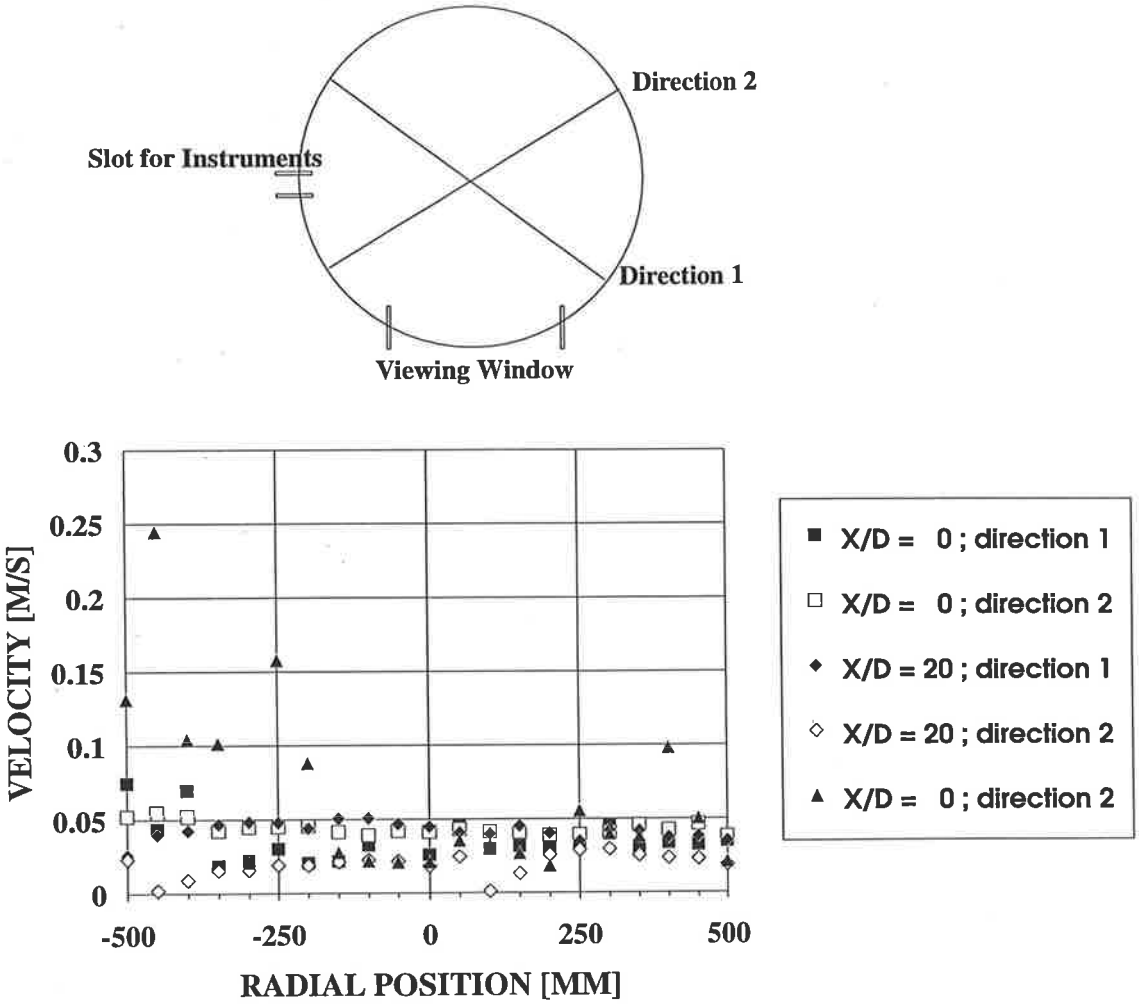

Figure 2.12: **Velocity distributions in the wind tunnel. Note that the data for $x/d_e=0$ defined by the triangle was taken in a poorly sealed tunnel. Data defined by the white square was obtained after the tunnel was sealed**

In conclusion, the low velocity wind tunnel has been found to provide well defined boundary conditions for the investigation of the precessing jet flow. It provides an adequately uniform, low velocity co–flow which satisfies the entrainment appetite of both a simple turbulent jet and a precessing jet, while keeping a low turbulence level. This enables the investigation to be conducted in an environment which excludes all significant influences from the surroundings.

2.3 Flow Visualisation Techniques

2.3.1 Smoke Visualisation

A conditional flow visualisation technique is used to identify characteristic flow patterns generated by precessing jet flows in air.

The Smoke:

Because the velocities are relatively high when using air, good visualisation requires dense smoke which is achieved by injecting SO_2 and NH_3 through separate tubes into the jet flow or into the surrounding air. The three gases react as follows to produce $S(NH_4)$, which is a highly reflective, dense white powder which is itself non–toxic.

$$SO_2 + NH_3 + \text{air} \rightarrow S(NH_4) + S + H_20 + \text{air}$$

The marker gases were injected tangentially to the exiting jet at one phase in the cycle with about the same velocity as the jet to minimise the influence of the gas injection on the flow. The timing and pulse width of the injection can be controlled to within $\pm$1ms using an in-house controller. BOSCH automotive fuel injectors are effective as solenoid valves for the technique and are timed to fire at a predetermined phase of the precession cycle, referenced to the trigger pulse provided by the Hall effect sensor located adjacent to a passive trigger mounted on the drive shaft of the nozzle. Figure 2.13 shows the general arrangement of the technique. To ensure correct use of the toxic gases, a safety procedure was developed which complied with standards of the University of Adelaide Occupational Health and Safety Office.

Figure 2.13: **The smoke visualisation system mounted beside the nozzle and its variable speed drive. NH_3 and SO_2 are pulsed through two thin tubes to the right of the nozzle**

The Cameras:

Images were recorded with a KODAK Ekta Pro 1000 high speed motion analyser, which is capable of imaging at 30, 60, 125, 500 or 1000 frames/second. The maximum aperture of F1.8 enabled good contrast and illumination to be achieved for framing rates of up to 500 frames/second. A zoom lens allowed selection of an optimal field of view. The images were recorded on the FM tape drive of the Ekta Pro unit and were later downloaded on to standard VHS video format. A 1000W Halogen-U-Lamp was used to provide illumination of the flow field.

For single still pictures a Minolta SLR, 35mm camera was used with a standard 200 ASA black and white film. A manually operated shutter and an aperture of F11 provided good images. A standard camera flash was connected with a synchronisation cord and placed at 90^o to the camera axis to provide illumination. The flash was shielded on the side towards the camera to direct light fogging. The synchronisation cord was connected with the microcontrolled trigger box mentioned earlier to trigger the flash. This arrangement enabled optimisation of both the jet position relative to the camera and the pulse duration to obtain good images.

2.3.2 Laser Sheet Flow Visualisation

Laser sheet flow visualisation was used to gain deeper insight into the flow field of the precessing jet. The extreme Strouhal number cases only have been investigated with both the exit velocity of 40m/s and the Reynolds number held constant. Techniques for studying the high Strouhal number case with $St_p = f_p \cdot d_e/u_e = 15 \times 10^{-3}$ and a frequency of 60Hz, and the low Strouhal number case with $St_p = 2.15 \times 10^{-3}$ and a frequency of 8.6Hz using light sheets in the r–Φ plane and in the r–x plane are described below. Note that for these techniques a continuous smoke supply was introduced through the nozzle.

The Laser and the Laser Sheet:

A 15W copper vapour laser with a variable pulse repetition frequency (PRF) of between 2kHz and 20kHz was used as the light source. For the present investigation the PRF ranged between 5kHz and 20kHz. The pulse duration also varies with the PRF. For a

PRF of 5kHz the pulse width is typically 50ns, whereas at 20kHz it is reduced typically to 5ns with a maximum pulse energy of 6mJ. The pulsed laser has major advantages when compared with standard strobe illumination. Conventional strobe illumination systems have pulse widths of the order of milli–seconds, which tends to blur the image in high velocity flows. They can also be weak in intensity and so produce poor contrast. The copper vapour laser with its high intensity pulses and short durations enables the motion to be 'frozen' and so provides clear instanteneous pictures of the jet. In the present case the maximum flow velocity is 45m/s at the exit and the precession frequency is 60Hz. This means that, during the 50ns pulse, the flow moves less than 2.25×10^{-3}mm and rotates less than 1.296×10^{-3} degrees. The laser frequency controller also has an external input which can be used to trigger the laser from a high speed camera or a control box for single shots. This ensures precise synchronisation of laser pulse and camera shutter to obtain maximum illumination and contrast.

Two conical lenses are used to create a narrow vertical or horizontal light sheet of about 1-2mm thickness over the whole field of view of the cameras. Figure 2.14 shows a photograph of the visualisation arrangement with a vertical laser sheet passing through the axial plane of the flow from the mechanical nozzle.

Three different types of particles were used to reflect the laser beam. The particles were introduced directly into the jet to obtain a good seeding density and hence good reflection. A glycol based fluid vapour, which typically contains sub–micron particles, was generated by a commercial fog–machine. The particles of the vapour show almost no particle lag effect, as described in detail in Section 2.4.3. However, for flow visu-

alisation in the high velocity flow of the precessing jet, solid particles display better reflection and scattering characteristics. Both Titanium–Dioxide and glass beads with typical particle sizes of about 10μm and 40μm respectively have been introduced into the jet to yield instantaneous pictures of the jet with adequate contrast to allow for qualitative interpretation.

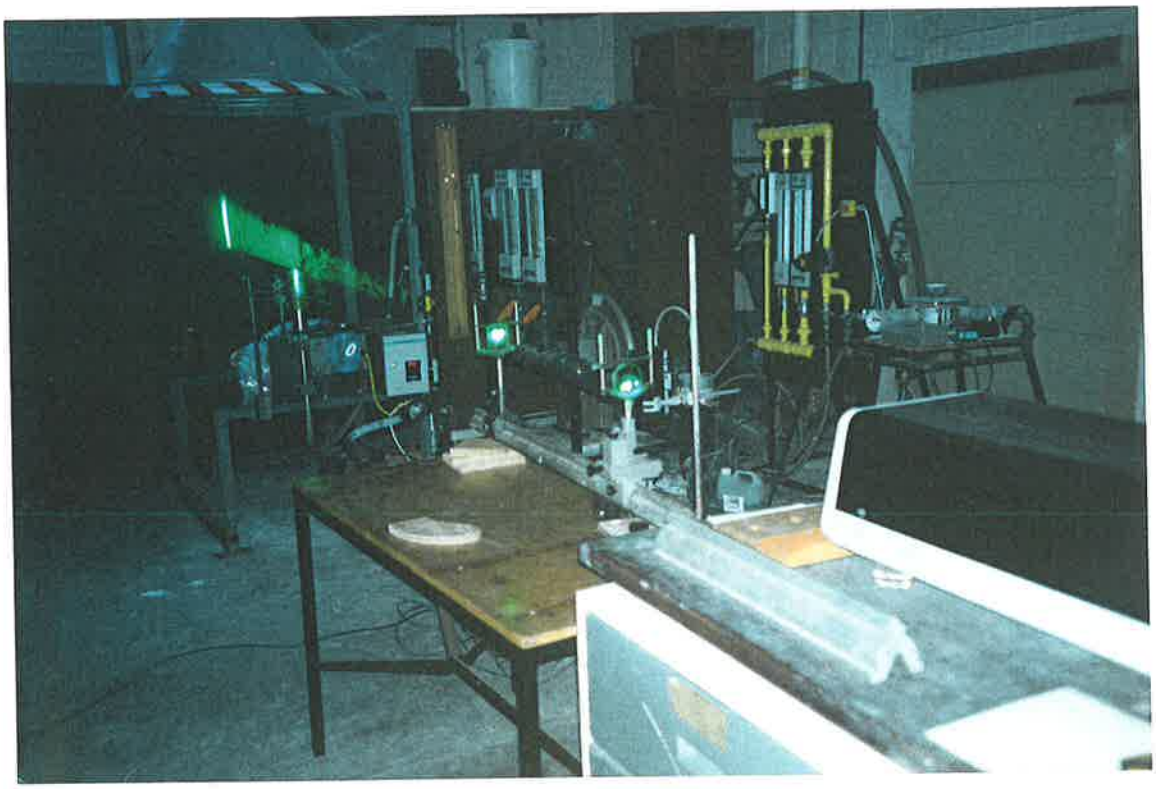

Figure 2.14: **Vertical laser sheet generated from the Copper Vapour laser**

The Cameras:

A PHOTEC 16mm High–Speed Rotating Prism camera system was used to record the phenomena illuminated by the laser sheet. The framing rate can be chosen between 100–1,000 frames/second in steps of 100 in the low range and 1,000–10,000 frames/second in

steps of 1,000 in the high range. A double perforated 16mm black and white negative 400 ASA film was used (KODAK RAR and ILFORD HP5 PLUS). The orientation of the camera was as close to being perpendicular to the laser sheet surface as possible to ensure maximum illumination and maximum information. Use of a 45mm lens gave a wide field of view. In most cases the camera trigger was connected to the frequency controller of the laser to synchronise the frequency of the pulses with the framing rate of the camera. The records without synchronisation are specifically indicated in the result sections of the thesis.

Figure 2.15: **The arrangement of cameras and object**

Still photographs of the phenomena in the laser sheet were taken using a NIKON F-801 SLR camera, also with a 45mm lens. The electronically controlled camera was

linked with the laser via a control box which enables synchronisation of shutter delay and laser pulse times. This enables optimal temporal resolution and the choice of single or multiple exposure photographs. The exposure time was varied between one and 9 bursts per frame with the laser pulsing at 5–20kHz. The shutter speed was set to 1/15s, 1/30s or 1/60s with a maximum aperture of F1.4. Standard 1600 ASA or 3200 ASA 35mm films were used to record 6 different horizontal levels (x/d_e=2–12) above the mechanical nozzle.

2.3.3 Laser Induced Fluorescence (LIF)

The water tank facility in which laser induced fluorescence, LIF, experiments were conducted is a square section perspex tank with a 750mm×750mm cross section and a height of 1.5m. A constant water level is maintained by an overflow weir with a thin knife–edged lip. The mechanical nozzle and the electric drive were suspended from a frame and directed vertically downwards with the exit plane of the nozzle about 400mm below the surface of the water. The water supply was fed from a 200 litres supply tank, fed from a centrifugal pump. The flow was measured by the flow rate meter before passing through the nozzle tip into the tank. The flourescent dye is diluted in the ratio of 0.1g of fluorescene to 200 litre and used to mark the jet fluid. The 488nm blue beam from a Spectra Physics 5W Argon–Ion laser was expanded with a combination of lenses into a 2mm thick light sheet. This light sheet was aligned to pass through the vertical x–axis of the mechanical nozzle and to illuminate the r–x plane from its origin to $x/d_e \approx 30$. A video camera was used to record the images in standard VHS format. Figure 2.16 shows the general arrangement and the detailed design of the technique is described by Newbold (1997).

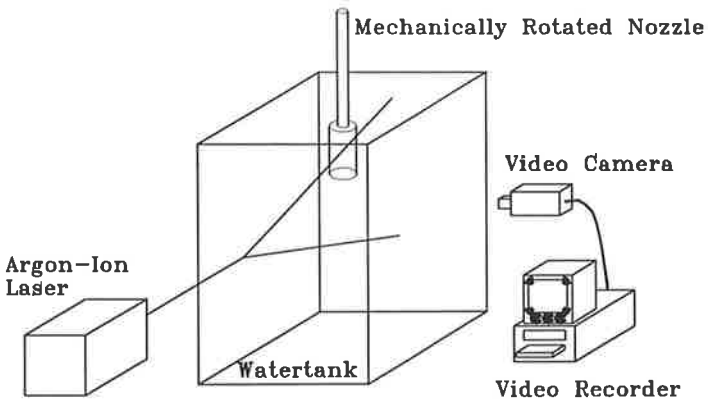

Figure 2.16: **Arrangement for the Laser Induced Fluorescence experiments**

2.4 Measurement Techniques

2.4.1 Hot-Wire Anemometers

Hot wire anemometry is based on the measurement of the heat loss from an electrically heated wire in fluid flow. In the constant temperature mode of operation the heat loss is compensated by a Wheatstone bridge arrangement (an amplifier in a feedback loop) to maintain a constant wire resistance, and hence a constant wire temperature for a given applied voltage. The correction current is related to the flow velocity. One of the simplest equations relating voltage to velocity is derived from Kings-Law (Perry 1962), originally derived in the form: $\mathrm{Nu} = \mathrm{a} + \mathrm{b} \cdot \mathrm{Re}^{0.5}$, which can be written as:

$$\mathrm{U} = \left[\frac{\mathrm{dU}^{0.5}}{\mathrm{dV}^2}(\mathrm{V}^2 - \mathrm{V}_0^2)\right]^2$$

where V represents the mean voltage measured and U represents the mean flow velocity at the hot–wire. Kings law is sufficiently accurate for our purposes in the range of

velocities greater than 5m/s. To account for any change in the calibration over the time period of the measurements (e.g. introduced by hot–wire 'drift') calibrations were performed before and after each set of measurements. It was found that the drift was very small. A typical calibration chart is shown in Figure 2.17 and is well represented by the velocity–voltage relationship

$$U = (5.0538(V^2 - 0.49415))^2$$

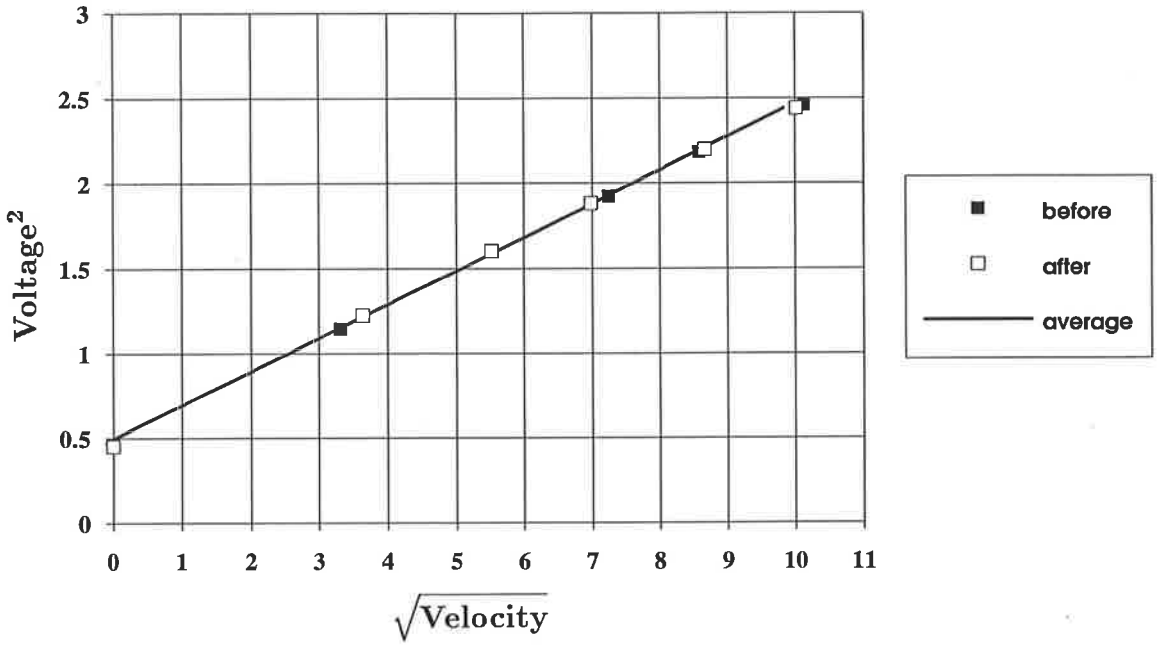

Figure 2.17: **A typical hot-wire calibration curve, showing data collected before and after an experimental run.**

The hot-wire measurements were conducted using a standard 5μm Tungsten constant temperature hot-wire with an active length of 1mm. The wire was calibrated against a pitot static tube over the range 10 m/s to 100 m/s in the flow produced by a planar jet nozzle, and at 0m/s. The calibration nozzle provides a top-hat profile at the exit plane to within 1%, as tested by Nathan (1988). The unfiltered signal from the anemometer was converted to a digital signal and stored on a PC. For the calibration, 1000 samples were collected at a sampling frequency of 200 Hz.

2.4.2 The Cobra Probe

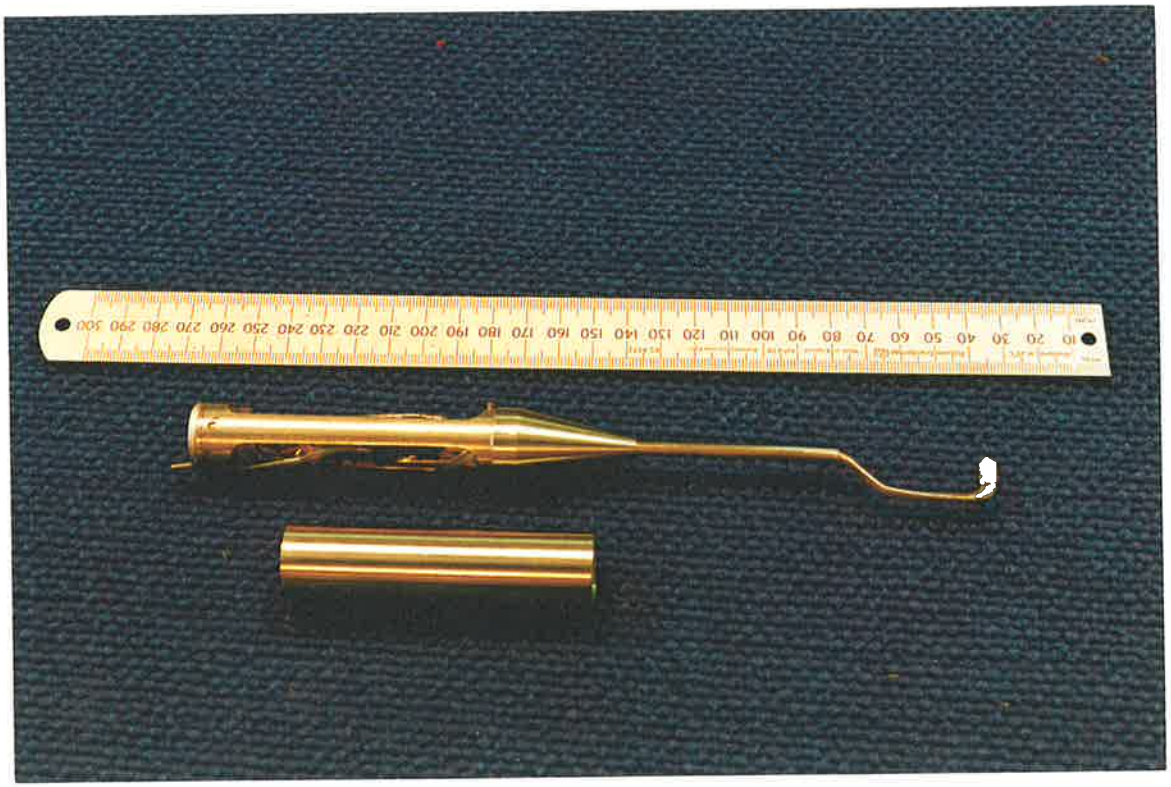

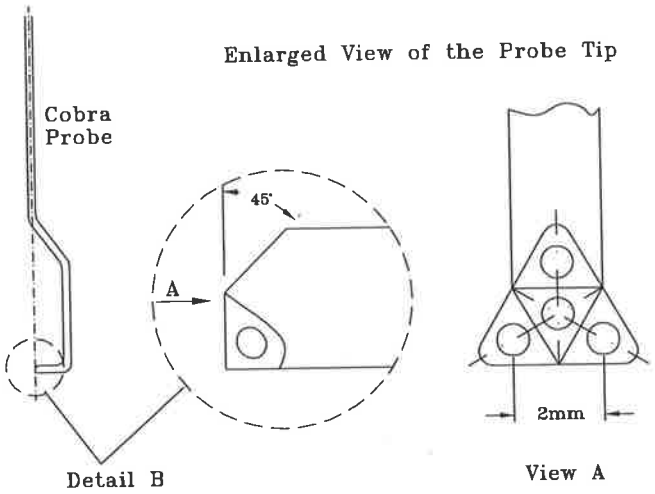

Figure 2.18: **A photograph and sketch of the Cobra probe**

Measurements of instantaneous, phase– and time–averaged, local static and dynamic pressures have been conducted using a four-hole 'Cobra' pitot probe (Fig.2.18). This probe has been delevoped at the CSIRO Division of Mineral and Process Engineering, Menai, Australia, and is able to detect magnitudes and orientation of velocity from

measurements of the pressure field around the probe head. In contrast to the five–hole spherical and hemispherical head geometry of Wright (1970), and the conical head probe of Judd (1975), the Cobra probe uses the four hole arrangement proposed by Shepherd (1981). The probe head consists of a group of 3 holes each located on its own small plane with each plane arranged at a 45 ^{o} angle relative to the centre hole (Fig.2.18). The arrangement ensures reliable measurement of the flow parameters within a 90^{o} cone angle by providing a well defined separation point at the tip. Thus the response of the probe is remarkably independent of the Reynolds number. The probe has been used successfully in various highly turbulent flow fields (Hooper and Musgrove (1991), Hooper et.al.(1992), Musgrove and Hooper (1993), Hooper and Musgrove (1995)). The four-hole Cobra probe used for the present investigation has a spatial resolution of approximately 8mm^3 with a distance of 2mm between the 0.5mm holes (Fig.2.18). The four Sensym detectors, mounted with four pre–amplifiers in the probe stem (Fig.2.18), have a standard pressure range from 0 to $\pm$1.0kPa, or an amplified range from 0 to $\pm$0.33kPa for better resolution of lower velocity flows. The pressure transducers have been specifically modified to give a frequency response up to 2,500 Hz. The characteristic response over that frequency range and the phase shift of the pressure signal are shown in Fig.2.19. From a comparison of the frequency response of the probe with that of a B&K microphone an experimental transfer function can be obtained to correct the signal in the frequency domain following Bergh and Tijdeman (1965) and Irwin et.al.(1979). A comparison of the corrected and uncorrected pressure signal indicates that the peak values of the signal suffer much smaller attenuation by application of this method (Fig.2.20).

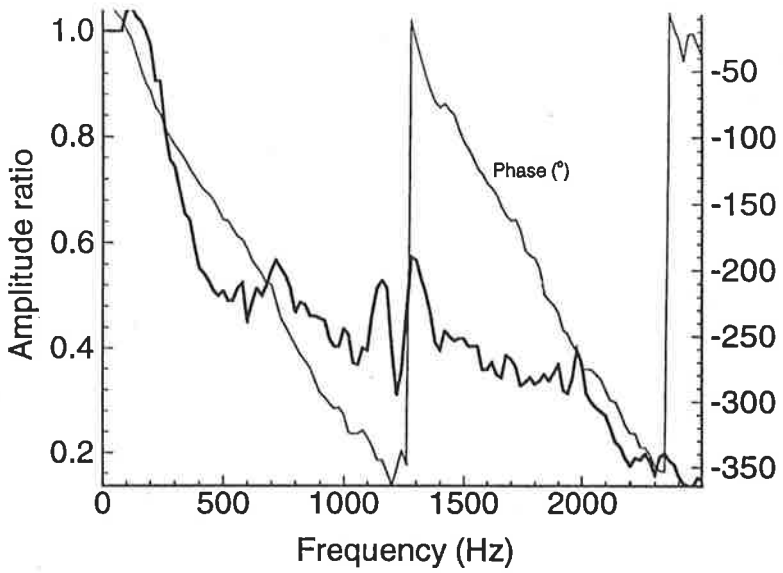

Figure 2.19: **Phase shift and frequency response of a pressure signal taken with the Cobra probe in a turbulent jet flow.**

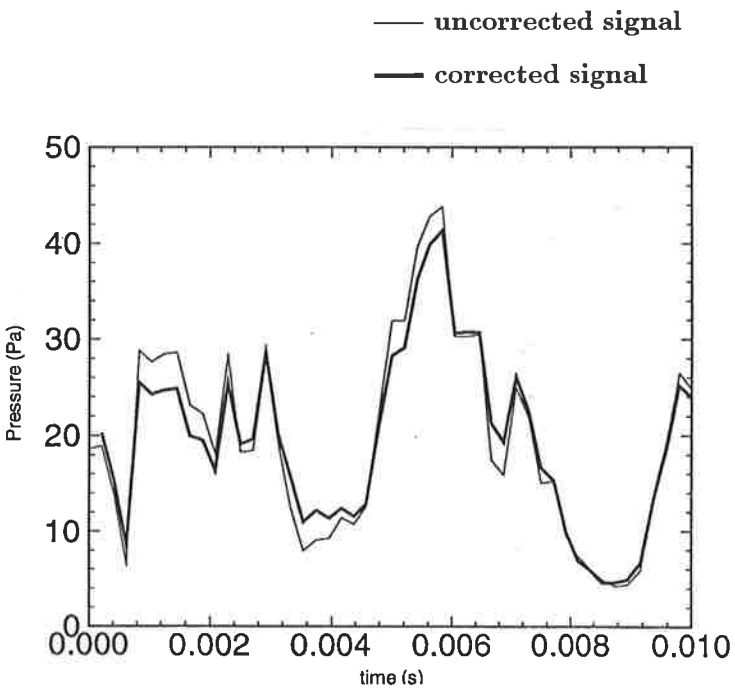

Figure 2.20: **Corrected and uncorrected pressure signal taken with the Cobra probe in a precessing jet flow.**

The Cobra probe and the four pressure transducers respectively were calibrated in two steps. First, approximately 6 to 7 different known static pressures were applied on all four holes to calibrate the transducers and to find the slope of the linear relation between pressure and the voltage output. Custom designed and developed software allows calculation of a linear curve fit and this procedure is repeated until a curve fit of 99.99% is achieved.

Following this procedure the probe was put in the 30m/s uniform flow within the core region of a simple turbulent jet to obtain the relationships between the pressure signal and the magnitude and orientation of the velocity. A calibration 'surface' was created by varying pitch and yaw angles through a range of $\pm 48^{o}$ in steps of 6^{o}. In the analysis of the probe response, pressure ratios are calculated. Following Shepherd (1981) and Hooper and Musgrove (1991) the pressure equations become:

$$X1 = (P_1 - P_2)/(P_0 - P_3) \tag{2.6}$$

$$X2 = (P_2 - P_3)/(P_0 - P_3) \tag{2.7}$$

$$Xd = (0.5\rho u^2/(P_0 - P_3) \tag{2.8}$$

$$Xt = (P_t - P_0)/(P_0 - P_3) \tag{2.9}$$

where P_0 is the central hole pressure, P_3 is selected to be the minimum of the outer hole pressures, P_1 and P_2 are selected cyclically from the two remaining outer hole pressures. P_t is the total pressure and u is the flow velocity. The variables Xd and Xt (and yaw and pitch angles) are calibrated against X1 and X2 at the known flow velocity and over the desired yaw and pitch angle range. Two of the typical parts of a calibration surface are shown in Figure 2.21.

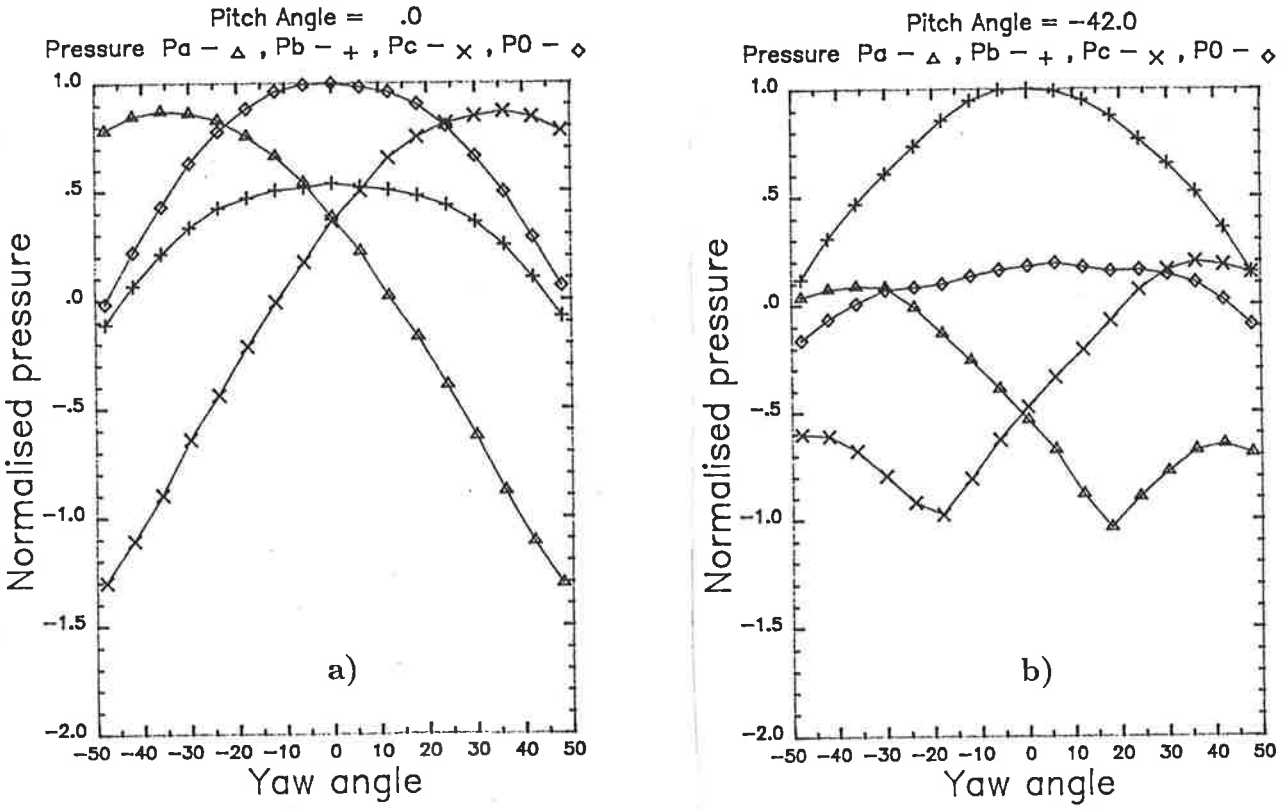

Figure 2.21: **Calibration Surface cut at pitch of: a) 0^o; and b) -42^o.**

For the measurements in the precessing jet flow the results were phase-averaged over multiple cycles of precession. Four channels of the pressure signal from the probe were collected simultaneously with a fifth channel containing a trigger signal to reference the angular position of the spinning nozzle. A good signal to noise ratio was achieved during the measurements and a typical signal is displayed in Figure 2.22.

The data were then phase–averaged relative to the reference signal, which marks Φ_0 ($\Phi = 0$), using software developed for the purpose. The sampling rate of 5kHz with

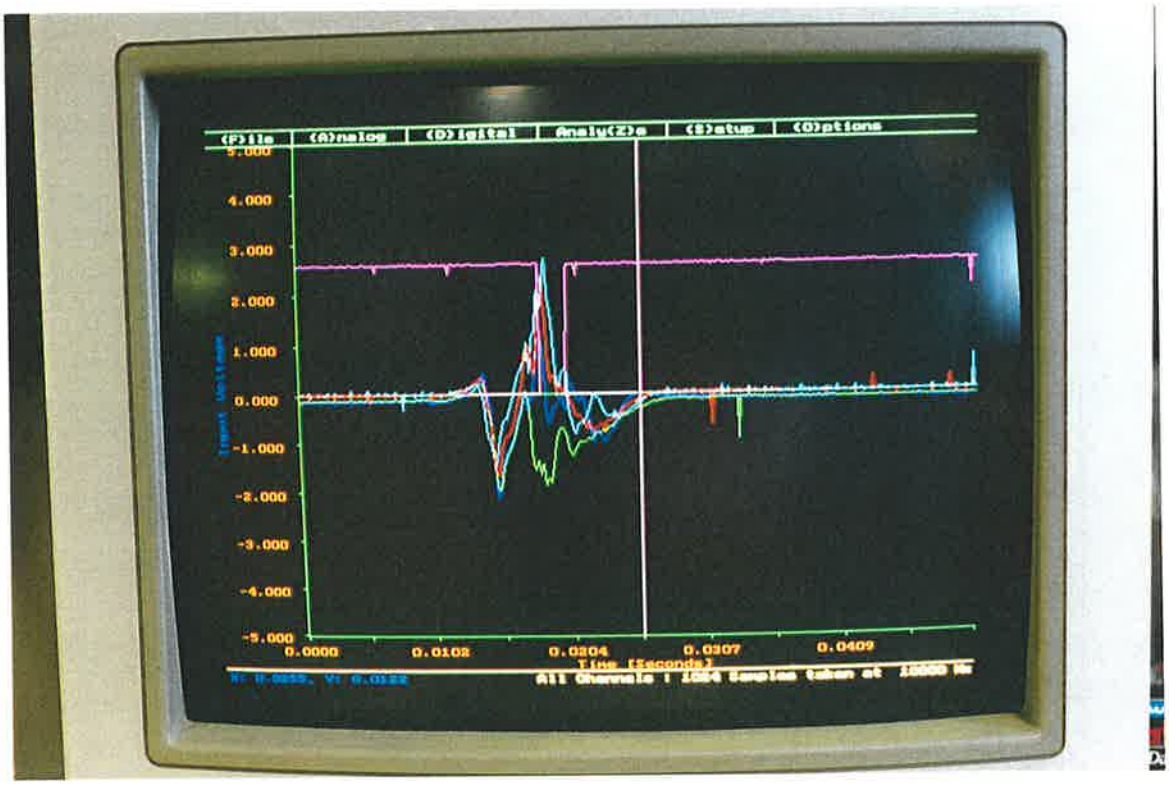

Figure 2.22: **A typical pressure signal from the Cobra probe showing one cycle of precession in the precessing jet flow.**

22,500 points recorded on each of the 5 channels, allows 67 cycles of the precessing flow to be recorded and phase-averaged for each probe position. The probe was traversed radially in 5mm increments. At each of the radial positions it was orientated at 6 different yaw and pitch angles to accommodate the 90° acceptance angle. The data were later combined, after rejecting data that corresponded to flow directions outside the acceptance angle, to produce the full 3-dimensional flow field.

There are three dominant sources of error associated with the measurements using a Cobra probe. The predominant source is the resolution of the pressure transducers. For the most sensitive pressure range ($-.33$kPa to $+.33$kPa) the corresponding velocity

range is ±23.38m/s. An absolute error of ±0.5%, i.e. ±1.67Pa corresponds to ±1.65m/s. Thus, the resolution of low velocity flows is limited and measurements of less than 2m/s must be treated with caution.

Secondary sources of error relate to the Reynolds number effects and to 'look–up' errors when interpreting the calibration curves. These sources have been examined by Hooper and Musgrove (1991) for a high velocity case. A flow of 110m/s was examined to recalculate the corresponding data for a calibration taken at 16m/s. The mean velocity error was found to be 1.7% with a standard deviation of 0.9m/s. The mean yaw angle error was 0.9^o (standard deviation of 1.9^o) and the pitch angle -0.3° (standard deviation of 2.8^o). This test included both the typical interpolation error in the calibration curves, and the Reynolds number effects for a fairly extreme velocity range. Since the calibration surfaces have steep gradients in some parts, no general level of accuracy can be given. However, sources of error such as these examined by Hooper and Musgrove (1991) are not likely to be significant for the present experiments since the velocity range involved is relatively modest.

The third possible source of error is the estimation of the probe transfer function. This could lead to errors in the order of 2% for the function used here. Because this error is frequency dependent, it mainly effects the fluctuating velocity components and not the mean values of velocity.

Other less significant sources of error are connected with the spatial resolution of the probe. These are hard to quantify but are known to become important in flows

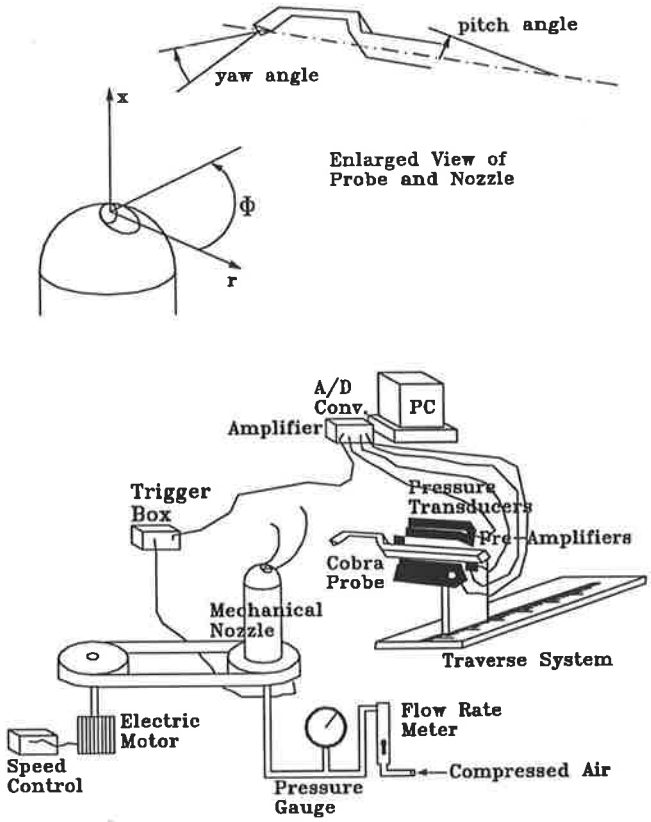

Figure 2.23: **Apparatus and coordinate system used in the Cobra probe measurements.**

with high shear gradients (Hooper and Musgrove,1995). The Taylor model of a frozen turbulent structure advected past the probe tip may be used as an estimate of the structures resolved by the probe. By the criteria of this model, the spatial resolution of the probe is well balanced with the temporal response. This criterion requires that for a frequency response of the probe of 2.5kHz and maximum velocity components of 21.2m/s the minimum structure that can be resolved has a scale of the order of one nozzle diameter, which is more than sufficient resolution for the current investigation. In the lower velocity regions the minimum structure size which can be resolved is obviously even smaller.

2.4.3 Laser Doppler Anemometer System

Three dimensional velocity measurements have been conducted at the University of Wales in Cardiff. A schematic of the experimental arrangement is shown in Fig.2.25. The LDA system is a DANTEC three–component backscatter system using a COHERENT Inova 70 series 5 Watt Argon–Ion laser.

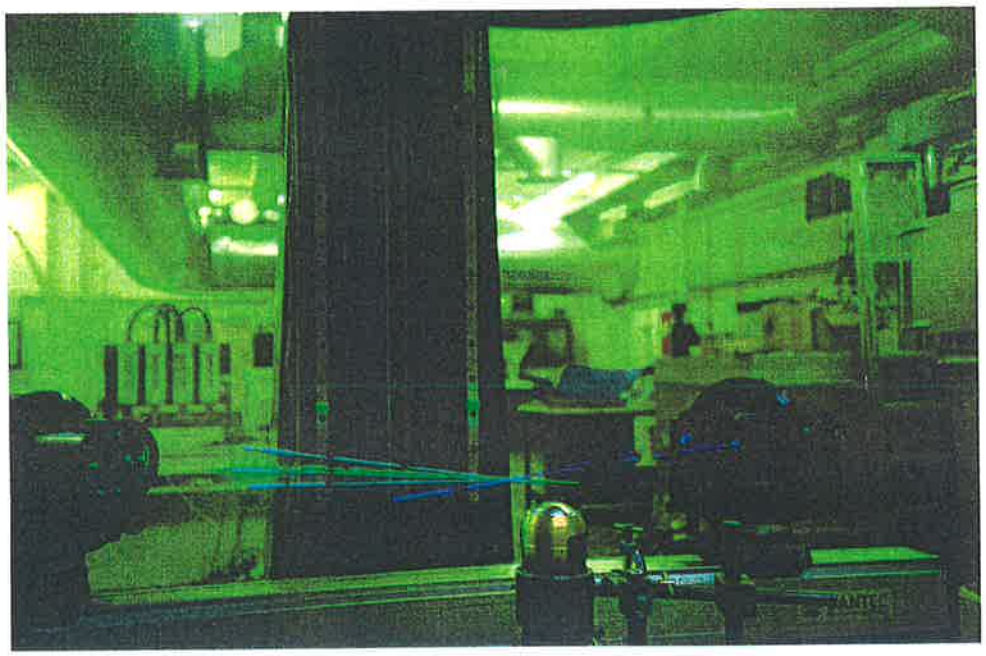

Figure 2.24: **The 3-D LDA system and the mechanical nozzle**

Optics:

To remove directional ambiguity, all three colours are frequency shifted by Bragg cells. After the colour separation and beam splitting, the six beams are optically coupled into two fibre optic probe heads. The two heads are set at 90 degree to each other and

arranged so that the six beams cross at a point 600 mm away from the heads. With this arrangement, direct measurement of each of the three velocity components is possible. The tangential, axial and the radial velocities in the present experiments have been measured using wavelengths of 514.5, 488.0, and 476.5 nm respectively. The lengths of the control volumes for each of the beams, calculated from the 600mm focal length of the lenses, the beam diameter, the wavelength and the incidence angle are: for the green beam dr=4.9mm; for the blue beam dr=4.6mm; and for the violet beam dΦ=4.5mm. The diameter of each of the control volumes is about 0.16mm.

Signal Processing and Data Acquisition:

In the experiments described here the signals from the three beams were sent to separate Burst Spectrum Analysers and the resulting frequencies were stored on the PC with their associated arrival times. In addition to the velocity signals, a fourth trigger signal, to reference the angular position of the spinning nozzle, was collected simultaneously. The data were then phase-averaged relative to that reference signal, which identifies Φ_0 (Φ = tangential direction at the exit plane), over multiple cycles of precession with a chosen resolution of 360 parts for each cycle (1 degree segments). A total number of 42,000 (3$\times$ 14,000) points were recorded on each of the channels, allowing more than 100 cycles of precession to be recorded and phase–averaged for each radial position. The software used for the averaging was developed by the University of Wales specifically for the present experiments.

Seeding:

To maintain a high data rate in the jet flow and in the external flow, both the jet and the ambient fluids were seeded. A ROSCO 4500 fog machine was used to produce

'HAZE', sub–micron glycol particles which were found to have negligible influence on the dominant flow patterns, and which have very good scattering characteristics. To ensure uniform seeding of the surrounding fluid and the jet fluid with one fog machine, different hose diameter ratios have been assessed.

Traversing:

The optical heads carrying the laser beams were mounted on an automatic DANTEC traverse system which locates accurately to within $\pm$ 0.05mm. The beams were traversed radially (along the green and blue beams) from the nozzle axis, r=0mm, to r=120mm in 5mm steps, thus collecting 25 radial positions for each plane. Six r–Φ planes at the distances x/d_e=2,4,6,8,10 and 12 were measured.

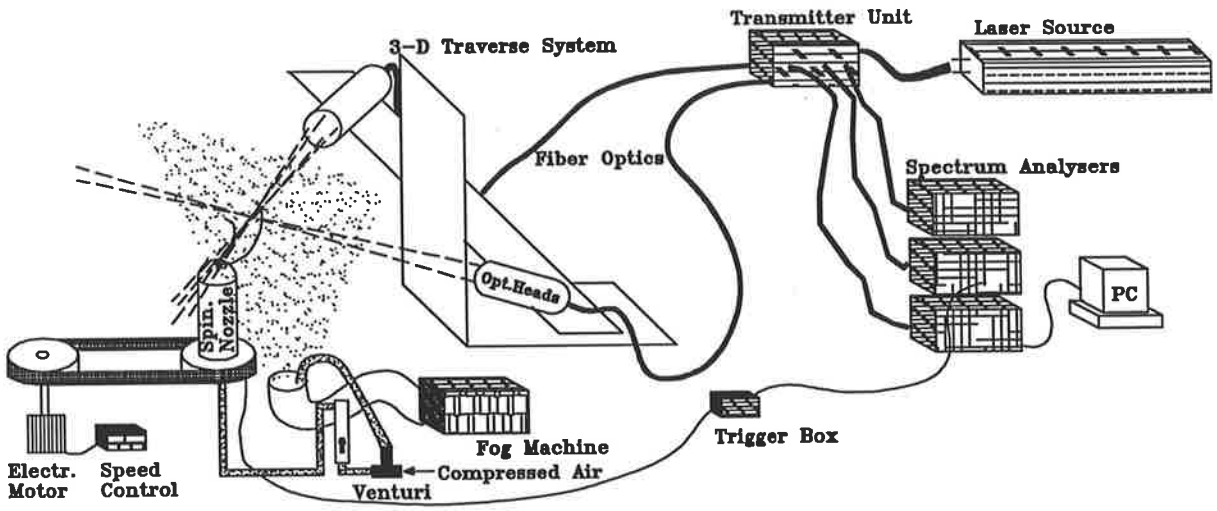

Figure 2.25: **The apparatus used for the LDA measurements**

Discussion of Accuracy:

The most significant limitation in the LDA technique used here is the inability to resolve large velocity gradients accurately. This is due to the length of the control volume and limited radial (5mm traversing steps) and angular ($1^o \cong$ 2mm at r_{max}=120mm) resolution, resulting in a broadening of the mean velocity. In the present case, for the tangential and the axial velocity (green and blue beams) the control volumes (lengths of 4.9mm and 4.6mm respectively) and the traversing are orientated along a radial line. This causes poor resolution for the gradients $\frac{du_\Phi}{dr}$ and $\frac{du_x}{dr}$, whereas the gradients $\frac{du_x}{d\Phi}$ and $\frac{du_x}{dx}$ are resolved with a much higher accuracy due to the angular resolution of 1^o and the diameter of the control volume of 0.16mm.

The control volume of the violet beam, measuring the radial velocity component, lies in the tangential direction. This leads to poor resolution in the gradients $\frac{du_r}{dr}$ and $\frac{du_r}{d\Phi}$. The size of the traversing steps determines the resolution in radial direction, compared to a small width of the control volume. In the tangential direction, the length of the control volume is 4.5mm, which defines the resolution, being larger than the 1^o angular resolution. In the present case the errors in the components $\frac{du_\Phi}{dr}$, $\frac{du_x}{dr}$, $\frac{du_r}{dr}$ and $\frac{du_r}{d\Phi}$ are difficult to estimate, since the velocity gradients in a precessing jet flow are not known apriori. Durst et al. (1981) suggest the error should be estimated from the series

$$< U > - U \approx \frac{V_x^2}{2}(\frac{d^2U}{dx^2}) + \frac{V_x^4}{8}(\frac{d^4U}{dx^4}) + ... \qquad (2.10)$$

where $< U >$ is the spatial average of the particle velocity U over the scattering volume V_x at a point x. Estimates by Durst et al. (1981) and by Komori and Ueda (1985) applying this equation found that the limitations of spatial resolution in a simple

turbulent jet are insignificant ($< \pm 0.4\%$). Since the control volume in the present case is less than the 9mm of Komori and Ueda (1985), while the nozzle diameter is the same, the error in the present case can be inferred to be in an acceptable range.

The velocity bias towards higher velocities which is inherent in the LDA technique, was first recognised by McLaughlin and Tiederman (1973). The fact that the anemometer detects particle motion rather than the fluid flow directly leads, for fluctuating flow fields, to a bias in the measurement which favours higher velocities. The probability of sampling a particle is:

$$N_s = U \cdot M \cdot A_p \cdot dt \tag{2.11}$$

where N_s is the average number of samples obtained during the time interval dt, U is the magnitude of the velocity vector, A_p is the projected area of the measurement volume and M is the average particle number density. After integration the equation becomes

$$\frac{N_L}{N_H} = \frac{U_L}{U_H} \tag{2.12}$$

where the subscripts L and H indicate low and high velocities and the number of samples respectively. This demonstrates the positive bias in the technique towards higher velocity particles. To reduce this inaccuaracy, both the surrounding fluid and the jet fluid were uniformly seeded with a high particle density, following Edwards (1981). A controlled processor was also used; this samples the validated data at equally spaced intervals using only the first signal to arrive in that interval. Winter et.al. (1991) have shown the advantages of these procedures, both theoretically and experimentally, in comparison with other methods.

Fringe bias, or angle bias, occurs because particles crossing the control volume in a direction perpendicular to the fringes are required to produce a minimum number of cycles to be recorded and accepted as a valid signal. Particles crossing at an angle, or in the outer regions of the control volume, do not produce the minimum number of required cycles and so are not registered. The equation for the polar response of the probe volume

$$P_R(\Theta) = \left[1 - \left(\frac{\frac{NF}{NF_t}}{\cos\Theta} + \frac{U_F}{U}\right)^2\right]^{\frac{1}{2}} \tag{2.13}$$

shows the dependancy of the response on the angle Θ of the arriving particles. In equation (2.13) NF is the minimum required number of fringe crossings for a valid signal, NF_t is the total number of fringes in the probe volume (before the frequency shift), Θ is the angle of incidence of particles with respect to the plane of the fringes, U_F is the fringe velocity and U is the magnitude of the particle velocity vector. To eliminate angle bias the aim is to keep the polar response constant during the measurements, which means that for the present experiments an appropriate frequency shift had to be applied to each of the three beams (Durst et al. 1993). The shift to a higher frequency leads to an increasing number of fringes in the control volume and hence the directional sensitivity can be reduced or even eliminated. In the experiments a frequency shift of 40 MHz was set to minimise the fringe bias.

That the shift to a higher frequency leads to a 'clock-induced' error was disvovered by Graham et al. (1989). They found increased values of measured velocity with increasing frequency shift, which leads to the assumption that the data were biased towards higher frequencies which would result in a lower number of clock pulses. The limited speed of

the clock will limit the resolution of the controlled processor R_c, which can be calculated from f_D = the Doppler frequency in Hz, where $f_D = f_U + f_{Shift}$ and f_U is the actual frequency induced by the velocity of a seed particle in Hz. If NF is the number of cycles required by the processor for signal validation and τ is the time for one clock cycle, the equation for the controller resolution is then

$$R_c = \frac{NFf_D}{NF - \tau f_D} - f_D \tag{2.14}$$

The present system was operated with a frequency shift of 40 MHz. At this frequency clock bias could be detected and was corrected as recommended by Graham et al. (1989).

Particles of HAZE, the glycol based fluid, have a typical diameter $d_p < 1\mu$m and a density ratio relative to air of $\sigma = 800$. Melling and Whitelaw (1975) and Durst et al. (1981) used an approximate equation, derived from the Stokes equation, to determine the frequency response of the particles and found that they satisfy to the criterion: *amplitude of particle oscillation/amplitude fluid oscillation* $> 99\%$. The equation

$$\omega \leq \frac{0.4 \cdot \nu}{d_p^2 \cdot \sigma} \tag{2.15}$$

predicts a frequency response, ω, of the HAZE particles to be up to 7.5 kHz, which is much larger than the expected maximum turbulence frequency in the jet.

From the dimensions of the control volume, the velocity of the flow and the number of bursts per second, a number density of the scattering particles can be calculated to be $N = 3.5 \times 10^{10}$ particles/m^3. This concentration is sufficient to resolve velocity fluctuations in excess of 200kHz using the equation of Durst et al. (1981). This frequency

is orders of magnitude higher than the frequency fluctuation in the turbulent jet and thus it can be concluded that the particle arrival rate is adequate (Durst et al. 1981). An equation to give an estimate of the statistical error, ϵ, that can be expected in a randomly sampled data set of length N with the given data rate η, a standard deviation σ_u of the mean velocity $\tilde{u}$ and the integral time scale T_u, was used by Winter et al. (1991) and by Bremhorst (1993):

$$\epsilon^2 = \frac{2T_u}{N}\left[1 + \frac{1}{2\eta T_u}\right]\left[\frac{\sigma_u}{\tilde{u}}\right]^2 \tag{2.16}$$

Equation (2.16) suggests that the statistical errors in the present experiments are expected to be insignificant.

Finite transit time broadening is negligible, since the measurements were taken in a flow field with high turbulence intensities and the errors due to instrument broadening from the spectrum analyzer have been eliminated (Durst et al. 1981).

From the above discussion it may be concluded that the main source of errors in the LDA measurements are due to the size of the control volume and the high velocity gradients in the precessing jet flow, which leads to broadening of the data. However, it has been shown that the errors due to spatial resolution are expected to be small and that other sources of error have been eliminated or reduced to an insignificant size.

Chapter 3

THE DEPENDENCY OF THE PRECESSING JET ON THE STROUHAL NUMBER

3.1 The Non–Rotating Jet

A precessional Strouhal number of St_p=0 represents the case of a stationary (i.e. non–rotating, f_p=0), simple turbulent jet. An investigation of that flow serves to test whether the exiting flow from the mechanical nozzle is perturbed by the nozzle profile and upstream flow path. The nozzle tip with an exit angle of 45° is used here and in all of the subsequent measurements. Velocity profiles are taken with a single hot-wire probe and a two dimensional Laser Doppler Anemometer.

From a detailed review of the literature, and with particular reference to the work of Abramovich (1963), Crow and Champagne (1971), Wygnanski and Fiedler (1969) and

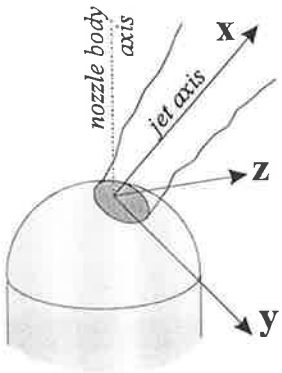

Figure 3.1: **The x–y–z coordinate system for the non–rotating jet** *only*

Rajaratnam (1976), a list of the characteristics which typify a simple turbulent round jet has been assembled and used as a basis of comparison for the present nozzle. To facilitate comparison with the cartesian based data of the above authors the cylindrical coordinate system used for the main body of the thesis has been transformed to a cartesian system for the present discussion. Note that the x–axis defines the direction of the jet, the y–axis is normal to the jet axis and the axis of the nozzle body and z is the third rectangular component (Fig.3.1). Visualisation of the whole flow field has been combined with hot–wire anemometry (Section 2.4.1) and laser Doppler anemometry (Section 2.4.3) to provide data which can be compared directly with those referenced above.

To identify the structures in a non–precessing turbulent jet, images have been formed using the laser induced fluorescence technique described in Section 2.3.3. The exit Reynolds number of the jet is 26,000. The jet from the mechanical nozzle, directed along the x–axis (which is at 45^o to the axis of the main nozzle assembly), shows features which are typical of a conventional free jet. From Fig.3.2 a half spreading angle, typically 12^o (Abramovich 1963), can be observed. Orderly structures similar to those described and visualised in a turbulent jet by Crow and Champagne (1971) and by Bradshaw et al. (1964), are also visible. These authors describe two kinds of structures

Figure 3.2: **Image of the non–rotating water jet issuing from the 45° mechanical nozzle. LIF technique, Re=26,000.**

in the Reynolds number regime around 10^4: surface ripples on the jet column and a tenuous train of large scale vortical puffs. Figure 3.2 displays the flow issuing from the present nozzle, in which 'orderly' structures and a train of large vortex puffs can be seen clearly.

An important parameter which influences the development of a jet issuing from a nozzle is the uniformity of the exit velocity profile. Figures 3.3 and 3.4 show hot–wire measurements of the profiles, in the xy– and xz–planes, with the jet exiting from the non–rotating mechanical nozzle. A small initial asymmetry at x/d=0.5 is apparent in both of these planes. This asymmetry decays rapidly and, at least in the subsequent profile taken with the hot-wire at x/d=3.0, satisfactory symmetry is reached and maintained as the jet progresses downstream. The maximum asymmetry $\Delta u/u$ in this initial region of the the jet is $< 8\%$.

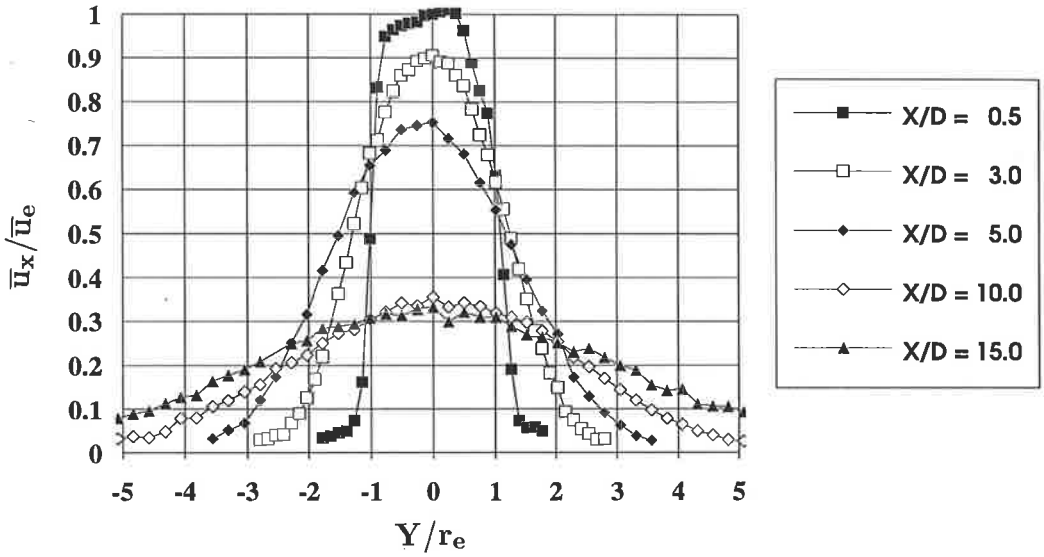

Figure 3.3: **Velocity profiles, traversed in y-direction, in the non–rotating jet issuing from the $\alpha_e = 45^o$ mechanical nozzle. Re=26,000**

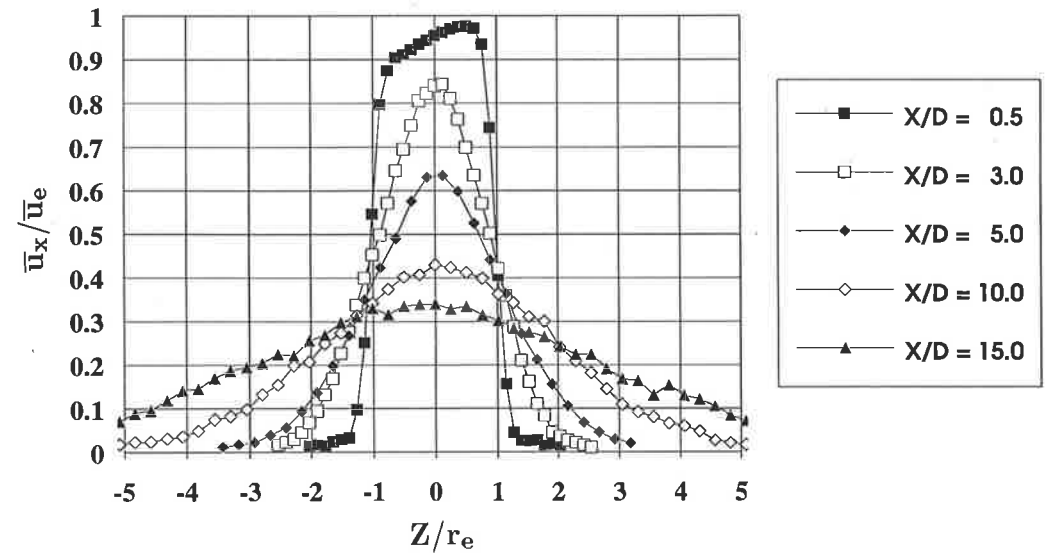

Figure 3.4: **Velocity profiles, traversed in z-direction, in the non–rotating jet issuing from the $\alpha_e = 45^o$ mechanical nozzle. Re=26,000.**

To complement the hot-wire measurements velocity profiles at x/d_e=1.0 have been taken with a laser Doppler anemometer system (Section 2.4.3). The results in Figure 3.5 show that the initial asymmetry which was apparent at x/d_e=0.5 is insignificant at x/d_e=1.0 from the nozzle exit.

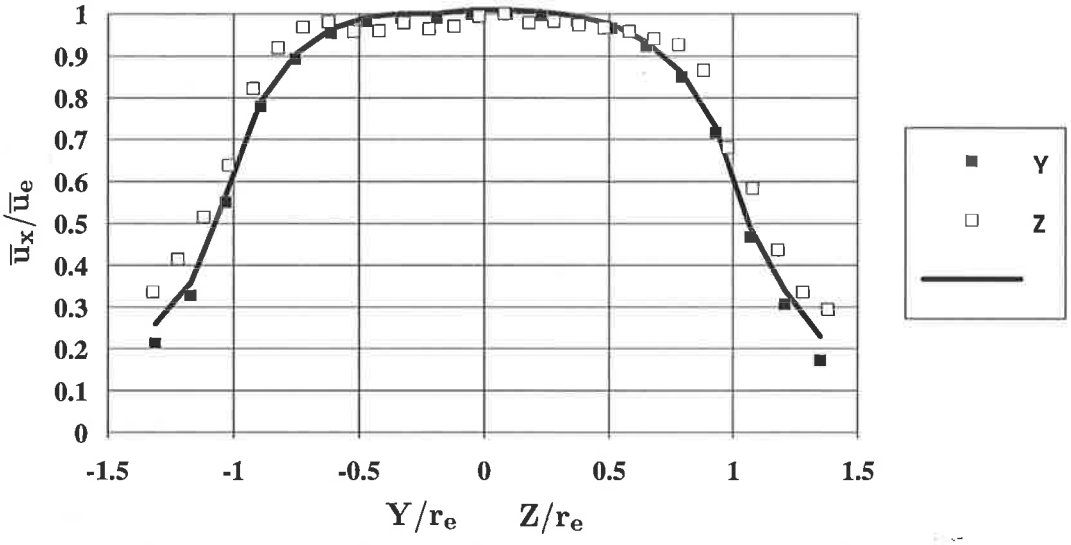

Figure 3.5: **Velocity profiles at x/d_e=1.0 and a symmetric line of best fit in the non-rotating jet issuing from the $\alpha_e = 45^o$ mechanical nozzle obtained by LDA. Re=26,000**

Based on the velocity profiles two 'internal' dimensions of the jet can be determined:

- a linear extrapolation of spreading angle of the jet (Figure 3.7), using the radius $r_{0.5}$ where the velocity has decreased to half the centerline velocity, defines the location of the virtual origin to be at $x/d_e \approx -4$

- decay of the average centerline velocity indicates that the downstream limit of the potential core is in the range $2.3 < x/d_e < 2.5$.

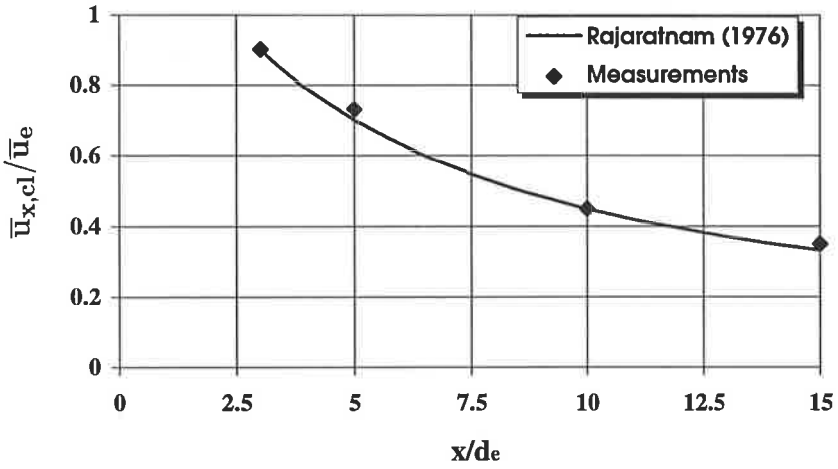

Figure 3.6: **Centerline velocity decay of the non–rotating jet. Re=26,000.**

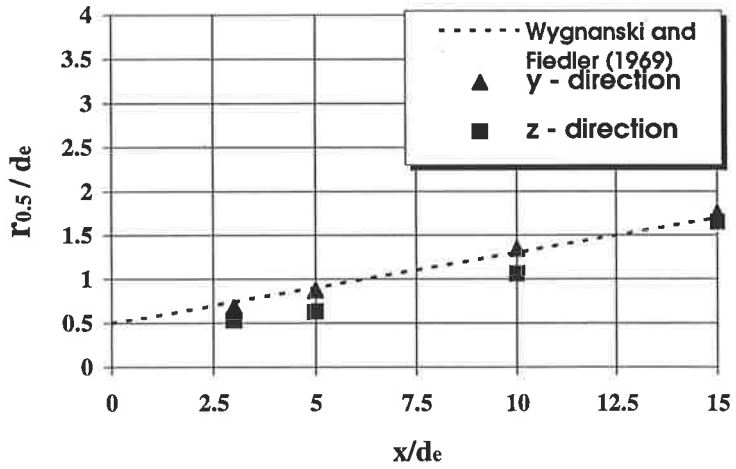

Figure 3.7: **Spreading angle of the non–rotating jet. Re=26,000**

The location of the virtual origin, $x_0/d_e = -4$, for the jet issuing at 45° from the mechanical nozzle can be directly substituted into the equation for the velocity decay of the centerline in an axial turbulent jet (Rajaratnam 1976):

$$u_{x,cl}/u_e = 6.3 \cdot (x - x_0/d_e)^{-1} \tag{3.1}$$

where $u_{x,cl}$ is the local centerline velocity, u_e is the exit velocity of the jet, x is the axial distance from the nozzle and x_0 is the location of the virtual origin. Rajaratnam considered a large number investigations which show a range of different locations of the virtual origin. He assumes, based on the evidence, a fixed length of 6.3 nozzle diameters from the start of the virtual origin to the end of the potential core. The average decay of the centerline velocity in the present jet shows good agreement with this equation (Figure 3.6). As the jet entrainment increases with the axial distance from the nozzle (Ricou and Spalding, 1961), the jet centerline velocity decays and the jet spreads according to the entrainment rate. The spreading of the jet issuing from the mechanical nozzle is compared with the 5° half angle found by Abramovich (1963) for a simple turbulent jet in Figure 3.7. Good agreement is found in the y–direction and in the z–direction the agreement is still adequate with the maximum deviation from the 5° spreading angle being $\Delta r_{0.5}/d_e = 0.027$, where $\Delta r_{0.5}$ is the deviation.

If the turbulent jet is self–similar the normalised hot-wire velocity profiles at downstream locations should collapse on a single curve. Normalising the velocity with the local centerline velocity, and normalising the radial position with the local radius $r_{0.5}$, the radius at which the centerline velocity has decayed to half of its value, leads to the results presented in Figures 3.8 and 3.9. Reasonable self-similarity is displayed in both the y– and z–directions. Figures 3.8 and 3.9 also show good agreement with a theoretical profile derived by Tollmien (1936) from the mixing length theory, which shows good agreementwith results of various experimental investigations.

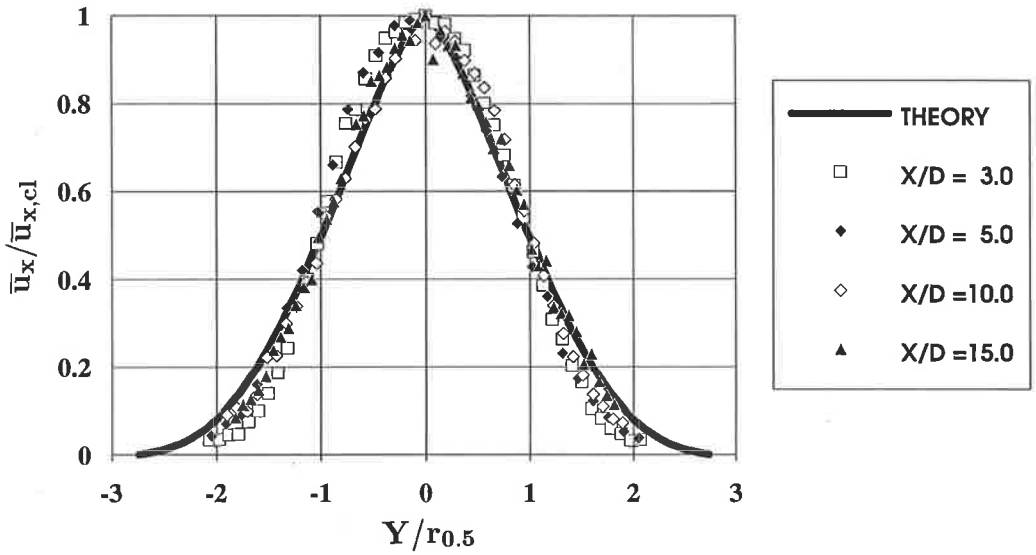

Figure 3.8: **Self–similarity of the non–rotating jet in y-direction. Re=26,000**

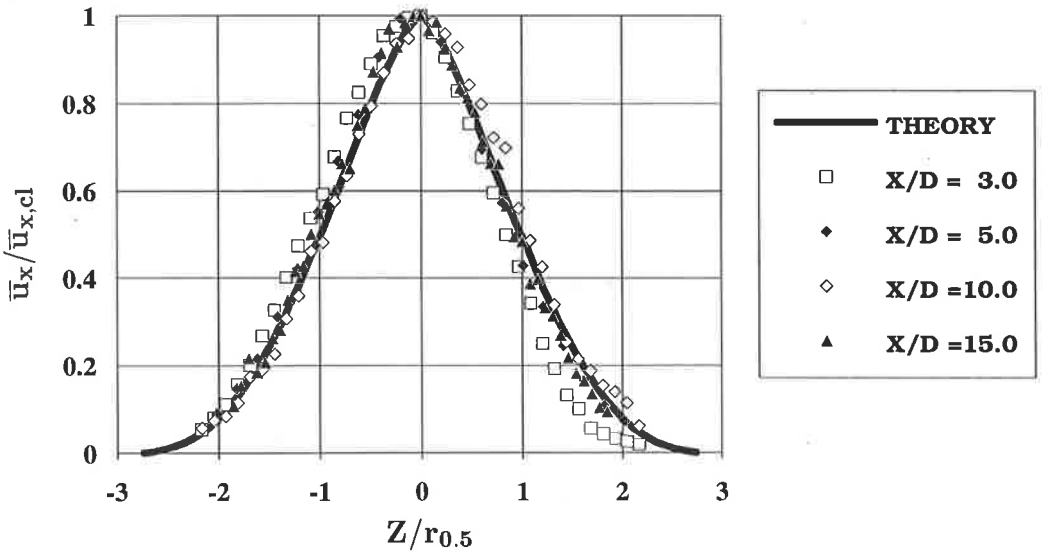

Figure 3.9: **Self–similarity of the non–rotating jet in z-direction. Re=26,000**

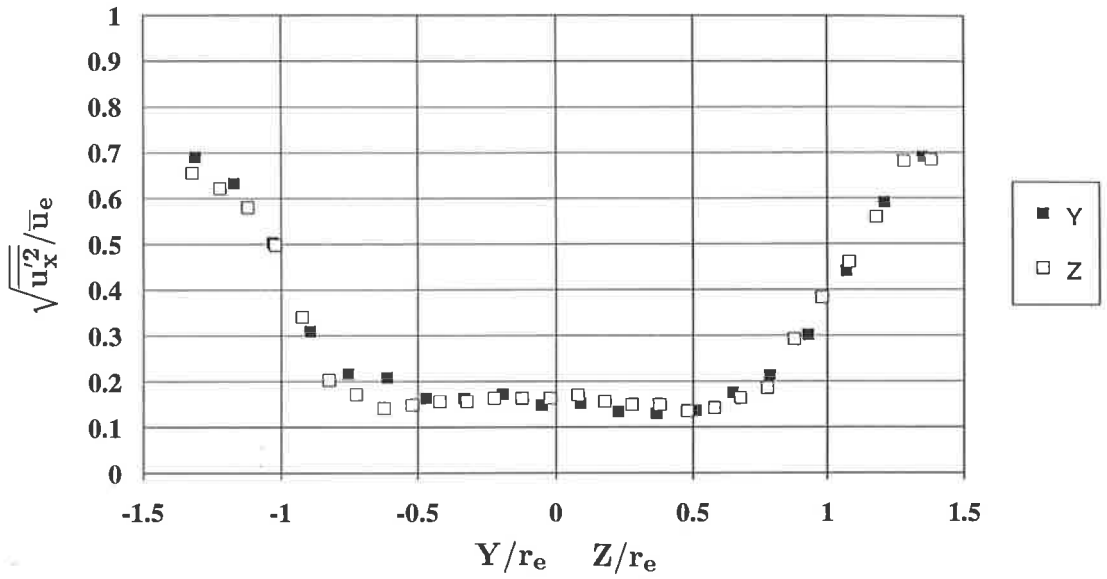

Figure 3.10: **Axial turbulence intensities at x/d_e=1.0 in the non–rotating jet obtained by LDA. Re=26,000**

The final feature of the simple turbulent jet addressed in this Section is the effect of the particular inlet conditions of the tested nozzle on the turbulence intensities. Figure 3.10 shows profiles at x/d=1.0 obtained by the Laser Doppler Anemometry. The measurement planes include the potential core, and the turbulence level of about 15% within that core agrees well with the turbulence levels found in the investigations referenced above (see also Figure 2.7 in Section 2.1.3). The symmetrical rise of the turbulence level in the turbulent shear layer of the jet confirms the good degree of symmetry of the jet deduced earlier from the velocity profiles above.

It can be concluded that, within the accuracy of the measurements, the turbulent jet issuing from the present 45° nozzle does not vary significantly from the simple turbulent axial jets investigated by Rajaratnam (1976), by Abramovich (1963) and by Wygnanski and Fiedler (1969). Thus the nozzle is an appropriate tool for investigating the effect of precession on the characteristics of a jet.

3.2 The Low Strouhal Number Jet

In the previous section it was demonstrated that, when it is not rotating, the mechanical nozzle produces a turbulent jet which is conventional in all major aspects. In Sections 2.1.2 and 2.1.3 it was shown that the spinning motion of the mechanical nozzle in the absence of a jet has only an insignificant influence on the flow field. Thus the effect of causing the jet to precess by rotating the nozzle can be expected to be dominated by the precession and not by features of the nozzle itself. First, the nozzle is rotated at a modest frequency of 8.05Hz causing a jet with u_e=40m/s to precess. These conditions correspond to a Strouhal number of 2×10^{-3} and a Reynolds number of 26,600.

Flow visualisation techniques allow global observations of the flow field. To quantify the observations, measurements of the three velocity components have been made using a three dimensional LDA system. From these measurements phase–averaged and time–averaged representations of the data are derived. Measurements are taken in r–Φ planes at $x/d_e = 2, 4, 6, 8, 10, 12$. A total number of 42,000 points per radial position ensures over 100 points for each mesh point in the phase averaged domain. This provides reasonable statistics not only of the mean components, but also of the turbulence components and the Reynolds stresses. The total number of 42,000 points enables good resolution of the higher order moments to be obtained in the time–averaged domain.

3.2.1 The Overall Flow Field

The first visualisation experiments were conducted using the conditional smoke pulse technique, described in Section 2.3.1, in which smoke is injected parallel to the exiting jet. Figure 3.11 shows an instantaneous picture of the rotating jet obtained by this

means. Two consecutive cycles of the precession are marked at the same angular position by puffs of smoke and the flow field is illuminated by a Halogen U–Lamp. The two smoke puffs are not deflected from the 45^o exit angle but follow each other along the same straight path. It also seems that no fluid is recirculated. This shows that the flow trajectories in a low Strouhal number jet (here $St_p = 0.002$) are similar to those in a simple turbulent jet.

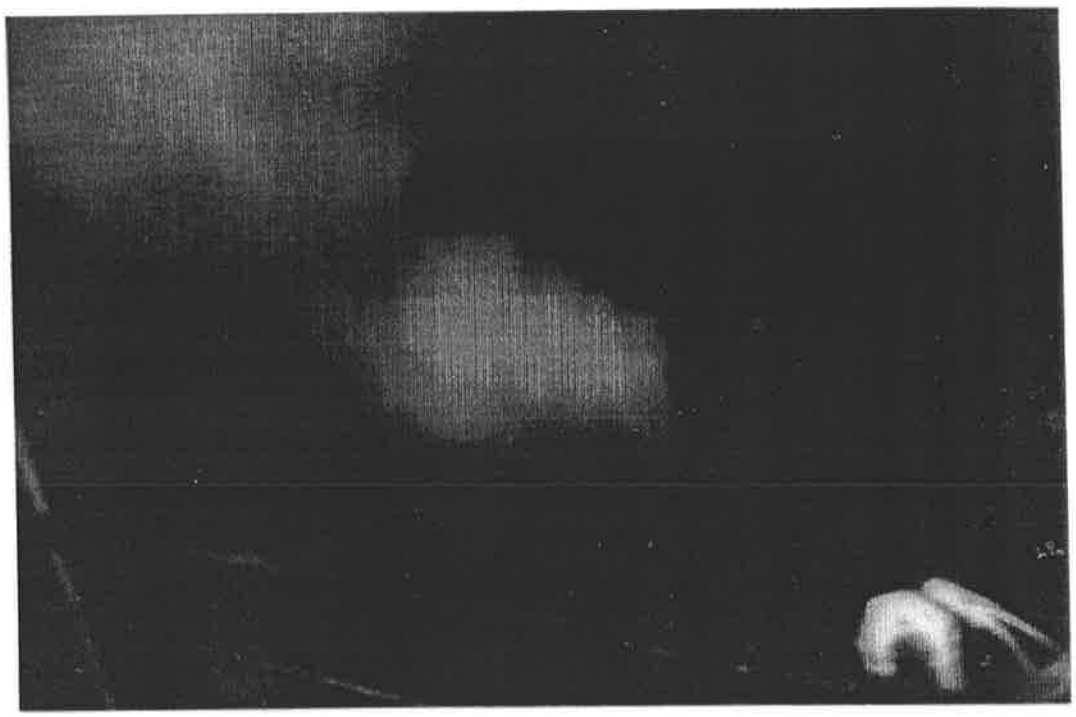

Figure 3.11: **Two consecutive cycles of precession in the low Strouhal number jet (here St_p=0.002). The beginning of each cycle is marked by a smoke pulse. Re=26,600**

A laser sheet flow visualisation technique in air (Section 2.3.2) is used to examine the above findings in more detail. Figure 3.12 shows this technique applied with glass beads of d< 40μm used to mark the jet fluid. The picture is taken with an SLR camera through the x–r plane of the precessing jet. It indicates that locally the flow closely resembles that in a simple turbulent jet. The structures of the 'preferred' mode of the jet (Hussain and Zaman, 1982) are also visible. Comparison of the LIF image of the stationary jet,

Figure 3.2, and the low Strouhal number precessing jet, Figure 3.12, show their main features to be similar. The jet remains in the light sheet, indicating that there is no deflection in the tangential direction. Also the path of the jet relative to a 45° line is almost undeflected. Only a slight deviation indicates that a small pressure gradient exists.

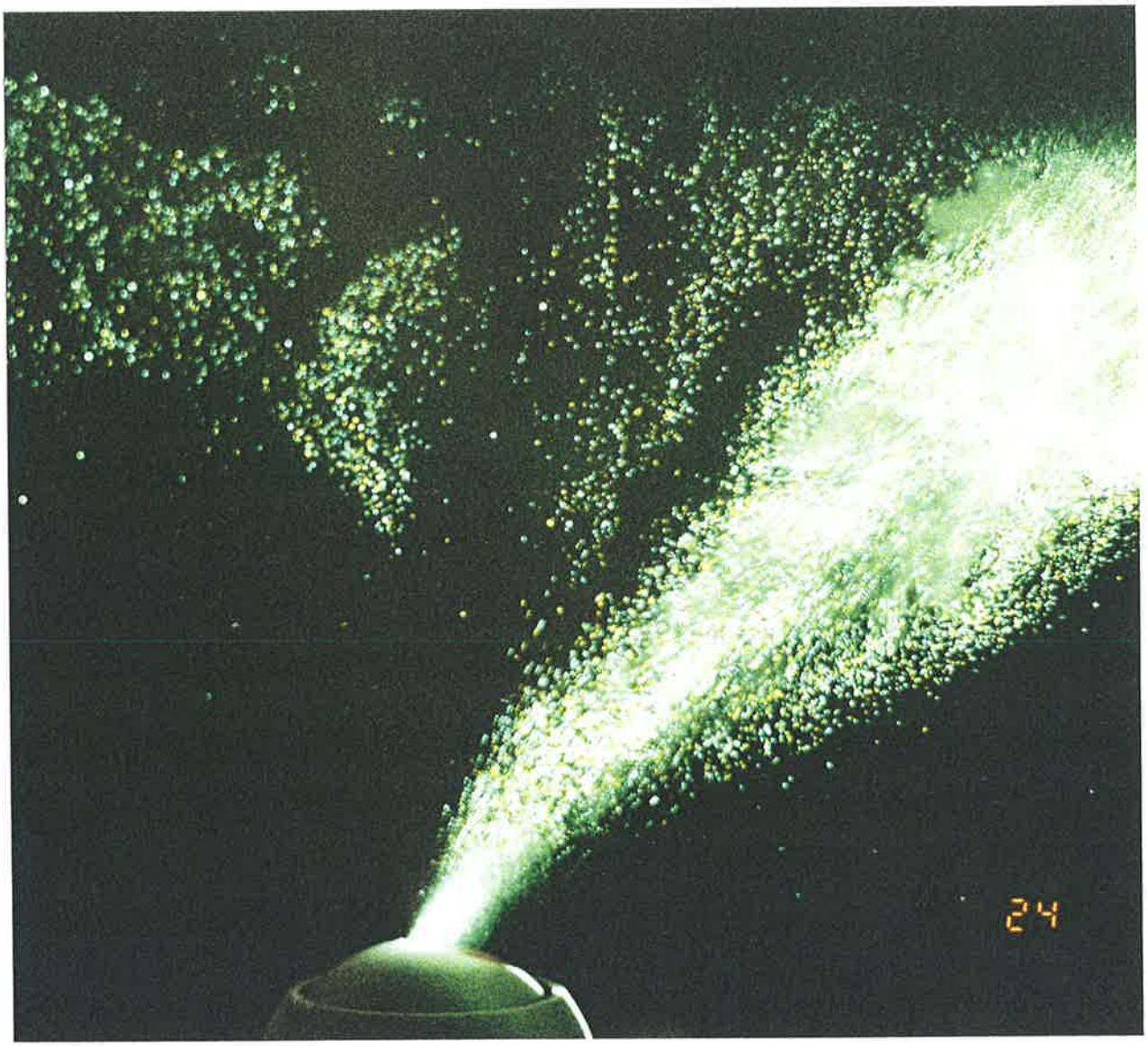

Figure 3.12: **Vertical Light Sheet from $0<x/d_e<12$ through the r–x Plane in the low Strouhal number Jet marked with glass beads. $St_p=0.002$.**

3.2.2 The Axial Velocity Component

Contours of the phase–averaged axial velocity in the low Strouhal number precessing jet flow, measured with the LDA system, are shown in Figure 3.13 and Figure 3.14. The colour scales of the contours are adjusted individually for each figure to show the highest velocity in red and the lowest in blue. Hence the colours in these figures should not be used when comparing different figures. For all data the exit Reynolds number is Re=26,600 and the Strouhal number of precession is $St_p = 2 \times 10^{-3}$.

Figure 3.13 and Figure 3.14 also show instantaneous images of the jet at corresponding axial distances. For these images a horizontal light sheet (r-Φ plane) produced by a copper vapour laser is used to illuminate glass beads of $< 40\mu$m diameter which mark the jet fluid (Section 2.3.2). The mechanical nozzle, seen in the background, is illuminated by light scattered from the particles. The jet in the visualisation experiments is not in phase with the velocity measurements and nor is it in phase from one axial distance to the next. The precession in the experiments is clockwise when viewed in the negative x–direction. These figures enable direct comparison of the visualised instantaneous contour of the jet and the phase–averaged axial component of the precessing jet. Strictly, only images of particles in the high velocity core region of the jet should be trusted since the glass beads ($< 40\mu$m) used for seeding the jet have initial momenta which is too large to follow the flow accurately (see Stokes equation 2.15).

At $x/d_e = 2$ the initially round jet is not deformed by the precession but its cross section appears to be elliptical since the jet is inclined by 45° to the r–Φ plane of the measurements. This is also revealed by the instantaneous image. A slight flow reversal of approximately 1m/s is measured in the region between the precessing jet and its spinning axis, but in the front and 'lee' side of the jet no reversed flow is detected. At the next position downstream from the nozzle exit, $x/d_e = 4$, the core of the jet is still relatively unaffected by the precession. A tail starts to develop in the 'lee' side of the jet. Reverse flow of about 0.5–1m/s is detected both on the inside and outside of the precessing jet. The instantaneous glass bead image reveals the presence of a region which bears some resemblance to a wake developing in its 'lee' side. Otherwise the jet is almost undeformed.

Further downstream at $x/d_e = 6$ and 8 the influence of precession becomes more evident. The core of the jet remains relatively undeformed, but the tail or 'wake' in the low velocity region grows rapidly. The reversed flow zones on the two sides of the jet become well established and are of the same order, 1m/s, as in the earlier measurement planes. The characteristics revealed in the instantaneous images are consistent with those of the phase–averaged LDA measurements. The trends at the axial distances of $x/d_e = 10$ and 12 are similar.

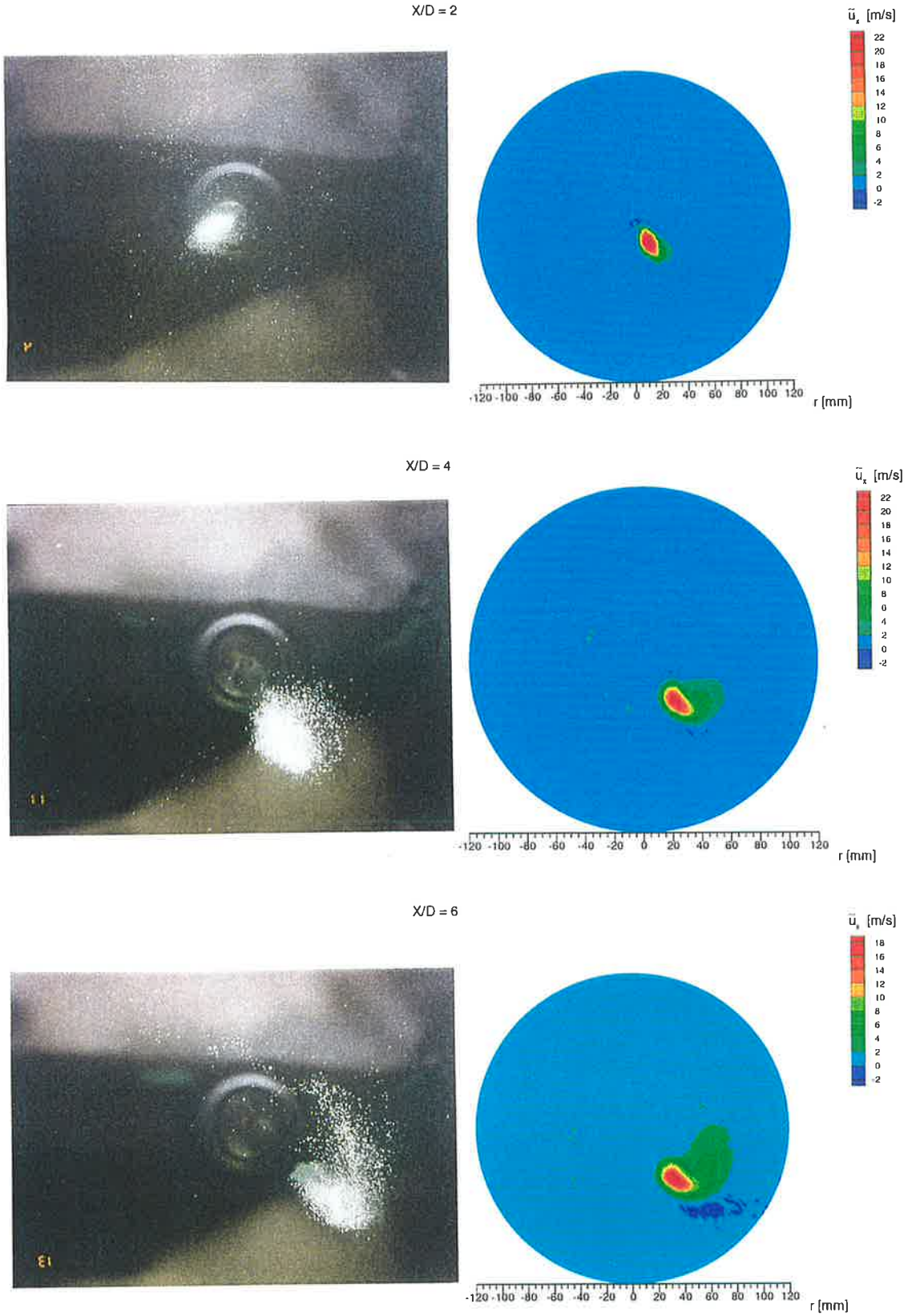

Figure 3.13: **Instantaneous particle images and phase-averaged axial velocity $\tilde{u}_x$ contours at x/d_e=2, 4, 6. St_p=0.002, Re=26,600.**

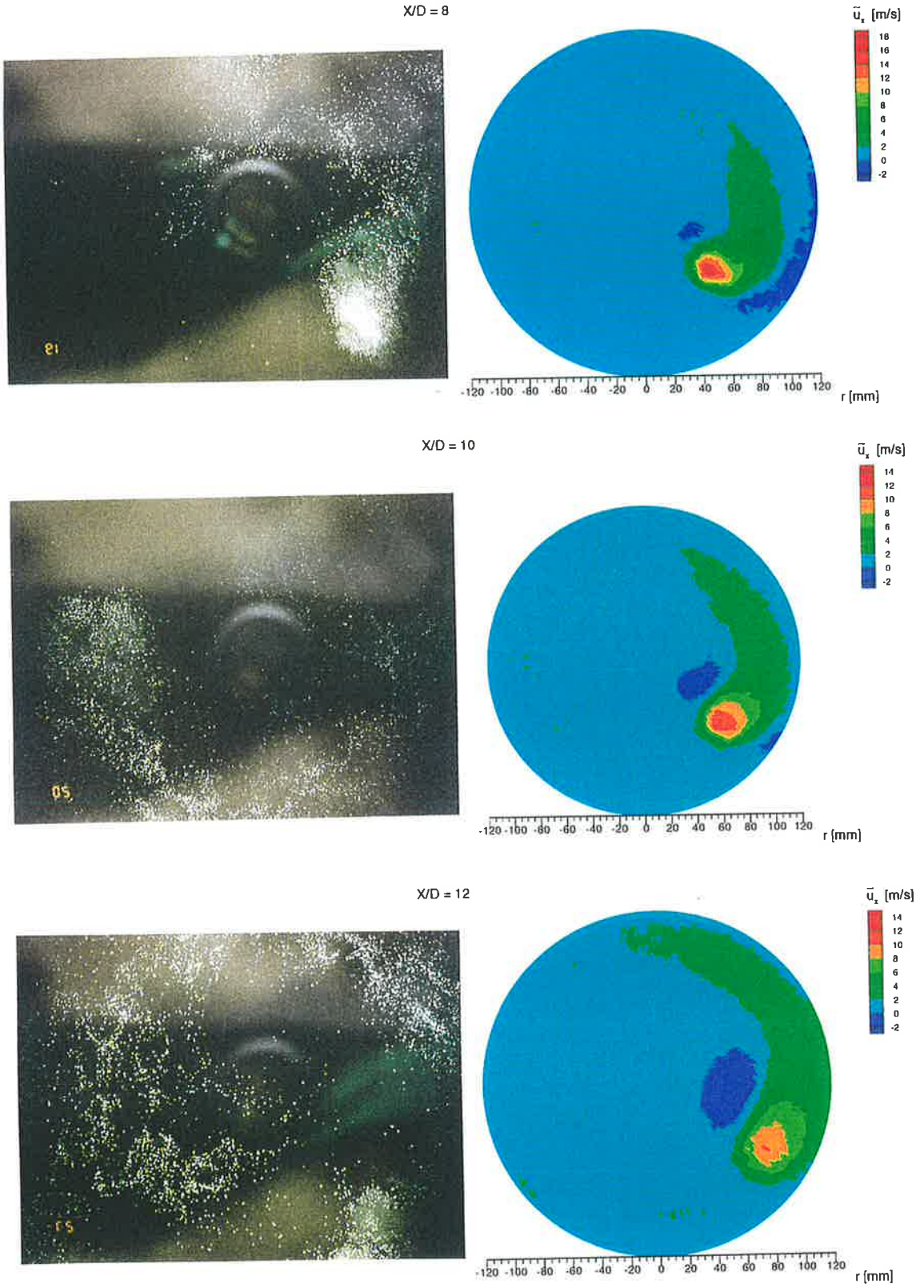

Figure 3.14: **Instantaneous particle images and phase-averaged axial velocity $\tilde{u}_x$ contours at x/d_e=8, 10, 12. St_p=0.002, Re=26,600.**

In Figure 3.15 are plotted the time–averaged axial velocities in the low Strouhal number regime (St_p=0.002), measured on radial traverses from x/d_e=2 to x/d_e=12. The reverse flow regions detected in the phase–averaged measurements are not evident in the time–averaged domain and thus appear to be weak phenomena which occur only in the immediate instantaneous vicinity of the jet. The peaks of the profiles can be used to trace the translation of the jet by its mean velocity component in the radial direction.

At $x/d_e = 2$ and 4 the maximum time averaged velocity occurs at r/d_e=2 and 4 respectively, which corresponds to the initial 45° direction of the jet. At $x/d_e = 6$ and 8 the jet has been deflected, relative to the 45° trajectory, by approximately one nozzle diameter toward the spinning axis. At $x/d_e = 10$ and 12 this deflection is increased to two nozzle diameters. The deflection is consistent with a zone of reduced pressure which has been identified between the jet and its spinning axis in the low Strouhal number regime, as will be shown in Figs.4.5 to 4.8 of Section 4.3.2; (see also Schneider et al. 1993).

It is also apparent that the profiles become progressively more asymmetric with increasing distance from the nozzle. The steeper velocity gradients on the 'inner' side of the jet relative to those on the 'outer' side are consistent with the stronger pressure gradients near the spinning nozzle, as will be shown in Section 4.3.2.

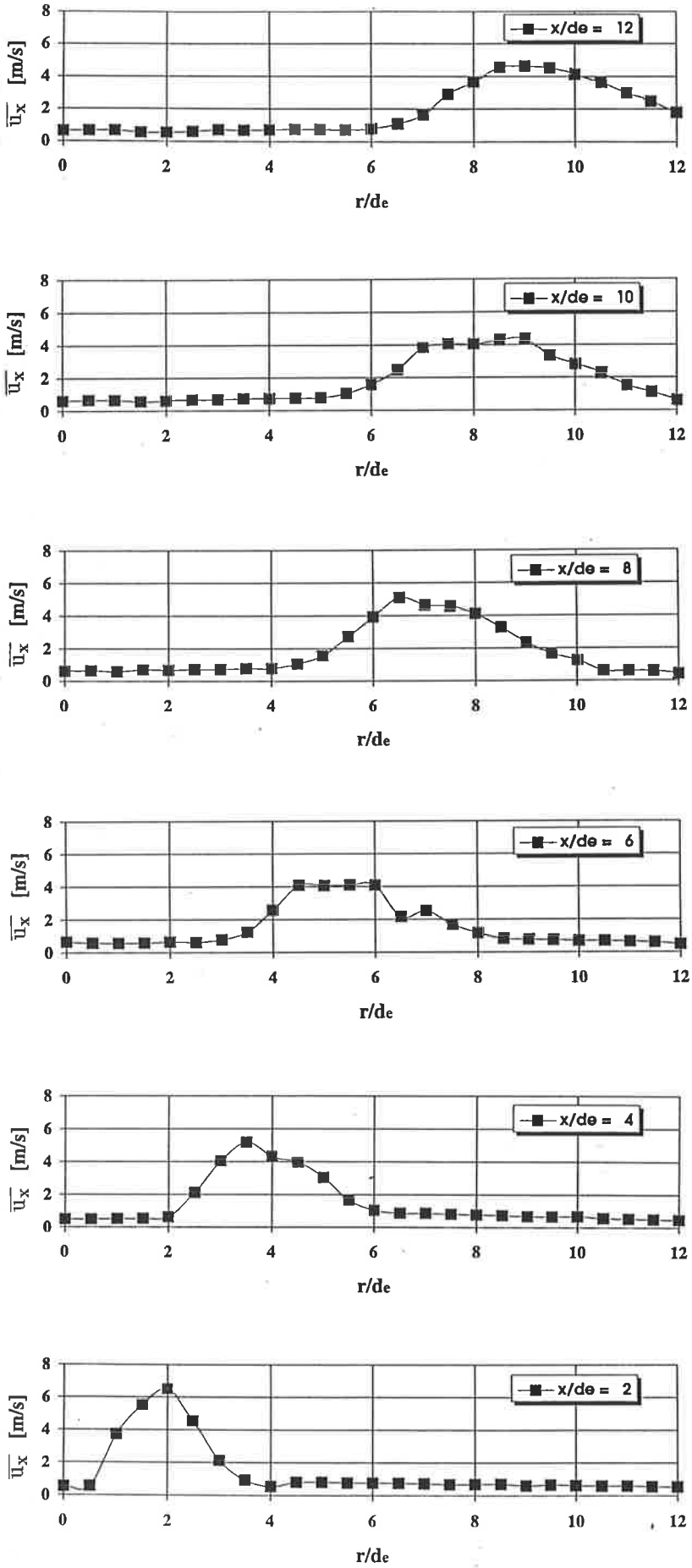

Figure 3.15: **Time–averaged axial velocity $\overline{u}_x$ at x/d_e=2 to 12. St_p=0.002, Re=26,600.**

3.2.3 The Radial and Tangential Velocity Components

Both the phase–averaged radial component as well as the phase–averaged tangential component for the low Strouhal number case (St_p=0.002) are combined to form velocity vectors in the r–Φ planes (Figure 3.16). In the vector plots the colour scale is not adjusted between the plots to emphasise the decay of the components. However, the length of the vectors are scaled for each figure to allow the direction of the low velocity flows to be seen.

Close to the nozzle, at $x/d_e = 2$, the red vectors clearly define the region occupied by the precessing jet. The vectors indicate a tangential velocity component which is negative (in the direction of the precession) in front of the jet and positive (against the direction of the precession) in the 'lee' side of the jet. The spread of the vectors, and thus the spread of the precessing jet, seems to be greater than the 12^o half angle typical of a simple turbulent jet. This observation is re-visited in the concluding section of the present chapter. At $x/d_e = 4$ the velocity of the precessing jet has decayed rapidly (green vectors), due to high shear stresses in the jet. Further downstream, at $x/d_e = 6$, the green vectors in the 'lee' side of the jet show a small positive tangential velocity component (against the precession). Tangentially, in front of the jet the vectors possess a small negative tangential and radial component. This is more evident at the next two axial planes, $x/d_e = 10$ and 12. A slight vortical motion can be detected tangentially in front of the jet.

The time–averaged radial velocity component is displayed in Figure 3.17. It is comparable to the axial velocity in the time domain, supporting the finding that the jet is hardly deflected from its initial direction of 45°. The peaks of the profiles are located at the same radial distances as the axial profiles. The values are generally lower than the axial component, due to the 'tail' in the axial velocity contours. Close to the nozzle exit (x/d_e=2, 4 and 6) a slight overall inflow towards the jet seems to occur. This indicates that there is a radial entrainment by the jet.

The time–averaged tangential velocity component is displayed in Figure 3.18. The values are much lower than the other two velocity components, since the jet exits on the axis of rotation and does not have any initial tangential component ($u_{\Phi,0} = 0$). At x/d_e=2 the peak value of 2.5m/s is located radially slightly inward from the location of the centreline of the precessing jet. At x/d_e=4 the peak tangential velocity has decayed to 1.2m/s and the peak is again slightly inwards (smaller r–coordinate) compared to the peaks of u_x and u_r. The minimum of the tangential velocity is just on the inside edge of the jet, where negative values of -0.5m/s are measured at almost all the axial distances.

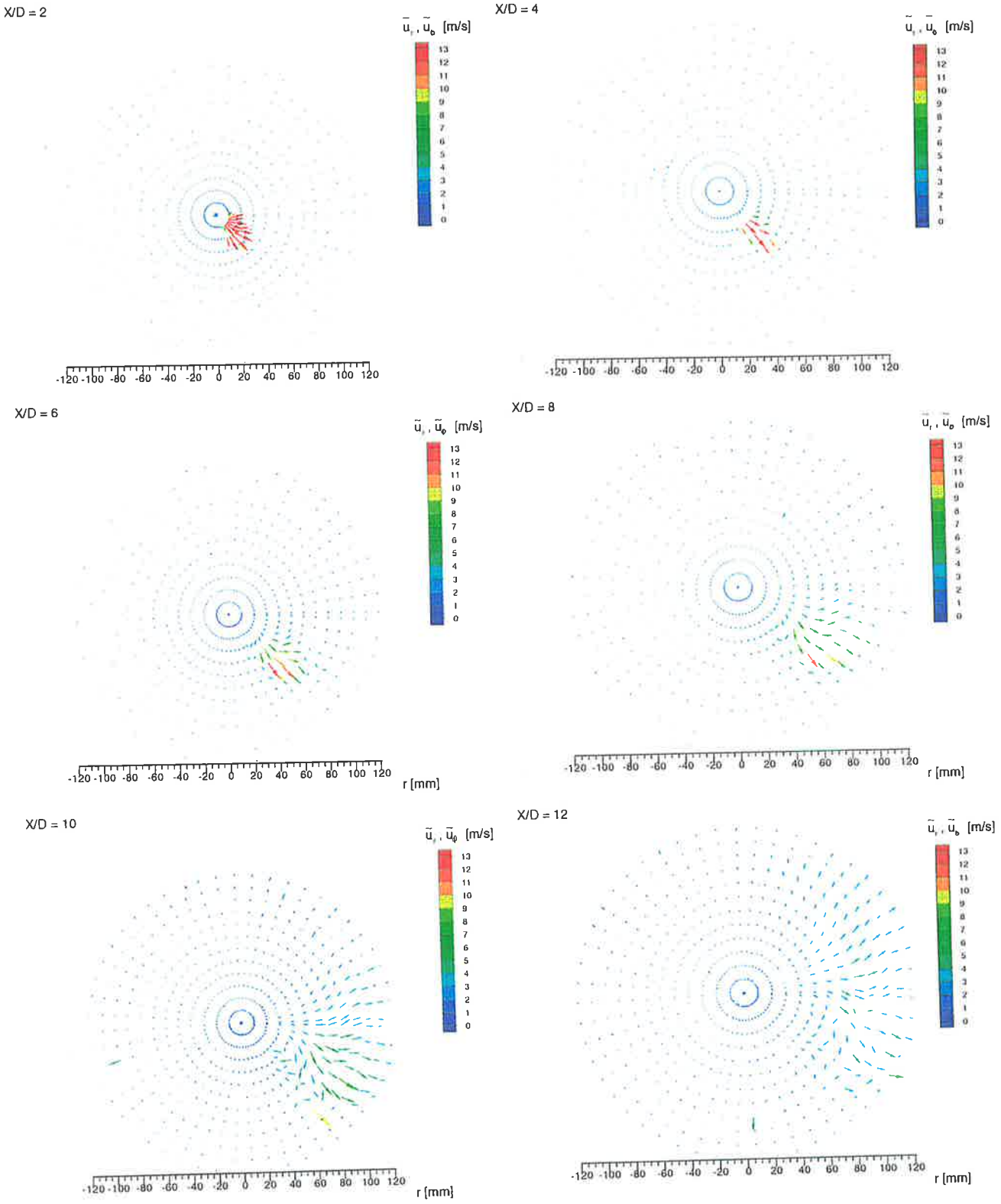

Figure 3.16: **Phase-averaged radial $\tilde{u}_r$ and phase–averaged tangential $\tilde{u}_\Phi$ velocities combined to form vectors, x/d_e=2, 4, 6, 8, 10, 12, St_p=0.002, Re=26,600.**

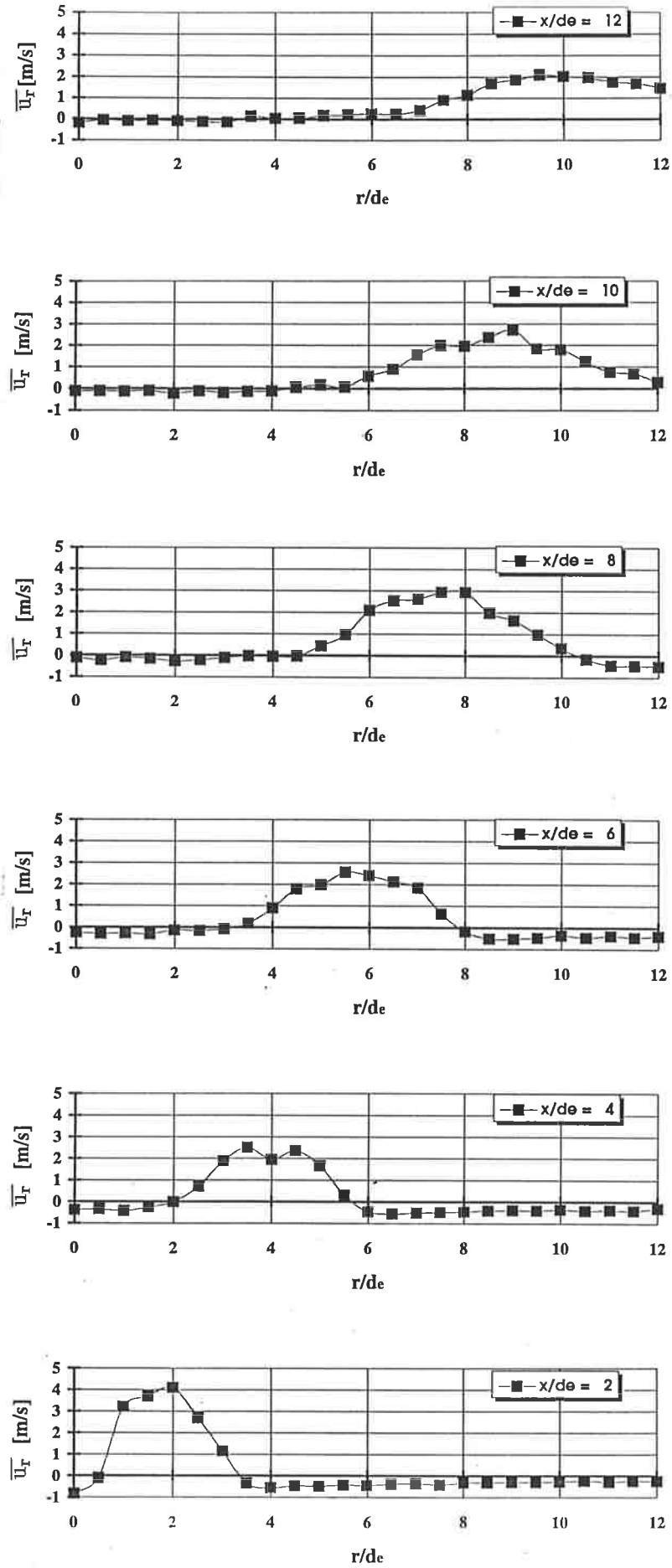

Figure 3.17: **Time–averaged radial velocity $\overline{u}_r$ at x/d_e=2 to 12. St_p=0.002, Re=26,600**

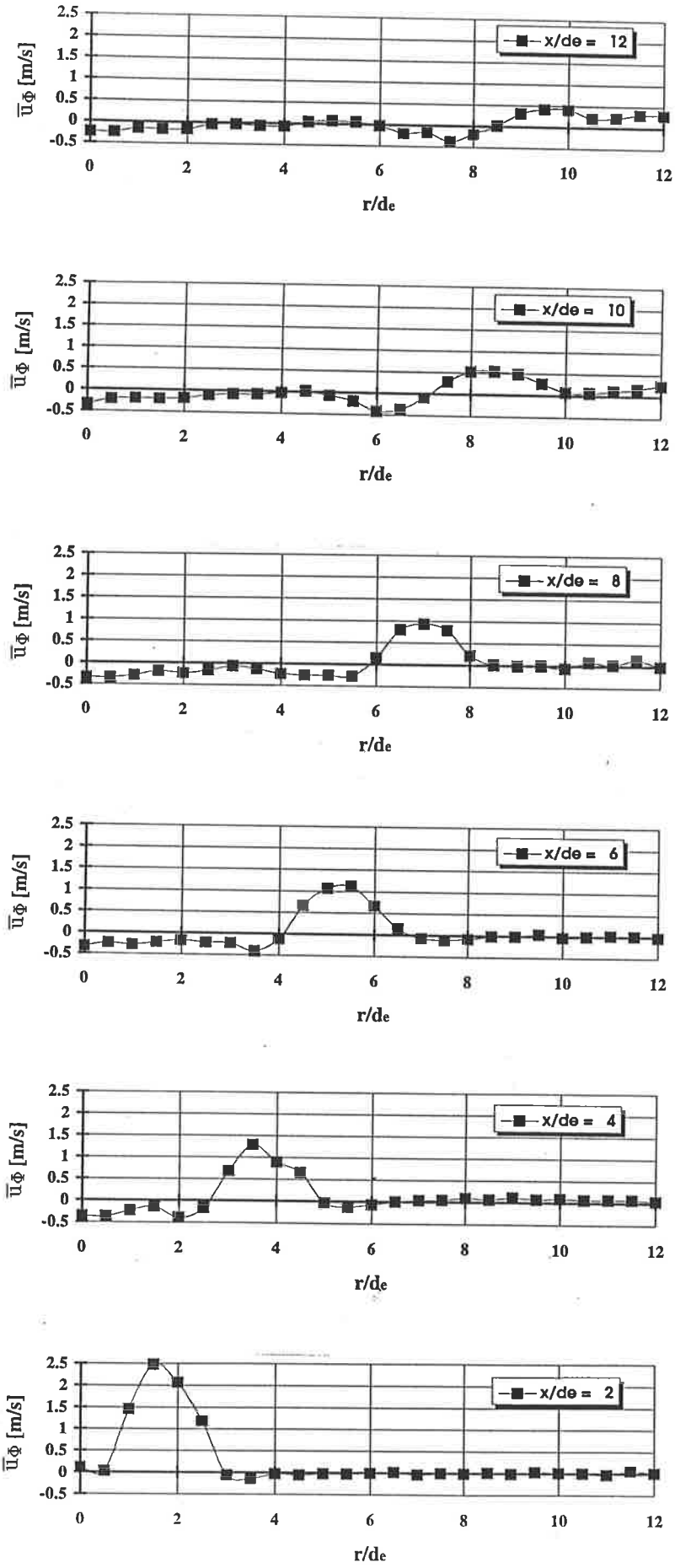

Figure 3.18: **Time-averaged tangential velocity $\overline{u}_\Phi$ at x/d_e=2 to 12. St_p=0.002, Re=26,600.**

3.2.4 The Turbulence Intensities

The turbulence intensity is defined as the normalised root-mean-squared (RMS) of the fluctuating velocity component, $\sqrt{\widetilde{u'^2_{x,r,\Phi}}}$ for the phase–averaged components and $\sqrt{\overline{u'^2_{x,r,\Phi}}}$ for the time–averaged component. The RMS value is non–dimensionalised with the respective local phase–averaged mean velocity component to demonstrate the turbulence level at each individual location. However, this leads to much higher levels of turbulence than are found in the literature for simple jets. As in a simple turbulent jet the RMS values are normalised by the maximum total velocity, i.e. the local centreline velocity, in the plane of the measurements. The present time–averaged turbulence data is displayed dimensionally in meters/second. In the Figures 3.19 to 3.23 the colour scale is the same for all x/d_e locations to enable direct comparison of the turbulence components.

The Axial Turbulence Intensity:

The contours of the axial turbulence intensity in Figure 3.19 identify the edges of the phase–averaged jet. The maximum intensity values (red) of up to 500% are located tangentially in front of the jet and on both sides (from the centre of the jet radially inward and outward). This forms a crescent which appears elliptical because of the 45° angle between the direction of propagation of the jet and the direction of views. This is consistent with a 'focus' of a vortex puff structure passing through the plane of measurements, which will be described in Section 4. A 'ring focus', coinciding with the high shear region of the phase–averaged jet, concentrates high turbulence intensity (Section 1.2.2) as shown by Liepmann and Gharib (1990) and Maxworthy (1970). The

high velocity core of the jet displays only lower turbulence levels (dark green) of 100% to 200% as does the 'lee' side of the jet. With increasing axial distance the regions remain similar in shape and similar in the levels of the turbulence. The ring focus grows in size as the jet grows and entrains fluid. It remains in almost the same angular position, confirming the straight, undeflected trajectory of the low Strouhal number jet. Two regions of very low turbulence intensity develop, one between the centre of rotation and the jet, and the other on the outer edge of the jet. These zones are deduced to coincide with the 'boundary' of the vortex structure, where in fact reverse flow was measured (Section 3.3.2).

The time-averaged axial turbulence intensity is presented in Figure 3.20. Clear peaks of the turbulence level can be identified which coincide with the centre of the precessing jet (note the turbulence is plotted in absolute units). As the jet grows with axial distance the peaks become lower and wider. Close to the exit of the jet, x/d_e =2 and 4 the turbulence reaches values up to 10m/s, which is comparable to the bulk mean exit velocity of 40m/s. At the furthest planes of measurements, $x/d_e = 10$ and 12, the peak turbulence has decreased to about 4m/s which is less than half the initial values.

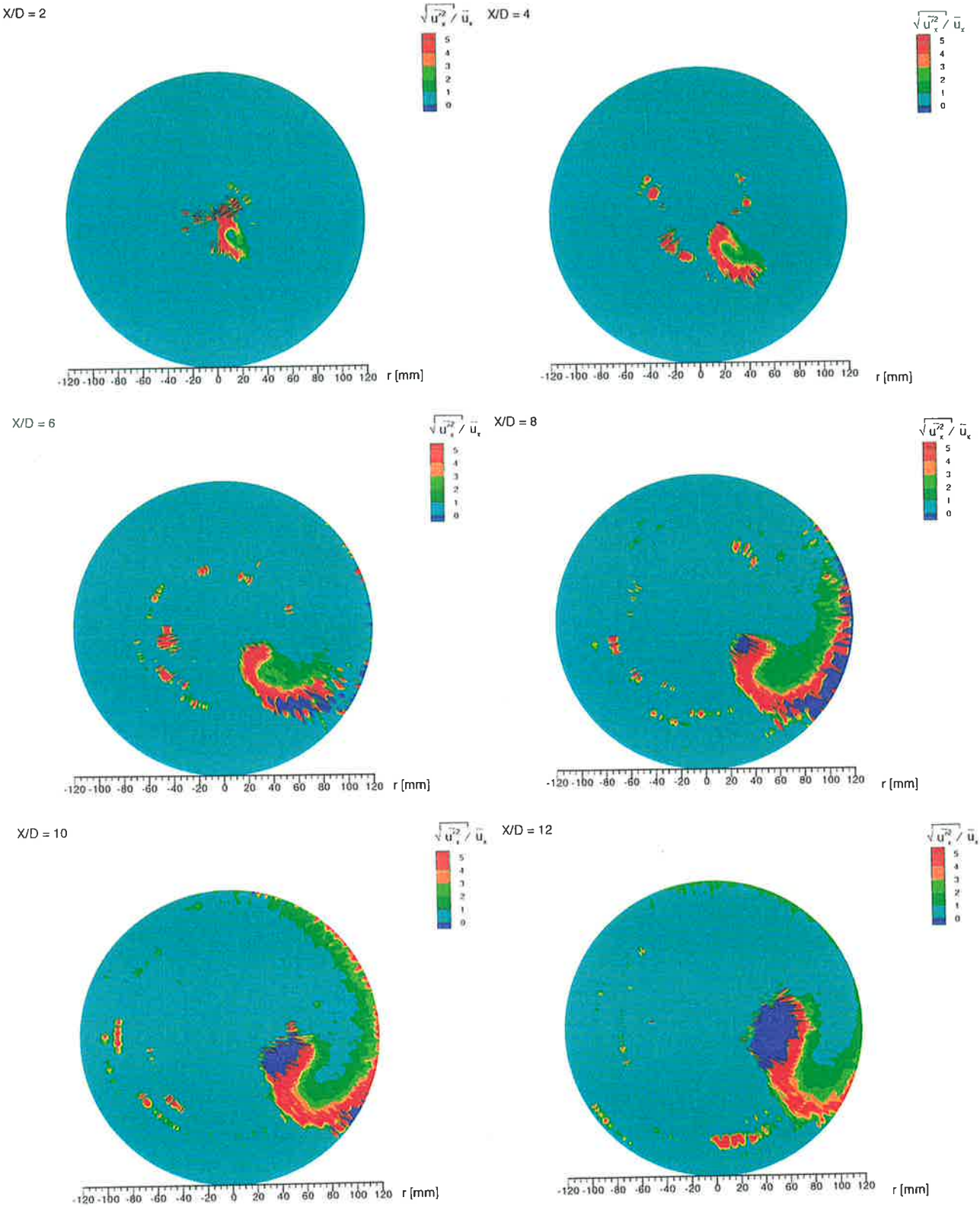

Figure 3.19: **Phase-averaged axial turbulence intensity at x/d_e=2, 4, 6, 8, 10, 12. St_p=0.002, Re=26,600.**

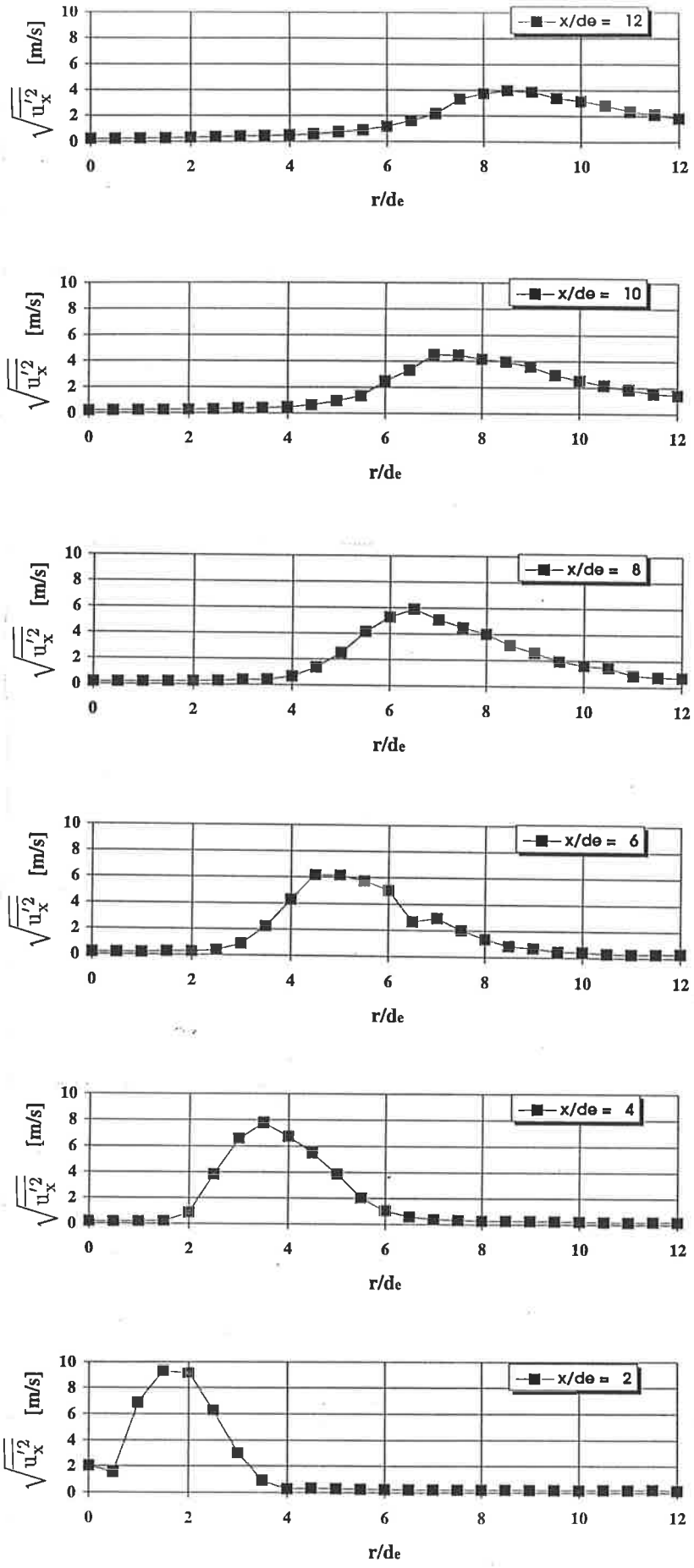

Figure 3.20: **Time–averaged axial turbulence at x/d_e=2 to 12. St_p=0.002, Re=26,600.**

The Radial Turbulence Intensity:

In Figure 3.21 the phase–averaged radial turbulence component is displayed. The elliptic cross section through the round jet is visible. The high turbulent regions (red) of up to 500% are located mainly on the outer edge of the precessing jet, with small regions in the front and 'lee' side of the jet. This could be interpreted as a 'ring focus' of the vortex structure passing through the plane of measurements, which will be described in Section 4. But the structure is distorted or destroyed earlier than in the axial turbulence component. As with the axial components the high velocity centre of the jet has turbulence levels of about 100% (dark green). As the jet is convected downstream the green region, roughly coinciding with the inflow and recirculation region (Fig.3.16), grows with the jet. The outer edge of the jet continues to have a high turbulence level of 400% to 500%.

The time–averaged radial component of turbulence, shown in Figure 3.22 is almost identical with the axial component. This is consistent with the findings of the flow visualisation (Section 3.2.1) that low Strouhal number PJ flows are only slightly deflected from their original trajectory, in this case $\alpha_e = 45°$. The turbulence levels peak at about 8–10m/s at x/d_e=2 and decrease to levels of about 2–4m/s at x/d_e=12. As with the axial components, the peaks of the radial turbulence intensity profiles correspond with the location of the maximum phase–averaged velocity.

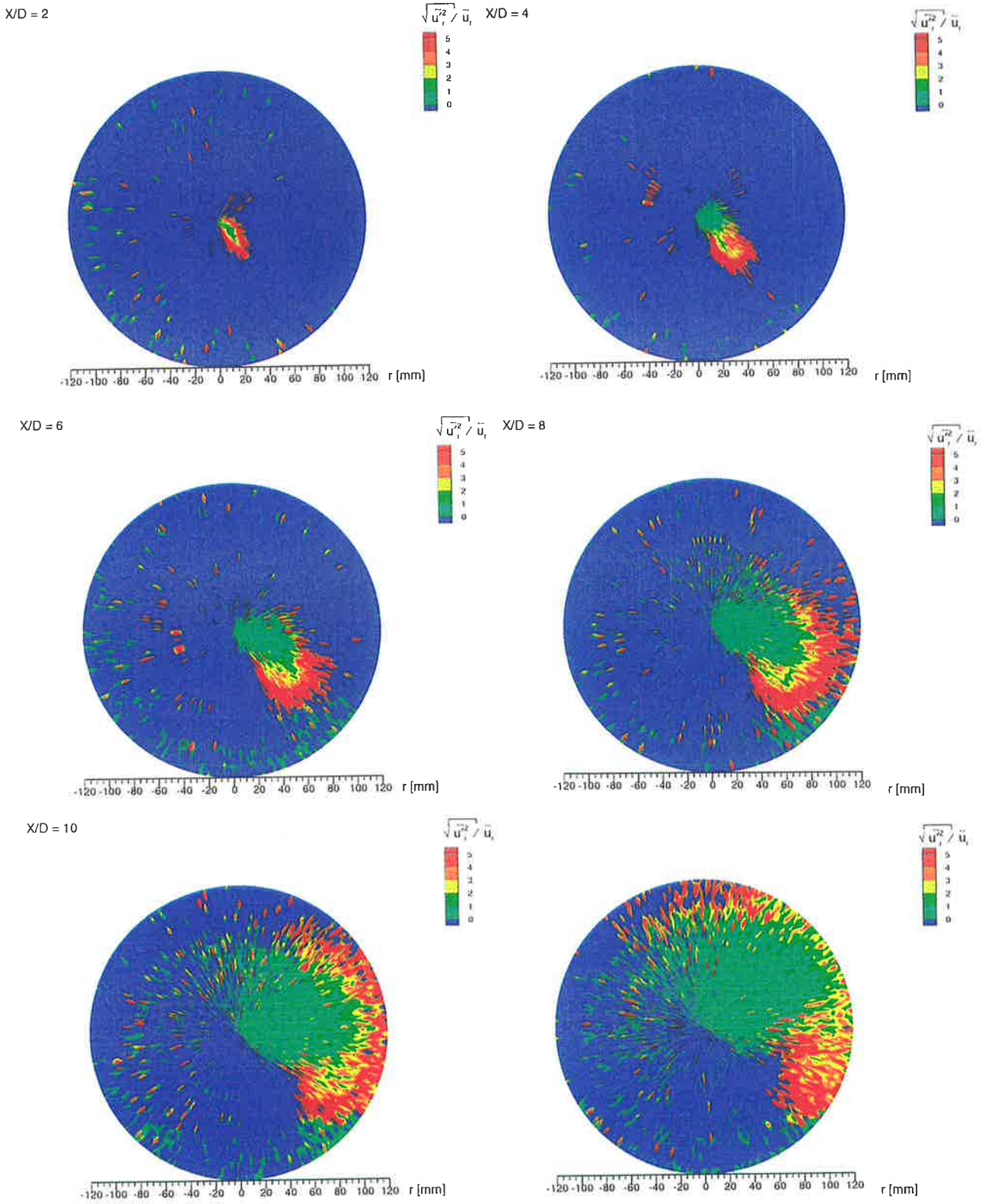

Figure 3.21: **Phase-averaged radial turbulence intensity at x/d_e=2, 4, 6, 8, 10, 12. St_p=0.002, Re=26,600.**

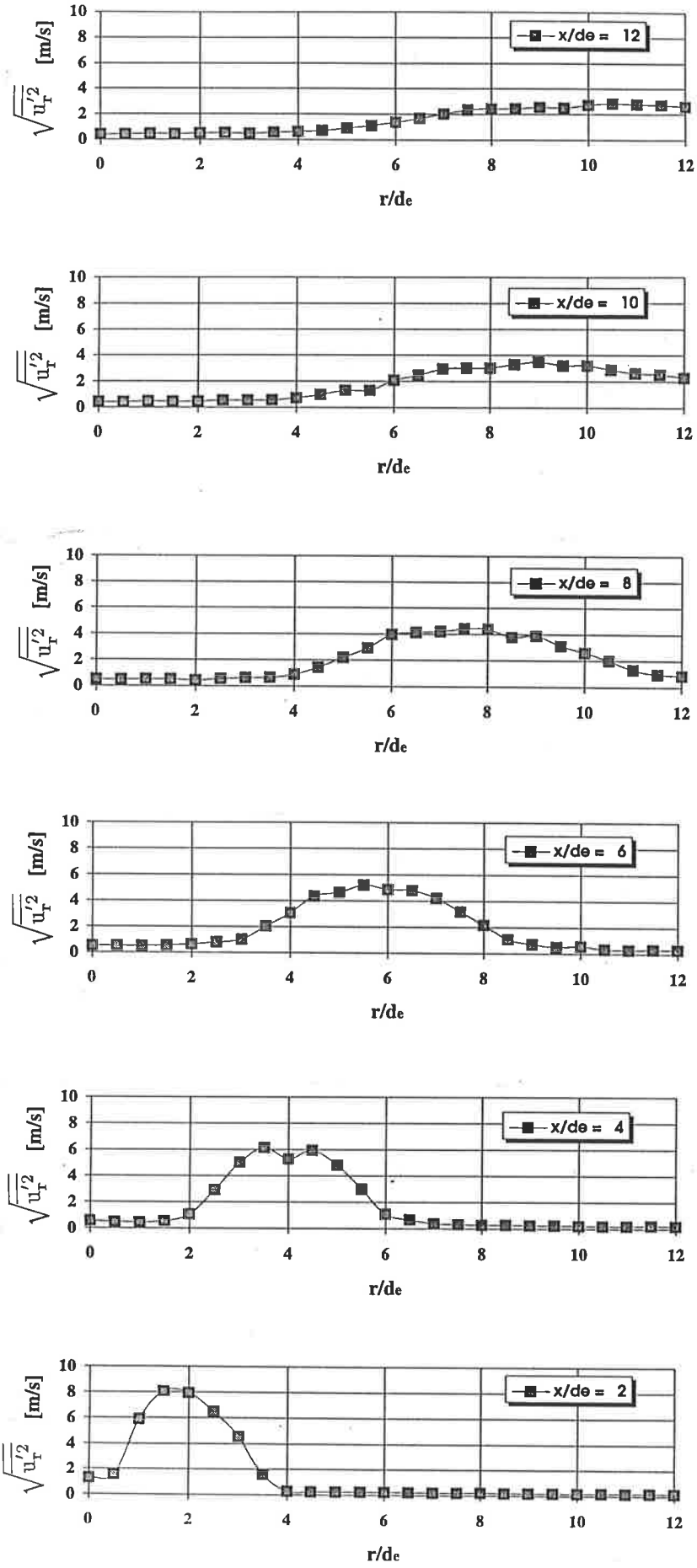

Figure 3.22: **Time–averaged radial turbulence at x/d_e=2 to 12. St_p=0.002, Re=26,600.**

The Tangential Turbulence Intensity:

Since the precessing jet does not inherit an intial tangential velocity component, the component of the phase–averaged tangential turbulence intensity does not show the distinctive jet contour. The region shown in red in Fig.3.23 represents a turbulence intensity of 400%–500% and corresponds to the high shear region in the jet (at x/d_e=4 and 6 on its front and 'lee' side). However, regions of low turbulence (dark blue) in Fig.3.23 dominate the turbulence field. These areas correspond to the inner edge (re-circulation region) and the outer edge of the jet, where reverse flow was also measured (Fig.3.16).

In the time–averaged tangential component of the turbulence intensity, Figure 3.24, the peaks also correspond to the centre of the precessing jet, as found for the other components. The levels of turbulence are generally lower than those found in the axial and radial components. At x/d_e=2 the level is about 5m/s. This value decreases to 3m/s at x/d_e=6 and to about 2.5m/s at x/d_e=12.

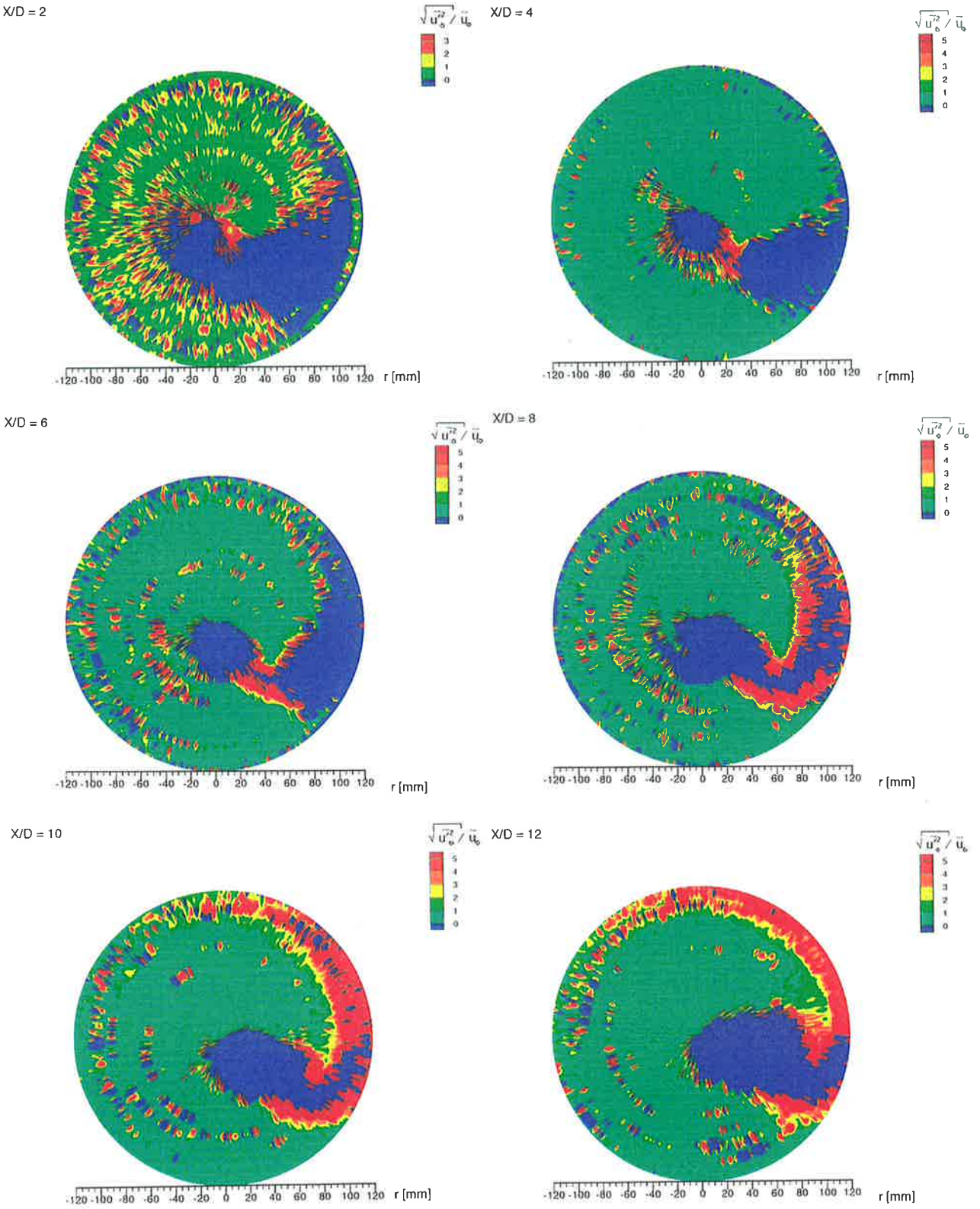

Figure 3.23: **Phase-averaged tangential turbulence intensity at x/d_e=2, 4, 6, 8, 10, 12. St_p=0.002, Re=26,600.**

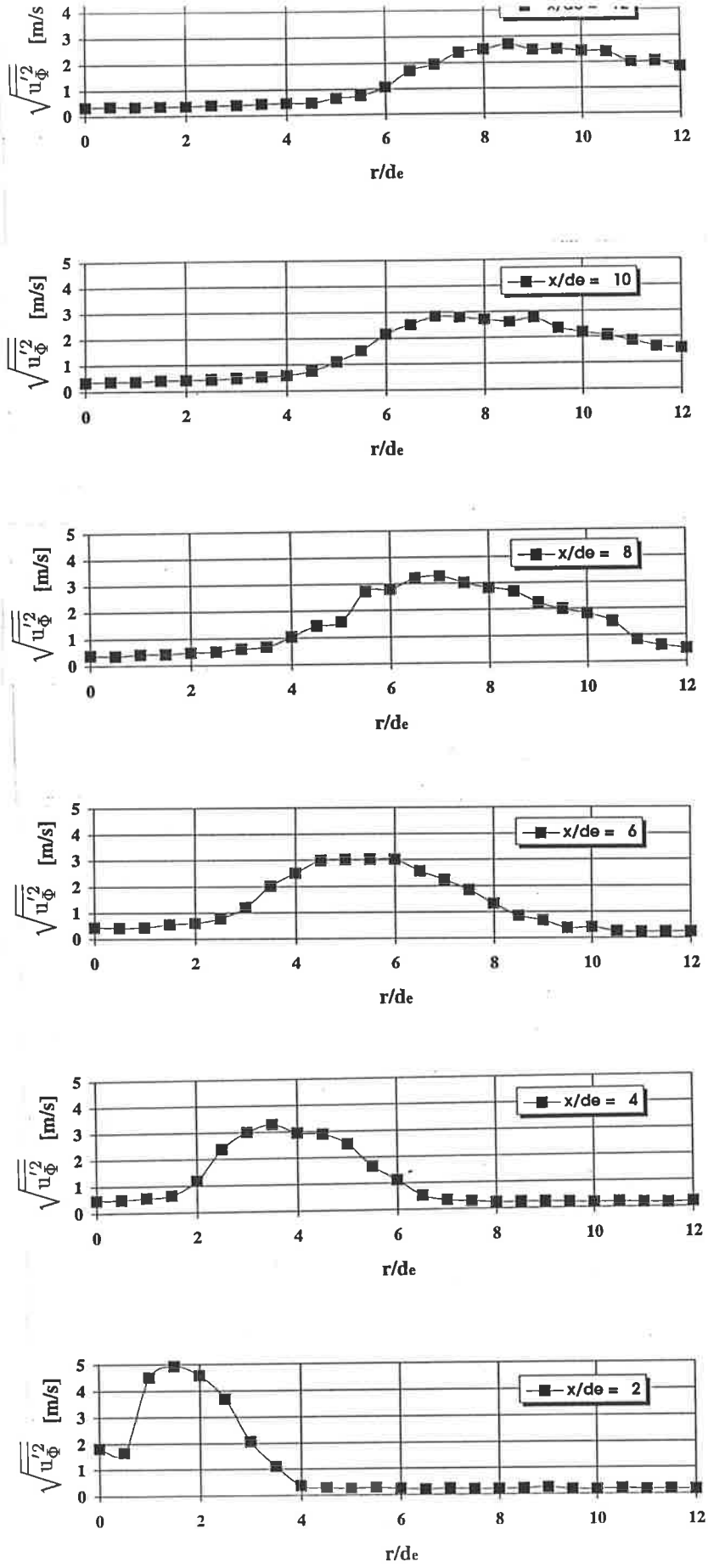

Figure 3.24: **Time–averaged tangential turbulence at x/d_e=2 to 12. St_p=0.002, Re=26,600.**

3.2.5 The Reynolds stresses

Reynolds stresses are related to transfer of energy from the mean flow to provide energy for the turbulent fluctuations (Tritton 1988). This transfer increases the turbulence level and hence the entrainment (Bremhorst and Hollis, 1990). The phase–averaged Reynolds stresses measured by LDA in a low Strouhal number jet are presented in the Figures 3.25 to 3.27. The turbulent stresses are defined as the mean value of the product of two fluctuating velocity components. The results of the measurements are shown in non–dimensionalised form, which is achieved by dividing the combined mean value by the product of the individual phase–averaged values of the velocity components. The colour scale of the phase–averaged Reynolds stress contours, shown in Figures 3.25 to 3.27, is unchanged for the six axial planes of measurements. It is important to note that the change of colour in the background of the plots resulted from unavoidable software adjustments and should not be confused with the changes in the flow field.

The $\frac{\widetilde{u_x' u_r'}}{u_x u_r}$ Reynolds stress combines the fluctuating parts of the two major velocity components. The elliptical cross section through the round jet can therefore be seen in the normalised Reynolds stress contours (Fig.3.25). The dark blue region, corresponding to the high velocity core of the jet, has very low normalised stress levels in the range of 0 to 0.25 at x/d_e=2. The magnitude of the relative stresses in the core of the phase-averaged jet increases with axial distance to the range 0.5–0.75 at x/d_e=6. In the high shear regions of the jet around the core, the stress levels are between 0.25 and 0.5 at x/d_e=2 and remain high (up to 0.75 at x/d_e=10). The red region in Figure 3.25, which represents the highest normalised Reynolds stresses, exceeding unity, is concentrated between the jet and the spinning axis and coincides with the recirculating fluid identified in Figs.3.13 and 3.14. The stress levels in the core of the PJ, in the range of 0–0.25,

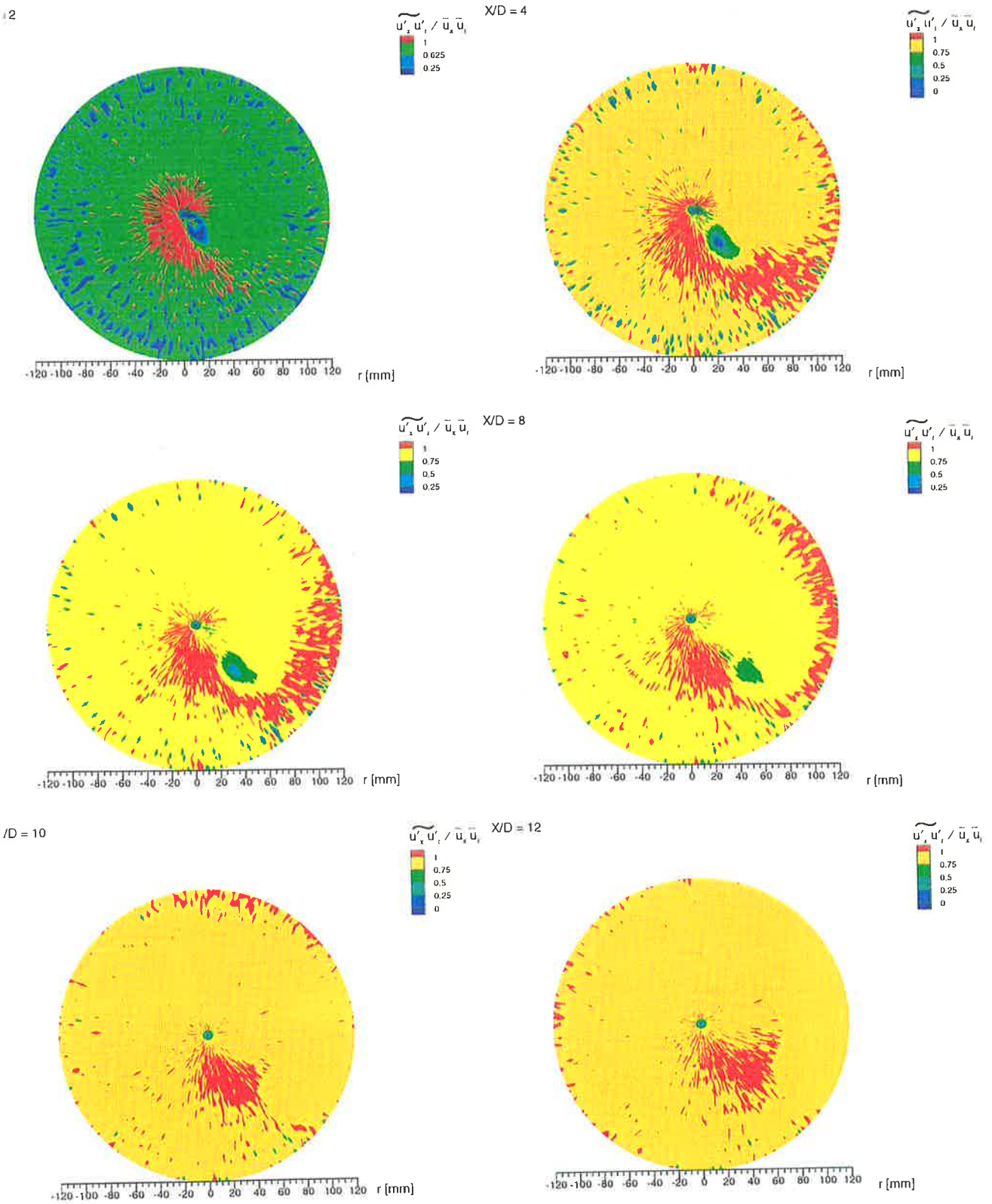

Figure 3.25: **Normalised phase-averaged $\frac{\widetilde{u'_x u'_r}}{\widetilde{u}_x \widetilde{u}_r}$ Reynolds stress component at x/d_e=2, 4, 6, 8, 10, 12. St_p=0.002, Re=26,600.**

are in the same order of magnitude as the stresses in the core of a simple turbulent jet (Wygnanski and Fiedler, 1969). The recirculation zone and the outer edge of the precessing jet (red regions in Fig.3.25) show higher stress levels than in the main body of the jet which indicates that the recirculation region plays a key role in the enhanced entrainment measured in the PJ flows (Nathan, 1988). This effect will be shown to be even more marked in the high Strouhal number flow (Section 3.3.5).

The normalised component $\frac{\widetilde{u_x'u_\Phi'}}{u_x u_\Phi}$ of the Reynolds stresses is shown in Figure 3.26. The centre of the jet at x/d_e=2 corresponds with values of stresses between 0 and 0.2. In the regions of high velocity gradient around the jet centre the values rise to 0.75. At x/d_e=4 the normalised stresses in the core of the jet increase to 0.5 and are encircled by higher values of 0.75. Two red regions develop on the sides of the jet, i.e. between and distal from the spinning axis and the jet. These regions are believed to be associated with the 'ring focus' of a vortex puff or ring (Section 1.2.2 and Section 4) where very high normalised Reynolds stresses exceeding unity occur. This feature is also evident at x/d_e=6. The centre of the jet is not detectable beyond x/d_e=6, but the red regions of the ring focus remain.

The combination of the radial and the tangential fluctuating components is shown in Figure 3.27. Initially, at x/d_e=2, the jet is identifiable by the dark blue region indicating stresses of up to 0.3. This region is again encircled by the green values of about 0.3–0.6. At x/d_e=4 the centre of the jet has already 'disappeared' into the background level of the surrounding fluid. Only small green regions identify the inside and outside edges of the jet. At locations further downstream the stress field of the whole region affected by the jet is seen to have high $\frac{\widetilde{u_r'u_\Phi'}}{u_r u_\Phi}$ values of 0.75 to 1.

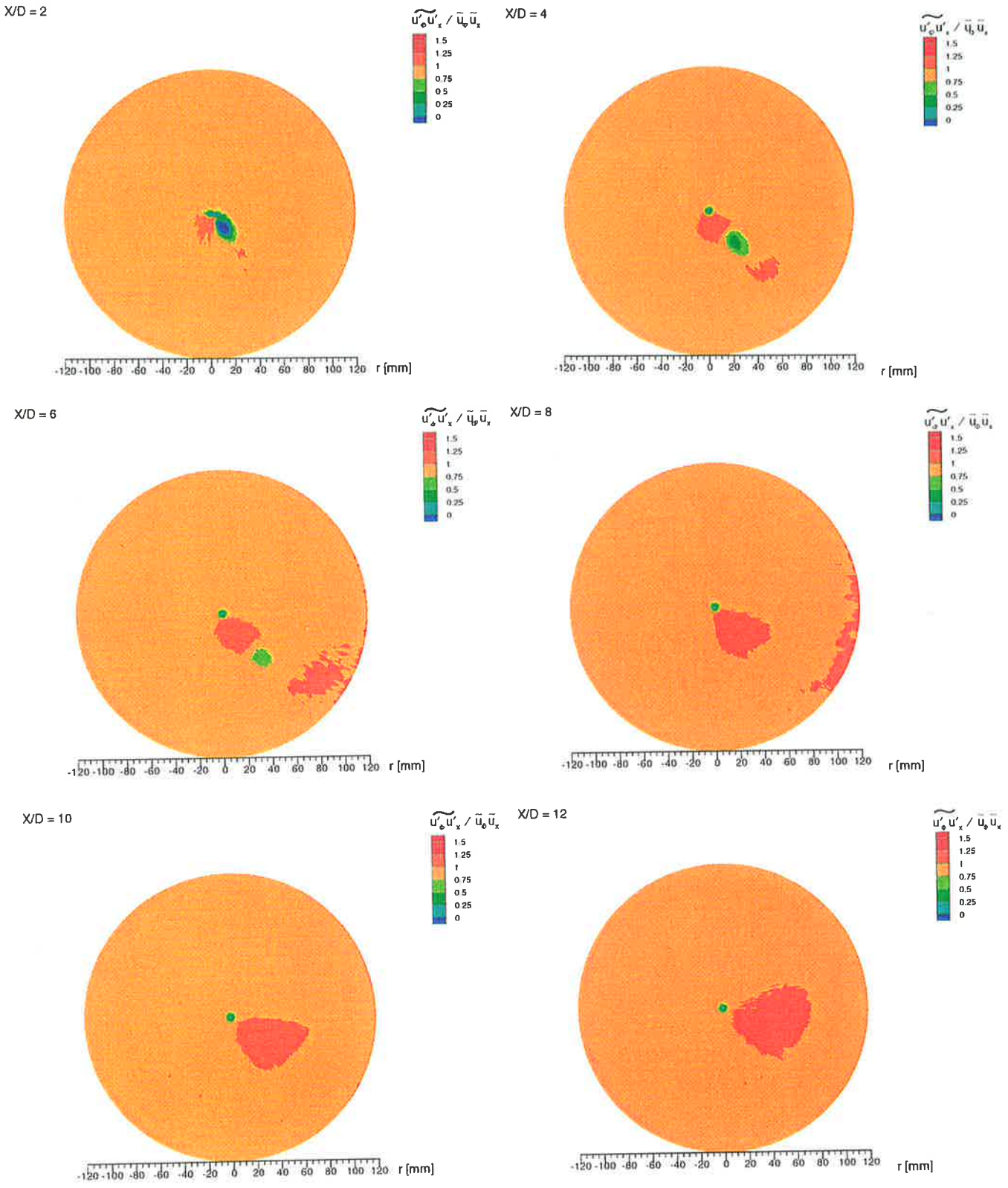

Figure 3.26: **Normalised phase-averaged $\frac{\widetilde{u_x u_\Phi}}{\tilde{u}_x \tilde{u}_\Phi}$ Reynolds stress component at x/d_e=2, 4, 6, 8, 10, 12. St_p=0.002, Re=26,600.**

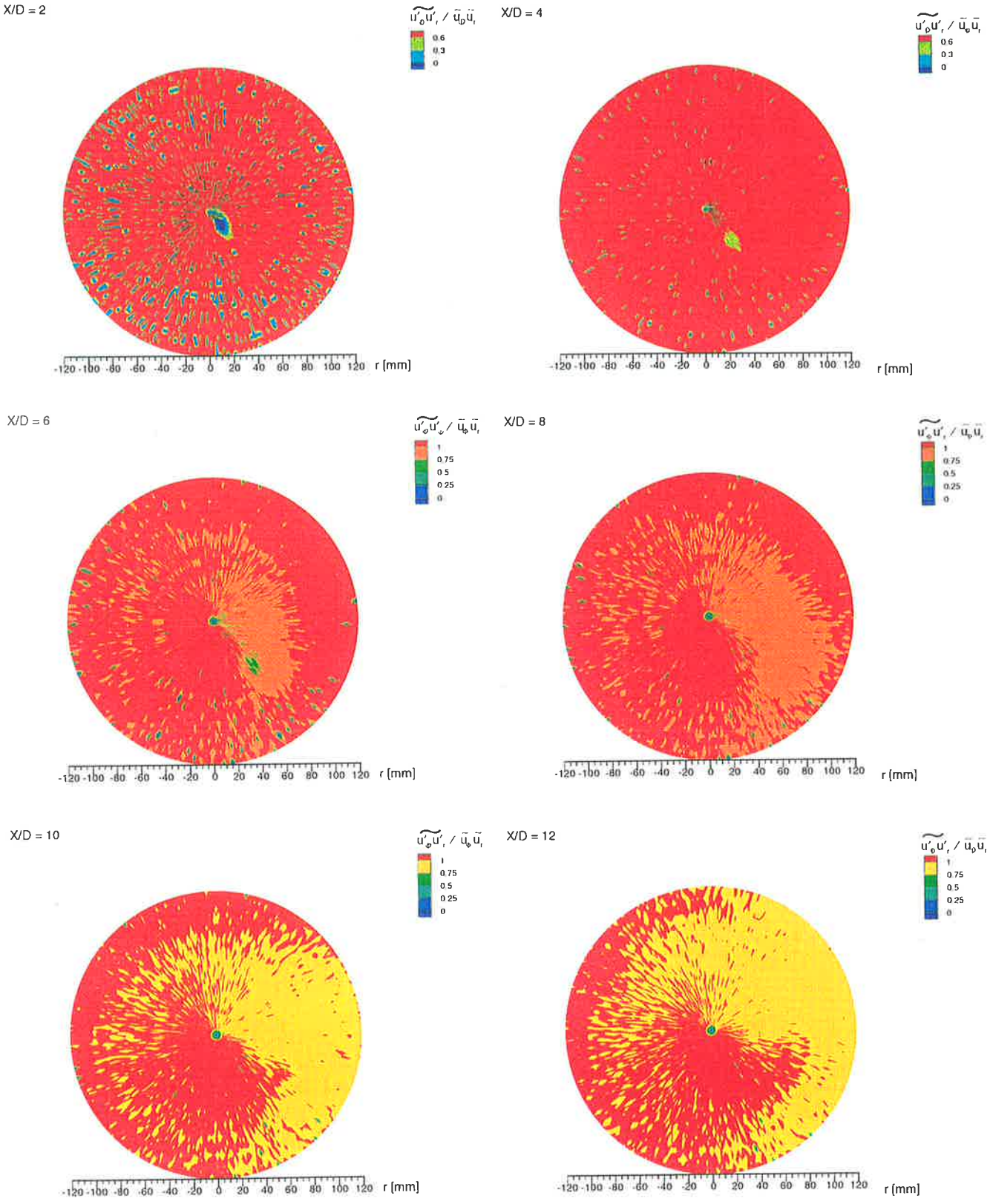

Figure 3.27: **Normalised phase-averaged $\frac{\widetilde{u'_r u'_\Phi}}{\tilde{u}_r \tilde{u}_\Phi}$ Reynolds stress component at x/d_e=2, 4, 6, 8, 10, 12. St_p=0.002, Re=26,600.**

3.2.6 The Skewness and Flatness

In homogeneous turbulence the velocity fluctuations have a Gaussian distribution. In shear flows, such as jets, the velocity distribution becomes skewed (third moment) and distorted (fourth moment), especially at the edges of a jet where the shear stresses are high. The skewness distribution gives insight into the turbulent transfer of energy from regions of high turbulence intensity to regions with lower turbulence intensity and about the degree of symmetry of the distribution of velocity data around its mean. A negative skewness implies a velocity distribution which leans towards the low velocity side relative to a Gaussian curve, whereas a positive skewness means that the high velocity end is favoured.

The flow near the edge of a turbulent jet is intermittent, meaning that the flow changes between slow (irrotational) fluctuations of low intensity and rapid (rotational) fluctuations of high turbulence intensity. The flatness, or kurtosis, is a measure of the changes in fluctuations in the flow field and describes the degree of peakedness or flatness of the velocity distribution relative to a Gaussian curve. For flatness greater than three, the distribution around the mean velocity forms a distinct peak , whereas for values between zero and three it forms a flat plateau. For a flatness value of three the velocity distribution is Gaussian.

The third moment, skewness, is calculated by the equation

$$\text{Skewness} = \frac{1}{N}\sum_{j=1}^{N}\left[\frac{u_j - \overline{u}}{\sigma}\right]^3. \tag{3.2}$$

For the fourth moment, flatness, the defining equation is

$$\text{Flatness} = \frac{1}{N}\sum_{j=1}^{N}\left[\frac{u_j - \overline{u}}{\sigma}\right]^4. \tag{3.3}$$

In Equations 3.2 and 3.3 N is the number of samples for each data point in the time–averaged domain. To ensure good statistical reliability for these higher order moments N is greater than 40,000 (Section 2.4.3). The velocity u_j represents one measurement in the data array for a given velocity component, $\overline{u}$ is the time–averaged mean velocity and σ is the standard deviation of the velocity distribution.

The time–averaged skewness and the flatness factors of each of the three velocity components are presented in Figures 3.28 to 3.33. The skewness and the flatness of the axial component are shown in Figs.3.28 and 3.29. In the high velocity region of the jet the skewness is high and exceeds a value of two at the axial locations from x/d_e=2 to x/d_e=12. This is comparable with the values found in a simple turbulent jet (Wygnanski and Fiedler, 1969). In the high shear regions between the jet and the spinning axis, the skewness reaches its peak postive value of six, indicating a high rate of transport of turbulent energy from the high velocity region of the jet into the recirculation region between the jet and the spinning axis. On the outer side of the jet, the values reach their minimum with negative values of about minus two.

Similar behaviour is observed in the flatness distribution of the axial velocity component (Fig.3.29). Constant values of three in the high velocity region of the jet indicate a Gaussian distribution and hence intermittency is not a dominant factor in the flow field. The peaks on either side of the high velocity region of the jet, in the high shear region where intermittency is high, reach flatness values of up to 60 at x/d_e=8 and x/d_e=12.

Figures 3.30 and 3.31 show the higher order radial moments. It was expected that the radial skewness and flatness would be similar to the axial higher order moments, since in the low Strouhal number regime the jet is not significantly deflected from its 45° exit angle. However the data do not demonstrate this similarity. It appears that the precession, even in the low Strouhal number regime, has an effect on the higher order moments. In the high shear regions on either side of the high velocity region of the jet, non–Gaussian values of the skewness and flatness are measured.

The time–averaged tangential skewness and flatness are presented in Figures 3.32 and 3.33. In the region occupied by the precessing jet itself the values of the skewness seem generally positive (notably at x/d_e=2 and 4). In the high regions of the jet the skewness drops to values of between -2 and -4. Further downstream the skewness values are mainly negative within the range between -3 and 0. The flatness of the tangential velocity component is hard to categorise. High values are achieved initially on the outer edge of the jet (x/d_e=2, 4 and 6) and the profiles of the flatness decay to the Gaussian value of 3. Occasional peaks are detected on the inner side of the jet (x/d_e=10 and 12).

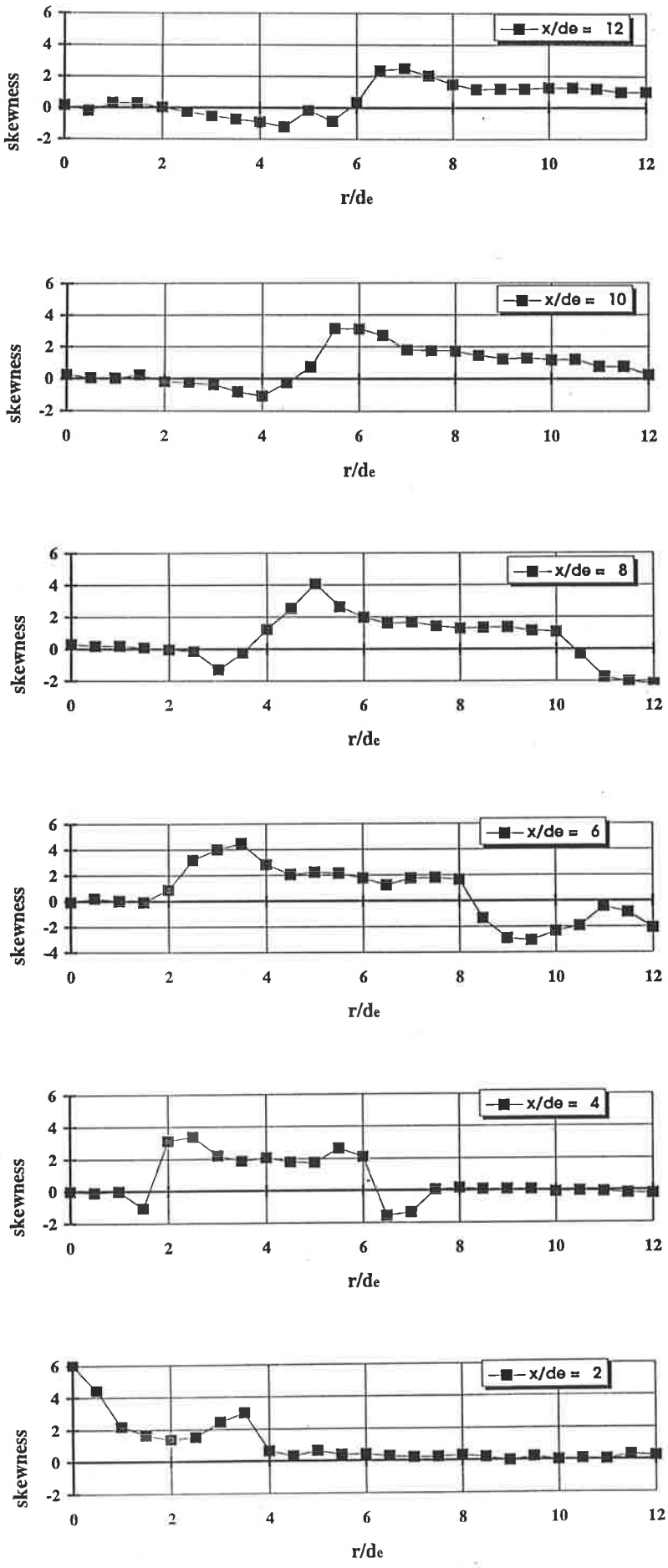

Figure 3.28: **Time-averaged axial skewness at x/d_e=2 to 12. St_p=0.002, Re=26,600.**

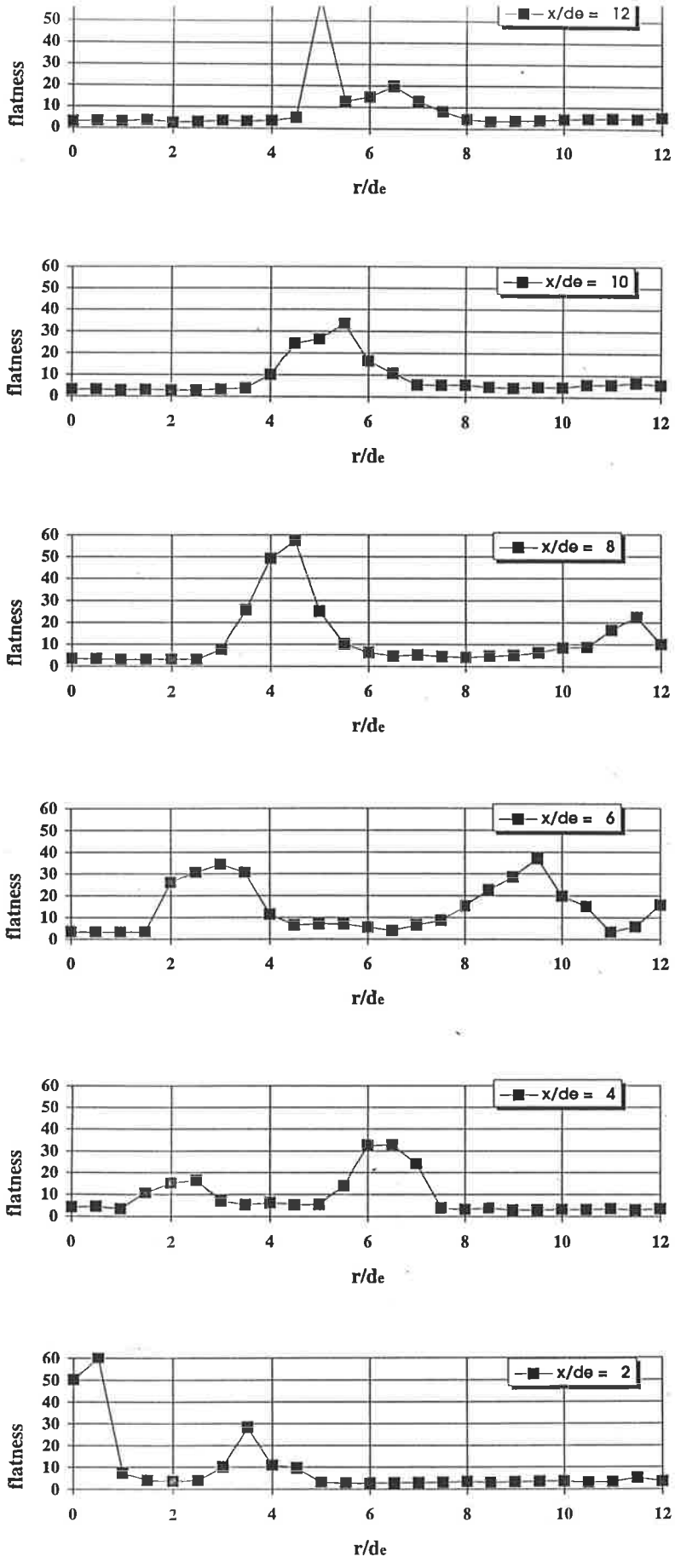

Figure 3.29: **Time–averaged axial flatness at x/d_e=2 to 12. St_p=0.002, Re=26,600.**

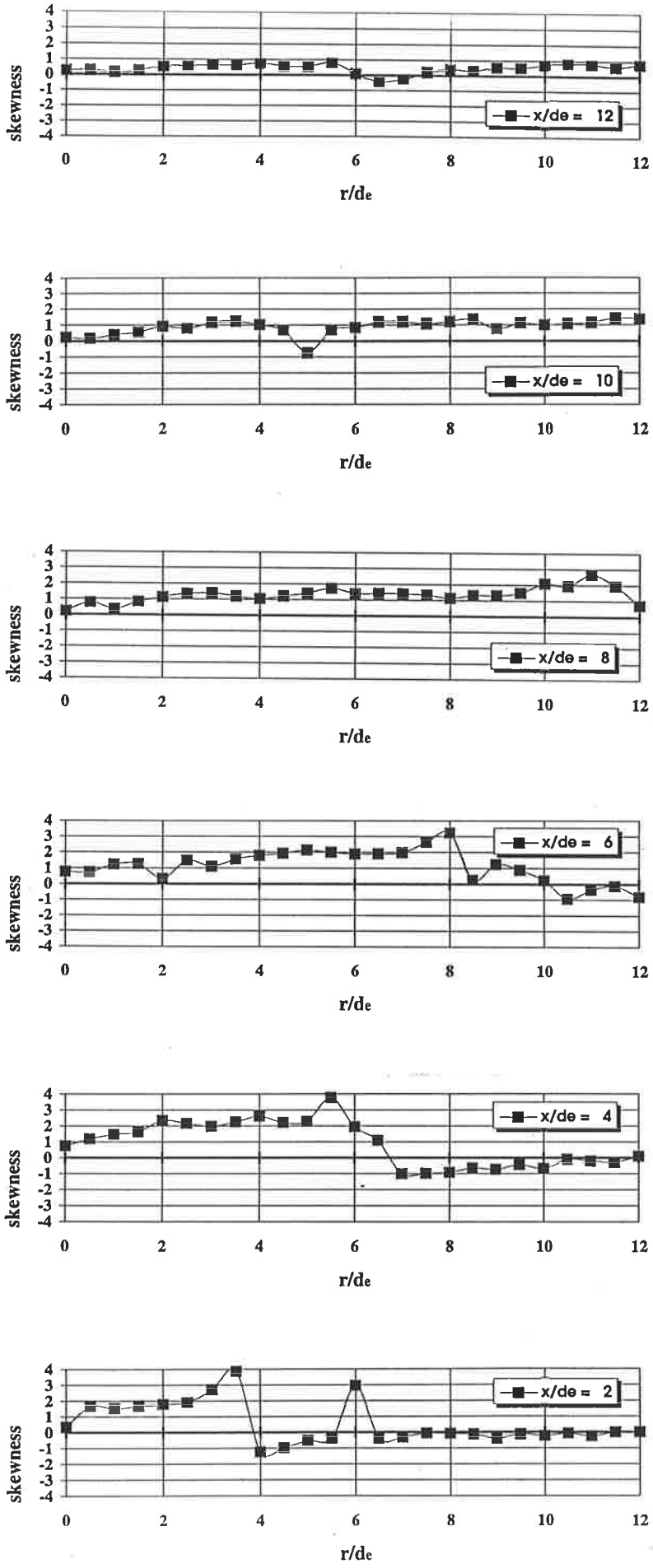

Figure 3.30: **Time–averaged radial skewness at x/d_e=2 to 12. St_p=0.002, Re=26,600.**

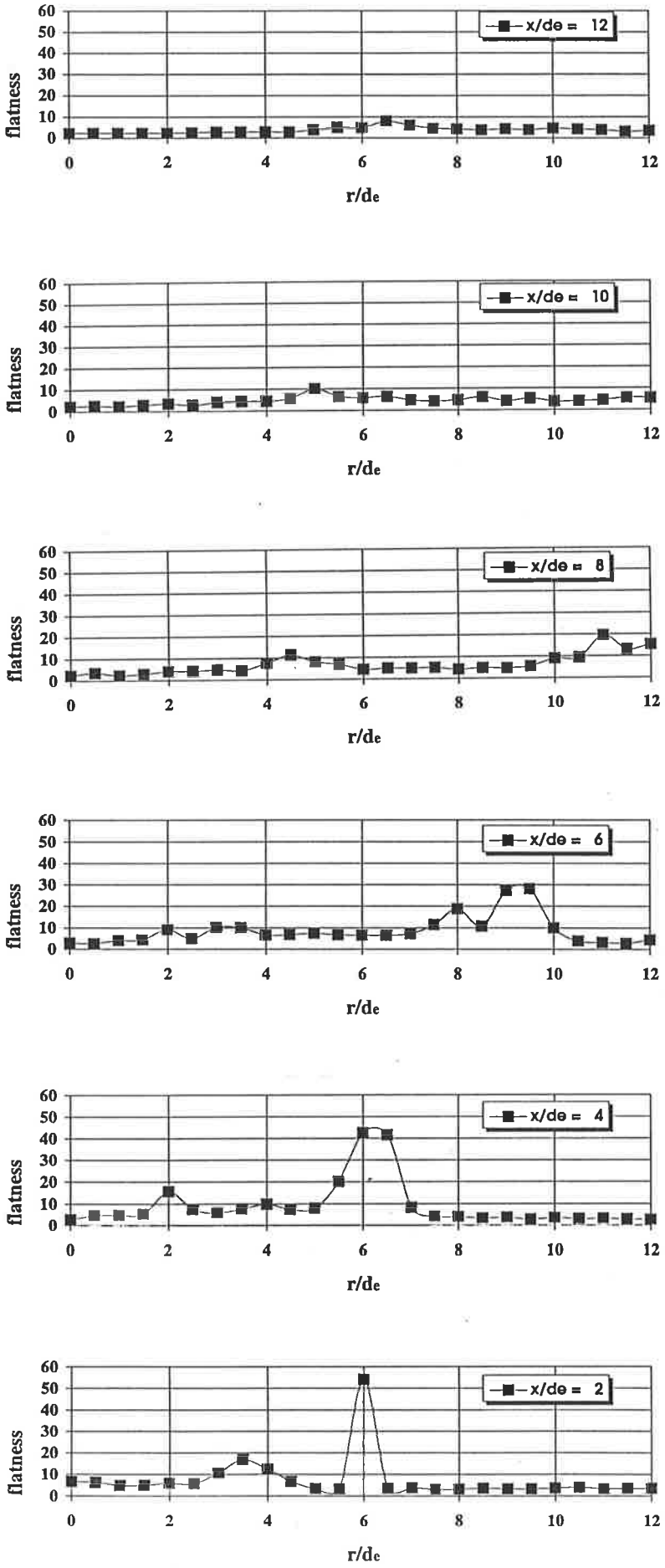

Figure 3.31: **Time–averaged radial flatness at x/d_e=2 to 12. St_p=0.002, Re=26,600.**

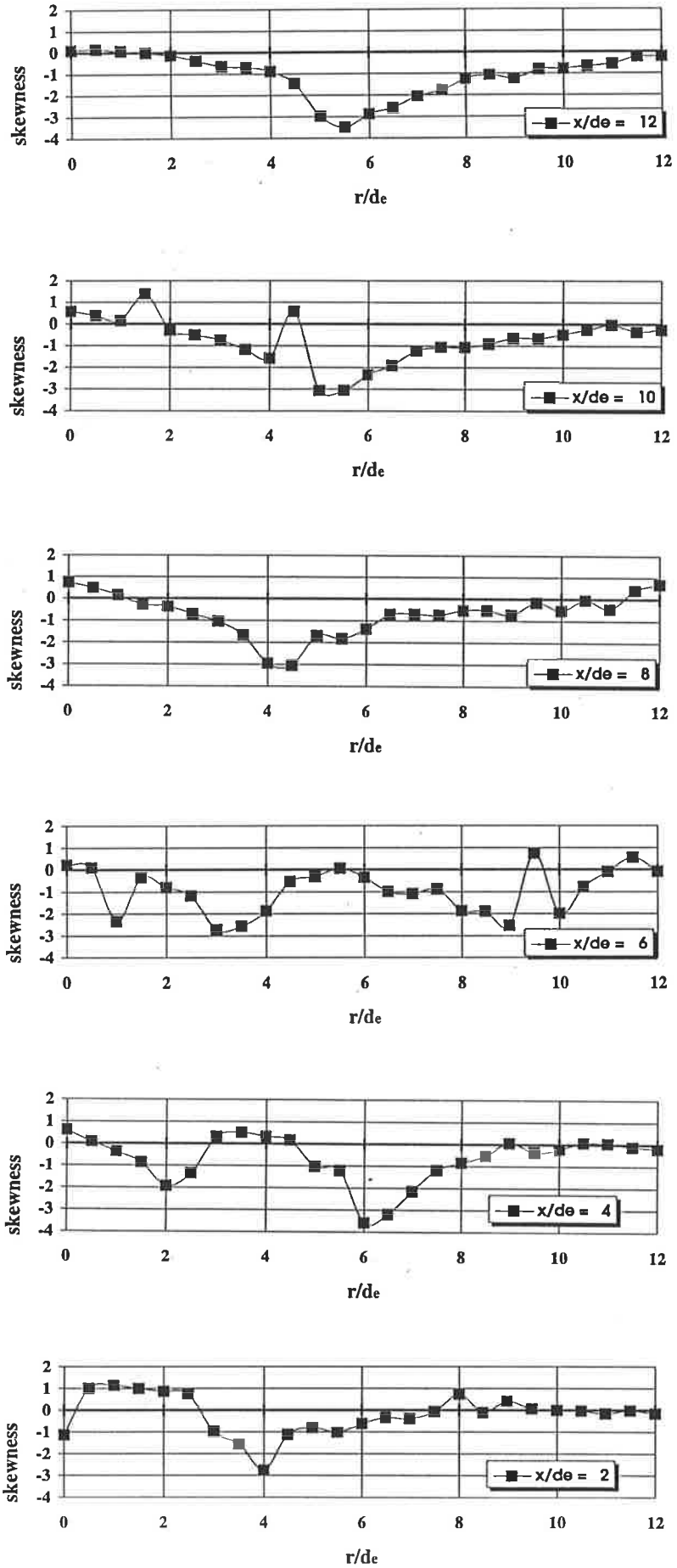

Figure 3.32: **Time–averaged tangential skewness at x/d_e=2 to 12. St_p=0.002, Re=26,600.**

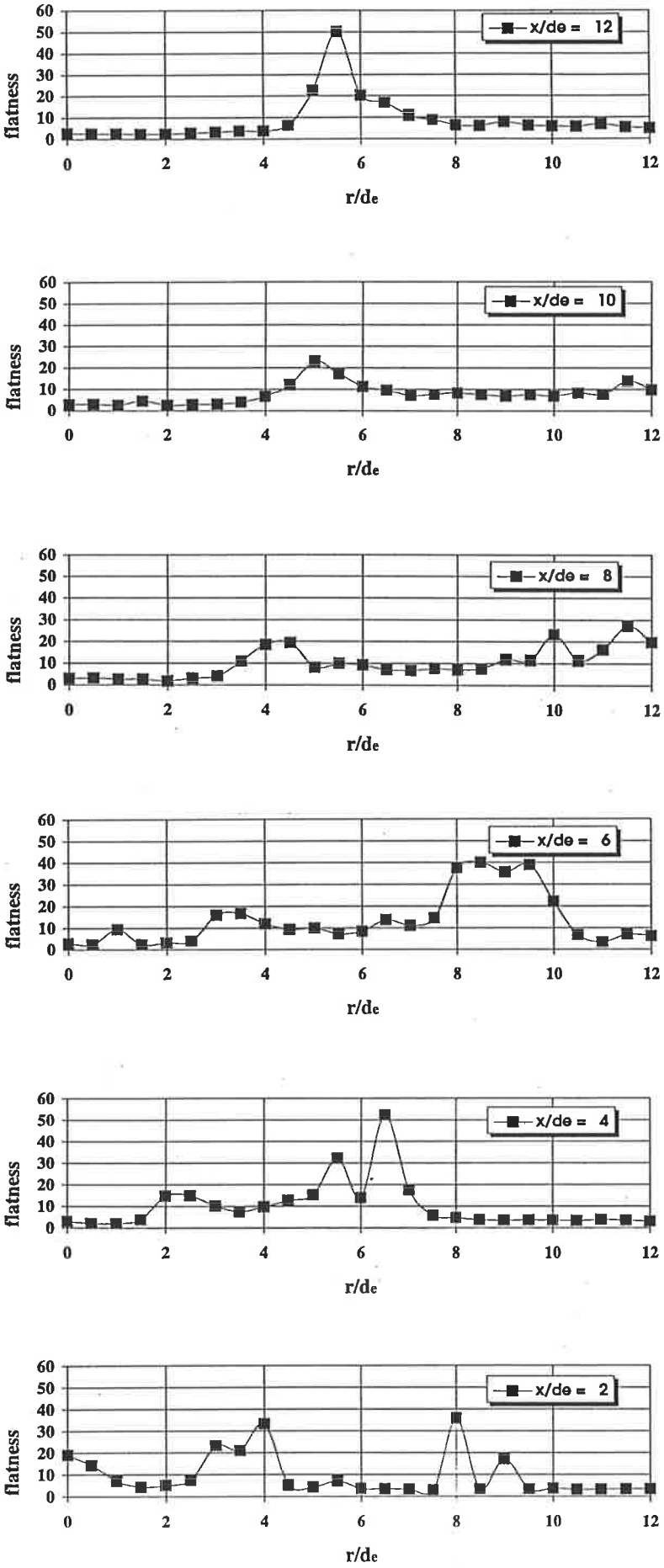

Figure 3.33: **Time-averaged tangential flatness at x/d_e=2 to 12. St_p=0.002, Re=26,600.**

3.3 The high Strouhal Number Jet

In this section the precessing jet is rotated at 59.12Hz, corresponding to a Strouhal number of 0.015 which falls within the 'high Strouhal number' regime. The Reynolds number of 26,600 and other experimental conditions are identical to those used in the experiments for the low Strouhal number regime discussed in the previous section, which enables a direct comparison of the results.

The same flow visualisation techniques as were used in the low Strouhal number investigation have been applied for general observation here. The same LDA system is used to obtain phase–averaged and time–averaged data (Section 2.4.3).

3.3.1 The Overall Flow Field

A comparison of Figure 3.34 and Figure 3.11 shows that the low and the high Strouhal number flows are dramatically different. In the high Strouhal number flow the jet is highly deflected in both the radial and tangential directions and a distinct recirculation of fluid is evident. The pressure gradients associated with this change of character (see Section 4) increase with increasing Strouhal number. The jet is deflected towards the spinning axis and the tangential path is now more tightly curved than the Archimedian spiral described at low Strouhal numbers.

To visualise the turbulent motion in the high Strouhal number jet the same laser sheet flow visualisation as was used for Figure 3.12. The same seeding with glass beads and

Figure 3.34: **Two consecutive cycles of precession in the high Strouhal number jet (here St_p=0.015). The beginning of each cycle is marked by a smoke pulse. Re=26,600.**

the same laser sheet illumination (Section 2.3.2) have been used to obtain Figure 3.35 except that now the image is exposed by five rather than the one laser pulse used for Figure 3.12. In Figure 3.35, the jet exits from the bottom centre of the image and moves upwards toward the left. The five laser pulses in this semi–quantitative PIV type picture are clearly evident in the high velocity region close to the jet exit. Downstream from the exit region a vortical structure develops, which is described in Figure 4.17 in Section 4.4. The jet is inclined towards the axis of rotation, recirculation is evident and the magnitude of the velocity is decreased everywhere except very close to the nozzle. A second large vortical structure, again similar to the one described in Figure 4.17, is apparent on the right side of the picture. In the centre of that second structure the magnitude of the velocity appears to be comparable to the exit velocity.

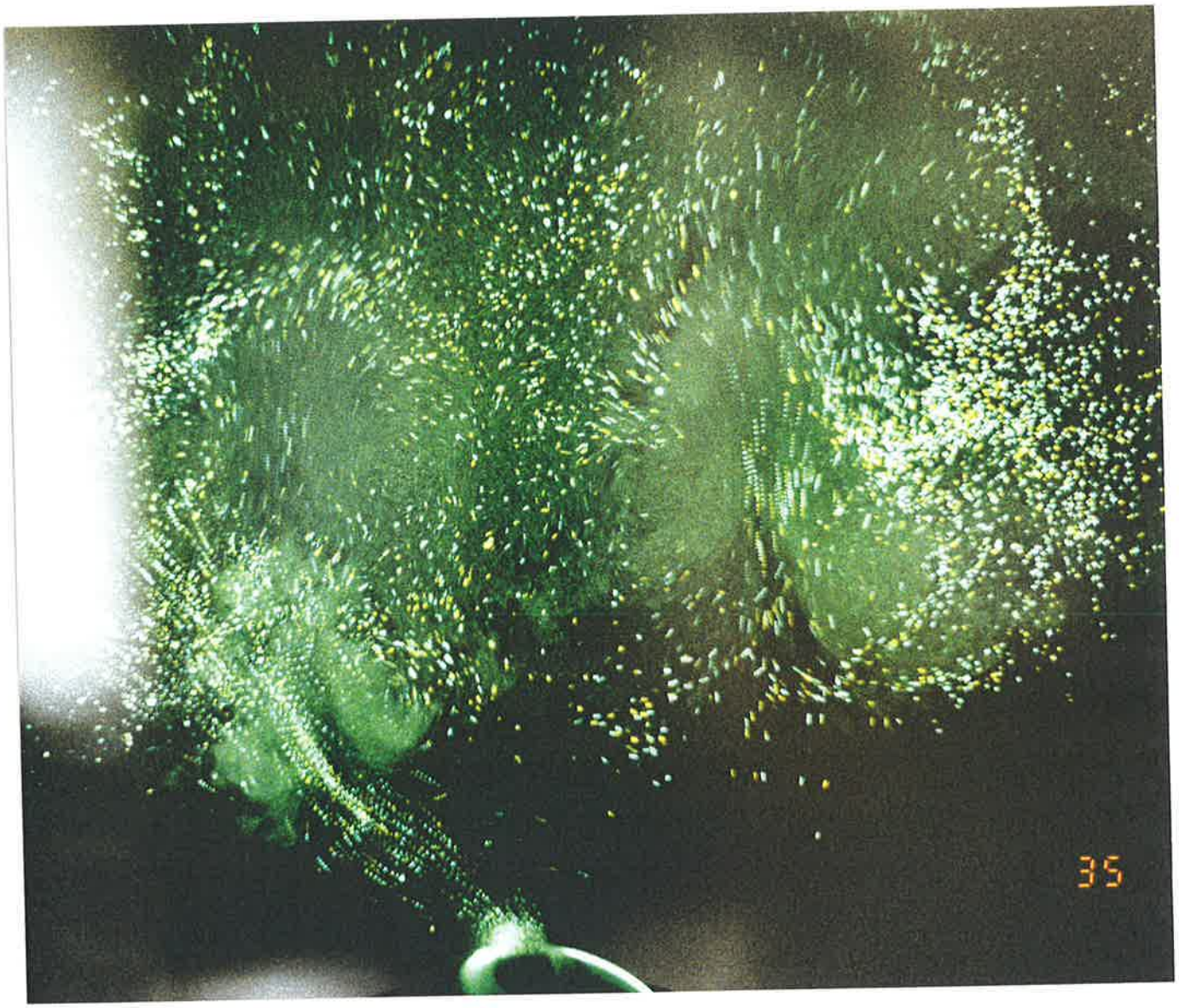

Figure 3.35: **Vertical laser sheet from $0< x/d_e <12$ through the r–x plane in the high Strouhal number jet marked with glass beads (multiple exposure). St_p=0.015, Re=26,600.**

3.3.2 The Axial Velocity Component

Contours of the phase–averaged axial velocity in the precessing jet flow, measured with the LDA system, are shown in Figures 3.36 and 3.37. The colour scale of the contours is adjusted individually for each cross–section in the figure to show the highest velocity in red and the lowest in blue. Thus colours should not be used to compare the different cross–sections. Instanteneous images of the jet, marked by particles and illuminated by a laser sheet in the r–Φ plane, at the corresponding axial distances are again presented to assist interpretation, as for the low Strouhal number case (Figs.3.13 and 3.14).

Close to the exit, at x/d_e=2, the $\tilde{u}_x$ component of the jet has roughly an elliptically shaped core region (Figure 3.36), as may be anticipated given the 45° angle of the exiting jet relative to the measurement plane. This is evident both in the flow visualisation and the velocity data. However, some distortion of the ellipse is evident at this position, and an axial upward flow along the 'leeward' side of the jet can also be observed. Two distinct regions of reversed flow exist, one between the jet and the spinning axis, and the other on the outer edge of the jet.

The end of the potential core of the phase–averaged precessing jet flow, where the maximum velocity in the precessing jet is less than the exit velocity of u_e=39m/s, occurs at approximately $x/d_e \approx 1.8$. This was determined by extrapolation of a polynomial curve fit through the axial velocity components measured at each plane of the axial sequence.

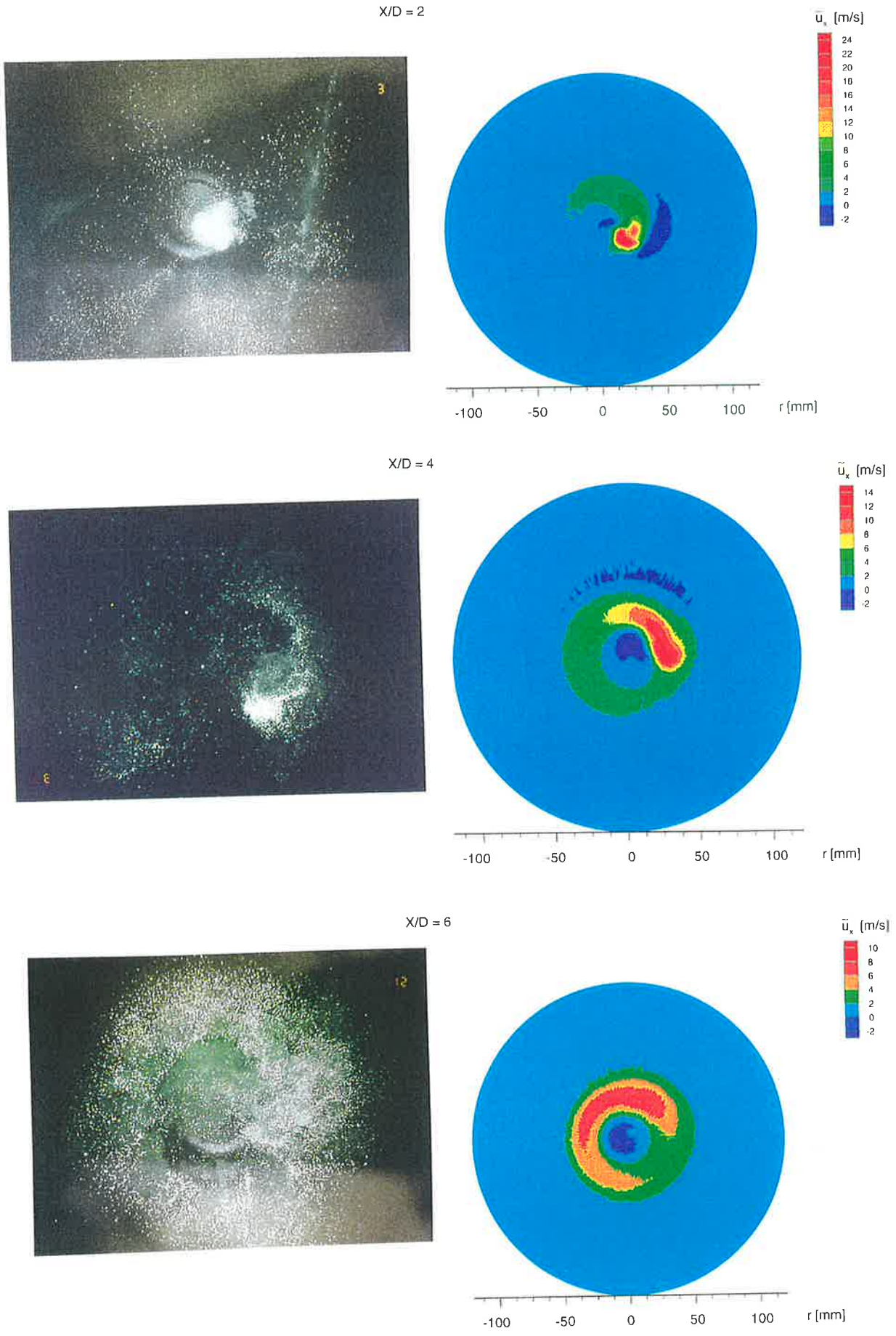

Figure 3.36: **Instantaneous particle images and phase-averaged axial velocity $\tilde{u}_x$ contours at x/d_e=2, 4, 6. St_p=0.015, Re=26,600.**

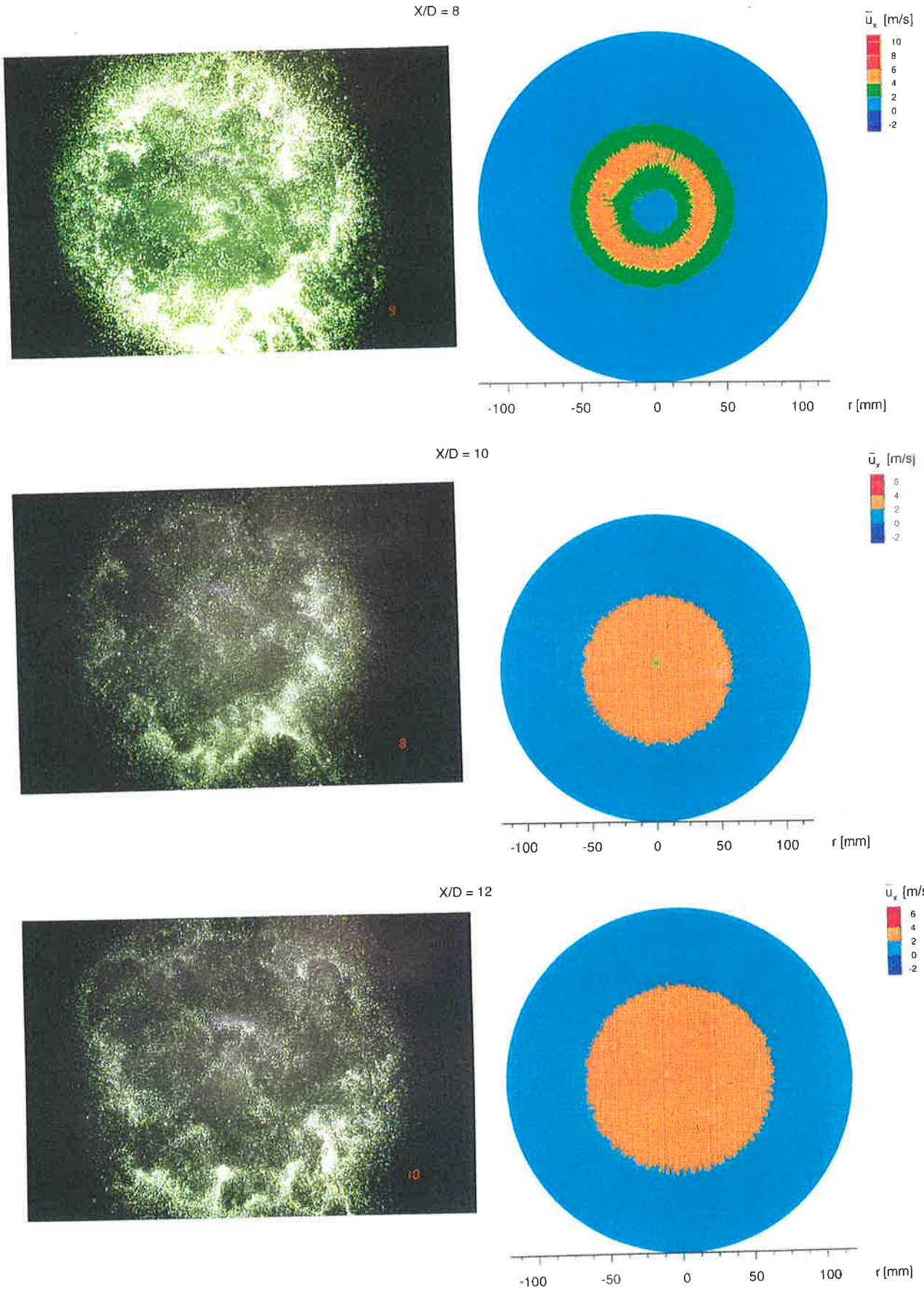

Figure 3.37: **Instantaneous particle images and phase-averaged axial velocity $\tilde{u}_x$ contours at x/d_e=8, 10, 12. St_p=0.015, Re=26,600.**

The flows at x/d_e=4 and x/d_e=6, are qualitatively similar to each other. The phase–averaged reverse flow zone between the jet and its spinning axis (central recirculation) is present at both axial positions. The maximum recorded negative axial velocity is –3.5m/s which is about 25% of the local maximum velocity. This occurs in the central recirculation region at x/d_e=4. Also the phase–averaged reverse flow, located radially outward from the precessing jet is apparent at both positions. The deformation of the jet increases with the downstream distance, so that the jet is highly skewed at x/d_e=4. By x/d_e=6 the 'wake' or 'tail' extends around most of the circumference.

In the contours from x/d_e=8 to 12 reversed flow regions are no longer present. The phase–averaged flow field is almost axisymmetric and there is no structure in the flow at the frequency of precession.

In Fig.3.38 the time–averaged velocity components are shown. At x/d_e=2 the central recirculation zone is also evident in the time–averaged flow. The reverse flow is strongest in the region $4 \leq x/d_e \leq 6$ and its diametral extent is approximately twice the nozzle exit diameter. The jet and the recirculation zone both precess. It is interesting to note that the velocity contours become more uniform with increasing axial distance, but that the radial extent of the flow does not increase significantly between x/d_e=8 to x/d_e=12.

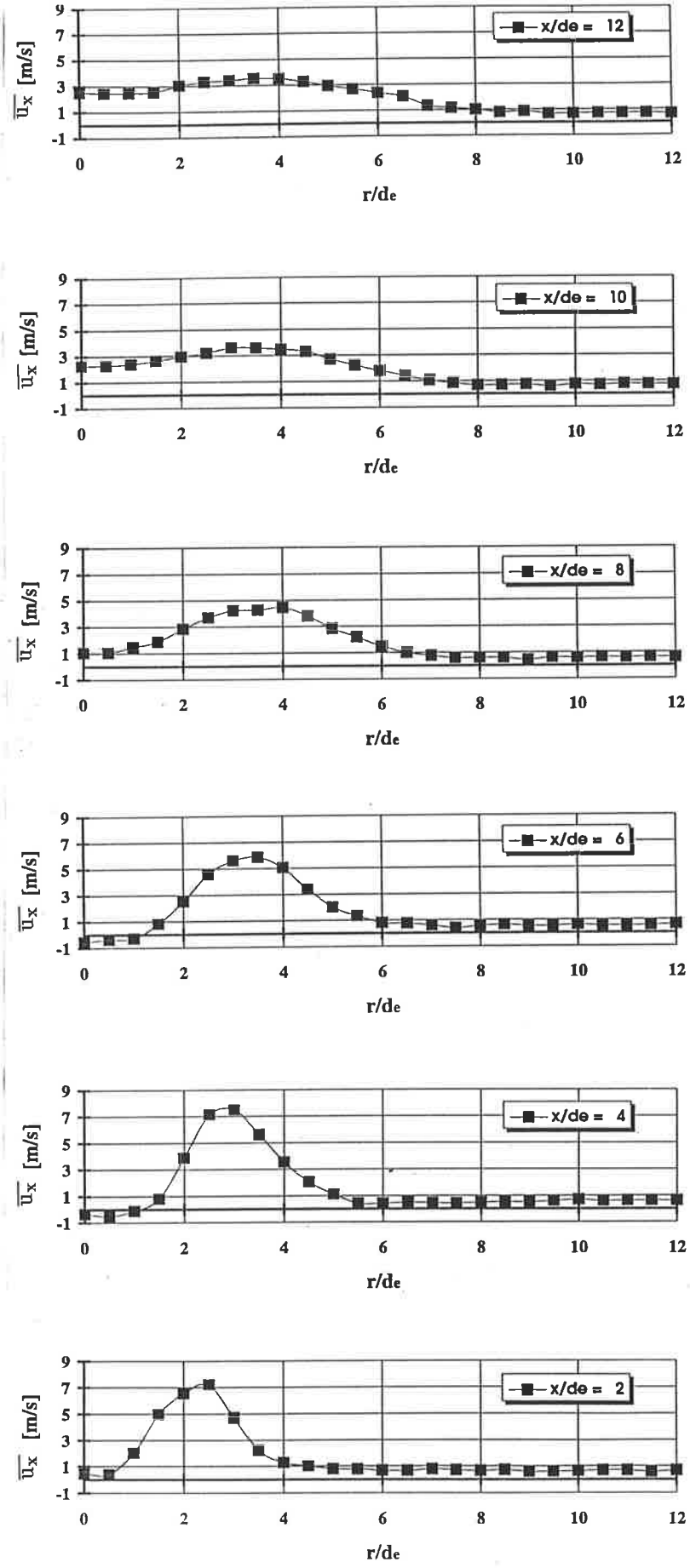

Figure 3.38: **Time–averaged axial velocity $\overline{u}_x$ at x/d_e=2 to 12. St_p=0.015, Re=26,600.**

3.3.3 The Radial and Tangential Velocity Components

Fig.3.39 shows the phase–averaged radial and phase–averaged tangential velocities combined in vector plots. Unlike the plots of the axial velocity, the colour scales are consistent and the figures may be compared directly. However, the lengths of the vectors are scaled individually for each plot to show the flow patterns clearly.

At x/d_e=2 a significant positive radial velocity component exists, resulting from the radial component associated with the 45° exit angle of the jet. However, beyond x/d_e=4 the positive radial component in the jet region has decayed to insignificant, indicating strong deflection of the jet toward the spinning axis. This is consistent with a low pressure region which has been found between the jet and the spinning axis, Section 4.4, and in an earlier investigation (Schneider et al. 1993).

The axial velocity contours and the vector plots presented in this section support the subdivision of the flow field of the high Strouhal number jet into three regions (see Section 4.1). The first subdivision is the potential core which ends at $x/d_e = 1.8$, just upstream from the first plane of measurements at $x/d_e = 2$. In this region the axial and radial component are almost identical since the jet exits at 45°. The second region is where the phase–averaged reverse flow occurs in the axial component ($x/d_e \leq 6$ for the present conditions). In the radial and tangential component a 'bifurcation' is visible tangentially in front of the jet. This consists of strong inflow just ahead (tangentially) of the jet and probably contains both jet and ambient fluid. Also, in the second region

a strong inflow towards the low pressure region near to the center of rotation can be seen. On the outer side of the jet only small positive radial components are found and there is a small inflow into the 'wake' of the jet.

The third region in the phase–averaged jet starts from $x/d_e \geq 8$. The radial and tangential velocities are small compared with the axial component. A small swirling component does exist in the direction of the precession. In the outer region of the jet both the radial and tangential velocity components are very small.

Fig.3.40 shows the time–averaged radial velocity component. For $8 \leq x/d_e \leq 12$ the positive radial velocity is very small. Closer to the axis of rotation the negative radial components indicate a net inflow – apparently into the recirculation zone. The tangential velocity component (Fig.3.41) is only significant in the initial region of the jet (at x/d_e=2, where the nozzle shape itself could be causing a small tangential component.However, after six nozzle diameters the tangential component is negligible everywhere.

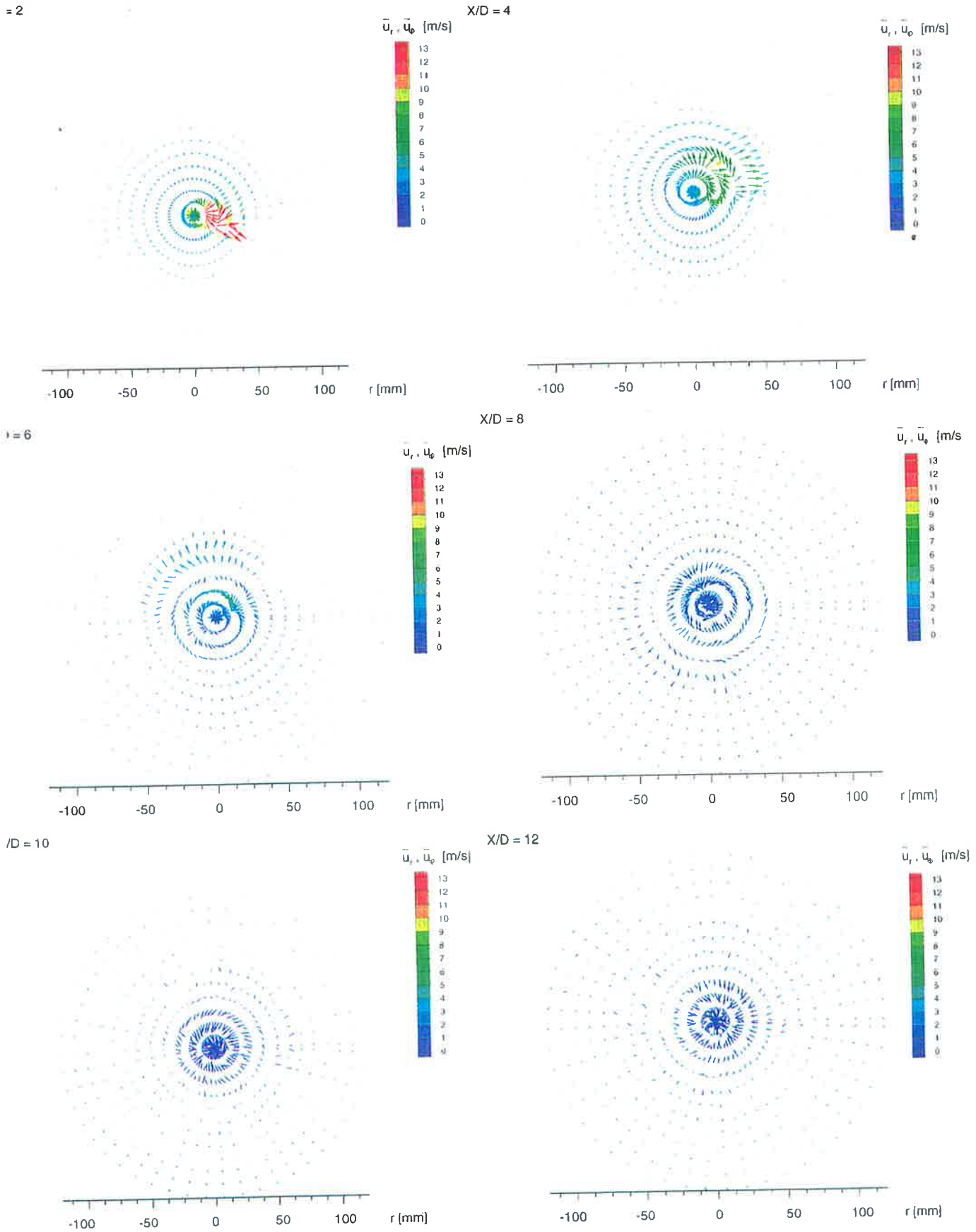

Figure 3.39: **Phase-averaged radial $\tilde{u}_r$ and phase–averaged tangential $\tilde{u}_\Phi$ velocities combined to form vectors, x/d_e=2, 4, 6, 8, 10, 12, St_p=0.015, Re=26,600.**

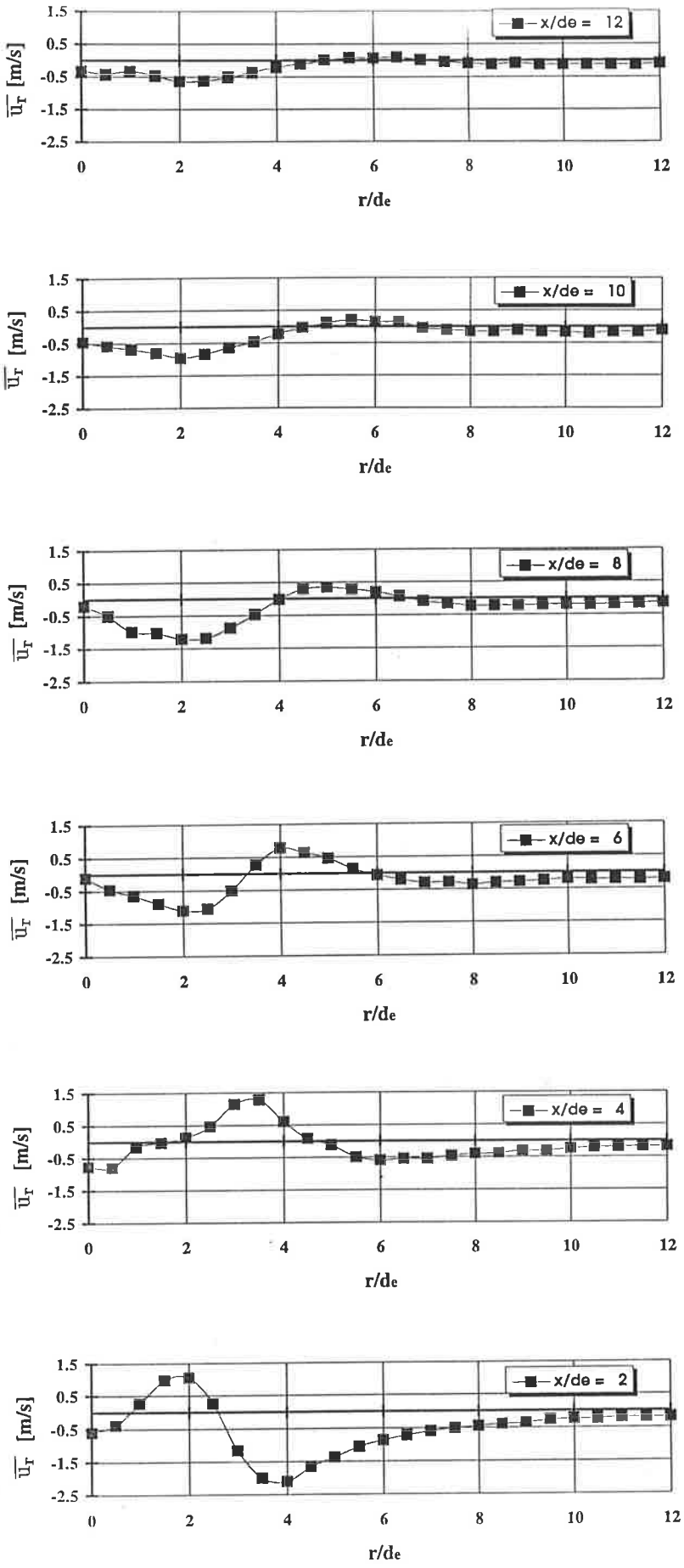

Figure 3.40: **Time-averaged radial velocity $\overline{u}_r$ at x/d_e=2 to 12. St_p=0.015, Re=26,600.**

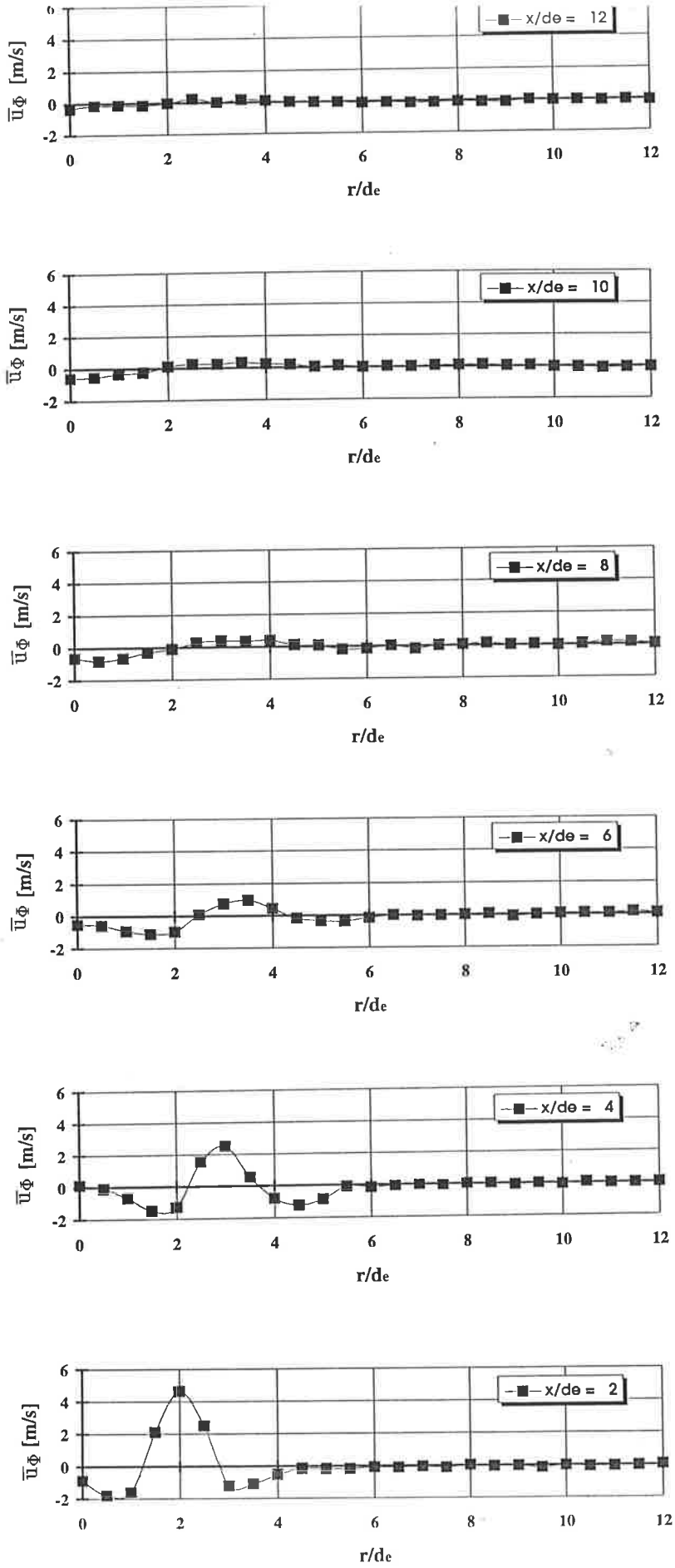

Figure 3.41: **Time–averaged tangential velocity $\overline{u}_\Phi$ at x/d_e=2 to 12. St_p=0.015, Re=26,600.**

3.3.4 The Turbulence Intensities

The phase–averaged colour contours of the three turbulence intensity components are presented in Figures 3.42 to 3.46. The turbulence levels and their distributions in the high Strouhal number flow are very different from those at the same Reynolds number in the low Strouhal number flow (Figs.3.19 to 3.23). The peak phase–averaged magnitude of the turbulence components relative to the local phase–averaged mean of the component velocity do not vary greatly with downstream distance x/d_e, but the distributions of the intensities do change substantially with downstream distance. The colour scales have been adjusted to show the full dynamic range of each data set and care must therefore be taken when comparing the plots.

The Axial Turbulence Intensity:

The axial turbulence intensity (Fig.3.42) is marked by high negative values of -300 to -400% (green and blue) in regions where recirculating fluid is detected (see Fig.3.36 and 3.37). Between the jet and its spinning axis and on the outer edge of the jet the high negative turbulence levels are maintained up to x/d_e=6. The front of the jet and the 'lee' side show positive levels of 200% to 500% (red). This region coincides with the region of maximum deflection of the jet (Sec. 4.1). Beyond x/d_e=6, where the flow seems to become axisymmetric, the turbulence intensities are all postive and the structural information in the phase–averaged flow has almost disappeared.

The time-averaged axial turbulence component (Fig.3.43) displays peaks in the region of maximum deflection in the precessing jet flow. These could be associated with either positive or negative streamwise velocity components. Turbulence values at x/d_e=2 peak at 8m/s. At x/d_e=4 the values have decreased to 6m/s and at x/d_e=6 are down to 4m/s. Beyond x/d_e=6 the turbulence levels decay from 2m/s at x/d_e=8 to 1m/s at x/d_e=12. The peak levels of the time–averaged axial turbulence are generally about 2m/s lower than those in the low Strouhal number flow. But the recirculation region maintains a high level of turbulence (2m/s), whereas the low Strouhal number flow in this region displayed only very low levels (< 0.2m/s).

The Radial Turbulence Intensity:

Figure 3.44 presents the phase–averaged radial turbulence intensity contours. The intensity levels in the jet reach values of between 300 and 500%. In the 'lee' side of the jet a blue region develops which respresents negative levels of up to -200%. As the jet reaches the end of the region of maximum deflection at x/d_e=6, it is 'bent' towards the spinning axis and the radial velocity component becomes very small (Section 3.3.3). Also the turbulence levels decrease to between 200 and 300% at x/d_e=8 and 100% at x/d_e=12. The dark blue region of negative values of up to -200% is present until x/d_e=12.

The time–averaged turbulence of the radial component is displayed in Fig.3.45. At x/d_e=2, 4 and 6 the peak values of $\sqrt{\overline{u_r'^2}}$ progressively decrease from 7m/s at x/d_e=2 to less than 4m/s at x/d_e=6. These values correspond to the high shear region on both sides (radially inwards and outwards) of the time–averaged jet. In fact a double peak

can be seen in the profiles, where the high velocity core of the jet corresponds with the 'valley' between the peaks. Further downstream at x/d_e=8, 10 and 12 the double peaks disappear and the turbulence level decays rapidly.

The Tangential Turbulence Intensity:

The data of phase–averaged tangential turbulence intensity shows considerable scatter (Fig.3.46). This is due to the low magnitudes of the tangential velocity component on which the RMS is normalised and it is also due to poorer resolution in the low velocity regions. However, the green regions at x/d_e=2, 4 and 6 identify turbulent structures which are located tangentially in front of the phase–averaged jet and in the recirculation zone on the axis of rotation. As the phase–averaged jet structure changes to a circular structure, for x/d_e >6, the green region in the tangential turbulence intensity disappears. The red circular region where turbulence levels exceed 200% suggests that the phase–averaged jet flow becomes axisymmetric.

The time–averaged tangential turbulence intensities in Fig.3.46 only show high values at x/d_e=2, 4 and 6. The peak values of 6m/s decay rapidly to 2m/s at x/d_e=8. Downstream from x/d_e = 8 the tangential turbulence becomes insignificant.

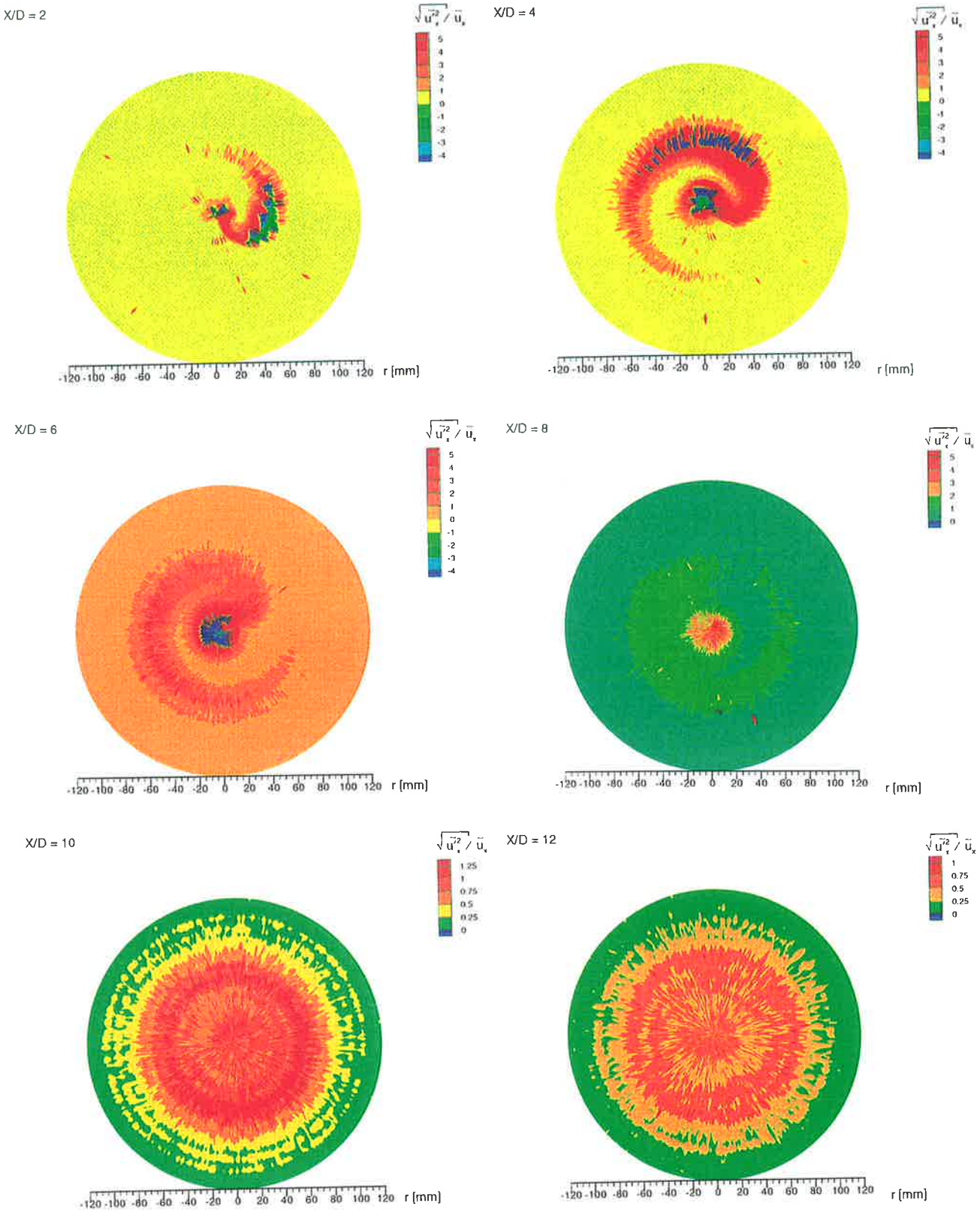

Figure 3.42: **Phase-averaged axial turbulence intensity at x/d_e=2, 4, 6, 8, 10, 12. St_p=0.015, Re=26,600.**

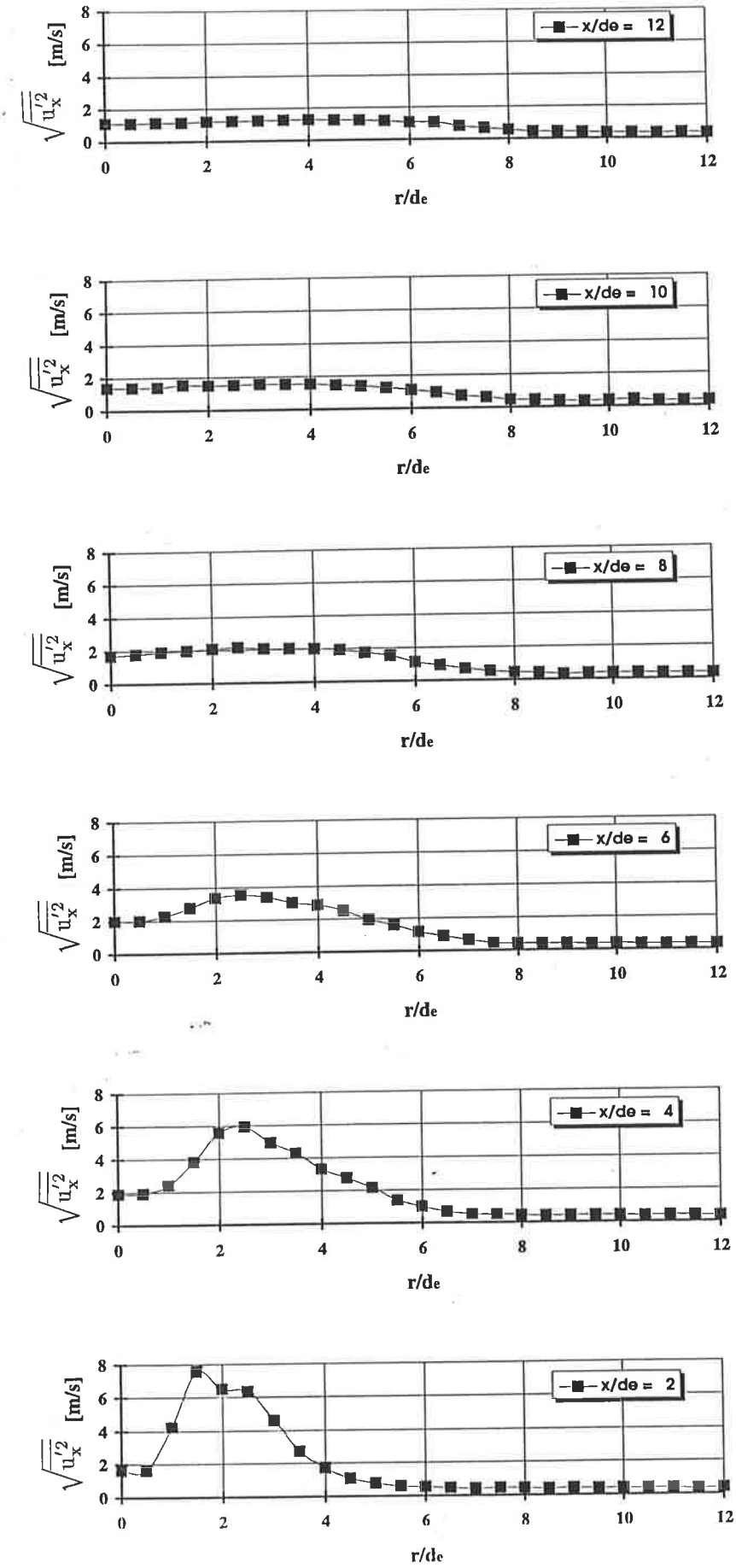

Figure 3.43: Time-averaged axial turbulence at x/d_e=2 to 12. St_p=0.015, Re=26,600.

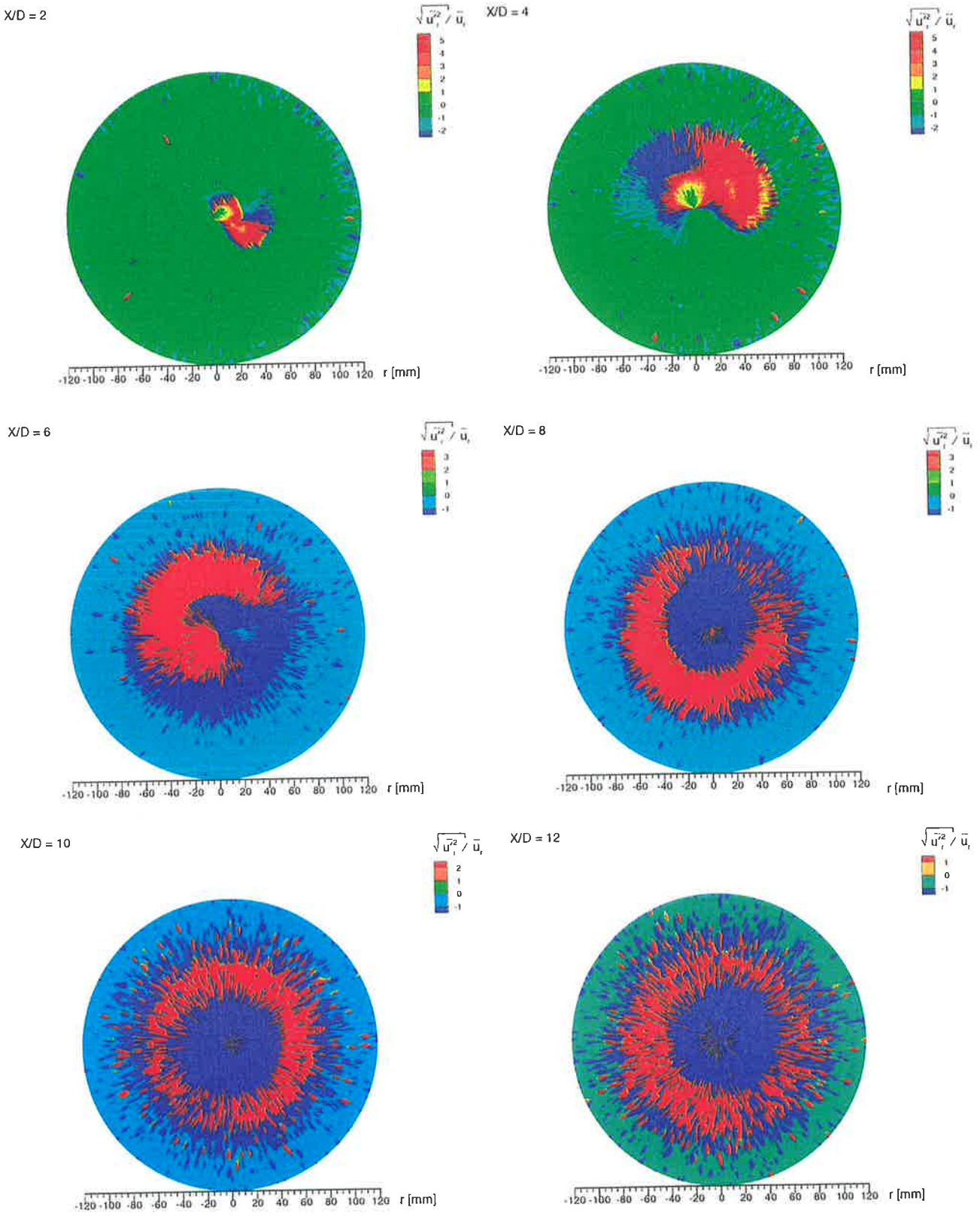

Figure 3.44: **Phase-averaged radial turbulence intensity at x/d_e=2, 4, 6, 8, 10, 12. St_p=0.015, Re=26,600.**

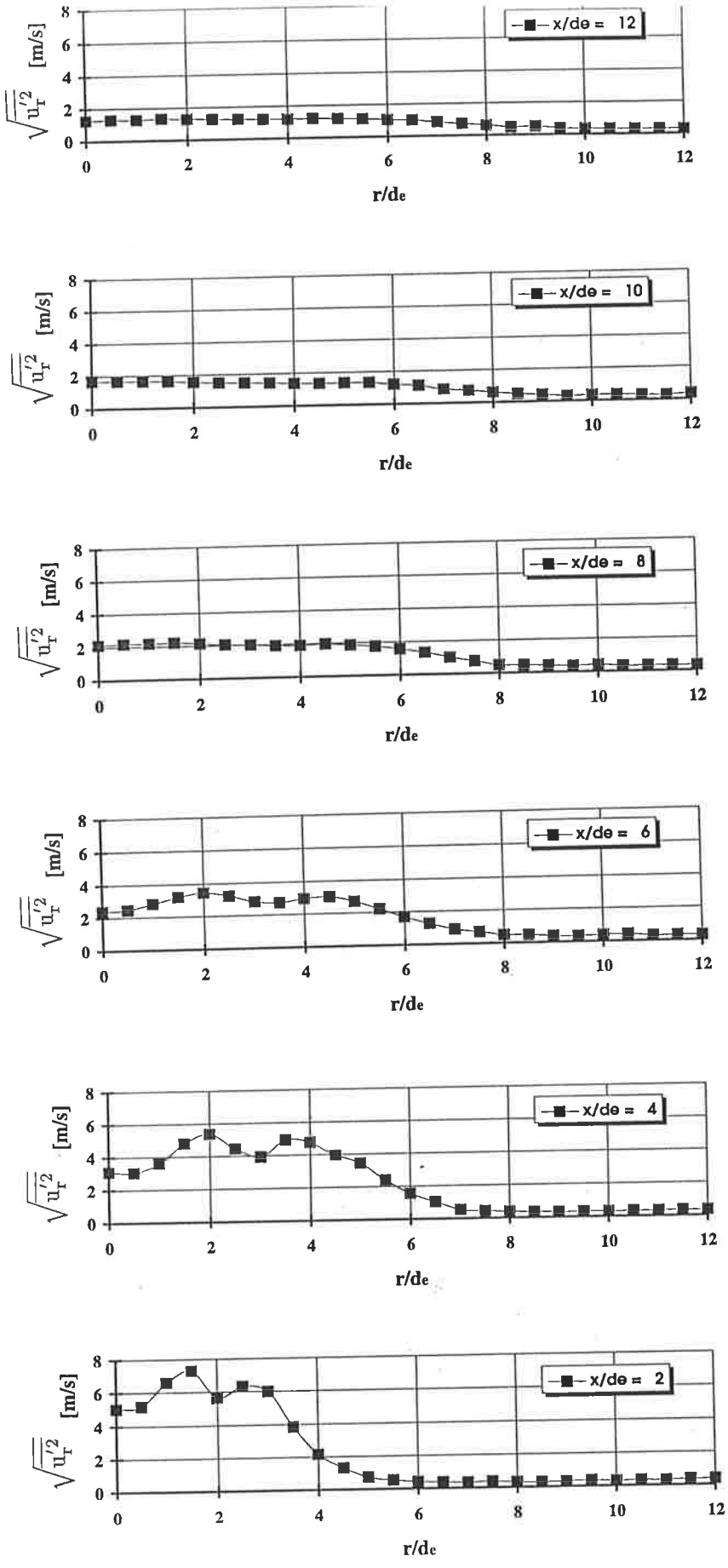

Figure 3.45: **Time–averaged radial turbulence at x/d_e=2 to 12. St_p=0.015, Re=26,600.**

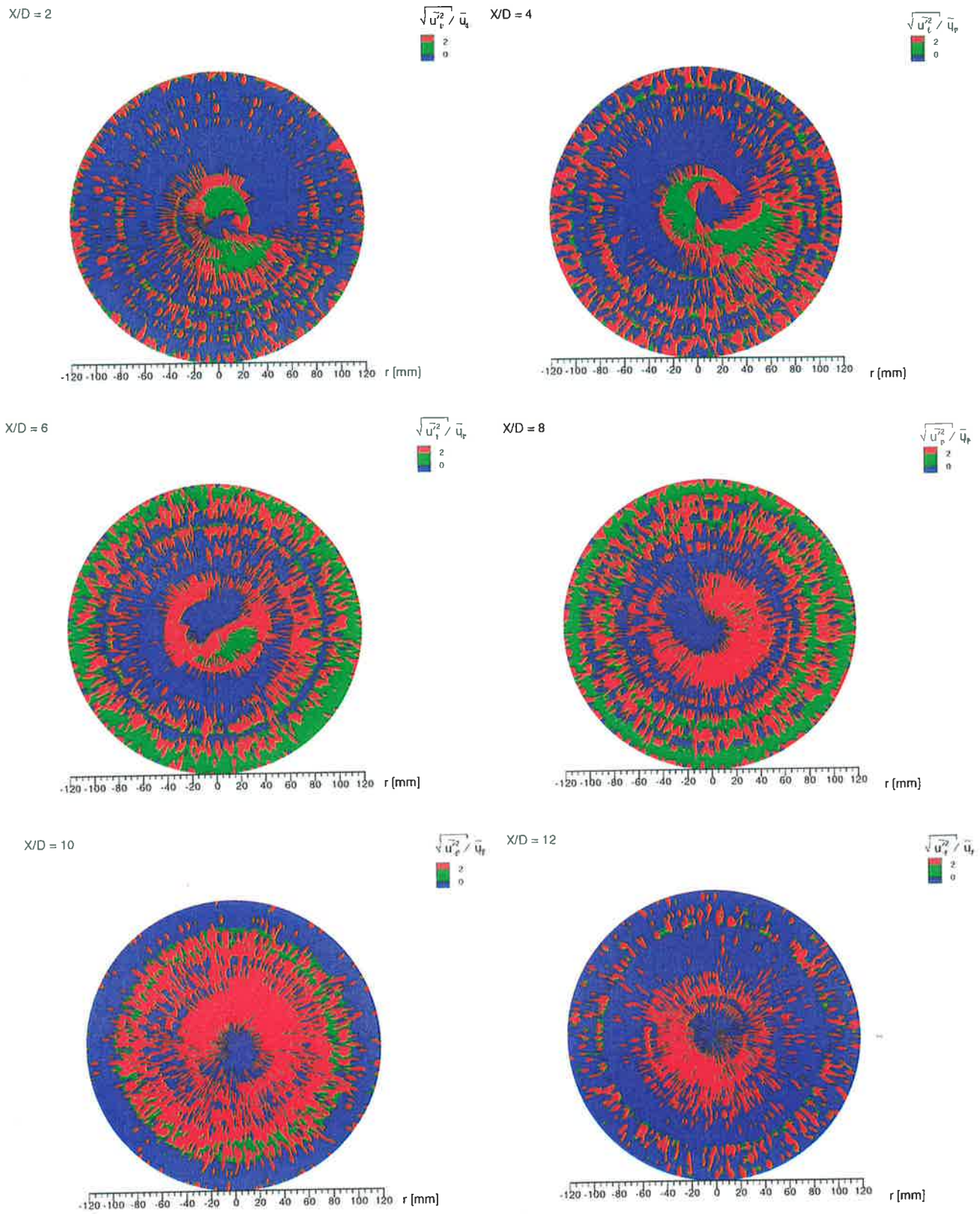

Figure 3.46: **Phase-averaged tangential turbulence intensity at x/d_e=2, 4, 6, 8, 10, 12. St_p=0.015, Re=26,600.**

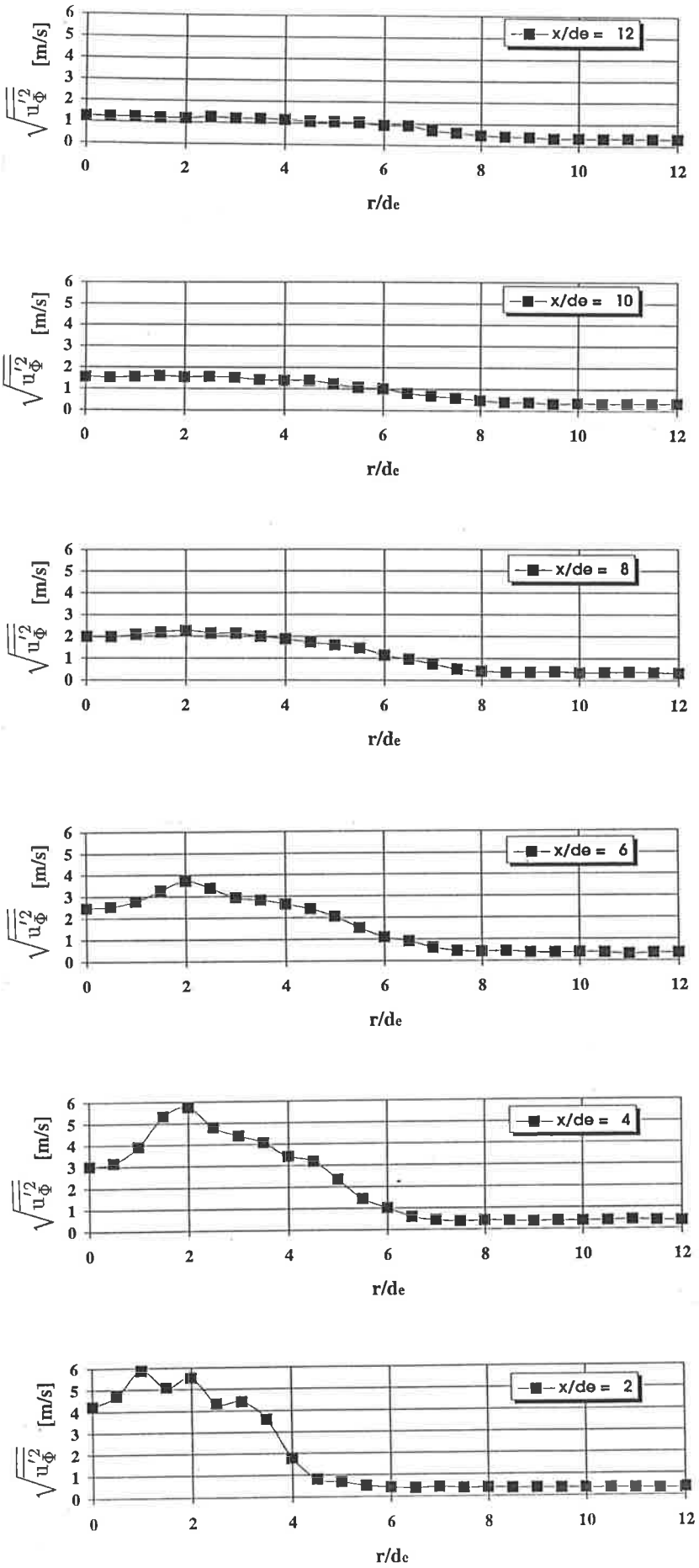

Figure 3.47: **Time–averaged tangential turbulence intensity at x/d_e=2 to 12. St_p=0.015, Re=26,600.**

3.3.5 Reynolds stresses

As described in Section 3.2.5, the high levels of Reynolds shear stresses are a measure of transfer of energy into the turbulent fluctuations and hence have an important bearing on the entrainment characteristics of the precessing jet. The phase–averaged Reynolds shear stresses are presented in Figures 3.48 to 3.50. The same definition of the Reynolds stresses and the same normalisation are used as in the low Strouhal number flow (Section 3.2.5), so that direct comparison of the two cases is possible. The colour scale of the phase–averaged Reynolds stress contours is different for each of the three stress components, since the dynamic range of the data is high.

The normalised phase–averaged $\frac{\widetilde{u_x' u_r'}}{u_x \cdot u_r}$ Reynolds stress is shown in Figure 3.48. The high fluctuations in the data are due to high turbulence levels in the high Strouhal number flow. The jet structure can be identified by the red region which corresponds to Reynolds stress levels in excess of 100%. In the recirculation region similar (red) stress levels are measured. The details and contours of the stresses can only be identified up to x/d_e=6. Further downstream the phase–averaged Reynolds stress field appears to become axisymmetric in contrast to the low Strouhal number case, where the jet retains its identity and the stresses are very much smaller (Fig.3.25).

As mentioned earlier, Bremhorst and Hollis (1990) related Reynolds stresses to the entrainment capacity of the jet. The increased stress levels in the high velocity region of the jet and in the recirculation zone are an order of magnitude higher than those in a simple turbulent jet (see e.g. Wygnanski and Fiedler, 1969). This finding also corresponds with the measurements of Schneider et al. (1996).

The remaining two Reynolds stress components, $\frac{\widetilde{u_x' u_\Phi'}}{u_x \cdot u_\Phi}$ $\frac{\widetilde{u_r' u_\Phi'}}{u_r \cdot u_\Phi}$ do not show any jet structure in the phase–averaged data (Fig.3.49 and Fig.3.50), again in contrast to the low Strouhal number case (Figs.3.26 and 3.27). The scatter of the data is high due to the normalisation of the data by the low phase–averaged values of the velocity components and to the high turbulence levels of the flow field. While this obscures detailed information about the Reynolds shear stresses, it does indicate a very high degree of mixing in the field.

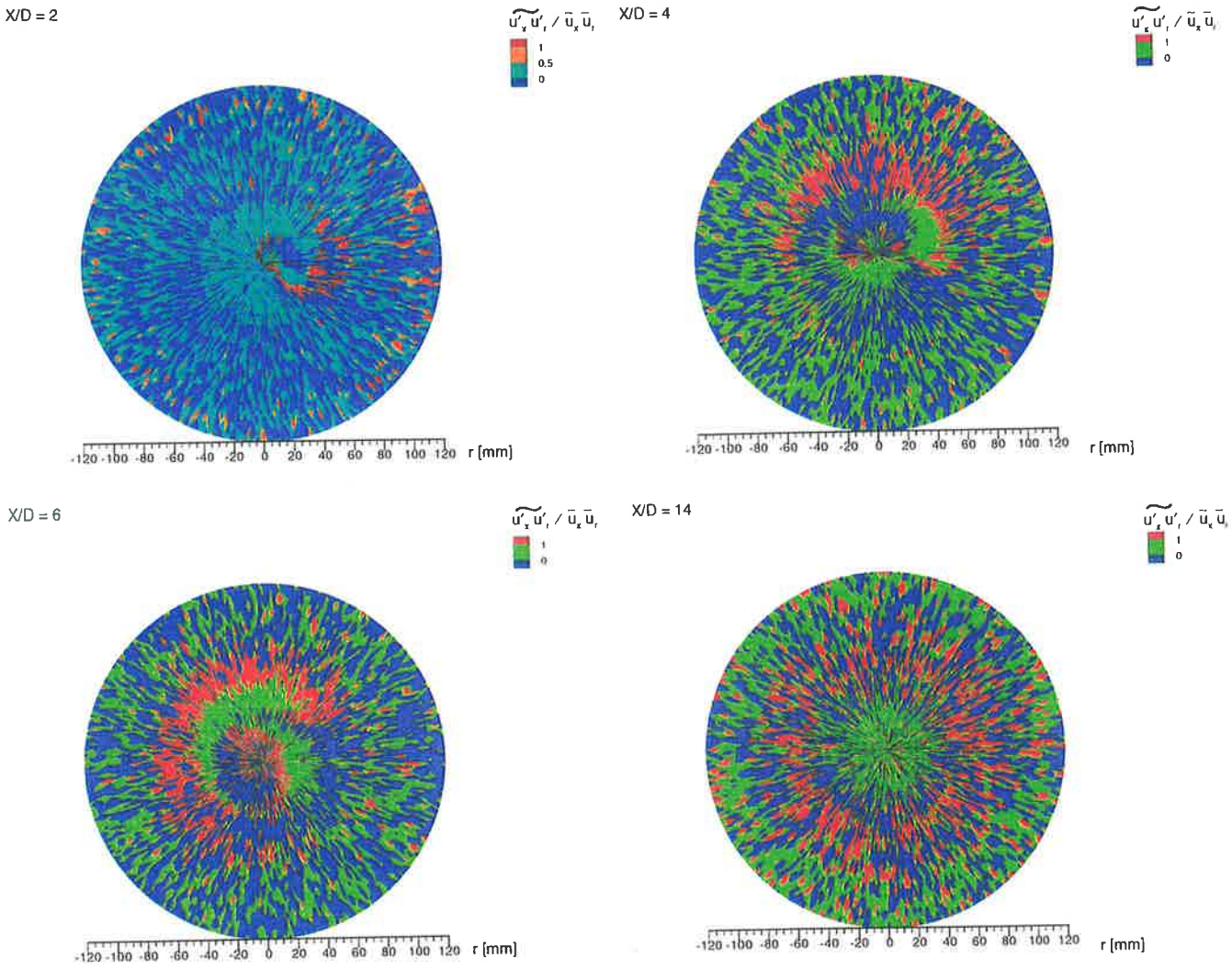

Figure 3.48: **Normalised phase-averaged $\frac{\widetilde{u_x u_r}}{\widetilde{u}_x \widetilde{u}_r}$ Reynolds stress component at x/d_e=2, 4, 6, 8, 10, 12. St_p=0.015, Re=26,600.**

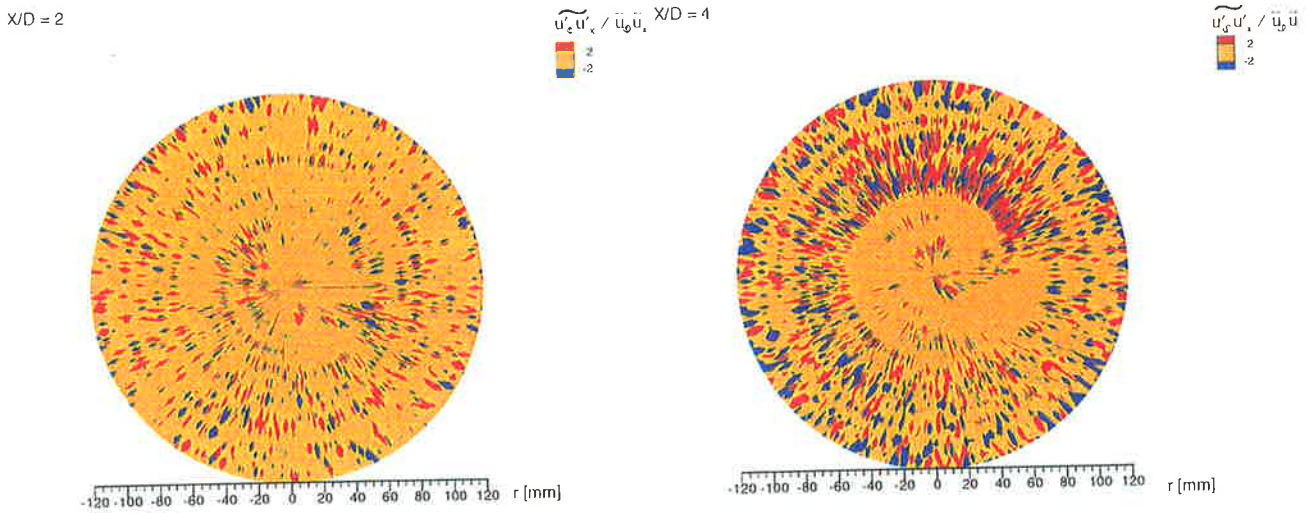

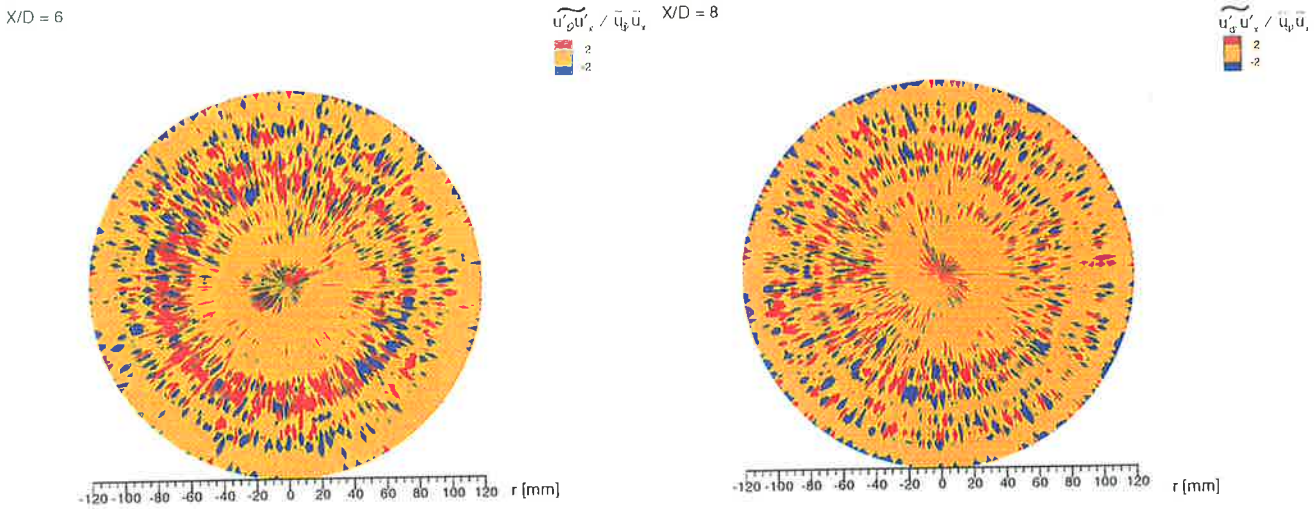

Figure 3.49: **Normalised phase-averaged $\frac{\widetilde{u_x u_\Phi}}{\widetilde{u_x}\widetilde{u_\Phi}}$ Reynolds stress component at x/d_e=2, 4, 6, 8, 10, 12. St_p=0.015, Re=26,600.**

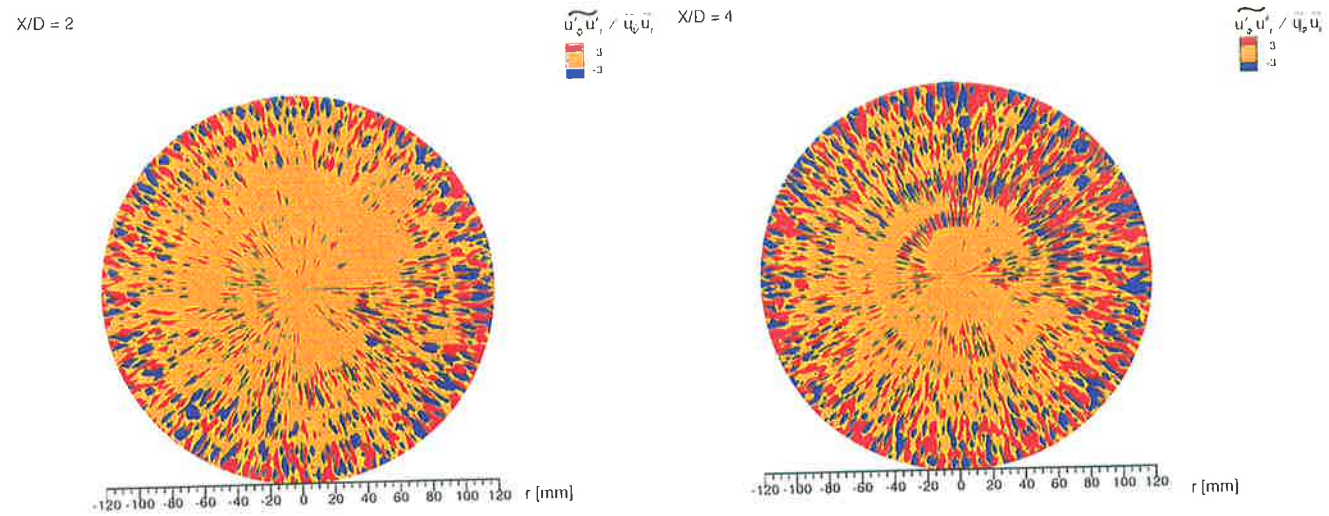

Figure 3.50: **Normalised phase-averaged $\frac{\widetilde{u_r u_\Phi}}{\widetilde{u_r}\widetilde{u_\Phi}}$ Reynolds stress component at x/d_e=2, 4, 6, 8, 10, 12. St_p=0.015, Re=26,600.**

3.3.6 Skewness and Flatness

The time–averaged skewness and flatness in each of the three velocity components is presented in Figure 3.51 to 3.56. Equation 3.2 in Section 3.2.6 is used to obtain the third order moment (skewness) and Equation 3.3 is used to calculate the fourth order moment (flatness or kurtosis). The skewness is related to the convection of turbulent energy, hence it is generally non-Gaussian in the high shear regions of the jet. Compared with a Gaussian distribution for which skewness is zero, a negative third order moment represents a velocity distribution skewed towards the lower velocity region, whereas a positive value of the skewness means the distribution leans towards higher velocities. The fourth order moment is related to the intermittency in the flow, which ranges from one extreme of low fluctuations with low intensity to the other extreme of high fluctuations of high intensity. The flatness for a Gaussian distribution is 3. Flatness values of greater than 3 imply a concentration of fluctuations around the mean velocity, whereas for values less than 3 the velocity distribution is more uniform, forming a flat plateau around the mean value.

The skewness of the axial component in the high Strouhal number jet displays significant deviation from the Gaussian distribution only close to the jet exit. At x/d_e=2 and 4 the values in the high velocity regions of the jet are between one and three. On the outer edge in the high shear region of the time–averaged jet, at x/d_e=2 the distribution is negatively skewed. Beyond x/d_e=4 the distribution is reasonably Gaussian with skewness values ranging between 0 and 1.

The flatness distribution of the axial component near the edges of the time–averaged jet at x/d_e=2 show high values of flatness (between 20 and 40), indicating high intermittency of the jet flow. In the time–averaged jet region the fourth moment shows almost Gaussian distribution. Beyond x/d_e=6 the distribution in the axial velocity approaches the Gaussian value of 3.

The skewness and flatness of the time-averaged radial component is displayed in Figs.3.53 and 3.54. In the outer regions of the time–averaged jet significant scatter of the skewness data is observed. However, in the inner regions, including the recirculation zone between the precessing jet and the spinning axis, the distribution appears to be almost Gaussian. The flatness shows similar behaviour. The values which are out of range in Fig.3.54 are due to the poor resolution in very low velocities measured near the outer edge of the jet, resulting in large uncertainty. In the jet and in the recirculation zone the velocity distribution resembles a Gaussian curve.

The tangential skewness and flatness, shown in Figs.3.55 and 3.56, reveal that the only significant deviation from the Gaussian distribution occurs at x/d_e=2 and 4. Again, the limited resolution in low velocity flows is probably the reason for the third and fourth order moments at the outer edge of the time–averaged jet reaching a skewness of -5 and a flatness which is out of range.

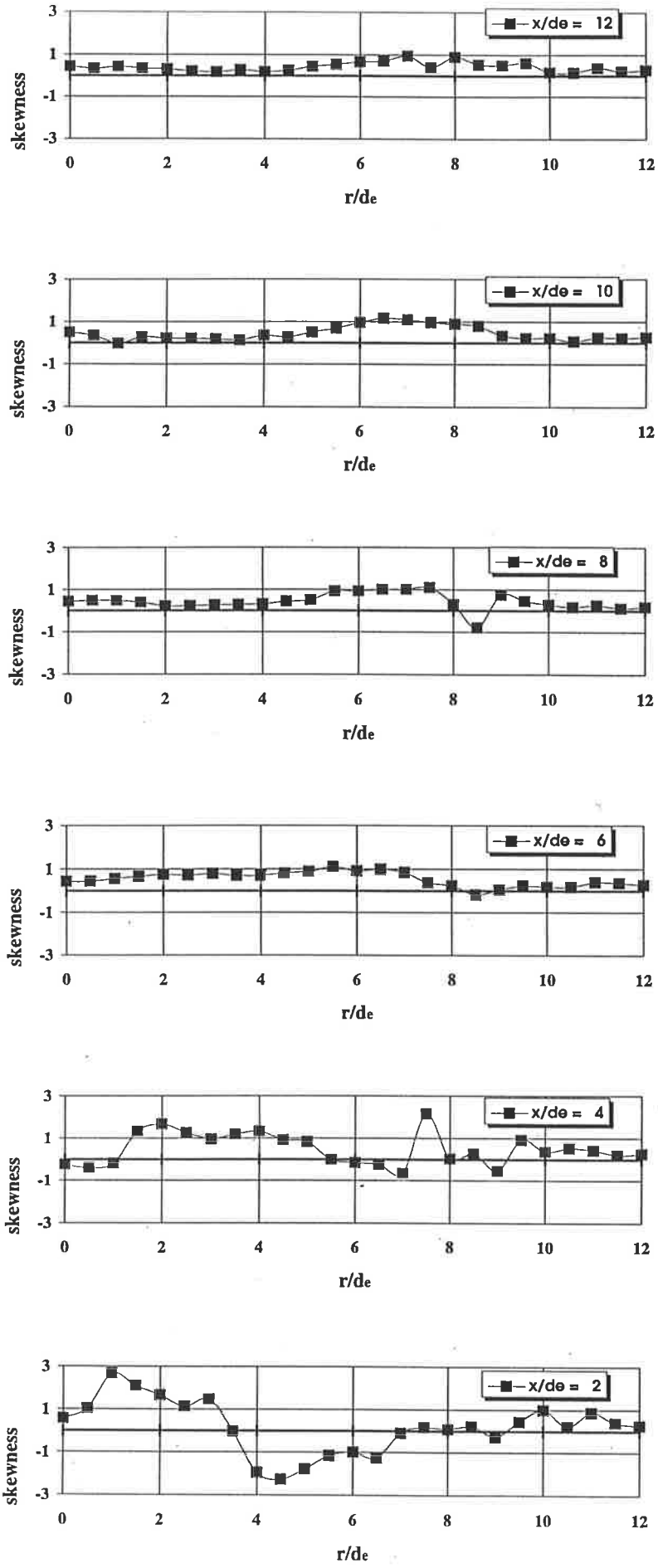

Figure 3.51: **Time–averaged axial skewness at x/d_e=2 to 12. St_p=0.015, Re=26,600.**

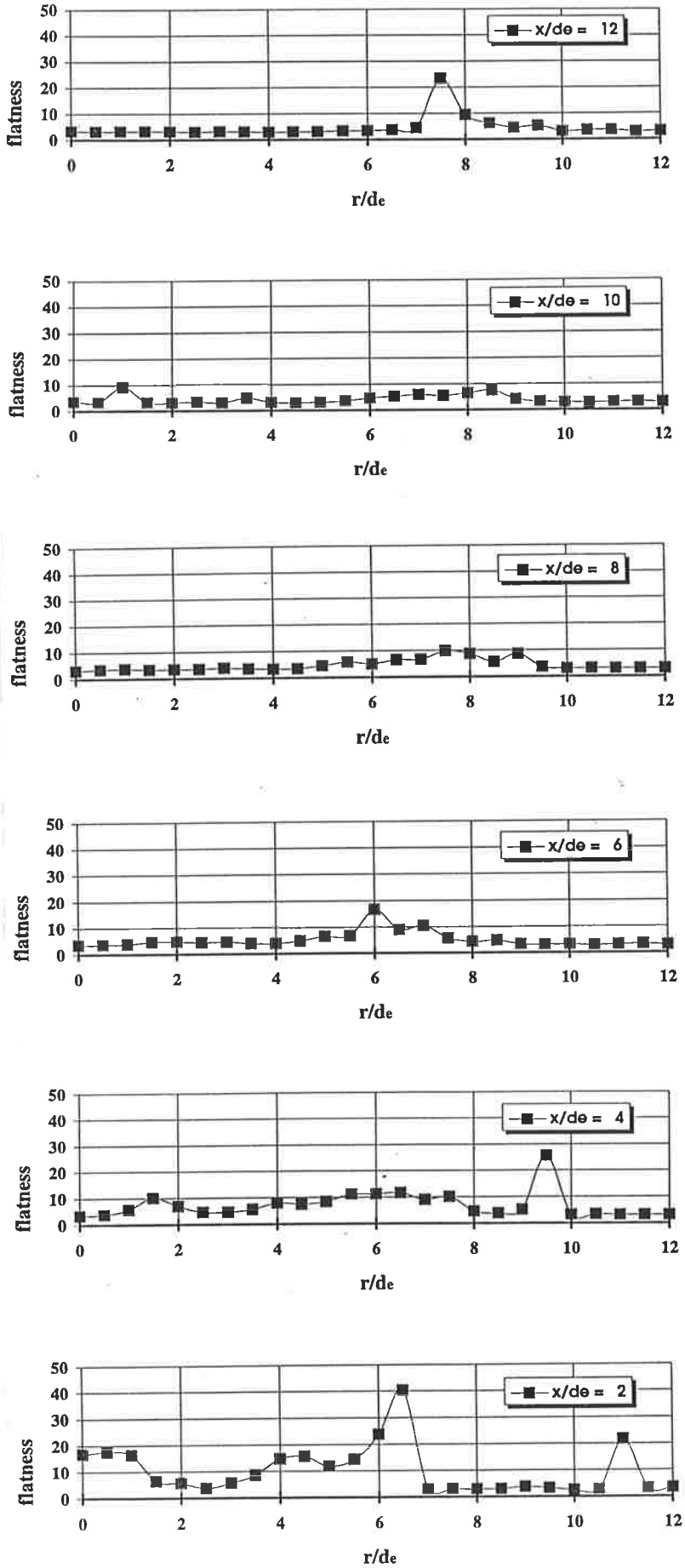

Figure 3.52: **Time–averaged axial flatness at x/d_e=2 to 12. St_p=0.015, Re=26,600.**

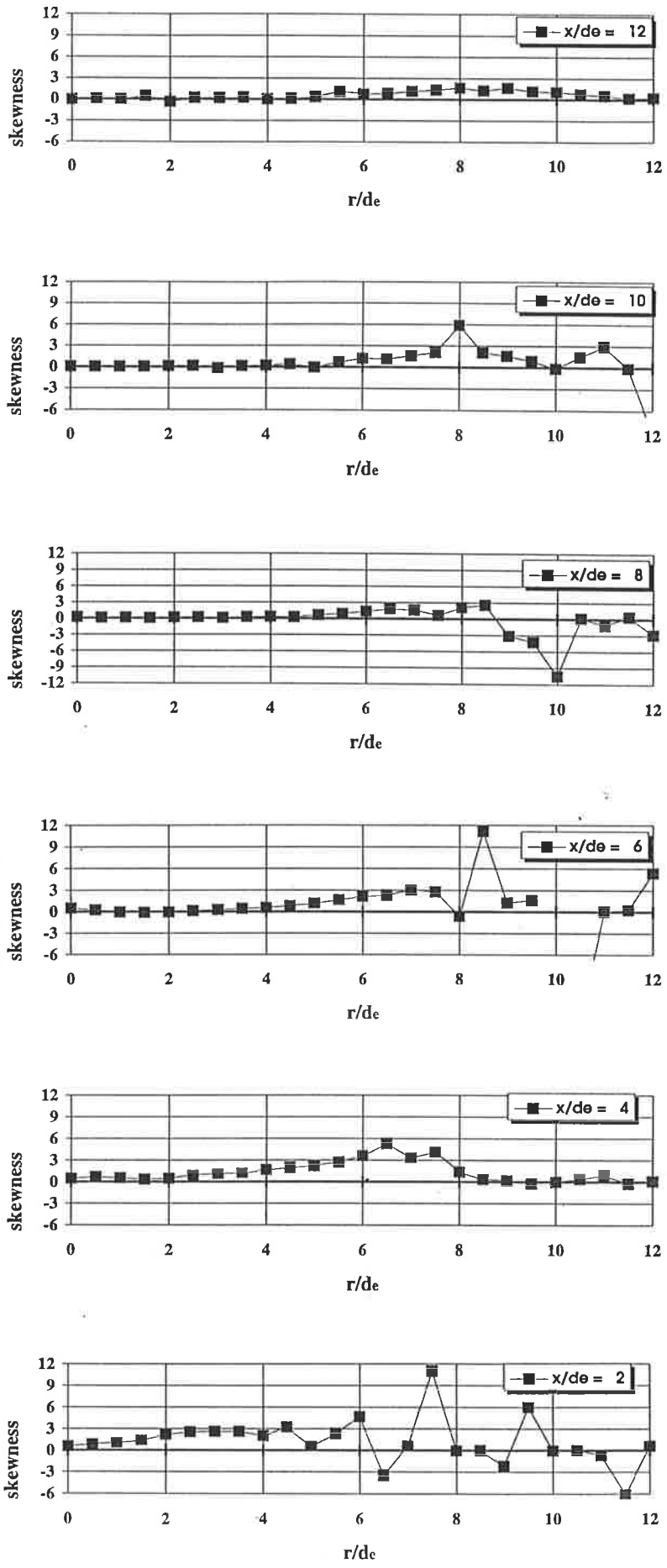

Figure 3.53: **Time–averaged radial skewness at x/d_e=2 to 12. St_p=0.015, Re=26,600.**

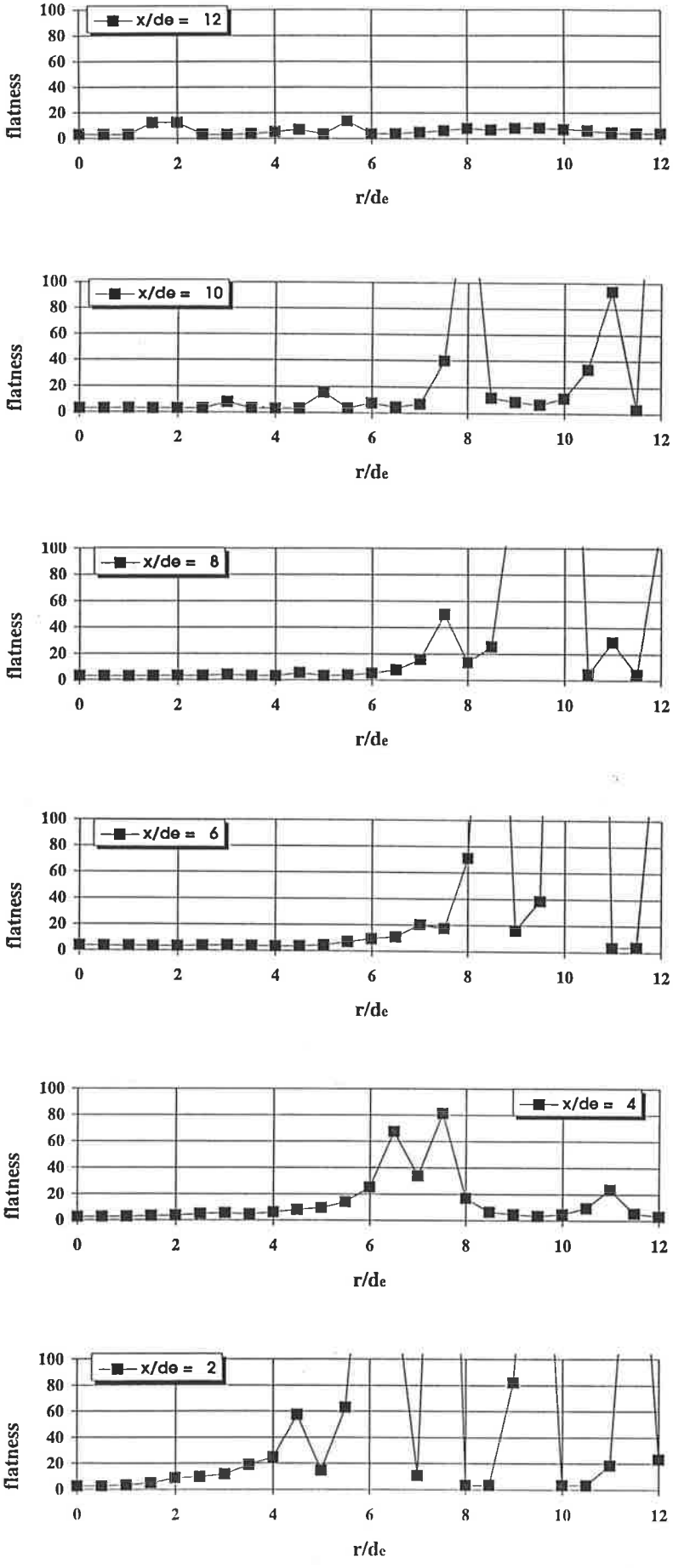

Figure 3.54: **Time–averaged radial flatness at x/d_e=2 to 12. St_p=0.015, Re=26,600.**

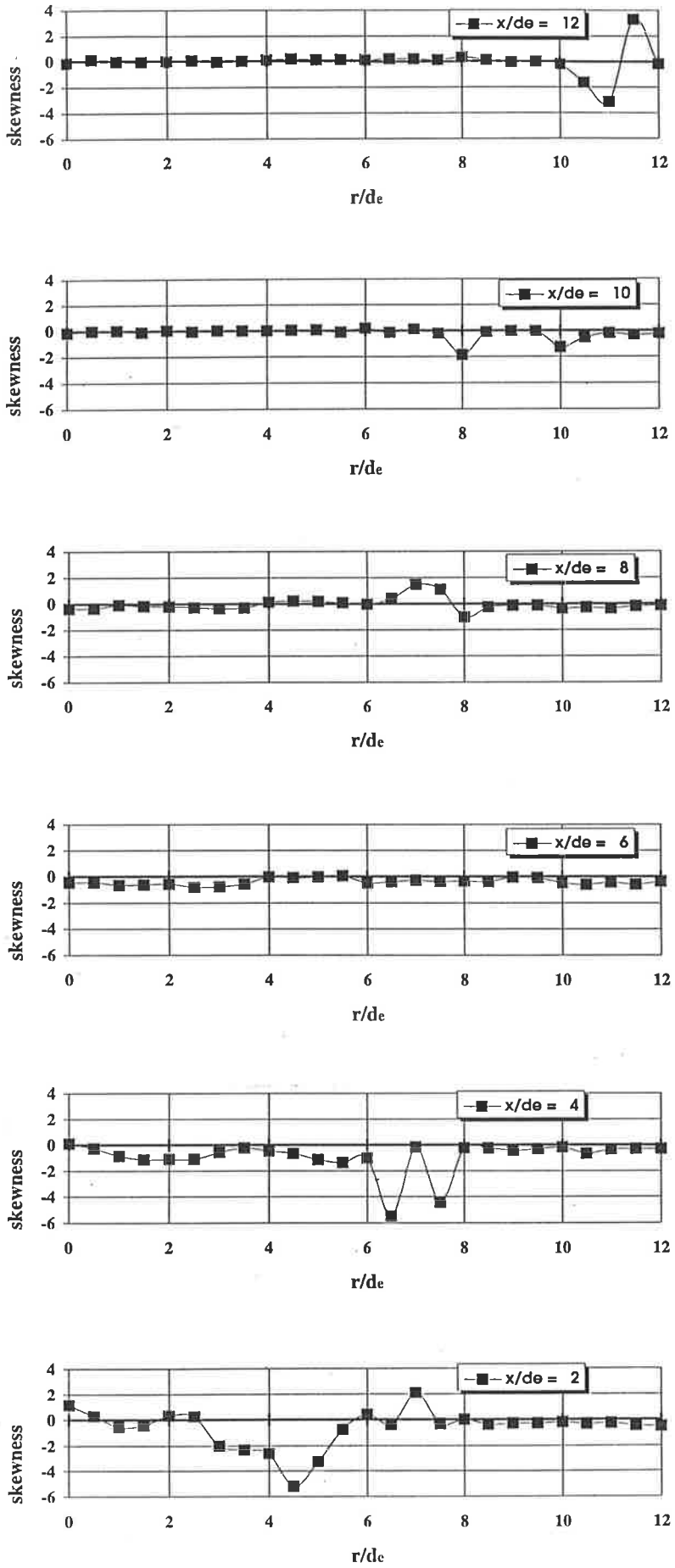

Figure 3.55: **Time–averaged tangential skewness at x/d_e=2 to 12. St_p=0.015, Re=26,600.**

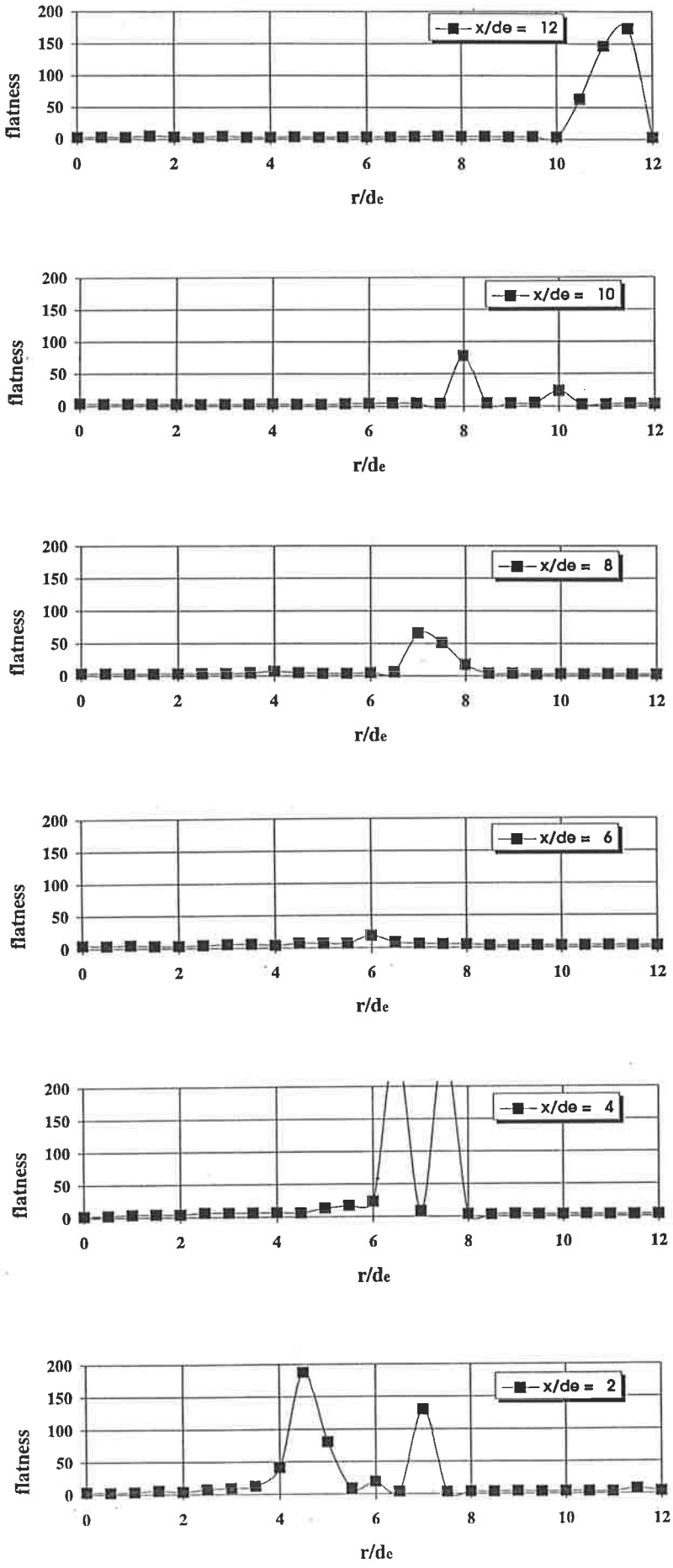

Figure 3.56: **Time-averaged tangential flatness at x/d_e=2 to 12. St_p=0.015, Re=26,600.**

3.4 Discussion

To enable a more complete evaluation of the Strouhal number dependency of the precessing jet two more Strouhal number cases have been studied. The detailed results of the cases for $St_p = 0.0058$ and $St_p = 0.0098$ are obtained under the same conditions as those in Section 3.2 and Section 3.3. The phase–averaged velocity components and turbulent stresses are attached in the Appendices C and D. The additional data confirm the trends shown in the data reported in the present Chapter and confirm that the transition from the low Strouhal number jet to the high Strouhal number is progressive and devoid of discontinuities.

One of the most important influences of precession on the flow of a jet is the deflection of its centreline. This deflection, summarised in Figure 3.57, shows the deflection of the jet in the negative r–direction, and Figure 3.58 shows the deflection in the positive Φ–direction. For comparison the path of a non–rotating simple turbulent jet issuing at an angle of 45^o is included in both Figures.

The deflection in r–direction clearly shows the increasing deviation of the 'centreline' of the phase–averaged jet from the 45^o exit angle. As the Strouhal number increases the low pressure region between the jet and its spinning axis increases (Section 4) and the jet path is bent more and more inwards towards the spinning axis. At a Strouhal number of 0.015 the jet becomes parallel to the spinning axis within the first eight nozzle diameters. In the initial region, at $x/d_e = 2$ all points lie on the 45^o line, hence the deflection at this point is zero in all cases.

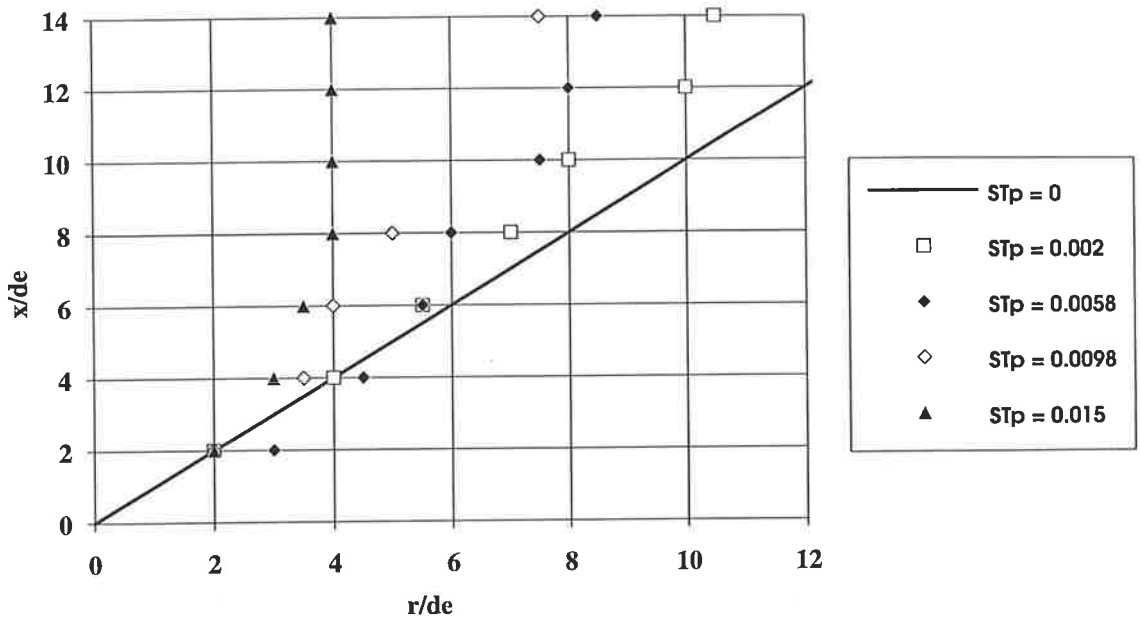

Figure 3.57: **The influence of the jet precession on the deflection in the x–r plane of the jet 'centreline'. The plot shows the axial and radial location of the point of maximum phase–averaged velocity as a function of the Strouhal number of precession.**

The deflection, in the tangential direction, or the 'backward' deflection of the jet, shows the same trend. The low Strouhal number jet hardly deviates from the straight line trajectory of the simple turbulent jet. With increasing Strouhal number the curvature of the path of the locus of maximum phase–averaged velocity increases dramatically.

Several methods of assessing the influence of precession on the decay rate of a jet are possible. The method used here is to compare the maximum axial velocity in a non–precessing jet aligned along the nozzle axis (α_e=0) with the precessing jet ($\alpha_e = 45^o$) assessed in this investigation. Presenting the data (Fig.3.59) in non–dimensional form, $\frac{\tilde{u}_{x,cl}}{u_e \cdot \cos 45^o}$, compensates for the differences in exit angles.

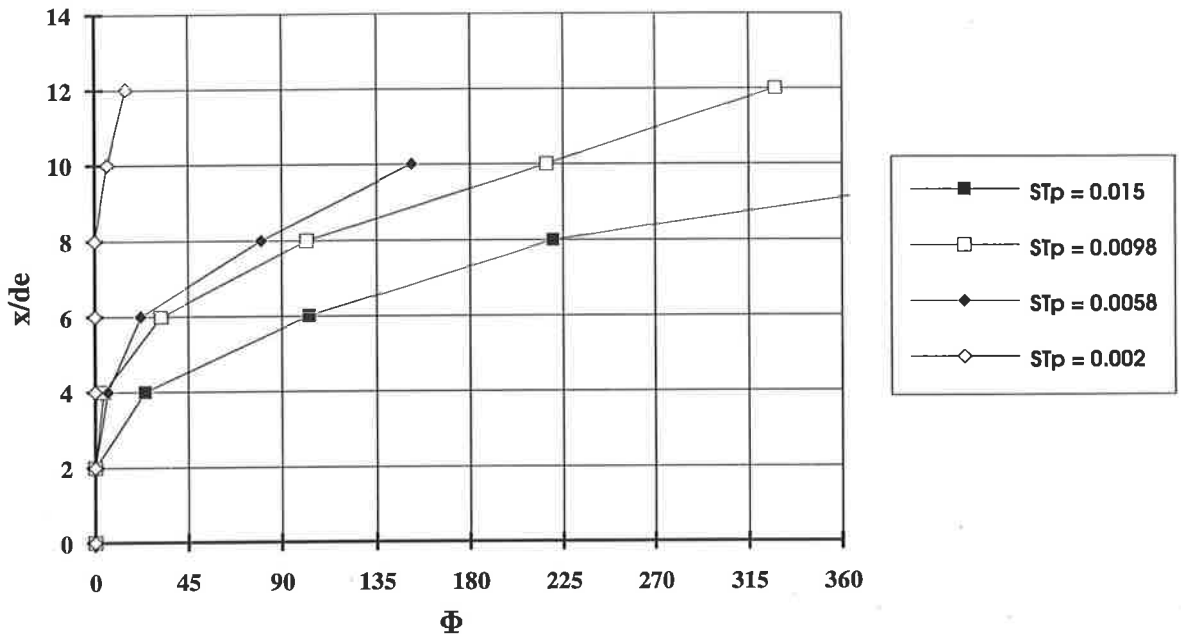

Figure 3.58: **The influence of the jet precession on the deflection in the x–Φ plane of the jet 'centreline'. The plot shows the axial and tangential location of the point of maximum phase–averaged velocity as a function of the Strouhal number of precession.**

The decay rate of the centreline velocity of a non–precessing axial jet is expressed in the empirical equation (3.1) suggested by Rajaratnam (1976), which he derived simply from conservation of linear momentum and the observation that pressure is independant of both x and r. An empirical constant was determined to provide the overall fit to the various experimental investigations included in his data set. The equation can be written in the form: $\frac{\overline{u}_{x,cl}}{u_e} = 6.3 \cdot (\frac{x}{d_e} - \frac{x_0}{d_e})^{-1}$, where $\overline{u}_{x,cl}$ is the mean axial centreline velocity, x is the axial distance from the nozzle exit and x_0 the distance from the virtual origin to the nozzle exit. In the case of a turbulent jet issuing from the mechanical nozzle with a 0^o exit angle, $x_0/d_e = -4$ and the end of the potential core is at x/d_e=2.3–2.5 respectively, the equation for the turbulent jet becomes $\frac{\overline{u}_{x,cl}}{u_e} = 6.3 \cdot (\frac{x}{d_e} + 4)^{-1}$. Figure 3.59 compares the decay of the axial component of the centreline velocity of the 45^o precessing jet with the above equation of the turbulent round jet.

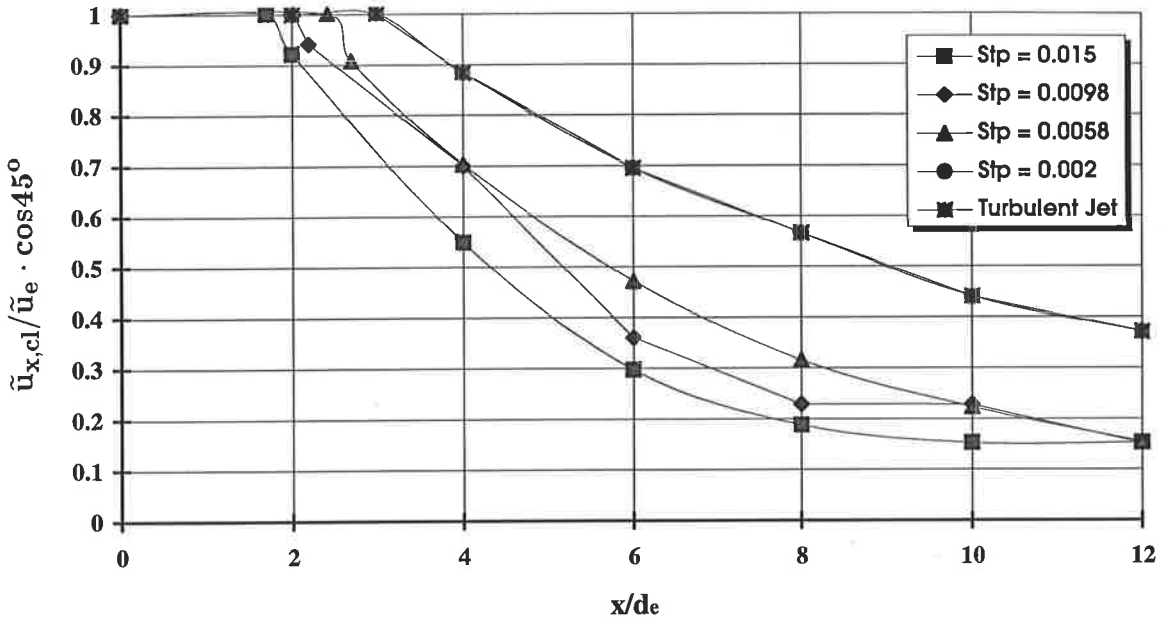

Figure 3.59: **The axial velocity decay along the locus of maximum velocity in the phase–averaged jet. Re=26,600.**

The decay in velocity of the centerline of the phase–averaged jet, where the centre is defined as the location of the maximum phase–averaged velocity, is strongly dependent on the Strouhal number. The low Strouhal number jet decays with the same rate as a simple turbulent jet, but with increasing Strouhal number the decay is markedly increased. Calculating the a linear correlation given by

$$R = \frac{\sum_i (x_i - \overline{x})(y_i - \overline{y})}{\sqrt{\sum_i (x_i - \overline{x})^2}\sqrt{\sum_i (y_i - \overline{y})^2}}$$

between rate of decay of the axial jet centreline velocity, $\frac{du_{x,cl}}{dx}$, and for the magnitude of the reverse flow in the central recirculation region, a value of R= -0.71 is obtained. This suggests that the jet is deccelerated, not only by the entrainment, but also by the reverse flow zone, or the low pressure region (Section 4). Increased entrainment is also observed when the spreading of the jet is investigated.

To compare the spreading of the precessing jet with a simple turbulent jet, a body fitted coordinate system is used for the PJ. The x' coordinate is defined as pointing along the local jet centreline, i.e. the locus of the maximum phase–averaged velocity. The r′ and Φ' coordinates are orientated in the local radial and tangential directions, respectively, which are each perpendicular to the local axial coordinate. The spreading is defined by the $r_{0.5}$ radius, where the velocity has decayed to half its phase–averaged centreline value.

The spreading in the radial direction (r′ in the body-fitted coordinate system) increases with the Strouhal number for all cases (Fig.3.60). The low Strouhal number case has a typical spread of $10 - 11^o$ for both the inside and ouside of the jet, that is for the section of the jet nearest and furthest away from the spinning axis (see Notation on page xxvi for explanation of 'inside', 'outside, 'front' and 'back' of the jet). For the highest Strouhal number case, angles of over 17^o can be detected for both proximal and distal edges of the jet. The spreading is not symmetrical. It seems that the inside of the jet, negative r', spreads less than the outer edge of the jet, positive r'.

The spreading in tangential direction Φ' (Fig.3.61) of the low Strouhal number jet in the body–fitted coordinate system is approximately symmetrical, with a half angle of $7.5^o \pm 0.5$. With increasing Strouhal number the spreading becomes highly asymmetric. Tangentially in front of the jet the spread increases 8.5^o ($St_p = 0.0058$), 12^o($St_p = 0.0098$), 20^o ($St_p = 0.015$), whereas tangentially behind the jet it goes from $12.5^o \pm 0.5$ ($St_p = 0.0058$) to over 30^o ($St_p = 0.0098$) and higher ($St_p = 0.015$).

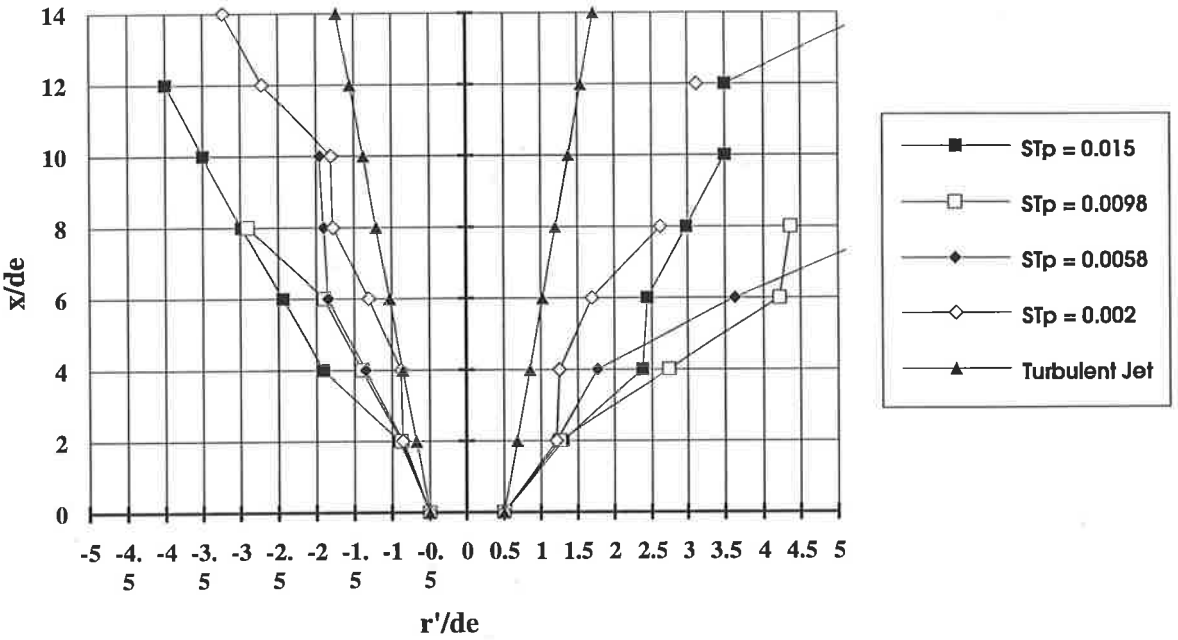

Figure 3.60: **The spreading of the phase–averaged precessing jet in radial direction. Body fitted coordinate system x', r', Φ'; Re=26,600.**

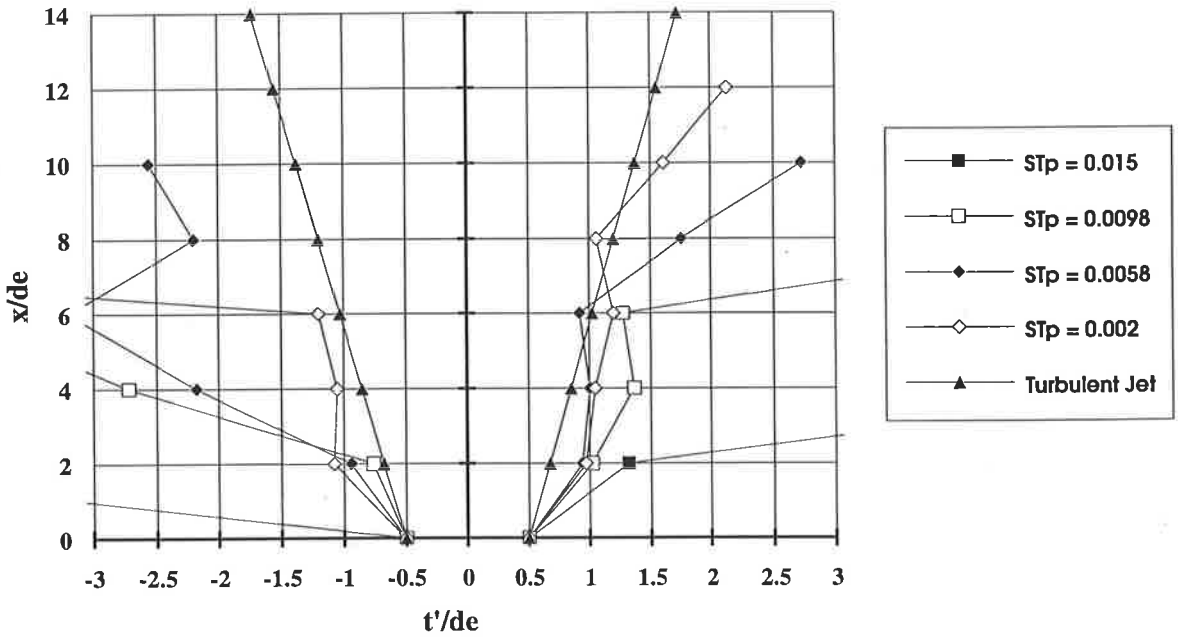

Figure 3.61: **The spreading of the phase–averaged precessing jet in tangential direction. Body fitted coordinate system x', r', Φ'; Re=26,600.**

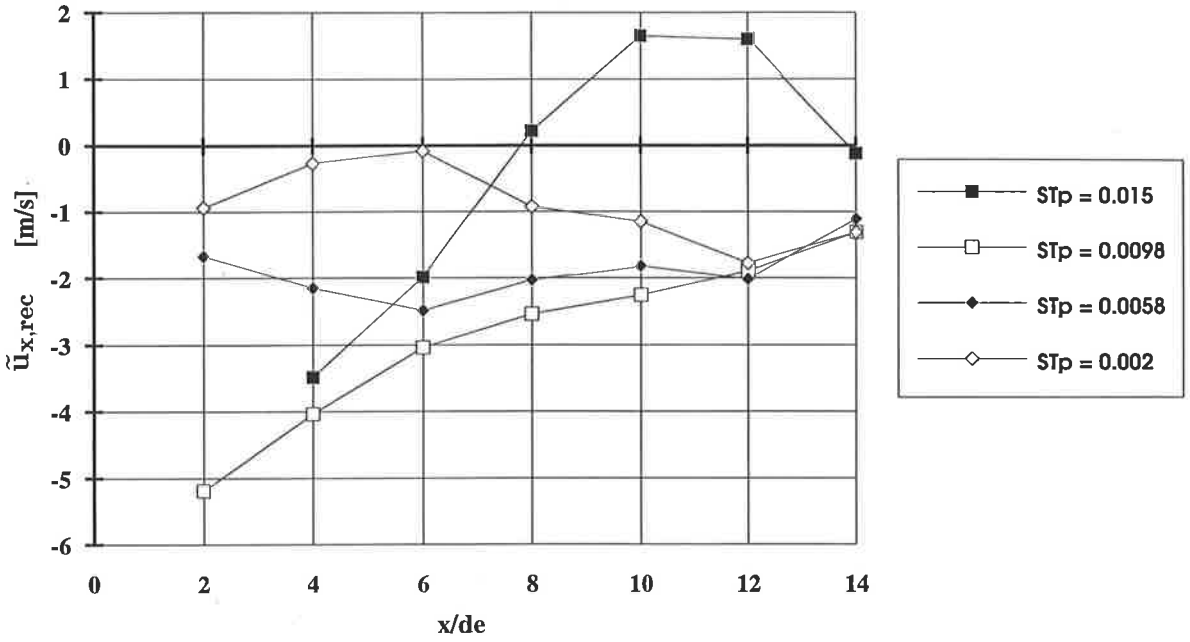

Figure 3.62: **The maximum negative axial phase–averaged velocity in the recirculation zone. Re=26,600.**

The magnitude of the reverse flow is also dependent on the Strouhal number. The reverse flow region becomes stronger with increasing Strouhal number. Fig.3.62 shows the maximum negative phase–averaged axial velocities dependent on the axial distance from the nozzle exit.

The dependency of the turbulence characteristics of the precessing jet on the Strouhal number is demonstrated using the time–averaged components. The maxima of the axial and radial turbulence, skewness and flatness are compared for the different Strouhal number cases (Figs.3.63 and 3.64) . In general the maximum turbulence, which is located in the high shear edges of the jet, decreases with increasing Strouhal number of precession. The structures in the jet flow are less dominated by shear, since the jet, as

the momentum source which supports the shear, is turned away faster with increasing Strouhal number,behind the structures. This reduced shear dominance is also reflected in the skewness and flatness. The initial high values in the low Strouhal number jet indicate high shear on the edges of the jet, similar to a simple turbulent jet. With increasing Strouhal number, both the skewness and the flatness are decreasing toward Gaussian values. It is tentatively suggested that the kinetic energy, which has to be conserved, is more concentrated in large scale structures and is not carried by the strong shear–induced turbulent fluctuations, and that the scale of the turbulent structures is increases with the Strouhal number. This assumption is supported by Mi et al.(1996). The effect of Strouhal number on the flow structures will be discussed in the next Section in relation to the vortical structures in the precessing jet.

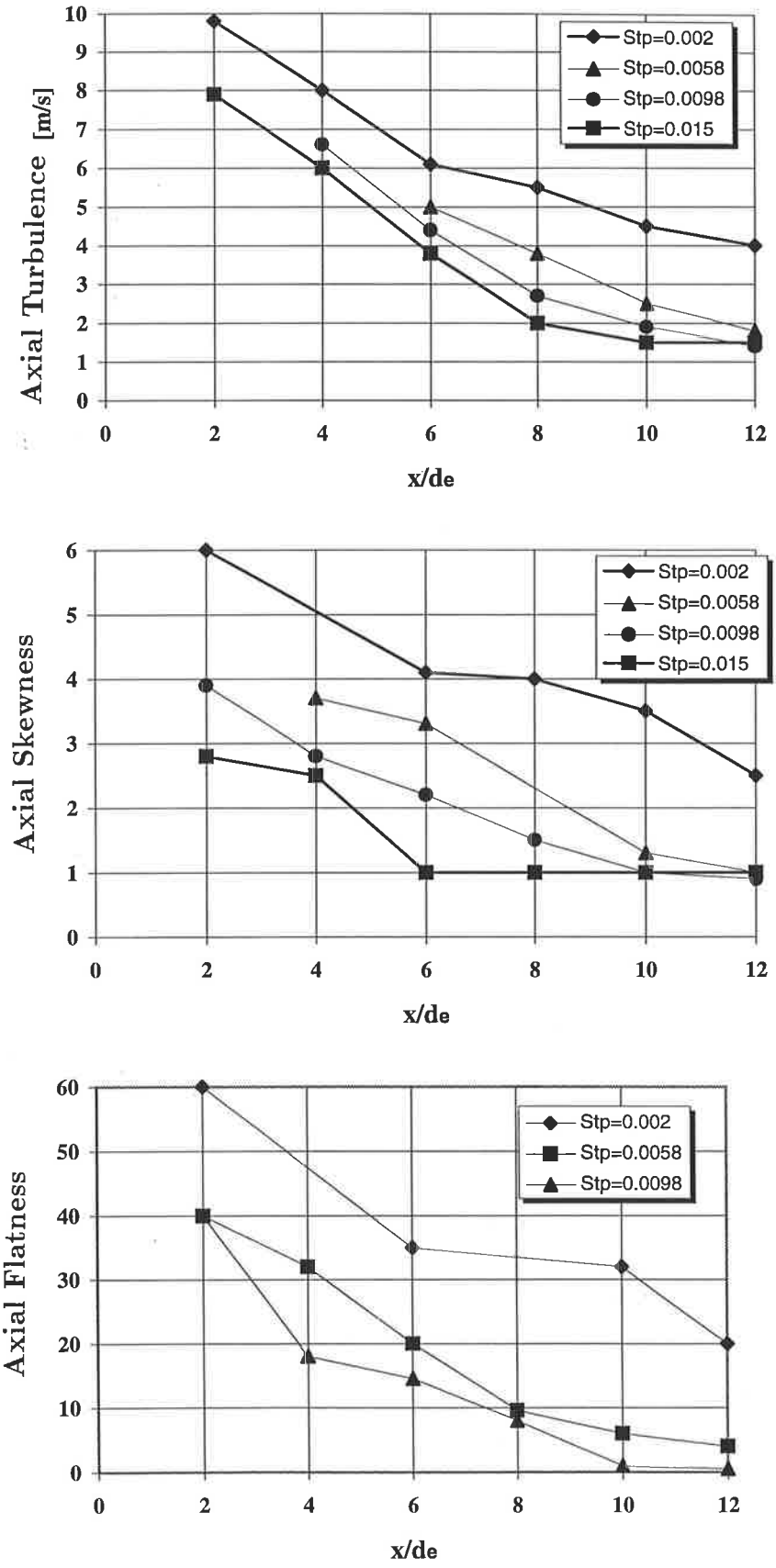

Figure 3.63: **The maximum time–averaged axial turbulence, skewness and flatness. Re=26,600.**

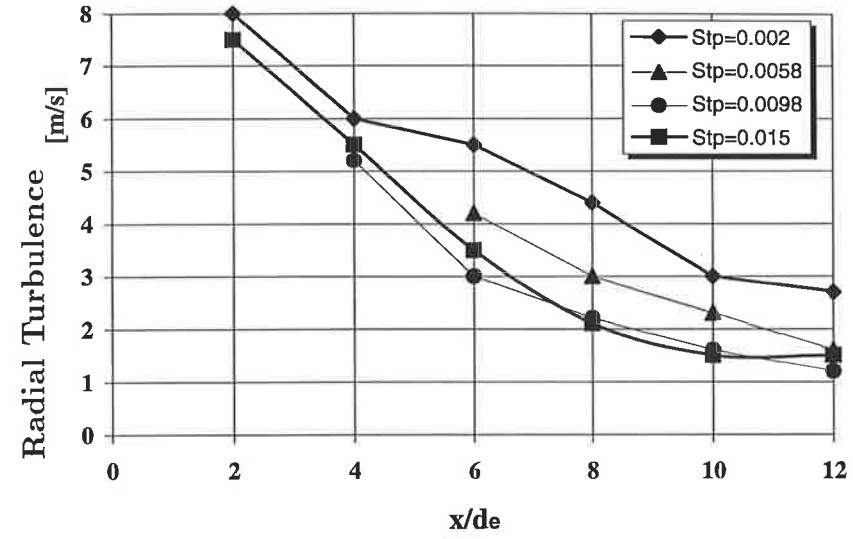

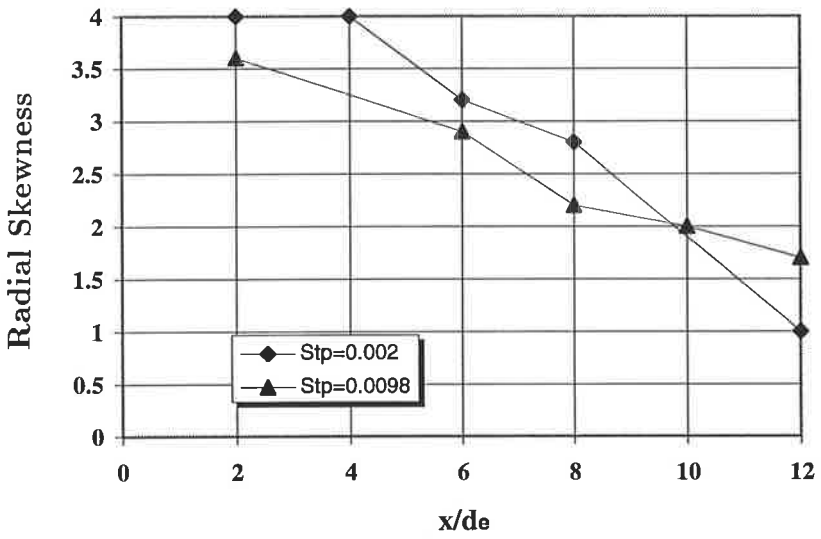

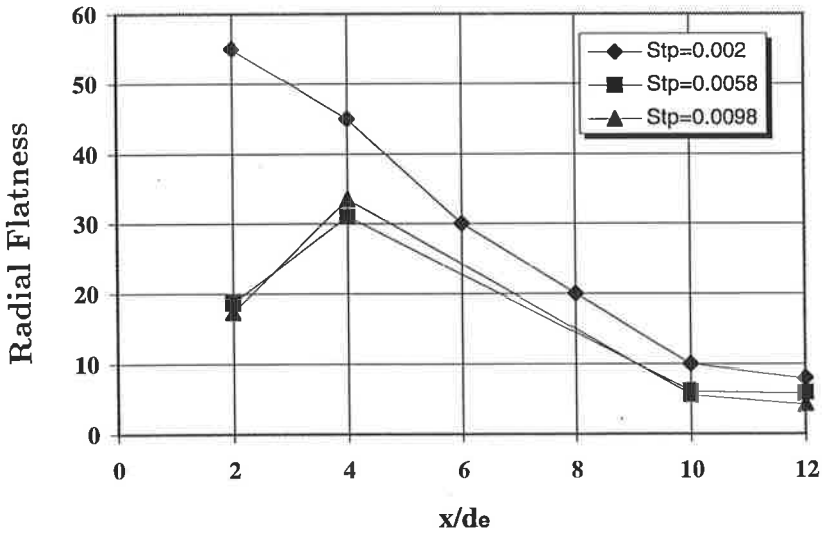

Figure 3.64: **The maximum time–averaged radial turbulence, skewness and flatness. Re=26,600.**

Chapter 4

VORTEX STRUCTURES AND MOTION IN A PRECESSING JET FLOW

The importance of understanding the large scale vortical motions in jet flows has been recognised in research spanning several decades (Crow and Champagne, 1971; Dimotakis et al. 1983; Hussain 1983, 1984; Husain and Hussain, 1993; Hussain et al. 1993). The precessing jet flow is described with reference to a postulate of the formation and evolution of vortical structures which occur in the two different Strouhal number regimes. The postulate presented here is supported by the flow visualisation and the LDA measurements reported in Section 3.

4.1 Characteristic Regions in a Precessing Jet

Studies by Abramovich (1963) and Rajaratnam (1976) have shown that a free turbulent jet can be divided into three characteristic regions. Three regions can also be identified in a precessing jet flow: a potential core region, in common with the simple jet, a precession dominated region, and a region in which no dominant frequency can be discerned.

4.1.1 Region I: the Potential Core Region

The first region in the precessing jet flow is the initial region or potential core region, where the field can be described by the equation for potential flow. The jet leaves the contraction inside the mechanical nozzle, which becomes parallel more than one nozzle diameter upstream of the exit plane, with a top–hat velocity profile and a symmetrical, circular cross–section (Section 3.1). The boundary layer around the circumference at the exit is very thin and rapidly becomes distorted and folded into the Brown–Rosko amalgamating vortices (Brown and Roshko, 1974) or some other rapidly growing core instability which 'eats up' the core region, in which the phase–averaged velocity is uniform. Experiments have shown (Section 3) that the shape of the circular jet is not deformed, from which it is deduced that the static pressure is equal to that in the surroundings and that the length of the core in the present experiments is almost independent of the Strouhal number of precession. For the stationary jet with an exit angle $\alpha_e = 45^o$, the end of the potential core was found to be at x/d_e=2.1, while for the case with the nozzle rotating at the maximum frequency of 60 Hz the end was located at $x/d_e \approx 1.8$, in the cylindrical coordinate system where the jet is angled in 45° to the x–axis. No dependence of the length of the potential core on the Reynolds number was observed within the range of conditions tested, (6,600 < Re < 26,600 in Section 5.2).

4.1.2 Region II: the Precession Dominated Region

The second region of the PJ is downstream from the potential core ($x/d_e > 2$), corresponding to approximately $3 \cdot d_e$ measured in the direction of the jet, in which the centreline velocity starts to decay. The characteristics of the jet flow (e.g. the shape of the jet, the spiral path of the jet and its deflection) are highly dependent on the Strouhal number of precession (Section 3).

For the low Strouhal number jets investigated here, $St_p = 0.002$ and 0.0058, the length of this second region is 'infinite'. Frequency spectra in the jet show that the precessional frequency is dominant even in the far field of the jet (measured up to $x/d_e = 40$, Fig.4.12). The deflection of any elemental section of the jet is found to be small and the jet path, projected in the r–Φ plane, follows an Archimedian spiral path (Fig.4.9).

By contrast, in the high Strouhal number regime, e.g. for $St_p = 0.0098$ and 0.015 as investigated here, velocity and pressure gradients are steep, causing Region II to be confined to the relatively short zone $2 \leq x/d_e \leq 8$. In particular, frequency spectra show that motions at the precessional frequency cannot be detected beyond this region (Fig.4.19). In this region the jet path is highly deflected from the Archimedian spiral (Fig.4.16) and a recirculation region is established (Section 3.3.2).

4.1.3 Region III: the Region of no Dominant Frequency

The third region is the region where no dominant frequency can be detected (Fig.4.19). When phase–averaged at the frequency of precession the flow becomes axisymmetric and no recirculation of fluid occurs (Section 3.3.2). The magnitudes of the time–averaged and phase–averaged velocities are identical (Section 3.3). This region does not exist for low Strouhal number flows (Section 3.2). It begins at $x/d_e \geq 8$ for the high Strouhal number case investigated in Section 3.3.

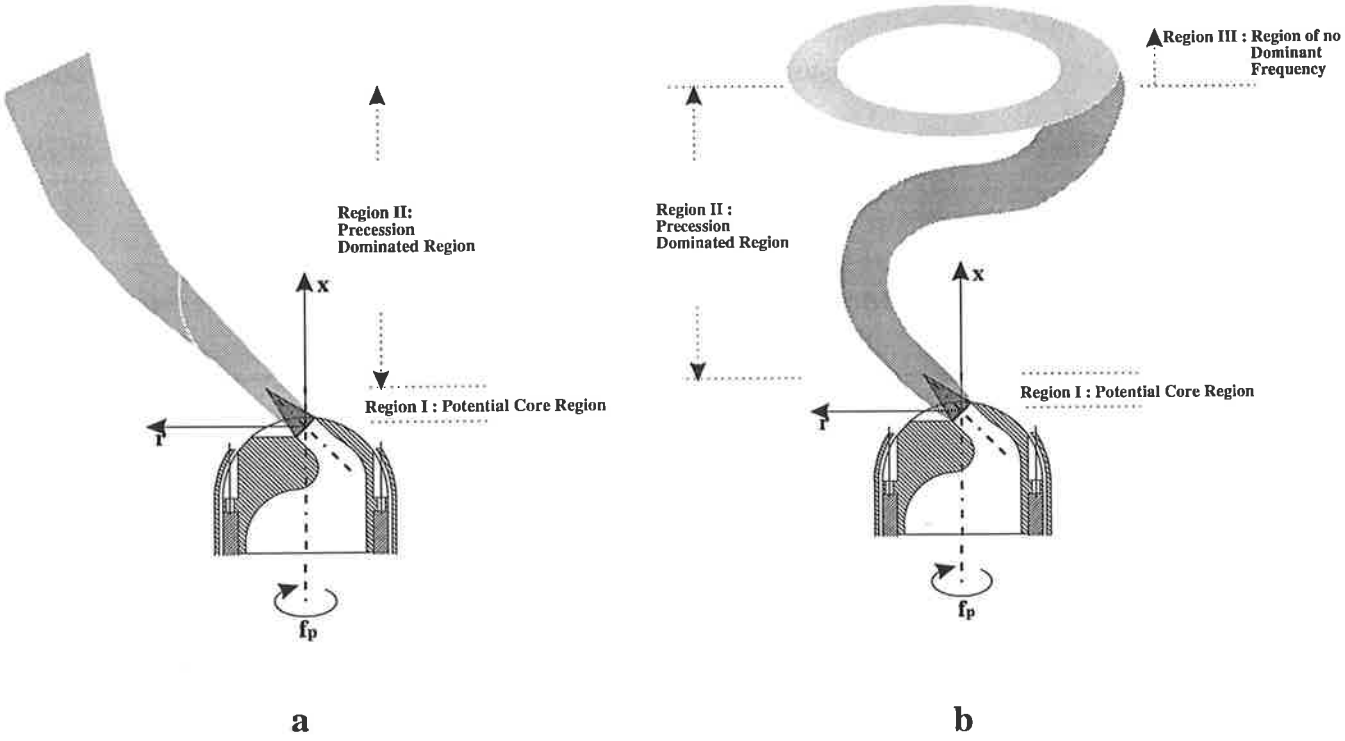

Figure 4.1: **Characteristic flow regions which have been identified in the phase–averaged domain for: a) the low Strouhal number jet; b) the high Strouhal number jet**

4.2 An Overview of the Behaviour of Precessing Jet Flows

4.2.1 The Formation of Vortical Structures in the Potential Core Region

Vortical structures are generated within the shear flow at the edge of the potential core in Region I of a precessing jet flow. Crow and Champagne (1971) describe flow structures in a conventional turbulent jet, initiated in the boundary layer which is formed on the inside of the nozzle walls upstream from the nozzle exit. Downstream from the nozzle exit the shear layer is unstable and develops instability waves via the Kelvin–Helmoltz mechanism (Liepmann and Gharib,1992). These waves grow in the shear layer and roll into primary vortical structures. In a round jet, pairing and amalgamation of these ring vortices takes place and causes contraction and expansion of the azimuthal primary vortex ring structures (e.g. Paschereit et al. 1992). During the expansion process the jet core also develops azimuthal instabilities, analogous to the transverse Bernal–Roshko structures in planar shear layers (Bernal 1981, Bernal and Roshko, 1986), which grow in the highly strained region between two primary vortex rings. The secondary streamwise vortex structures interact with the primary azimuthal vortices (Liepmann and Gharib, 1992). The development of the two types of vortical structures may derive from dynamic instabilities in the potential core region of the jet (e.g. Hussain et al. 1993). With the potential core of the precessing jet being similar to that of a simple turbulent jet (as described in Section 4.1.1), a similar flow field and similar instabilities leading to the formation of comparable structures can be expected.

Near to the end of the potential core of a simple turbulent jet the formation of primary structures occurs at a characteristic frequency or mode which has been called the preferred mode (Hussain and Zaman, 1981; Crow and Champagne, 1971). The characteristic Strouhal number $St_c = f_c \cdot d_e/u_e$ is based on the characteristic frequency with which the structures are formed f_c, the exit velocity u_e and the exit diameter d_e. This Strouhal number is sensitive to the facility used (Hussain, 1986), but is in the range $0.2 < St_c < 0.85$. Crow and Champagne (1971) found it to be St_c=0.3.

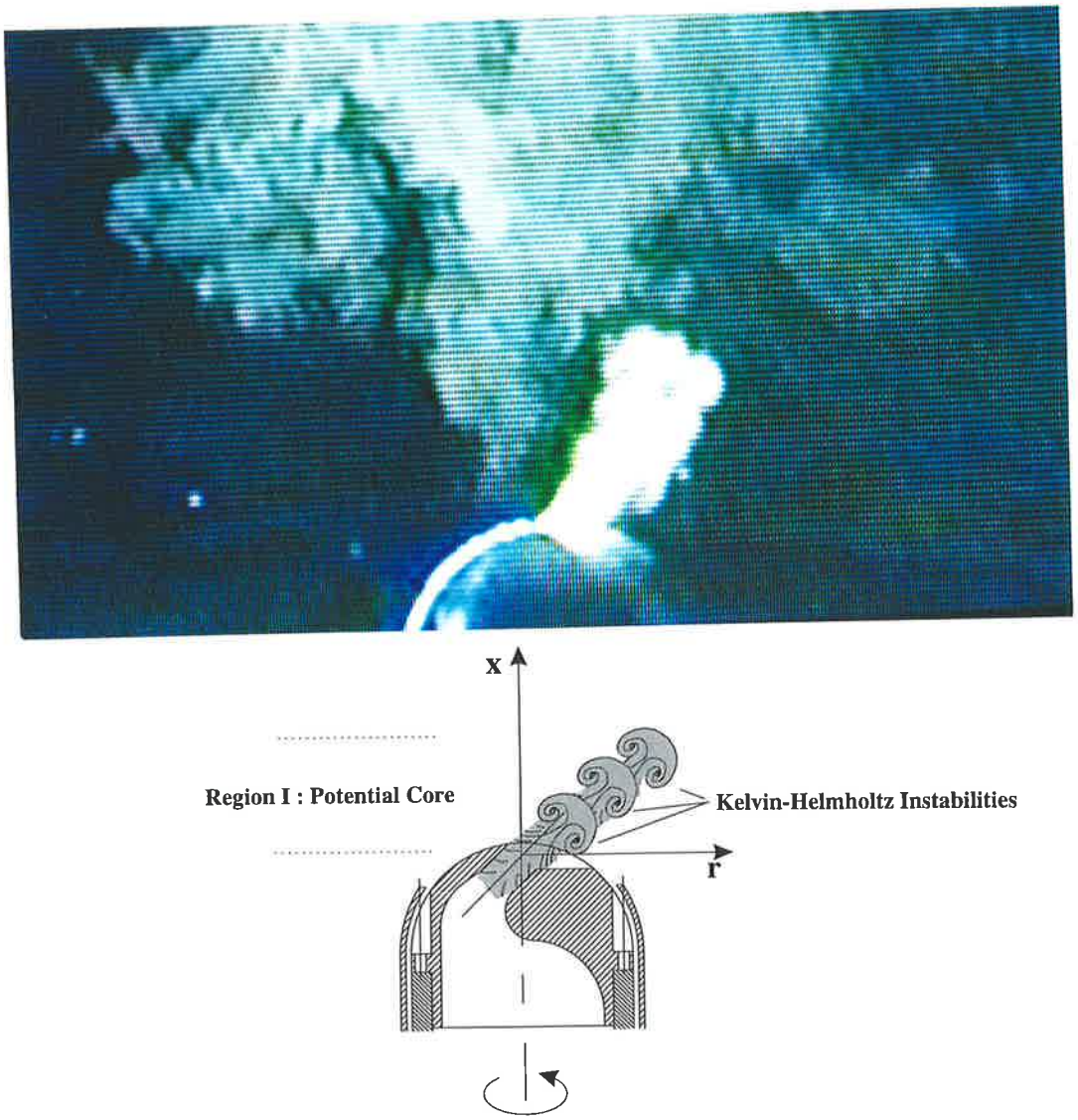

Figure 4.2: **Evidence of Kelvin–Helmholtz instabilities in the potential core region of the precessing jet flow**

Figure 4.2 shows the core region of the precessing jet, visualised by the laser–induced fluorescence (LIF) technique, in a water tank facility. The precessing jet fluid is marked with fluorescein and is illuminated with a laser light sheet in the x–r plane (Section 2.3.3). Structures resembling those in a turbulent jet are observed. An estimate of the Strouhal number of the (Kelvin–Helmholtz) vortex rings is obtained by counting the ring–type vortical structures within the potential core region. The Strouhal number so obtained is $0.5 < \mathrm{St_c} < 1$, which is in the range expected for a simple turbulent jet (Hussain, 1986).

Downstream from the potential core the centreline velocity of a jet starts to decay. Thus the velocity difference between the jet and the 'still' surroundings decreases, and so the magnitude of the shear that supports the primary azimuthal structures also decreases with distance. The jet breaks down into a train of vortex puffs which propagate downstream and grow in size as they entrain fluid (Crow and Champagne, 1971).

4.2.2 The Model of an Archimedian Spiral

The trajectory of a jet issuing in the r–Φ plane from an origin on the x–axis, which is also the axis of rotation, follows a trajectory which has the form of an Archimedian spiral. In the case of the precessing jet which is inclined by 45° to the r–Φ plane, a third coordinate along the axis of rotation is needed to describe the three–dimensional spiral trajectory. The movement of the jet fluid in the axial direction is defined by the the axial velocity component of the jet and is presented as the axial velocity decay in Figure 3.59 in Section 3.4. A projection of the precessing jet flow on to the r–Φ plane is

used here to provide a model of the evolution of the vortical structures described in the previous section. The projected component of the convection velocity of the structures can, at least initially, be expected to follow the Archimedian spiral.

The two–dimensional equation used to describe an Archimedian spiral in polar coordinates is

$$r = \frac{u_{e,r}}{2\pi f_p} \cdot \Phi \tag{4.1}$$

where r is the radius, Φ the angular position, $u_{e,r}$ the exit velocity component in radial direction and f_p the frequency of precession. To adapt the equation of a simple Archimedian spiral to give a better representation of the path described by a jet rotating about the x–axis but directed in the r–Φ plane, the jet velocity is modified to account for velocity decay. This modification is based on the axial velocity decay of a simple turbulent jet in the region downstream from the potential core, i.e. for $x/d_e > 1.9$. The path of the local precessing jet is here defined as the locus of the point of the maximum velocity in the phase–averaged flow. The jet velocity in the region $x/d_e > 1.9$ then becomes

$$\frac{\tilde{u}_c}{\tilde{u}_{r,e}} = 6.3 \cdot \frac{1}{x/d_e + 4.4} \tag{4.2}$$

as derived from Rajaratnam (1976) for a simple turbulent jet.

A characteristic of the Archimedian spiral is that the curvature, 1/R, expressed as

$$\frac{1}{R} = \frac{2\pi f}{\tilde{u}_c} \cdot \frac{\Phi^2 + 2}{(\Phi^3 + 1)^{3/2}} \tag{4.3}$$

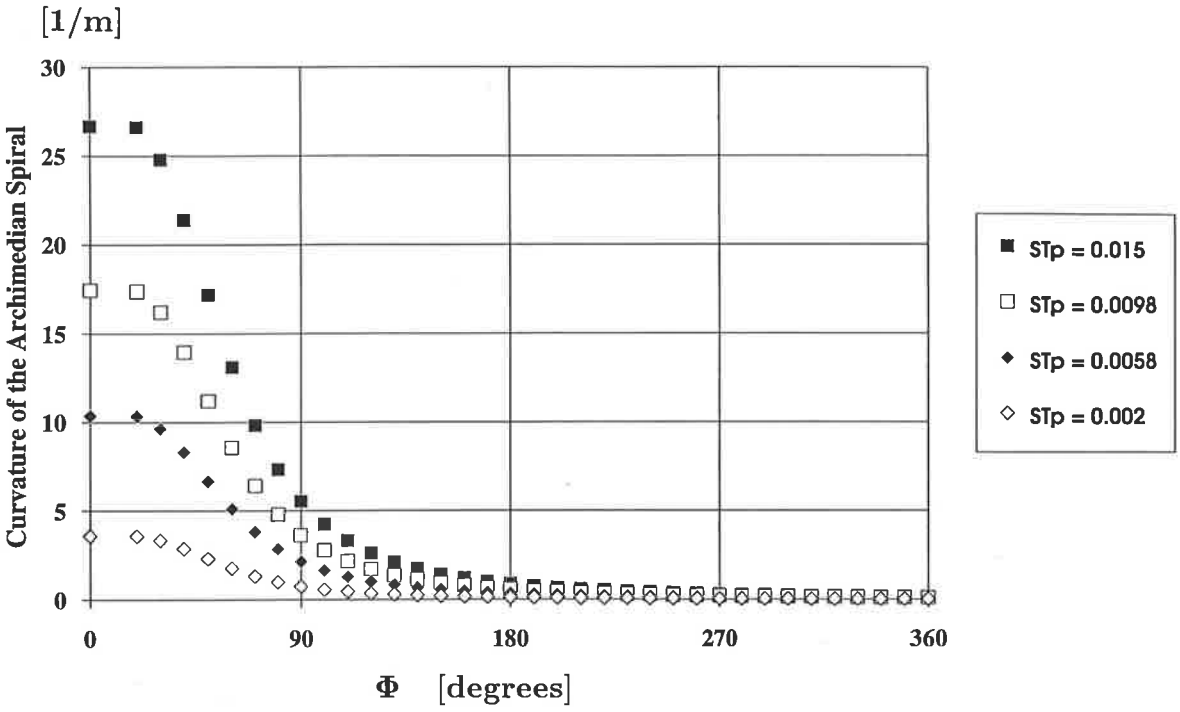

Figure 4.3: **Curvature, $\frac{1}{R} = \frac{2\pi f}{\tilde{u}_c} \cdot \frac{\Phi^2+2}{(\Phi^3+1)^{3/2}}$, of an Archimedian spiral**

(Bronstein and Semendjajew, 1981), is high in the initial part of the spiral and decreases asymptotically to zero. Figure 4.3 shows the differences in the curvature of an Archimedian spiral as a function of the angular coordinate Φ, for each of the Strouhal number flows investigated in this thesis. The trajectory of the jet, described by a projected Archimedian spiral, relative to the scale of the vortical structures in a jet, is postulated to be significant in increasing the asymmetry in the vortical structures formed in the core of the jet as the Strouhal number of precession is increased. Increased asymmetry in the phase–averaged flow results in a departure of the trajectory from the path described by a projected Archimedian spiral, as described in the following sections.

4.3 Structures in the Low Strouhal Number Regime

In the limit of zero Strouhal number, $St_p = 0$, the mechanical nozzle used in this investigation produces a simple turbulent jet (Section 3.1). When rotating the jet at a 'low' frequency of 8.05Hz, $St_p = 0.002$ (Section 3.2), and at 23.3Hz, $St_p = 0.0058$ (Appendix B), the structures produced in the potential core region (Section 4.2) group in a slightly asymmetric fashion when compared with a simple jet. As a measure of the asymmetry, the angle between the trajectory of two consecutive vortical structures at the end of the potential core can be calculated. A value of the characteristic Strouhal number for the formation of these vortical structures is selected to be 0.5 (Section 4.1.1 and Fig.4.2). If a typical exit velocity of 40m/s and the exit diameter of 10mm is used, the calculated angle between successive structures for the two frequency cases of 8.05Hz and 23.3Hz becomes 1.5^o and 4.2^o respectively. In this case the vortical puffs, or structures, line up directly behind each other so that the asymmetry in the flow is expected to be small (Fig.4.4). The experimental results confirm that there is a close similarity to a simple turbulent jet.

4.3.1 Asymmetry in the Evolution of the Vortical Structures

Figure 4.4 illustrates the evolution of vortical structures in the r–Φ plane for the low Strouhal number case. The locus of the points of maximum velocity in the phase–averaged precessing jet flow (i.e. the local jet centreline) is obtained from the experimental data presented in Section 3.2 for the flow conditions $u_e = 40$m/s, $d_e = 10$mm,

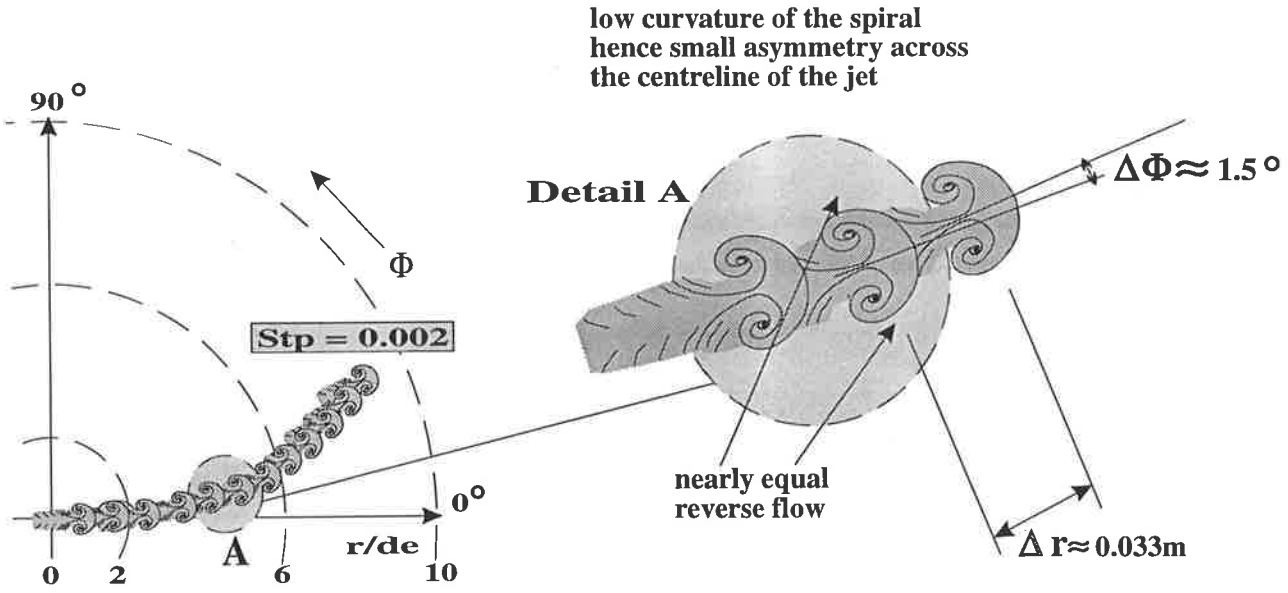

Figure 4.4: **Evolution of vortices in the low Strouhal number flow projected in the r–Φ plane (simplified sketch ignoring vortex pairing and growth)**

$\alpha_e = 45^o$. The curvature 1/R of an Archimedian spiral varies proportionally with the rotational frequency. Thus with a 'low' precessional frequency the curvature is small and the structures (Fig.4.3) line up almost as in a straight, simple turbulent jet. This leads to a small asymmetry only across the local centreline of the phase–averaged jet.

The asymmetry across the locus of the points of maximum phase–averaged velocity (i.e. the local jet centreline), may be explained in terms of two characteristics of a vortex puff structure. An isolated vortex puff consists of a toroidial core (ring focus) where the pressure is low and high vorticity is concentrated. Reverse flow can be detected on the outside of this ring–like core (see Section 1.2.2 and Fig.1.5).

To illustrate the point, consider a pearl necklace. Each pearl represents a vortex puff in a curved jet flow. With low curvature of the necklace, the pearls line up almost directly behind each other. With increasing curvature of the chain, the pearls start to touch on the inside of the curve while they are spread further apart on the outside. In the analogous flow structures, a concentration of low pressure and reverse flow on the inside of the centreline occurs, associated with attenuation of the reverse flow on the outside. That pressure gradient across the local centreline of the phase–averaged jet induces it to slow its rate of divergence from the axis of rotation and eventually, in the low Strouhal number regime in 'infinity', it approaches a helical path about the axis.

4.3.2 The Pressure Distribution

Temporally and spatially resolved pressure measurements have been conducted using the Cobra probe to quantify the pressure distribution in the PJ flow for the low Strouhal number flow case. The results of the pressure measurements using the Cobra probe technique (Section 2.4.2) are conducted with well defined boundary conditions on the flow. The phase–averaged pressure contours for the low Strouhal number case of St_p = 0.004 are presented in Figures 4.5 to 4.7 and the time–averaged pressure in Figure 4.8. In the phase–averaged pressure plots, the blue colour corresponds to a static pressure of -50Pa, whereas the green, yellow and red colour represent the progressively decreasing pressures to -80Pa. To show the relative position of the local jet, a velocity contour showing the region where $\tilde{u}_x \geq 0.5 \cdot \tilde{u}_{x,cl}$, obtained by hot–wire anemometry, is also shown in the phase–averaged contour plots for the positions x/d_e=7 and 10 (Schneider et al. 1993; Schneider et al. 1994).

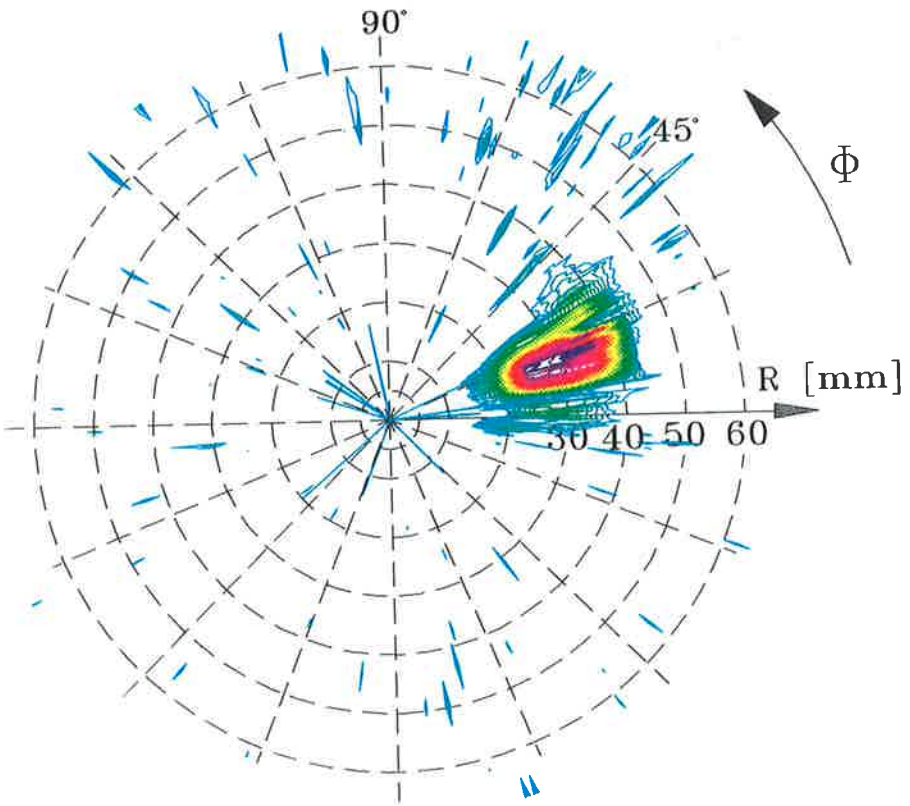

Figure 4.5: **The phase–averaged pressure field p_s–p_{atmos} <-50Pa at x/d_e=3. St_p=0.004, Re=30,000. Colour scale: blue(-50Pa) < green < yellow < red(-80Pa)**

The phase–averaged contour at x/d_e=3 (Fig.4.5) shows the jet just beyond the end of the potential core, which for these conditions ends at x/d_e=2.1. The pressure field is displayed for values of $p_s - p_{atmos} < -50$Pa. The shape of the initially round jet is hardly deformed from the elliptical cross section associated with the circular jet exiting at $\alpha_e = 45^o$ being viewed from the axial direction. A very small asymmetry in the radial direction can be detected, which is compatible with the presence of a weak low pressure region (blue) between the local jet (red, yellow and green) and its spinning axis. At this axial station the values of the low pressure in the core of the jet are between -30Pa and -70Pa, comparable with those in a simple turbulent jet (Vidakovic 1995).

Velocity Contour $\tilde{u}_x > 0.5 \cdot \tilde{u}_{x,cl}$

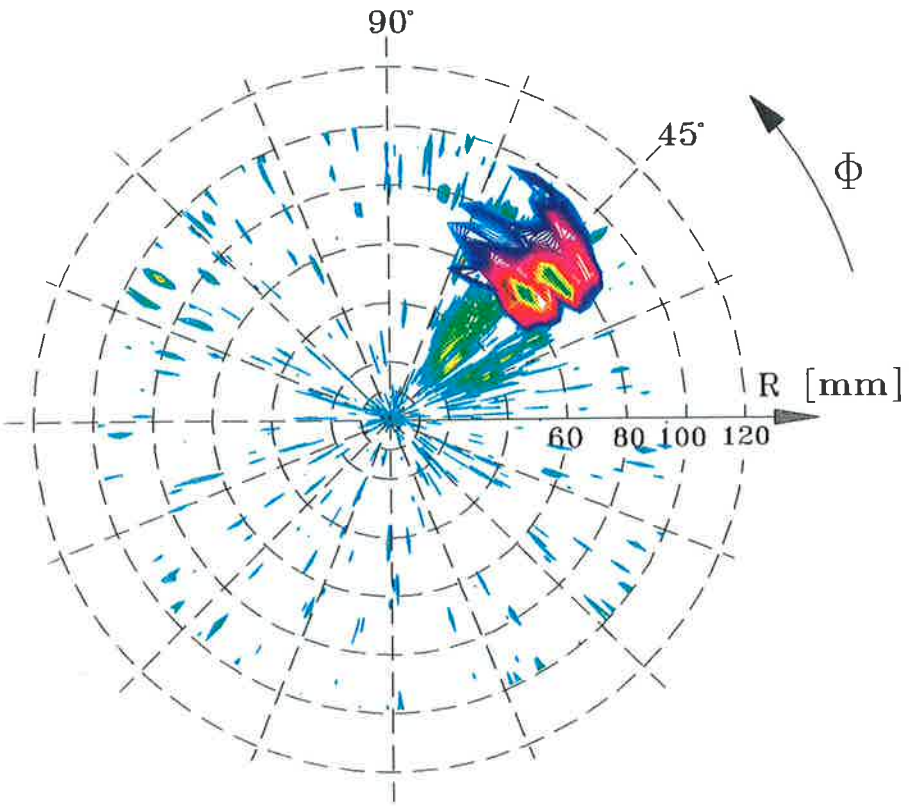

Figure 4.6: **The phase–averaged pressure field p_s–p_{atmos} <-50Pa at x/d_e=7 (velocity contour overlayed). St_p=0.004, Re=30,000. Colour scale: blue(-50Pa) < green < yellow < red(-80Pa)**

Figures 4.6 and 4.7 show the phase–averaged velocity contour overlayed on the relevant pressure field at x/d_e=7 and x/d_e=10. Again the contour of the pressure is shown for values $p_s - p_{atmos} < -50$Pa. A low pressure region between the jet and the spinning axis can be identified (green and yellow) which precesses with the same frequency as the nozzle. This low pressure core is deduced to be the cause of the small deflection of the jet towards the spinning axis relative to the Archimedian spiral (Fig.4.9).

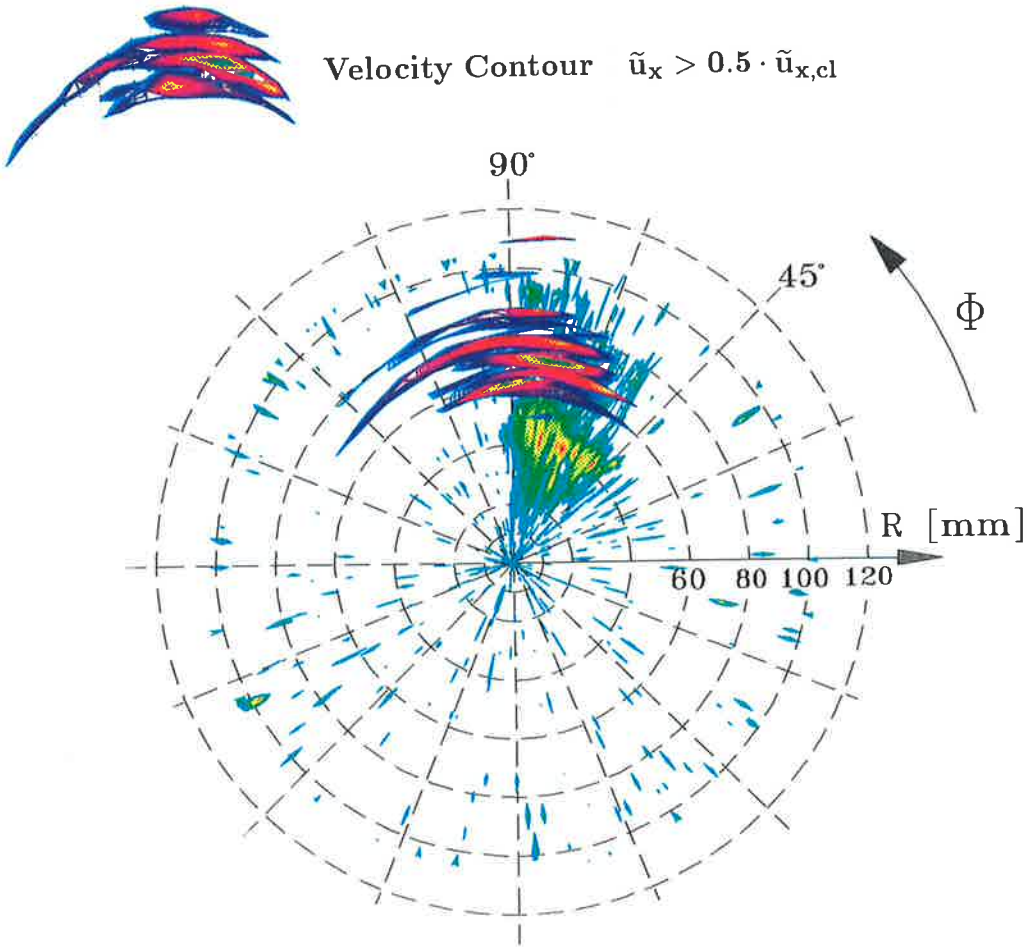

Figure 4.7: **The phase–averaged pressure field p_s–p_{atmos} <-50Pa at x/d_e=10 (velocity contour overlayed). St_p=0.004, Re=30,000. Colour scale: blue(-50Pa) < green < yellow < red(-80Pa)**

The time–averaged pressure fields at these downstream locations, normalised on the dynamic pressure p_d at the exit of the nozzle, are plotted in Figure 4.8. They confirm the presence of a low pressure region within the jet flow, which reaches its lowest value at x/d_e=6 where the relative pressure is -0.016.

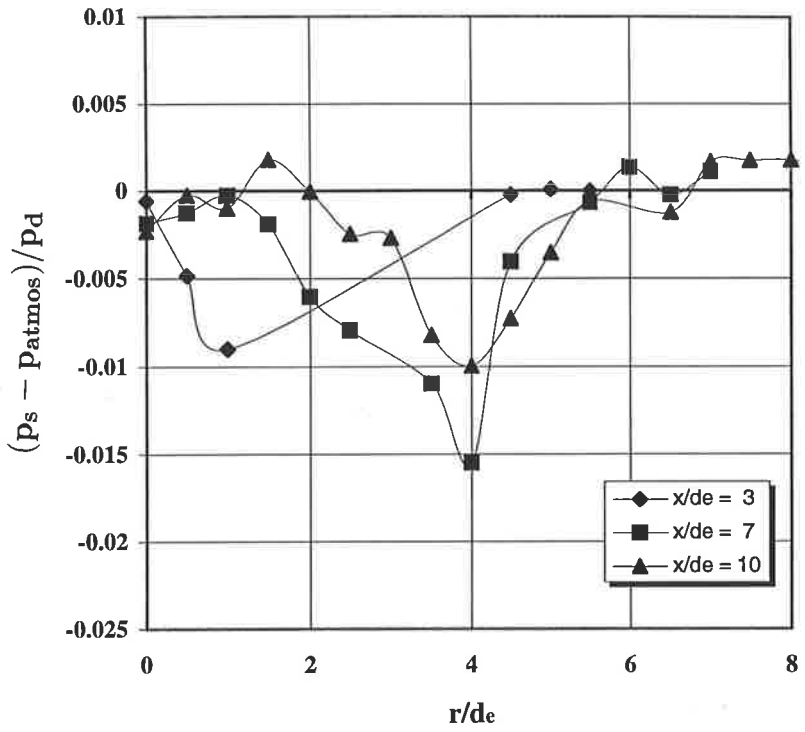

Figure 4.8: **The time–averaged pressure field in the high Strouhal number flow at x/d_e=3, 7 and 10. St_p=0.004, Re=30,000**

4.3.3 The Deflection of the Low Strouhal Number Jet

Having established the presence of a low pressure field between the phase-averaged jet and its spinning axis and deduced it to be the driving force to cause the jet to deviate from the path of the Archimedian spiral, we compare the path of the jet with the theoretical spiral curve calculated from Equation 4.1 and 4.2. The path of the jet is derived from the results of the LDA measurements presented in detail in Section 3.2 and Appendix B respectively. The comparison is shown in Figure 4.9 for two low Strouhal number jets. For a Strouhal number of St_p=0.002, the path of the local jet, defined as the locus of the points of maximum phase–averaged velocity, seems to lag the Archimedian spiral initially. This may be artificial given the approximated velocity decay of a simple jet in Equation 4.2 and the difficulty of defining the precise centreline of the

jet. With increasing Strouhal number the deviation of the phase–averaged jet from the relevant Archimedian spiral increases. In the flow with St_p=0.0058, the effect of the low pressure region, shown in Figures 4.5 to 4.7 is evident. The centreline of the local jet is deflected towards the axis of rotation relative to the Archimedian spiral, with the strongest deflection being in the region immediately downstream from the potential core.

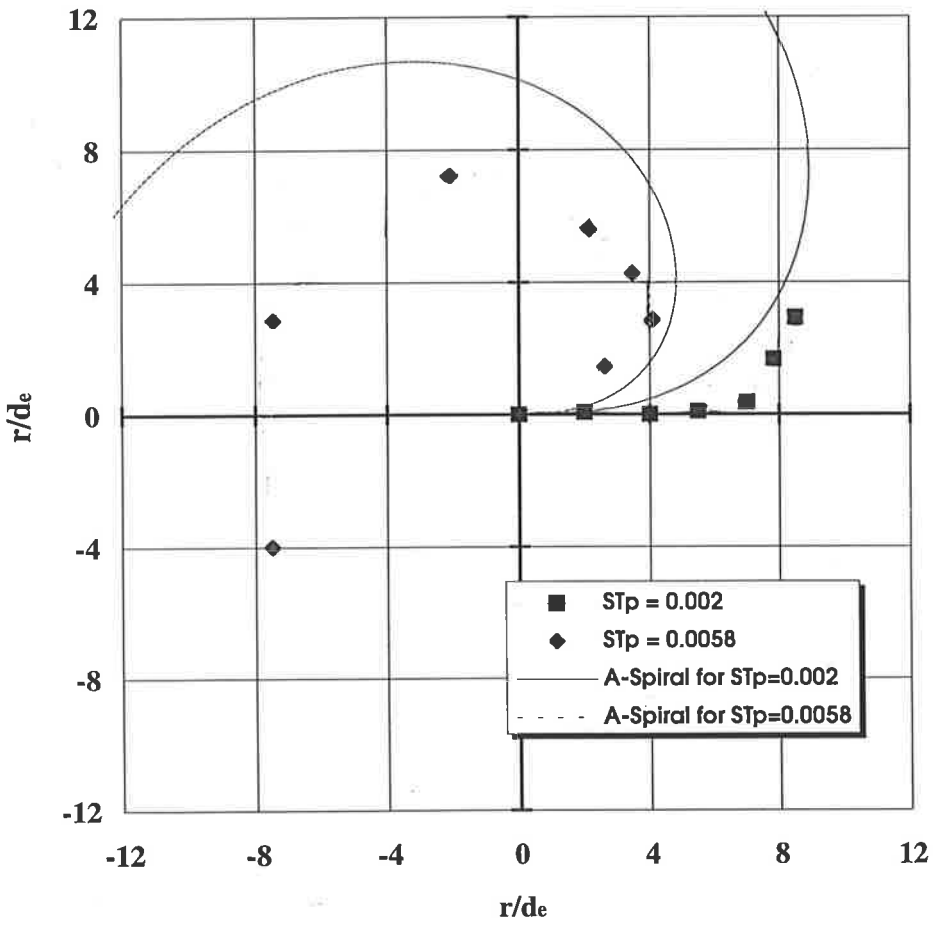

Figure 4.9: **Deviation of the locus of the points of maximum phase–averaged velocity in the precessing jet relative to the path of a projected Archimedian spiral in two low Strouhal number flows**

Figure 4.10 displays a cross section in the x–r plane through a low Strouhal number jet. It shows that the effect of precession on the jet is initially small and that the jet trajectory is hardly deflected from its original 45° exit angle. It can be deduced that the formation of vortical structures occurs almost in a straight line, so that the pressure distribution across the local centreline of the jet is almost symmetrical. Figure 4.10 confirms the similarity of the low Strouhal number PJ flow to a simple turbulent jet, where the shear in the jet supports the evolving vortical structures.

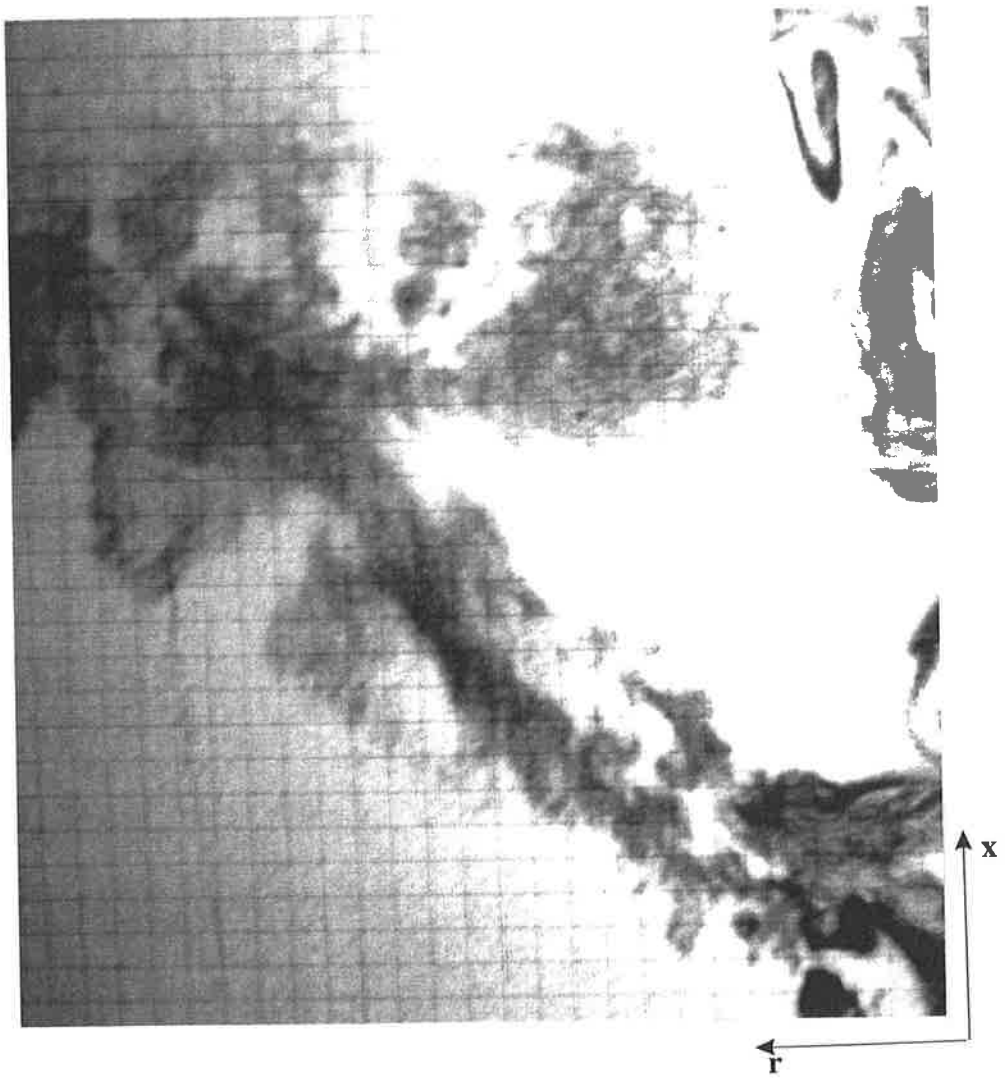

Figure 4.10: **Laser sheet flow visualisation of a low Strouhal number jet, using Glycol vapour to mark the jet. The light sheet is in the x–r plane and the exit conditions are: Re=26,600, St_p=0.002**

particles, appearing black on the negative picture. The jet is not significantly deformed from its original circular cross–section. It appears elliptical due to the 45° inclination relative to the laser sheet in the r–Φ plane.

4.3.4 Frequency Spectra in a Low Strouhal Number Jet

Two regions have been identified in the low Strouhal number jet, the potential core region and the region where the frequency of precession is the dominant frequency in the flow (Section 4.1). To confirm that the jet does not lose its structural coherence with axial distance, frequency spectra have been derived from hot–wire anemometer measurements. The hot–wire was placed at the radial distance from the nozzle axis which corresponds to the location of the maximum velocity at that particular axial position. A total number of 40,960 samples were taken, corresponding to 320 cycles of precession. The data were recorded with a sampling rate of 1000Hz, using an anti–aliasing filter set at 500Hz.

From the spectra shown in Figure 4.12 it can be seen that only one dominant frequency and its harmonics can be identified over the whole frequency band. This frequency corresponds to the frequency of precession and is apparent even in the far field of the jet at x/d_e=40. No other structures at other frequencies are detectable.

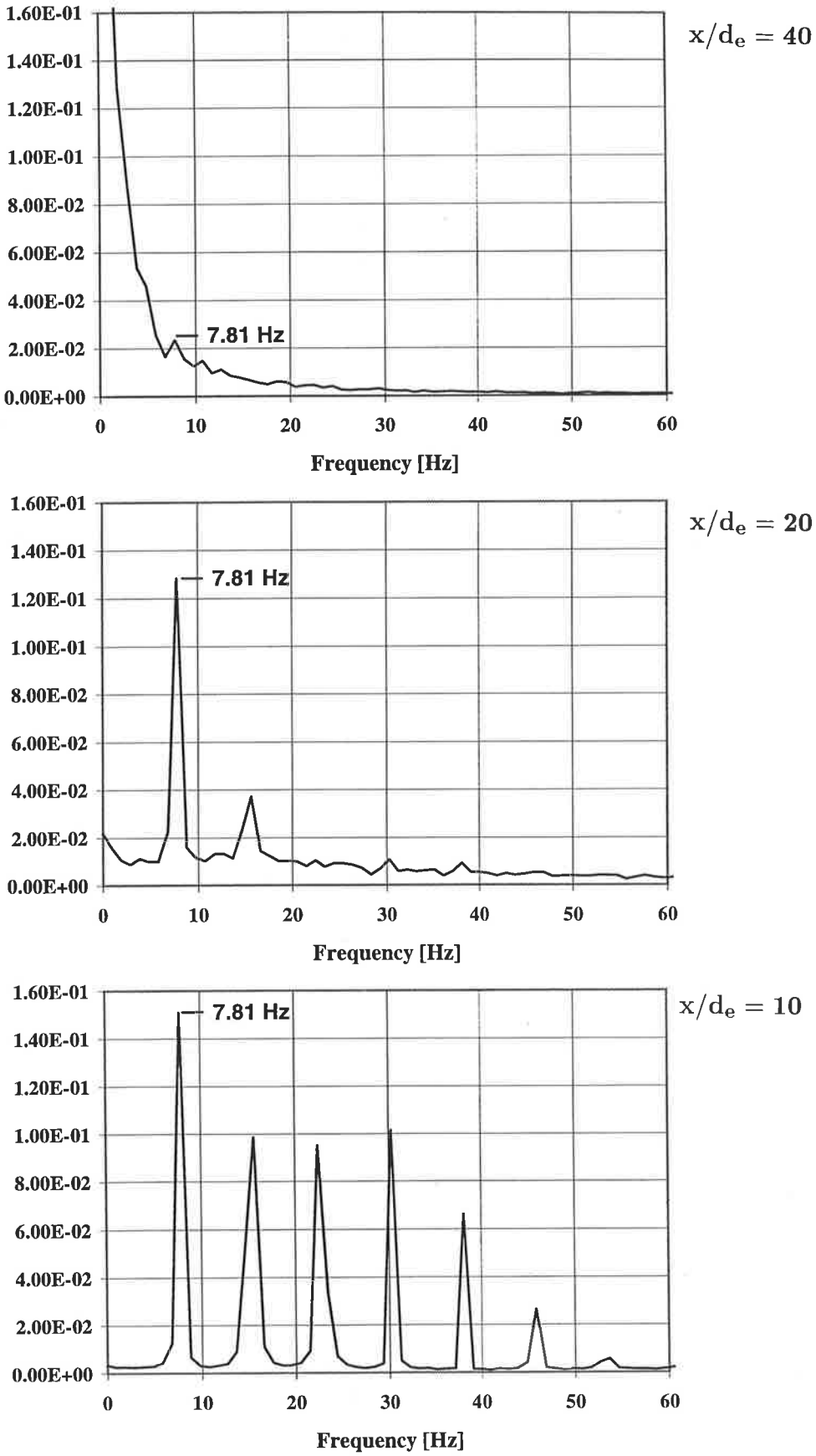

Figure 4.12: **Frequency spectrum on the jet centreline at x/d_e=10, 20 and 40**

4.4 Structures in the High Strouhal Number Regime

In the high Strouhal number regime, e.g. at St_p =0.0098 (Appendix C) and 0.015 (Section 3.3) as examined here, the vortex puffs tend to form at almost adjacent locations rather than one behind the other. This is due to the high curvature of the projected Archimedian spiral (Fig. 4.3). In this way the turbulent puffs are more 'isolated'. For the two Strouhal number cases examined here, the momentum source of the jet turns by 7.2° and 11° respectively in the time between the formation of consecutive structures at the end of the potential core of the jet. This angle is larger than the half width of a simple turbulent jet, which was found by Wygnanski and Fiedler (1969) to be 4.9°. Thus the structures are not supported by the shear produced with the jet acting as the momentum source, but are in fact in conflict with each other due to the opposite orientation of the vorticity on each side of the structures. While it is unlikely that the primary structures are truly isolated, since they are connected through the streamwise vortices being wrapped around the azimuthal rings (Liepmann and Gharib, 1992), here we concentrate on the primary vortex rings.

4.4.1 Asymmetry in the Evolution of the Vortical Structures

The 'isolated' primary structures have some similarities to a turbulent vortex ring or puff. Figure 4.13 illustrates the evolution of these vortices in the r–Φ plane for the high Strouhal number regime. The plot compares the trajectory of a projected Archimedian spiral, calculated from Equations 4.1 and 4.2, with the locus of points of maximum phase–averaged velocity obtained by LDA measurements. For these data the exit conditions from the nozzle were u_e = 40m/s, f_p = 39.1Hz and f_p = 59.1Hz, d_e = 10mm,

$\alpha_e = 45°$, corresponding to Strouhal numbers of precession $St_p = 0.0098$ and 0.015. Each individual structure leaves the mechanical nozzle on the axis of rotation (x–axis). Thus, the vortices do not exit with a tangential velocity component. Figure 4.13 shows the position of each vortex puff, ignoring pairing and growth, based on the trajectory of the projected Archimedian spiral so that the orientation of each structure is directed towards the centre of rotation. The high curvature of the Archimedian spirals (Fig.4.3) creates a much higher degree of asymmetry relative to the local phase-averaged jet centreline than occurs in the low Strouhal number case.

Following the illustration of the pearl necklace introduced earlier, it can be seen that as the necklace (Archimedian spiral) is curved more and more, the pearls (vortex puffs) touch each other on the inside of the bend, while on the outside the gaps are widened. For the puffs it means that the concentration of low pressure and reverse flow is amplified on the inside of the bend and attenuated on the outside. The asymmetry relative to the local axis of the jet, marked as the trajectory of the phase–averaged maximum velocity, is much higher than that of the low Strouhal number flow and leads to an asymmetry in the pressure field.

The asymmetry in the pressure field relative to the trajectory of the jet predicted by the projected Archimedian spiral is consistent with the development of a recirculation zone with increasing Strouhal number of precession. The recirculation flow zone is located in the region between the emerging jet and its spinning axis in the time– and phase–averaged domains (Section 3.3.2). Since it is associated with the reverse flow of the jet structures, it rotates with the same frequency as the nozzle.

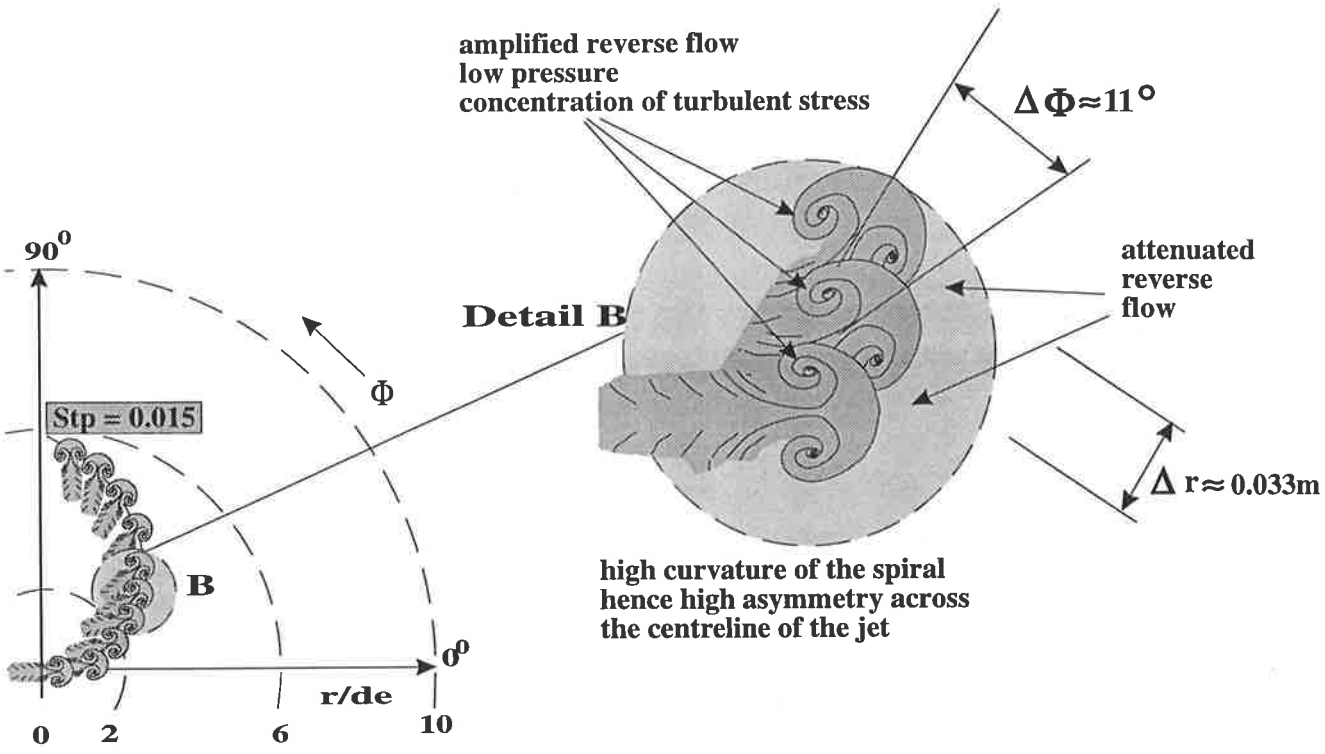

Figure 4.13: **Evolution of vortices in the high Strouhal number flow projected in the r–Φ plane (simplified sketch ignoring vortex pairing and growth)**

4.4.2 The Pressure Distribution

To measure the asymmetry in the rotating pressure field, the Cobra probe (Section 2.4.2) has been used with the nozzle operating in the low velocity windtunnel (Section 2.2). Figure 4.14 shows the phase–averaged pressure contour at $x/d_e = 2$, which is in the precession dominated region. The time–averaged pressure in the region $2 < x/d_e < 6$, where reverse flow is detected, is shown in Figure 4.15.

In the phase–averaged contour at x/d_e=2 a strong (dark) region between the jet and the spinning axis is apparent. This low pressure core ($p_s - p_{atmos} < -200$Pa) causes a high deflection of the jet toward the x–axis (Fig.4.16).

The time–averaged pressure field, shown in Figure 4.15, is normalised on the dynamic pressure at the exit of the nozzle. At x/d_e=2 the low dimensionless pressure in the

jet ($1.7 < r/d_e < 2.3$) is -0.018, whereas the low pressure core found in the phase–averaged contour ($0.5 < r/d_e < 1.5$), displays values down to -0.03. A similar pressure distribution is found at x/d_e=4, with the pressure in the jet ($3.7 < r/d_e < 5.3$) being -0.012, whereas the low pressure core ($1 < r/d_e < 2$) shows a minimum value of -0.03. At x/d_e=6 the low dimensionless pressure between the jet and the axis of rotation is weaker with a minimum value of -0.22. The axial distance corresponds to the end of the region of maximum deflection.

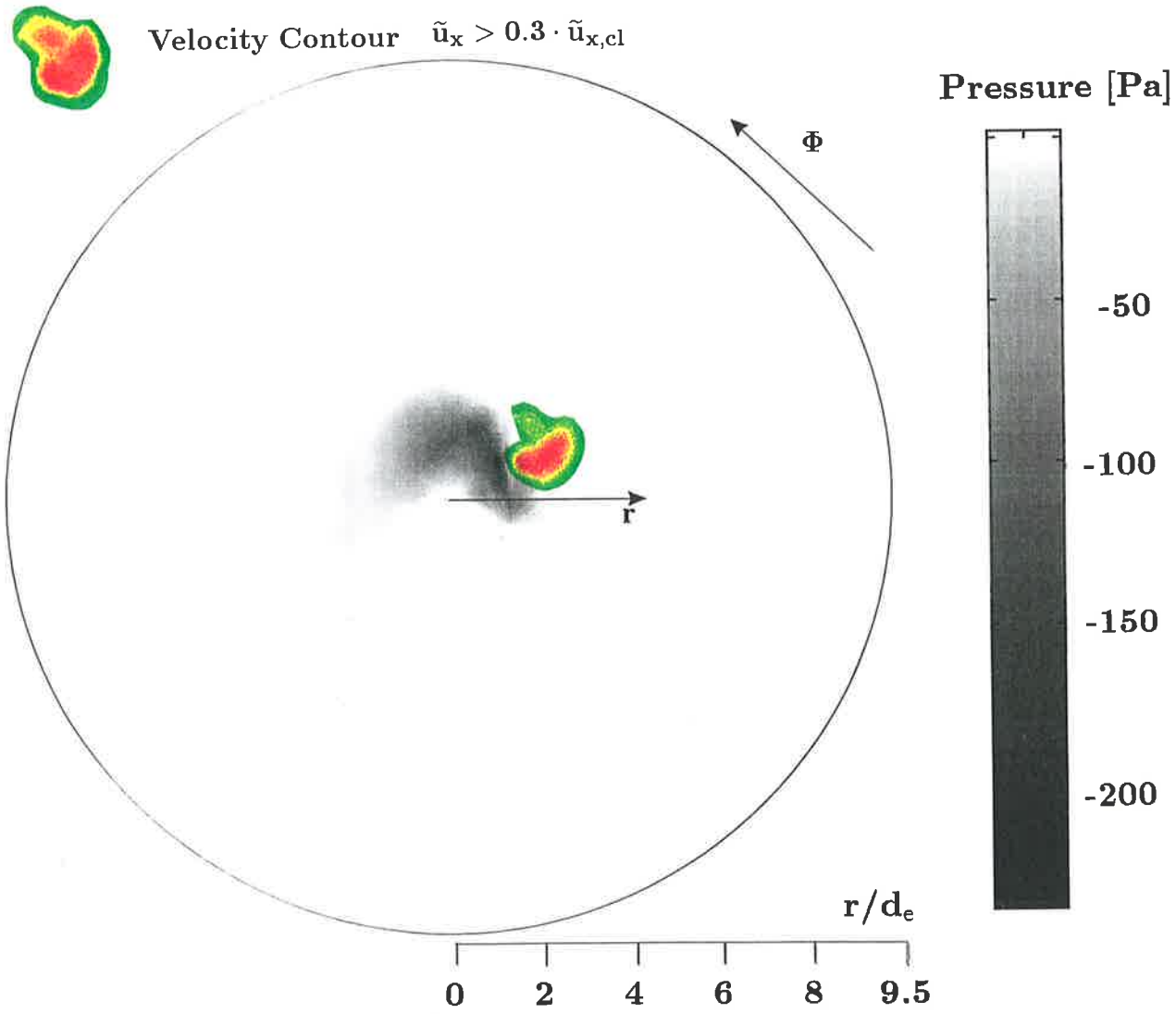

Figure 4.14: **The phase–averaged pressure field in the high Strouhal number flow at x/d_e=2 (overlayed contour of the jet). St_D=0.015, Re=26,600**

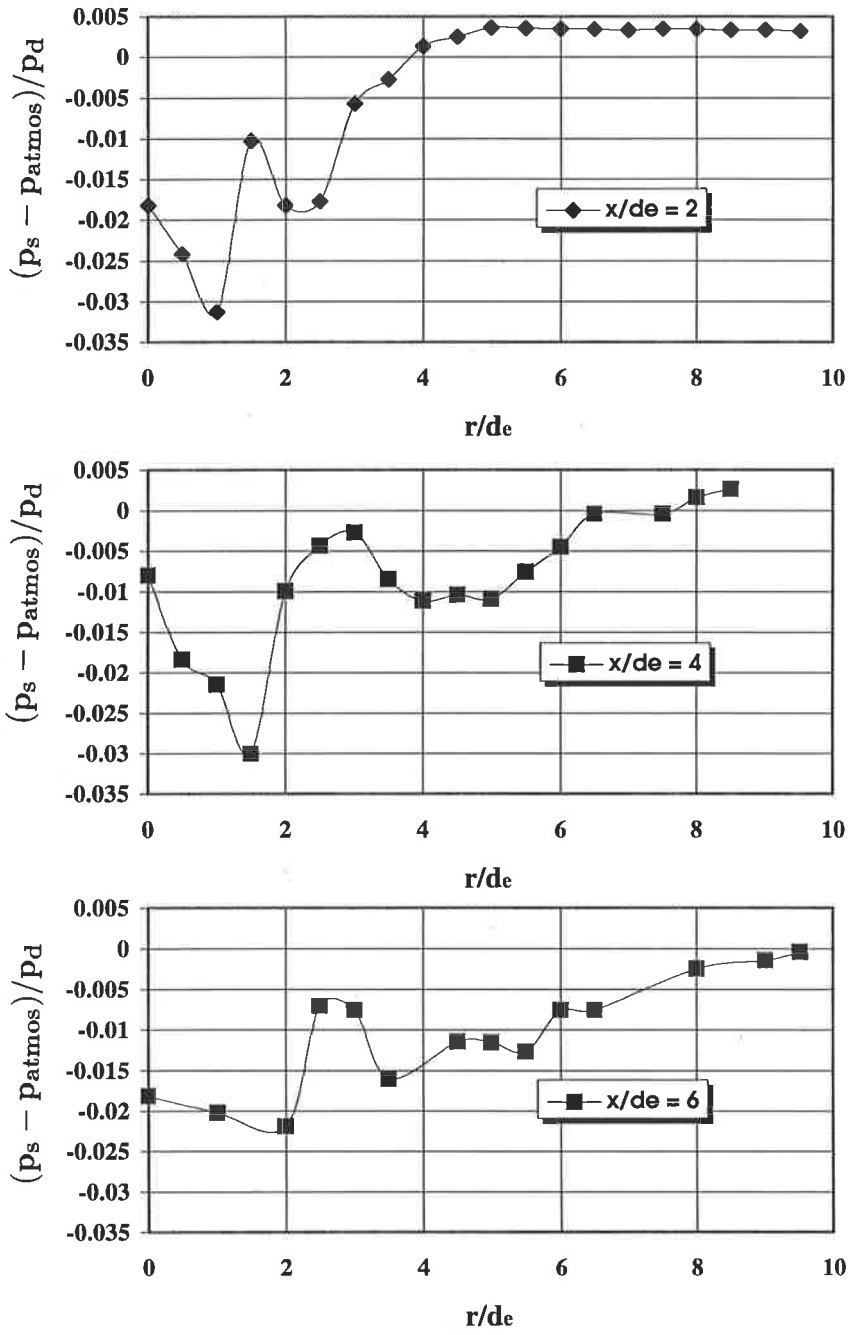

Figure 4.15: **The time–averaged pressure field in the high Strouhal number flow at x/d_e=2, 4 and 6. St_p=0.015, Re=26,600**

4.4.3 The Deflection of the High Strouhal Number Jet

The pressure gradients in the flow field lead to the deflection of the streamlines towards the radially inward and tangentially backward directions (Fig.3.57 and Fig.3.58), creating an azimuthal velocity component. The curvature of the streamlines and the locus of the maximum velocity of the phase–averaged jet are related to the pressure force and the low pressure core between the jet and its spinning axis.

Figure 4.16 illustrates the deviation of the locus of the maximum phase–averaged velocity, from the projected Archimedian spiral as calculated from Equations 3.1 and 3.2. The data for the jet trajectory was obtained from the LDA measurements described in Section 3.3. In both Strouhal number cases, the spiral path does not predict the results found in the experiments. The asymmetry across the centreline of the jet increases with increasing Strouhal number of precession. The increasing pressure gradient forces the trajectory of phase–averaged jet into increasingly tighter spirals than are predicted by the equations for the Archimedian spiral.

Figure 4.17 shows a cross section through a high Strouhal number jet in the x–r plane. It shows an 'isolated' vortical structure (1), which resembles a vortex puff of the type presented by Glezer and Coles (1990). The second vortex puff (2) in the light sheet appears to have originated from a previous cycle and has clearly been forced inwards by the low pressure region between the emerging jet and the spinning axis. The low celerity of the structures causes them to move very close to each other, which increases the reverse flow region between them (as illustrated in Fig.4.17).

A view of the jet fluid illuminated by a laser sheet in the r–Φ plane shows a turbulent puff within a precessing jet flow (Fig.4.18). That figure shows a sequence spanning about half a cycle of precession recorded with a HICAM film camera (Section 2.3.2). The sheet, at x/d_e=4, is located just downstream from the potential core of the jet and shows a primary vortex ring break up into a turbulent puff and the development of a turbulent tail, which is deduced to be illuminated by scattered light. No influence by one structure to another is observed, which supports the contention that they are relatively isolated. The turbulent puffs in the r–Φ plane follow the spiral path presented in Figure 4.16 for the high Strouhal number case of St_p=0.015.

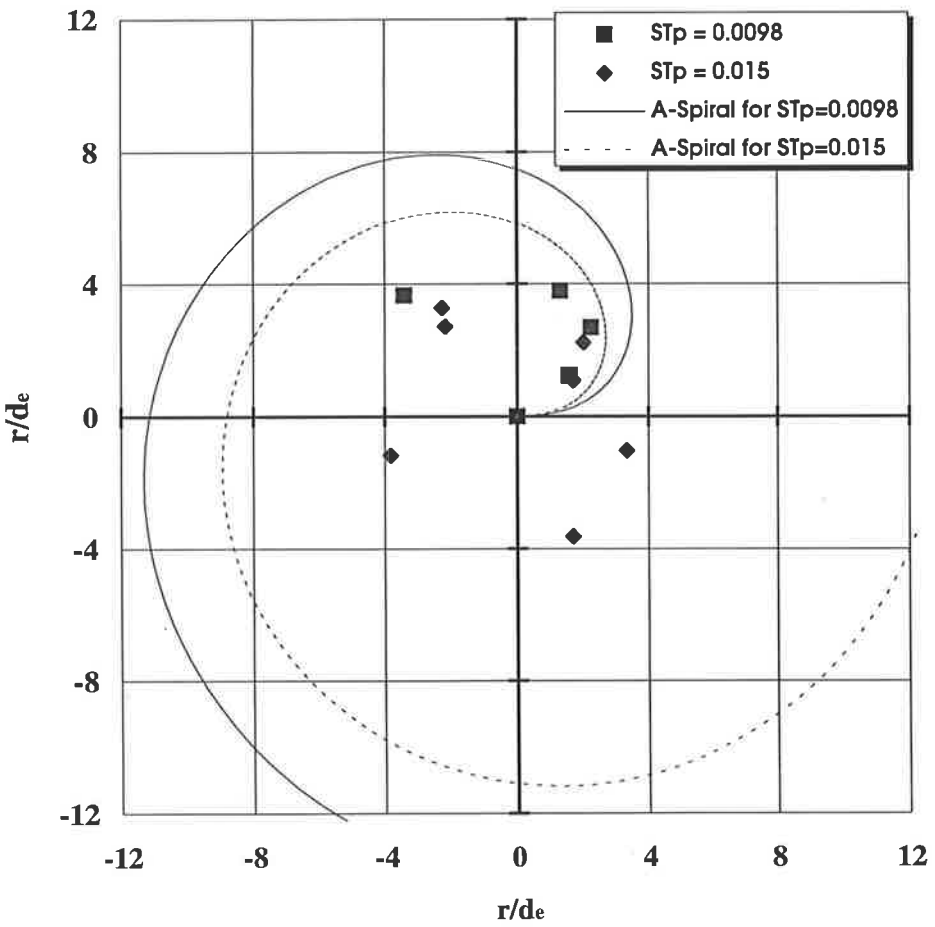

Figure 4.16: **Deviation of the locus of the points of maximum phase–averaged velocity in the precessing jet relative to the path of a projected Archimedian spiral in two high Strouhal number flows**

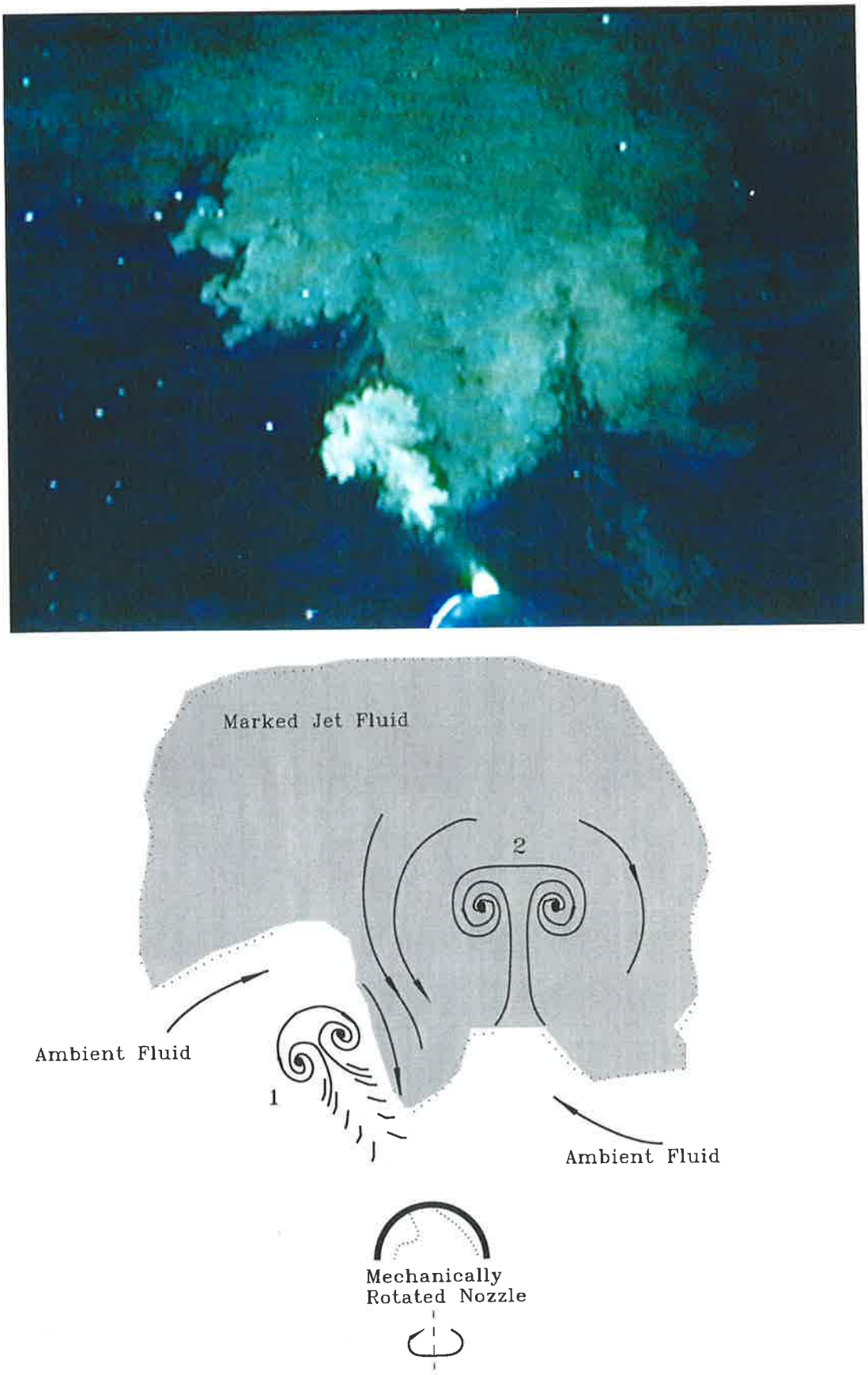

Figure 4.17: **Laser induced fluorescence in a water tank showing vortical structures generated with a high Strouhal number precessing jet flow: Note 'isolated' vortex structures (1) and (2). St_p=0.015, Re=26,600**

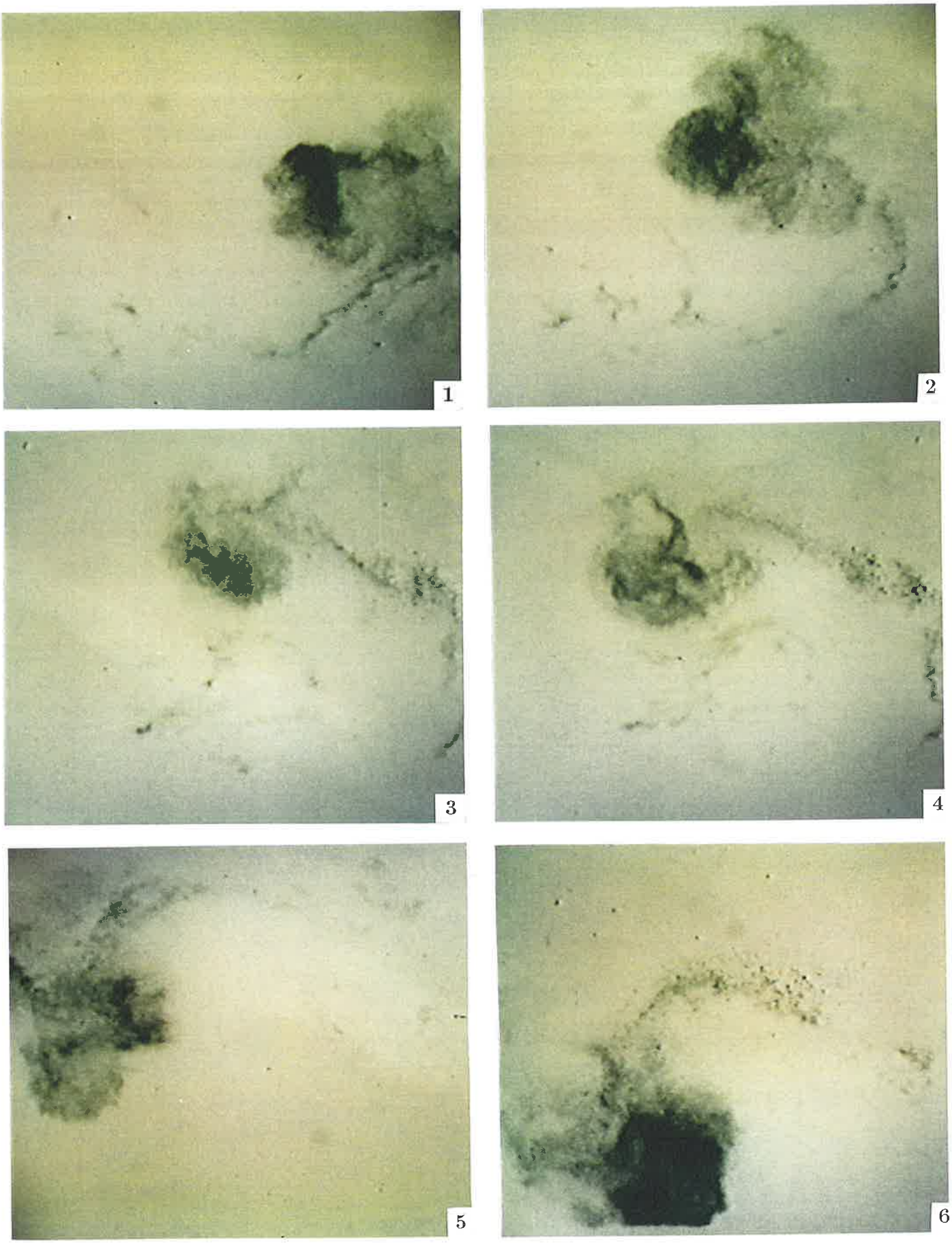

Figure 4.18: **A time–sequence of vortex structures through half a cycle of precession for a high Strouhal number flow. The light sheet is in the r–Φ plane at x/d_e=4. St_p=0.015, Re=26,600**

4.4.4 Frequency Spectra in the High Strouhal Number Jet

To confirm that the jet precession does not continue to dominate the high Strouhal number flow for distances $x/d_e > 6$, hot–wire anemometry is applied to obtain frequency spectra in the region of highest velocity in the jet at the axial distances x/d_e=10, 20 and 40. The same experimental conditions are applied as in the low Strouhal number flow. Again a total number of 40,960 samples were taken, which enabled 320 cycles of precession to be recorded. The sampling rate was 1000Hz and an anti–aliasing filter was set at 500Hz.

Figure 4.19 confirms that at x/d_e=10 there is no preferred frequency detectable. An expected peak at the frequency of precession of 40Hz does not appear above the 'noise' level of the spectrum and no other obvious peak is detectable. This supports the definition in Section 4.1 of the third region in the high Strouhal number flow. The jet flow becomes axisymmetric and no jet or vortex puff structure can be detected.

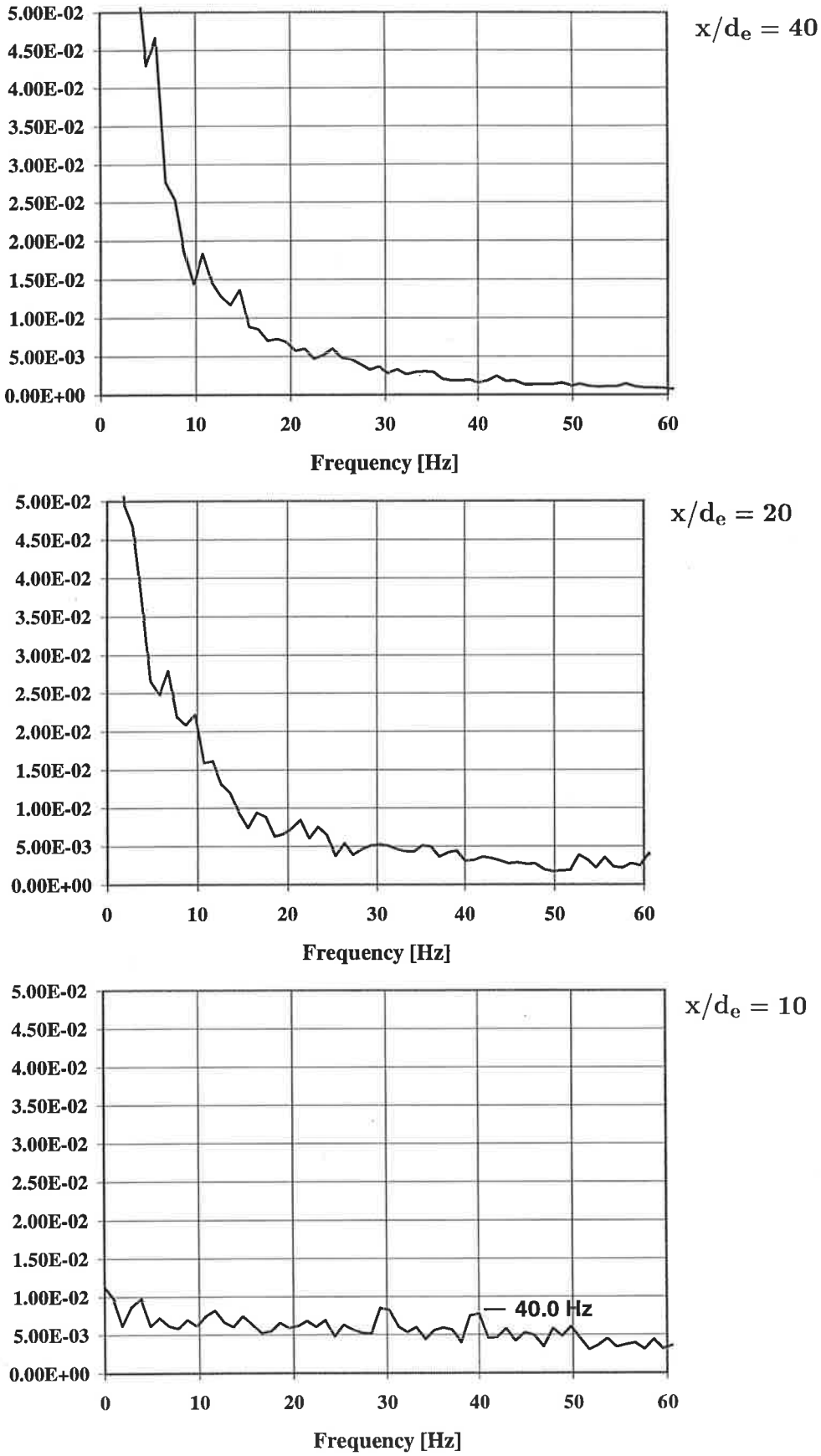

Figure 4.19: **Frequency spectrum on the jet centreline at x/d_e=10, 20 and 40**

4.5 Conclusions

The motion and the deflection of the vortical structures in the flow produced by a precessing jet are strongly dependent on the Strouhal number of precession. The low Strouhal number jet (St_p <5 to 6) is defined to be such that the deflection of the jet in negative r and positive tangential direction is insignificant. The insignificant deflection is associated with a small pressure gradient only between the jet and the spinning axis. The vortical structures remain similar to those in a simple turbulent jet, and are not strongly influenced by the jet precession. The jet as a momentum source supports the shear and the vortex puffs maintain their structure.

In the high Strouhal number flow (St_p > 6 to 7) the deflection of the locus of the maximum velocity is large. The vortex structures become 'isolated' vortex puffs. These puffs are deflected inwards (negative r–direction) and in the positive tangential direction. A low pressure core and a recirculation zone is developed bewteen the jet and its spinning axis. The vortical structures lose their 'identity' at x/d_e=8. No preferred frequency has been detected by a single point frequency spectrum in the far field of the jet and the precessing jet flow field becomes axisymmetric.

The mathematical model of an Archimedian spiral has shown reasonable agreement with the trajectory of the precessing jet in the low Strouhal number regime. However, the model fails to describe the behaviour of the jet in the high Strouhal number flow, due to changes in the pressure gradients which deflect the jet towards the axis of rotation. In the next Chapter an analytical evaluation, rather than a mathematical model, is used to describe the Strouhal dependency of the precessing jet.

Chapter 5

Analytical Evaluation of the Strouhal number Influence

The previous sections found the Strouhal number of precession to be the determining parameter in the precessing jet flow field. This is certainly found for the region after the potential core, where the flow field is truly time-dependent, three-dimensional and turbulent. An attempt is made in this section to determine if this behaviour is driven by the turbulent mixing field or is inherent within the Navier–Stokes equations of motion.

5.1 The Turbulent, Time–Dependent, Three–Dimensional Navier–Stokes Equations

5.1.1 The Laminar Equations of Motion

The Navier–Stokes equations for a laminar precessing jet flow in a cylindrical coordinate system are

$$\begin{aligned}\frac{\partial u_r}{\partial t} &+ u_r \cdot \frac{\partial u_r}{\partial r} + \frac{u_\Phi}{r} \cdot \frac{\partial u_r}{\partial \Phi} + u_x \cdot \frac{\partial u_r}{\partial x} - \frac{u_\Phi^2}{r} = -\frac{\partial p}{\rho \partial r} \\ &+ \nu \left[\frac{\partial^2 u_r}{\partial r^2} + \frac{1}{r} \cdot \frac{\partial u_r}{\partial r} - \frac{u_r}{r^2} + \frac{1}{r^2} \cdot \frac{\partial^2 u_r}{\partial \Phi^2} - \frac{2}{r^2} \cdot \frac{\partial u_\phi}{\partial \Phi} + \frac{\partial^2 u_r}{\partial x^2} \right] \end{aligned} \tag{5.1}$$

$$\begin{aligned}\frac{\partial u_\Phi}{\partial t} &+ u_r \cdot \frac{\partial u_\Phi}{\partial r} + \frac{u_r u_\Phi}{r} + \frac{u_\Phi}{r} \cdot \frac{\partial u_\Phi}{\partial \Phi} + u_x \cdot \frac{\partial u_\Phi}{\partial x} = -\frac{1}{r} \cdot \frac{\partial p}{\rho \partial \Phi} \\ &+ \nu \left[\frac{\partial^2 u_\Phi}{\partial r^2} + \frac{1}{r} \cdot \frac{\partial u_\Phi}{\partial r} - \frac{u_\Phi}{r^2} + \frac{1}{r^2} \cdot \frac{\partial^2 u_\Phi}{\partial \Phi^2} + \frac{2}{r^2} \cdot \frac{\partial u_r}{\partial \Phi} + \frac{\partial^2 u_\Phi}{\partial x^2} \right] \end{aligned} \tag{5.2}$$

$$\begin{aligned}\frac{\partial u_x}{\partial t} &+ u_r \cdot \frac{\partial u_x}{\partial r} + \frac{u_\Phi}{r} \cdot \frac{\partial u_x}{\partial \Phi} + u_x \cdot \frac{\partial u_x}{\partial x} = -\frac{\partial p}{\rho \partial x} \\ &+ \nu \left[\frac{\partial^2 u_x}{\partial r^2} + \frac{1}{r} \cdot \frac{\partial u_x}{\partial r} + \frac{1}{r^2} \cdot \frac{\partial^2 u_x}{\partial \Phi^2} + \frac{\partial^2 u_x}{\partial x^2} \right] \end{aligned} \tag{5.3}$$

In these equations the external forces such as gravity etc. are neglected.

The continuity equation is

$$\frac{\partial u_r}{\partial r} + \frac{u_r}{r} + \frac{1}{r} \cdot \frac{\partial u_\Phi}{\partial \Phi} + \frac{\partial u_x}{\partial x} = 0$$

5.1.2 The fully turbulent three-dimensional Equations of Motion

To expand the equations to the fully turbulent form, u_i is replaced with $\tilde{u}_i + u_i'$ and p with $\tilde{p} + p'$, where the values $\tilde{}$ represent the phase mean values and the $'$ represent the phase mean fluctuating componets. Reynolds averaging with the following rules (Hinze 1959)

$$\begin{aligned}
\widetilde{u'_i} &= 0 \\
\widetilde{u'_i} &= \widetilde{\tilde{u}_i + u'_i} = \tilde{u}_i \\
\widetilde{\tilde{u}_i \tilde{u}_j} &= \tilde{u}_i \tilde{u}_j \\
\widetilde{\tilde{u}_i u'_j} &= 0
\end{aligned}$$

leads to the fully turbulent Navier–Stokes equations in a cylindrical coordinate system:

$$\begin{aligned}
\frac{\partial u_r}{\partial t} &+ u_r \cdot \frac{\partial u_r}{\partial r} + \frac{u_\Phi}{r} \cdot \frac{\partial u_r}{\partial \Phi} + u_x \cdot \frac{\partial u_r}{\partial x} - \frac{u_\Phi^2}{r} - \frac{\widetilde{u_\Phi'^2}}{r} = -\frac{\partial p}{\rho \partial r} \\
&+ \nu \left[\frac{\partial^2 u_r}{\partial r^2} + \frac{1}{r} \cdot \frac{\partial u_r}{\partial r} - \frac{u_r + u'_r}{r^2} + \frac{1}{r^2} \cdot \frac{\partial^2 u_r}{\partial \Phi^2} - \frac{2}{r^2} \cdot \frac{\partial u_\phi}{\partial \Phi} + \frac{\partial^2 u_r}{\partial x^2} \right] \\
&- \left[\frac{\widetilde{\partial u_r'^2}}{\partial r} + \frac{\widetilde{\partial u'_r u'_\Phi}}{r \partial \Phi} + \frac{\widetilde{\partial u'_r u'_x}}{\partial x} \right]
\end{aligned} \tag{5.4}$$

$$\begin{aligned}
\frac{\partial u_\Phi}{\partial t} &+ u_r \cdot \frac{\partial u_\Phi}{\partial r} + \frac{u_\Phi}{r} \cdot \frac{\partial u_\Phi}{\partial \Phi} + u_x \cdot \frac{\partial u_\Phi}{\partial x} + \frac{u_r u_\Phi}{r} + 2 \cdot \frac{\widetilde{u'_\Phi u'_r}}{r} = -\frac{1}{r} \cdot \frac{\partial p}{\rho \partial \Phi} \\
&+ \nu \left[\frac{\partial^2 u_\Phi}{\partial r^2} + \frac{1}{r} \cdot \frac{\partial u_\Phi}{\partial r} - \frac{u_\Phi + u'_\Phi}{r^2} + \frac{1}{r^2} \cdot \frac{\partial^2 u_\Phi}{\partial \Phi^2} + \frac{2}{r^2} \cdot \frac{\partial u_r}{\partial \Phi} + \frac{\partial^2 u_\Phi}{\partial x^2} \right] \\
&- \left[\frac{\widetilde{\partial u'_\Phi u'_r}}{\partial r} + \frac{\widetilde{\partial u_\Phi'^2}}{r \partial \Phi} + \frac{\widetilde{\partial u'_\Phi u'_x}}{\partial x} \right]
\end{aligned} \tag{5.5}$$

$$\frac{\partial u_x}{\partial t} + u_r \cdot \frac{\partial u_x}{\partial r} + \frac{u_\Phi}{r} \cdot \frac{\partial u_x}{\partial \Phi} + u_x \cdot \frac{\partial u_x}{\partial x} = -\frac{\partial p}{\rho \partial x}$$
$$+ \nu \left[\frac{\partial^2 u_x}{\partial r^2} + \frac{1}{r} \cdot \frac{\partial u_x}{\partial r} + \frac{1}{r^2} \cdot \frac{\partial^2 u_x}{\partial \Phi^2} + \frac{\partial^2 u_x}{\partial x^2} \right]$$
$$- \left[\frac{\partial \widetilde{u'_x u'_r}}{\partial r} + \frac{\partial \widetilde{u'_x u'_\Phi}}{r \partial \Phi} + \frac{\partial \widetilde{u'^2_x}}{\partial x} \right] \qquad (5.6)$$

The high Reynolds number of 26,600 in the present investigation (Section 3) leads to the assumption that the viscous terms can be neglected, as would be the case in a simple turbulent jet (Abramovich 1963). This postulate will be examined in detail in Section 5.2 for the precessing jet flow. Neglecting the viscous terms in the Navier–Stokes equations leads to

$$\frac{\partial u_r}{\partial t} + u_r \cdot \frac{\partial u_r}{\partial r} + \frac{u_\Phi}{r} \cdot \frac{\partial u_r}{\partial \Phi} + u_x \cdot \frac{\partial u_r}{\partial x} - \frac{u_\Phi^2}{r} - \frac{\widetilde{u'^2_\Phi}}{r}$$
$$= -\frac{\partial p}{\rho \partial r} - \left[\frac{\partial \widetilde{u'^2_r}}{\partial r} + \frac{\partial \widetilde{u'_r u'_\Phi}}{r \partial \Phi} + \frac{\partial \widetilde{u'_r u'_x}}{\partial x} \right] \qquad (5.7)$$

$$\frac{\partial u_\Phi}{\partial t} + u_r \cdot \frac{\partial u_\Phi}{\partial r} + \frac{u_\Phi}{r} \cdot \frac{\partial u_\Phi}{\partial \Phi} + u_x \cdot \frac{\partial u_\Phi}{\partial x} + \frac{u_r u_\Phi}{r} + 2 \cdot \frac{\widetilde{u'_\Phi u'_r}}{r}$$
$$= -\frac{1}{r} \cdot \frac{\partial p}{\rho \partial \Phi} - \left[\frac{\partial \widetilde{u'_\Phi u'_r}}{\partial r} + \frac{\partial \widetilde{u'^2_\Phi}}{r \partial \Phi} + \frac{\partial \widetilde{u'_\Phi u'_x}}{\partial x} \right] \qquad (5.8)$$

$$\frac{\partial u_x}{\partial t} + u_r \cdot \frac{\partial u_x}{\partial r} + \frac{u_\Phi}{r} \cdot \frac{\partial u_x}{\partial \Phi} + u_x \cdot \frac{\partial u_x}{\partial x}$$
$$= -\frac{\partial p}{\rho \partial x} - \left[\frac{\partial \widetilde{u'_x u'_r}}{\partial r} + \frac{\partial \widetilde{u'_x u'_\Phi}}{r \partial \Phi} + \frac{\partial \widetilde{u'^2_x}}{\partial x} \right] \qquad (5.9)$$

These equations form the base for the normalisation in the next section.

5.1.3 Normalisation

First the boundary conditions have to be defined for the precessing jet case, when the jet is exiting with an 45^o angle relative to the x– and r–axes:

- r=0 : $u_x = u_e \cdot \cos\alpha_e = u_e \cdot \frac{\sqrt{2}}{2}$
- r=0 : $u_r = u_e \cdot \sin\alpha_e = u_e \cdot \frac{\sqrt{2}}{2}$
- r=0 : $u_\Phi = 0$
- t=0 : $\Phi = \Phi_0$

To normalise the Navier Stokes equation to a dimensionless form, the following characteristic scales are defined:

- only one time scale is available, which is based on the precessional frequency;
  time scale: $t = \frac{\hat{t}}{2 \cdot \pi \cdot f_p}$
- for the x–coordinate the nozzle diameter is the appropriate length scale available;
  x length scale: $x = \hat{x} \cdot d_e$
- for the r–coordinate the characteristic length scale is defined by the relation between the exit velocity and the frequency of precession (Section 4.2.2).
  r length scale: $r = \hat{r} \cdot \frac{\frac{\sqrt{2}}{2} u_e}{f_p}$
- pressure: $p = \hat{p} \cdot P = \hat{p} \cdot \frac{1}{2}\rho u_e^2$
- velocity scale: $u_{x,r,\Phi} = \hat{u}_{x,r,\Phi} \cdot u_e \frac{\sqrt{2}}{2}$

In these equations the values with the $\widehat{\ }$ are the dimensionless terms. While the full normalisation is not presented here, rewriting the Navier Stokes equations in terms of the new dimensionless variables yields a single determining factor St_p of the form $\frac{f_p \cdot d_e}{u_e}$. This is the definition of the precessional Strouhal number which was proposed by Nathan (1988) in his experimental study. It confirms the experimental investigation which found that (when neglecting the viscous terms) the Strouhal number of precession determines the characteristics of the precessing jet flow. Only the x–derivatives do not have the Strouhal number of precession as a parameter.

5.2 The Reynolds Number Effects

The assumption of neglecting the Reynolds number terms in the Navier–Stokes equations is investigated here. The Reynolds number can be defined by the general equation

$$\text{Reynolds number} = \frac{\text{inertial forces}}{\text{viscous forces}}$$

Abramovich (1963) describes the role of the viscosity in a free turbulent jet as follows:

"When a low–viscosity fluid flows around a solid body, the flow can be divided in two regions: a comparatively thin layer of fluid located close to the solid boundary – a boundary layer where viscosity, however small it may be, must be taken in to account, and the other part of the flow in which viscosity can be neglected and hence the flow can be described by laws of an ideal fluid. The boundary layer of the turbulent flow itself

is assumed to consist of a very thin sublayer bordering directly on the wall, with pure laminar flow and the remaining (turbulent) part of the boundary layer, in which the effect of viscosity is not significant.

Thus studies of flow around bodies, fluid motion through tubes, and in general viscous flow of a fluid in the presence of solid boundaries, in principle, do not permit the complete neglect of viscosity. A special characteristic of turbulent free jets is the absence of solid boundaries of flow, and consequently also of a laminar sublayer, which makes it possible to neglect completely the influence of viscosity in all cases of free turbulence and also explains the self–similarity of jets, independent of the Reynolds number over a very wide range."

Prandtl used the assumption for his theory of free turbulence. Wygnanski and Fiedler (1969) confirm the self–similarity in a free turbulent jet and find self–similar velocity profiles also in the near field, with true self–preservation appearing at distances of $x/d_e > 50$. Hence, downstream of $x/d_e = 50$ the knowledge of one length scale and one velocity scale only is sufficient to determine any structure in the flow field (Hinze 1959).

The results obtained in precessing jet flows are consistent with the above conclusion that Reynolds number effects are negligible in free turbulent jets. PJ flows can be generated by laboratory burner nozzles with capacities ranging from a few kW (Nathan 1988) through to large industrial burners of scales exceeding one hundred MW (Nathan and Rapson, 1995), a range of some four orders of magnitude, without significant changes

in flame characteristics (e.g. flame shape, emissions etc.). Nathan (1988) showed, in tests with air, that for a given nozzle size precession will occur over a range of velocities through the controlling orifice, the upper limit being set by choking in the orifice. With water flow through the nozzle the limit on the velocity is set by cavitation. In no case has it been found that an upper limit to the precession is set directly by the Reynolds number. The following results of LDA measurements confirm that the mechanical analogue of the fluidic precessing jet is also tolerant of the Reynolds number, at least for the modest range of Reynolds numbers possible.

To provide quantitative measurements of the effect of the Reynolds number, the velocity field was investigated using LDA in two flows with Reynolds numbers of 26,600 (u_e = 39.9m/s) and 6,600 (u_e = 9.9m/s) respectively. A comprehensive set of results over the whole measurement domain ($x/d_e = 2, 4, 6, 8, 10, 12$) is presented in the Appendices D and E. Both sets of LDA measurements have been conducted with a Strouhal number of precession of 0.0098 corresponding to a frequency of rotation of 39.2 Hz for the higher Reynolds number case and 9.7 Hz for the lower Reynolds number case. All other experimental conditions for the two cases are identical, with the exception of the total number of sampled points. For the high Reynolds number case 42,000 points have been measured for each radial position, giving over 100 points for each phase–averaged location (with 1^o segments per cycle). The lower Reynolds number case allowed only 14,000 points to be obtained for each radial position which provides about 39 points for each phase–averaged position.

5.2.1 Phase–Averaged Results

In Section 3 it was shown that the phase–averaged precessing jet ($\alpha_e = 45^o$), operated with a Strouhal number of 0.0098, is deflected towards the axis of rotation. This deflection causes the phase–averaged axial velocity component in the jet to become more dominant, when compared to the radial and tangential velocity components, with increasing axial distance. The phase–averaged axial velocity contour of the precessing jet is compared at three representative axial positions for the two Reynolds number cases. Two positions selected for the investigation, x/d_e=2 and 6, are in the 'precession dominated region' (Section 4.1.2). The third position is in the 'region of no dominant frequency' (Section 4.1.3) of the phase–averaged jet flow field at x/d_e=10. In general, smoother averages are displayed in the data from the higher Reynolds number case due to the larger number of samples collected. Comparing the contour plots at x/d_e=2 of the two Reynolds number cases in Figure 5.1, the same general features can be identified. The core of the jet (red) is deformed and a low velocity tail (dark green) develops tangentially behind the jet. Recirculating flow is detected in both cases on the two 'sides' of the phase–averaged jet: one is between the jet and its spinning axis, and the other is on the outer (i.e. radially outwards) side of the jet. These reverse flow regions are deduced to be due to the arrangement of vortex puff structures, as explained in Section 4, which attenuate the reverse flow on the outer edge of the jet and increase it between the jet and the spinning axis. In both cases these structures are similar in size and experience the same radial and tangential deflections (as shown in Figures 5.2 and 5.3).

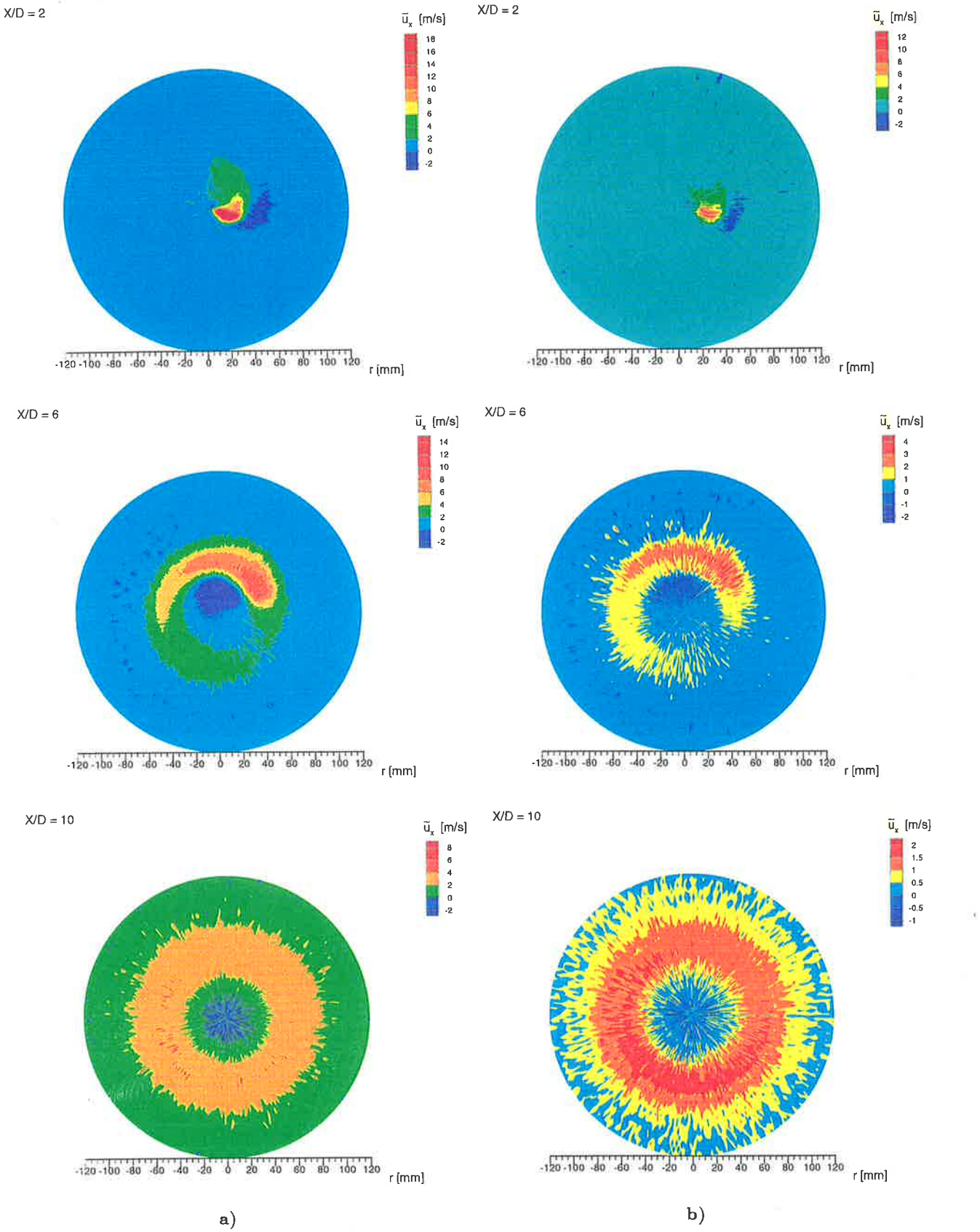

Figure 5.1: **Phase–averaged axial velocity contours at x/d_e=2, 6 and 10 for Reynolds numbers of a) 26,600 b) 6,600**

At x/d_e=6 the tail of the jet extends for almost the entire arc of the cycle. The recirculation zone between the jet and the spinning axis is, in both cases, of almost identical shape. The core of the jet (red) is deformed similarly in both cases. The reverse flow on the outer edge of the jet has become insignificant.

In the region x/d_e=10, described in Section 4.1.3 as the region of no dominant frequency, again the velocity contours are remarkably similar in the two cases. The radial extent of the ring structures is nearly the same in both cases. For Re=26,600 the inner radius of the ring is between r/d_e =0 and 0.5 which is the same as in the 6,600 Reynolds number case. The outer radius of the ring for the higher Reynolds number is at $r/d_e = 10.5$, whereas for the lower it is located at $r/d_e = 11$. These radii were determined by the $r_{0.5}$ criterion in each case, that is the location at which the phase–averaged mean axial velocity $\tilde{u}_x$ at $x/d_e = 10$ is decreased to half of its maximum value.

A good method to assess whether Reynolds number has an influence on the flow in a precessing jet is to compare the path of its 'centreline', defined as the locus of $\tilde{u}_{x,cl}$ in the phase–averaged domain. Fig.5.2 and Fig.5.3 show the path of the centreline in the x–r plane and x–Φ plane respectively. Both comparisons display reasonable agreement within the accuracy of the measurements, but a small influence of the Reynolds number can be observed. In the x–Φ plane a difference of $\Delta\Phi < 17^o$ at the distance x/d_e=4 and 6 is detected, while the remaining points experience almost identical deflections. For the centreline in the x–r plane the difference appears at x/d_e=6 and 8 and is of the order of $\Delta r/d_e$ <2. Obviously Reynolds number effects are observed in the phase–averaged regions where recirculating flow is detected. Besides these local differences, the overall path of the jet centreline, seems to be unaffected by varying the Reynolds number.

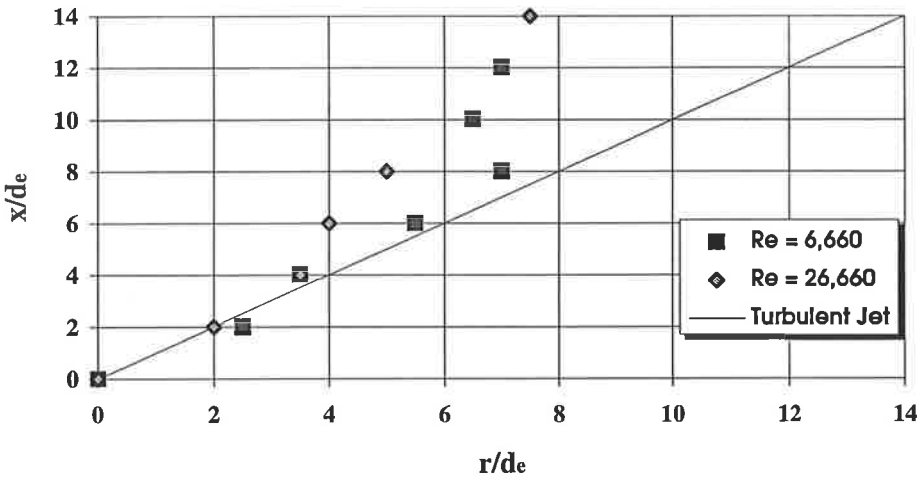

Figure 5.2: **The influence of the Reynolds number on the jet deflection in r–direction. St_p=0.0098.**

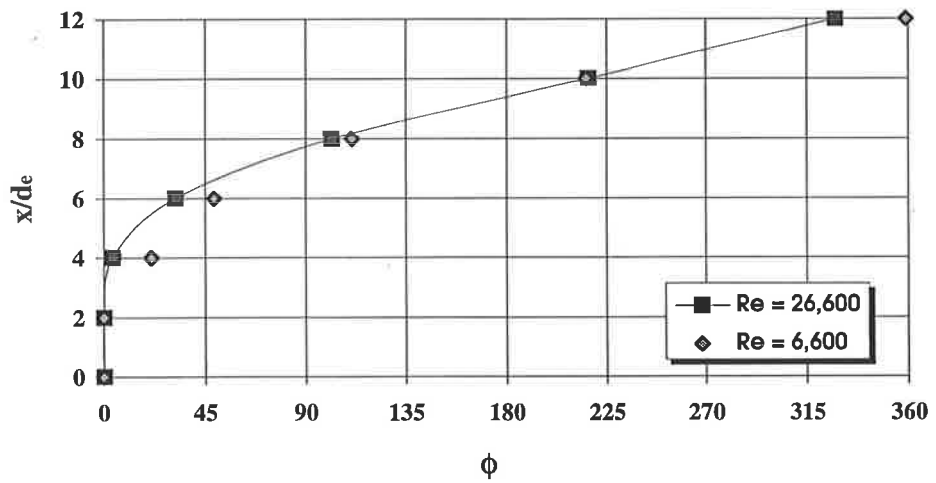

Figure 5.3: **The influence of the Reynolds number on the jet deflection in Φ–direction. St_p=0.0098.**

An important parameter which is often used to assess the entrainment characteristics of a jet is the decay in the mean phase–averaged axial velocity $\frac{\tilde{u}_{x,cl}}{u_{x,e}}$. The same two Reynolds number flows as used previously are compared here. Fig.5.4 shows the maximum phase–averaged axial velocity component $\tilde{u}_{x,cl}$, normalised by the mean axial

component of the exit velocity $u_{x,e}$, against the axial distance x/d_e. The velocity decay of a simple turbulent jet is included in the diagram to demonstrate the differences between the precessing jet flow and a free turbulent jet. The two Reynolds number cases are in good agreement. The maximum difference between the two cases, at x/d_e=6 and 8, is of the order of $\Delta\frac{\tilde{u}_{x,cl}}{u_{x,e}} = 0.07$.

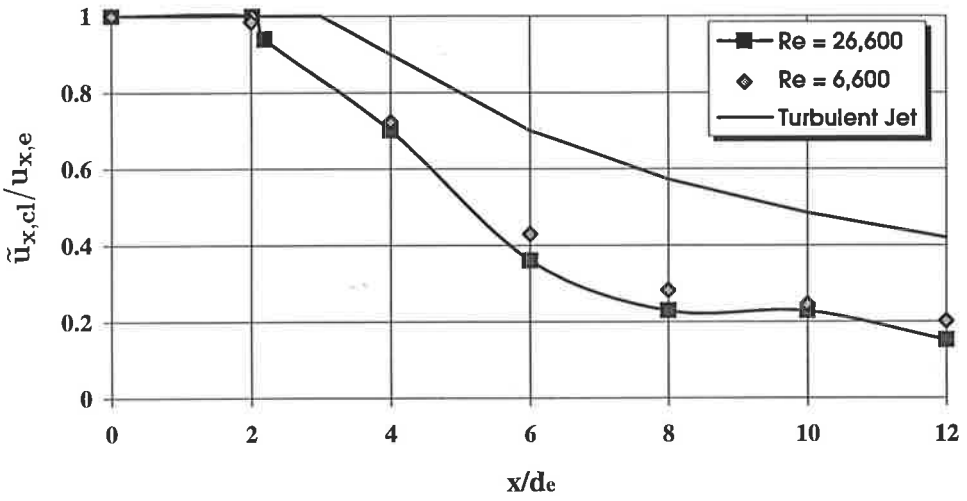

Figure 5.4: **The influence of the Reynolds number on the velocity decay. St_p=0.0098**

The last parameter to be used in the assessment of the effect of Reynolds number on the phase–averaged flow is the quantitative comparison of the negative axial velocity in the central recirculation zone. The axial velocity contours indicate that the zones are almost identical in shape and size (Fig.5.1). At $x/d_e = 6$ for Re=26,600, the maximum reverse flow is located at $r/d_e = 2.5$, and this is identical to the location in the lower Reynolds number case (Fig.5.1). In both cases the radial extent of the recirculation zone is $\Delta r/d_e = 3$ and the tangential spread is approximately 110°. The maximum negative axial velocity $\tilde{u}_{x,rec}$ between the jet and its spinning axis at each x/d_e location is shown

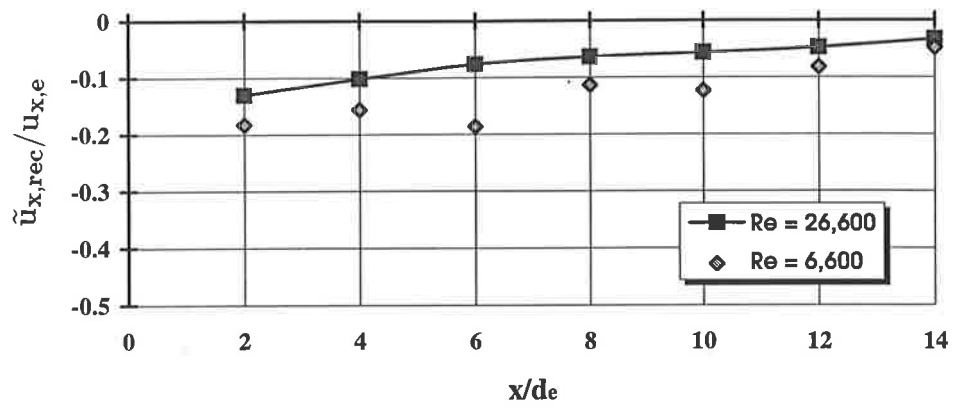

Figure 5.5: **Maximum reverse flow in the central recirculation**

in Fig.5.5. The data are normalised on the axial component of the exit velocity $u_{x,e}$. The only feature which shows a clear difference between the flows is the magnitude of the reverse flow, the maximum difference of which, $\Delta\frac{\tilde{u}_{x,rec}}{u_{x,e}} = 0.1$, is found at x/d_e=6.

5.2.2 Time–Averaged Results

Figs.5.6 to 5.8 show the time–averaged profiles of all three velocity components $\overline{u}_x$, $\overline{u}_r$, $\overline{u}_\Phi$ for the two Reynolds number flows. The velocities are normalised by the local maximum velocity component $\overline{u}_{x,max}$, $\overline{u}_{r,max}$, $\overline{u}_{\Phi,max}$. . For the Reynolds number of 26,600, each point has been calculated from 42,000 samples. This case is displayed with the symbols connected with a solid line. At the lower Reynolds number of 6,600, only 14,000 samples are available. Those data appear as symbols only.

The axial component of the mean velocity $\overline{u}_x$ is presented in Figure 5.6. In general the data from the two Reynolds number cases display reasonable agreement in shape, but the two curves appear to be offset relative to each other. Since the two data sets

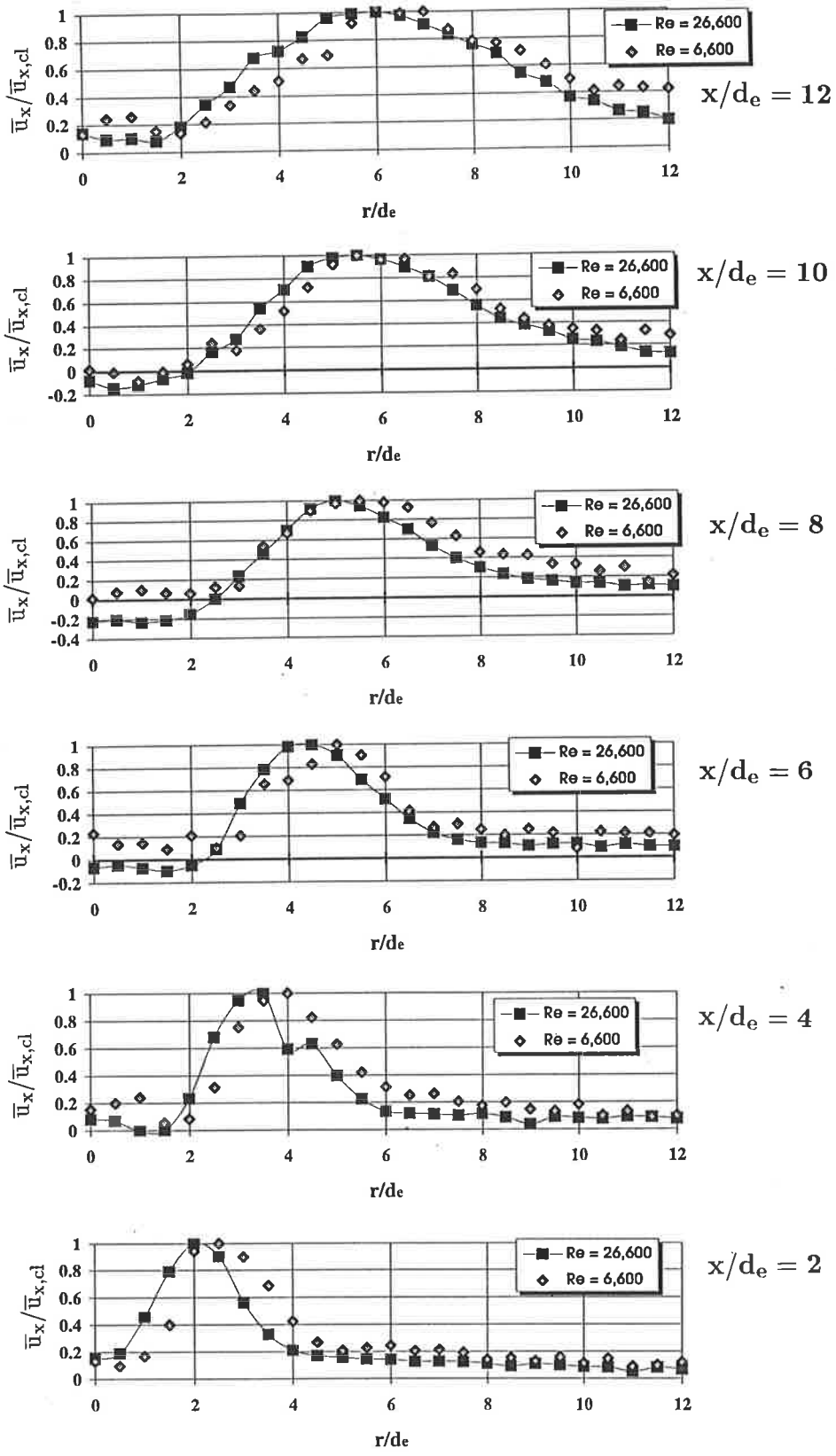

Figure 5.6: **Time–averaged axial velocity profiles normalised by its maximum value at the x/d_e location for Reynolds numbers of 26,600 and 6,600. St_p=0.0098.**

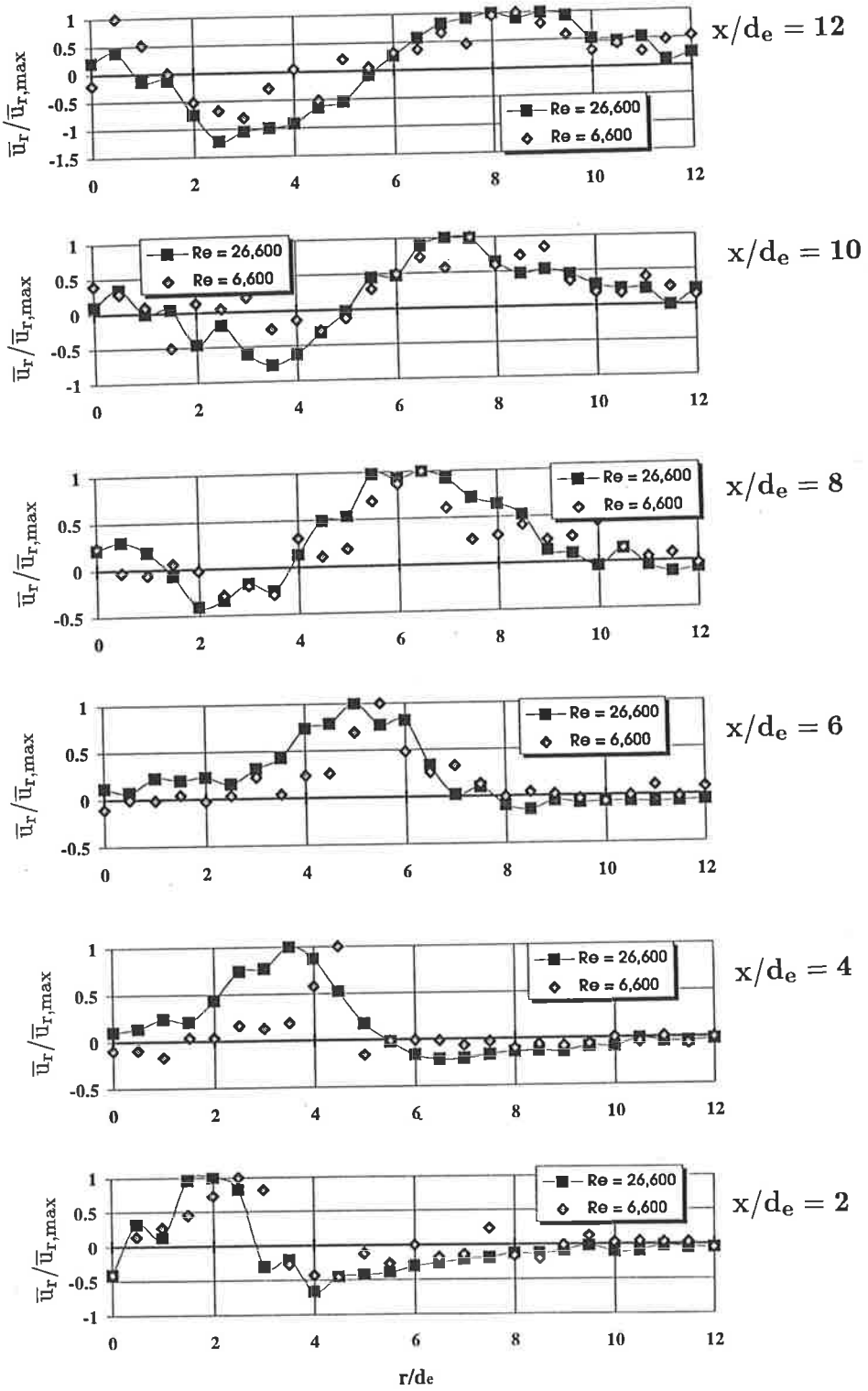

Figure 5.7: **Time–averaged radial velocity profiles normalised by its maximum value at the x/d_e location for Reynolds numbers of 26,600 and 6,600. St_p=0.0098.**

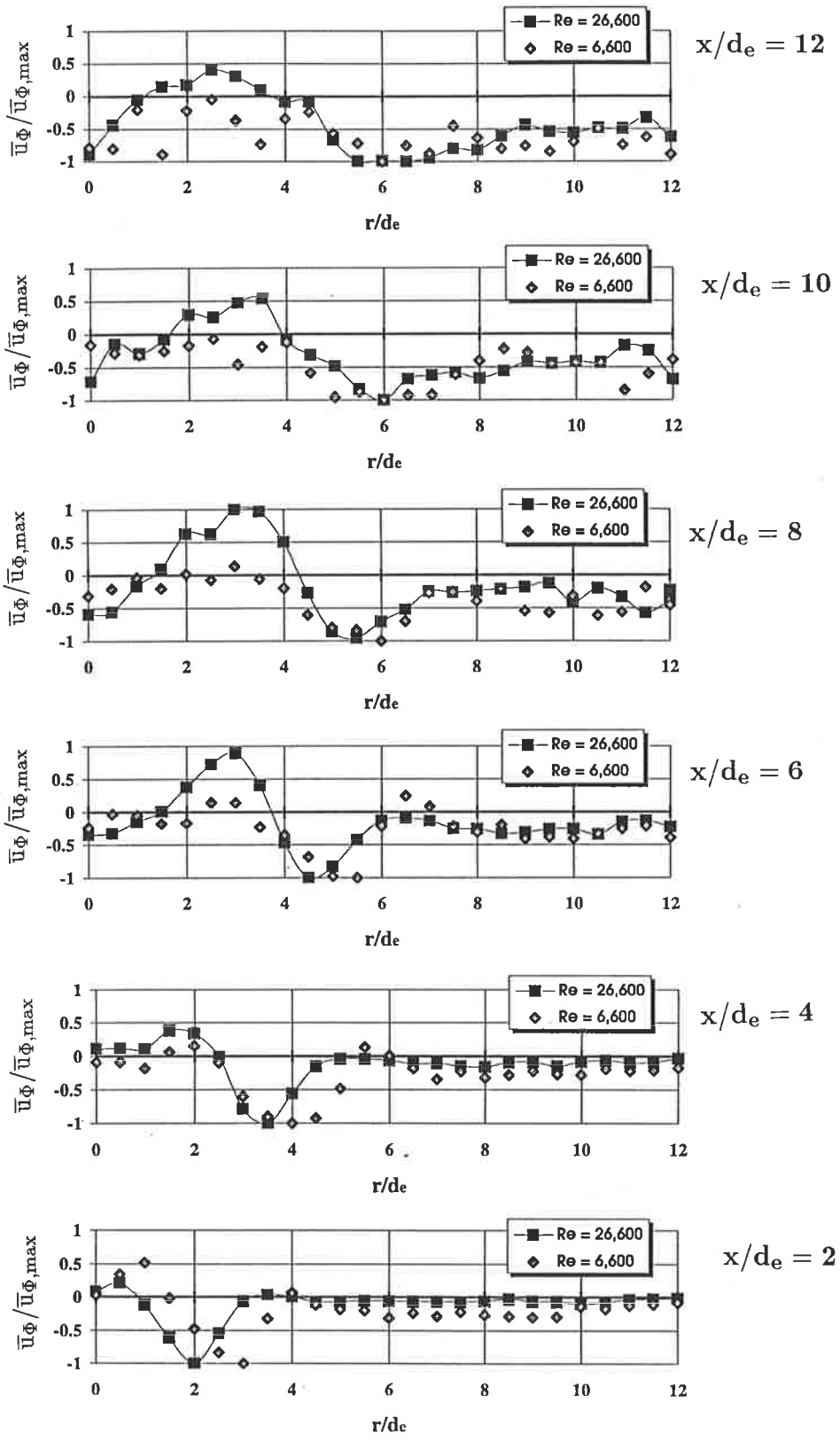

Figure 5.8: **Time–averaged tangential velocity profiles normalised by its maximum value at the x/d_e location for Reynolds numbers of 26,600 and 6,600. St_p=0.0098.**

have been obtained with an identical experimental setup, this offset may be genuine. The peaks of the two cases differ by approximately $\Delta r/d_e$=0.46 in all downstream positions. In the regions x/d_e=4, 6 and 8, where the phase–averaged results showed a small difference between the two cases, a difference in the central recirculation zone is apparent. For the high Reynolds number flow, the presence of a time–averaged mean negative velocity region can be identified for $4 < x/d_e < 10$, whereas in the low Reynolds number case the time–averaged recirculation of fluid, detected in the phase–averaged mean axial velocity, is only detected near x/d_e=10.

The profiles of the radial component in Figure 5.7 indicate reasonable agreement between the two Reynolds number flows. The scatter of the data is a result of the much lower radial velocity component overall. Also the normalisation on the local maximum velocity component $\overline{u}_{r,max}$ contributes also to an increased scatter of the data. The location of the maximum time–averaged values $\overline{u}_{r,max}$ in the radial component corresponds with the location of the maxima in the axial component. The radial distance to the location of the peak values increases with axial distance generating large scale secondary flow patterns. Following the curves from the spinning axis outwards (at x/d_e=6-12) a postive radial velocity component is observed followed by strong negative values which then lead into the maxima of the profiles. There is inflow into the recirculation zone, both from the spinning axis (r/d_e=0) outwards (r/d_e=2-3) and from the inner edge of the jet (r/d_e=5) inwards, into that reverse flow region (r/d_e=2-3) for both Reynolds number cases. In general, taking the low magnitudes of the radial component into account, the agreement is acceptable.

The profiles of the tangential velocity component $\overline{u}_t$ are displayed in Figure 5.8. The scatter of the data again is due to the low magntidues of velocity and the normalisaion on the $\overline{u}_{t,max}$. The maxima of $\overline{u}_\Phi$ do coincide with the high shear region of the precessing jet. The positive peaks coincide with the inner shear region of the jet (towards the spinning axis) and the negative peaks with the outer shear region. The values in the recirculation zone of the lower Reynolds number flow (6,600) at x/d_e=6 to 12 seem to be attenuated. However, in the jet region and at larger distances in the radial direction, the agreement of the data becomes adequate.

The turbulence intensities of the three components $\frac{\sqrt{\overline{u'^2_x}}}{\overline{u}_x}$ $\frac{\sqrt{\overline{u'^2_r}}}{\overline{u}_r}$ $\frac{\sqrt{\overline{u'^2_t}}}{\overline{u}_\Phi}$ are presented in Figures 5.9 to 5.11. The axial turbulence intensity $\frac{\sqrt{\overline{u'^2_x}}}{\overline{u}_x}$ is consistent with trends found earlier in the mean velocity profiles. A significant Reynolds number effect is only apparent in the region of the reverse flow. In that region extremely high turbulence is measured and values differ between the two Reynolds number cases differ by $\Delta\frac{\sqrt{\overline{u'^2_x}}}{\overline{u}_x}$ of between 4 and 6. However, these differences are restricted to the reverse flow zone and become insignificant at radial distances $r/d_e > 3$.

The radial and tangential turbulence components $\frac{\sqrt{\overline{u'^2_r}}}{\overline{u}_r}$, $\frac{\sqrt{\overline{u'^2_t}}}{\overline{u}_t}$ in Figures 5.10 and 5.11, being the minor velocity components, show agreement only close to the nozzle exit. At x/d_e=2 and 4 reasonable agreement can be found (outside the recirculation zone). With increasing axial distance, and hence with decrease in the magnitude of the velocities, it is likely there is a random error component in the data, and hence it is not reasonable to attempt to discuss differences as no trend is apparent.

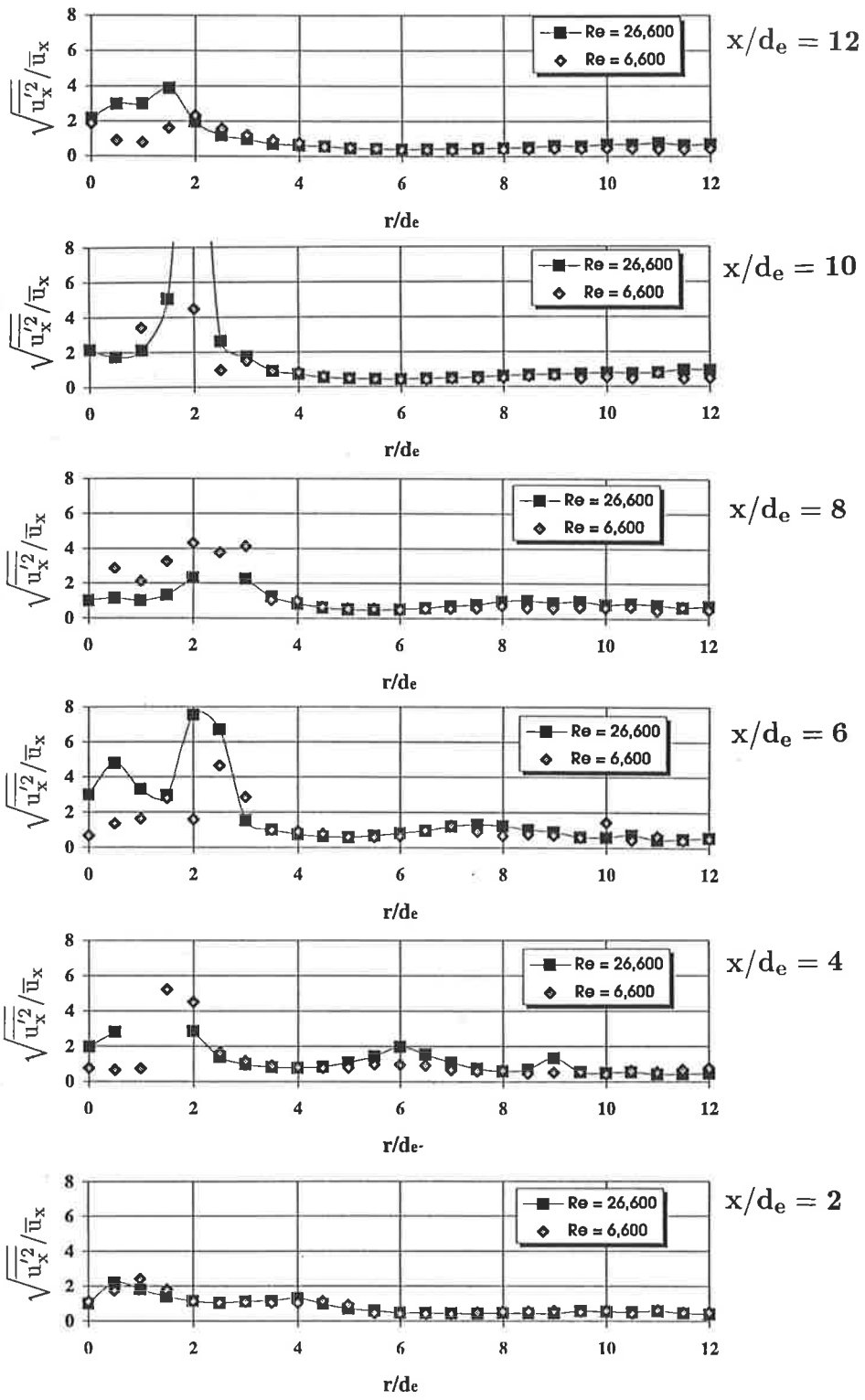

Figure 5.9: **Time–averaged axial turbulence intensity for Reynolds numbers of 26,600 and 6,600. St_p=0.0098**

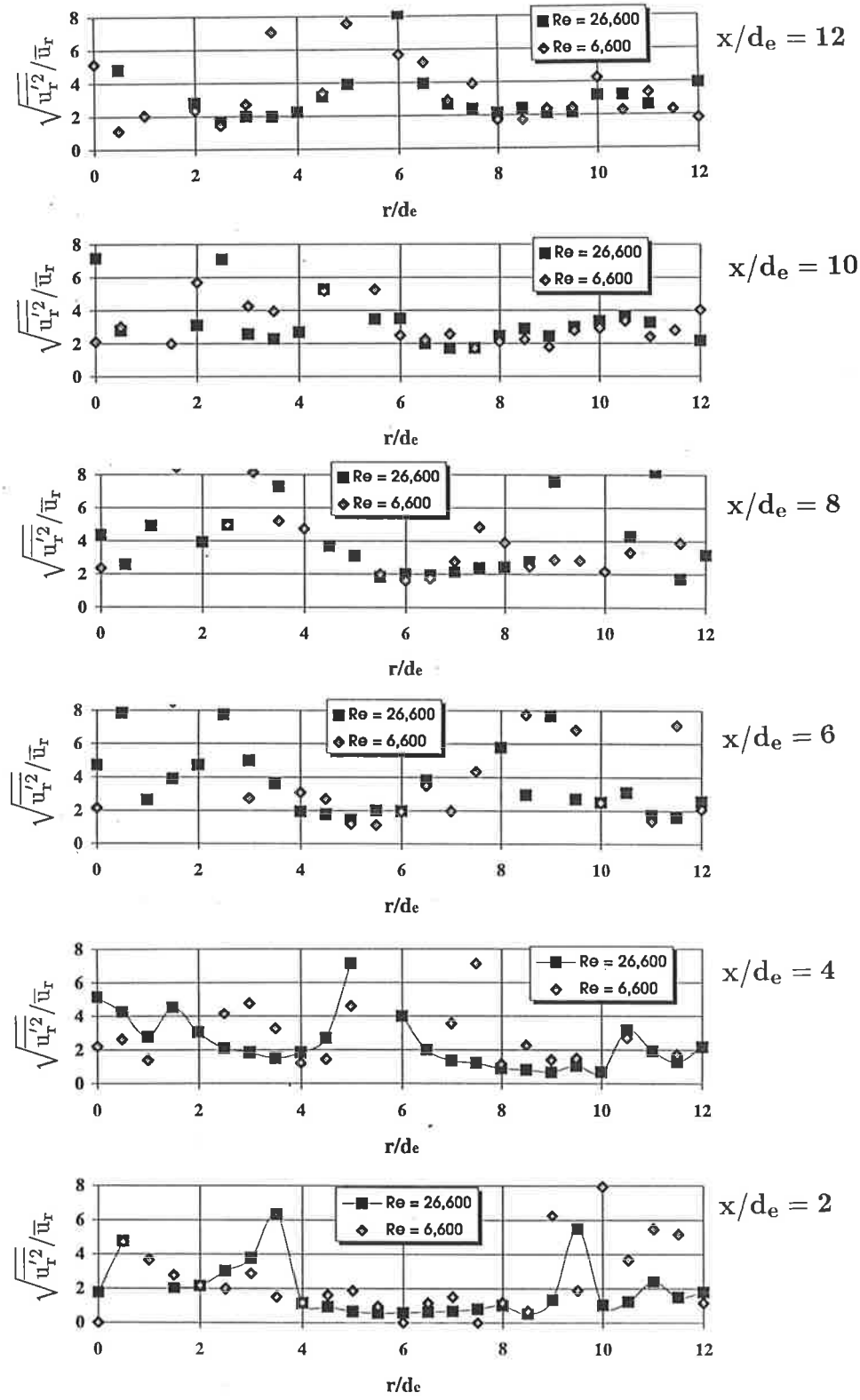

Figure 5.10: **Time-averaged radial turbulence intensity for Reynolds numbers of 26,600 and 6,600. St_p=0.0098**

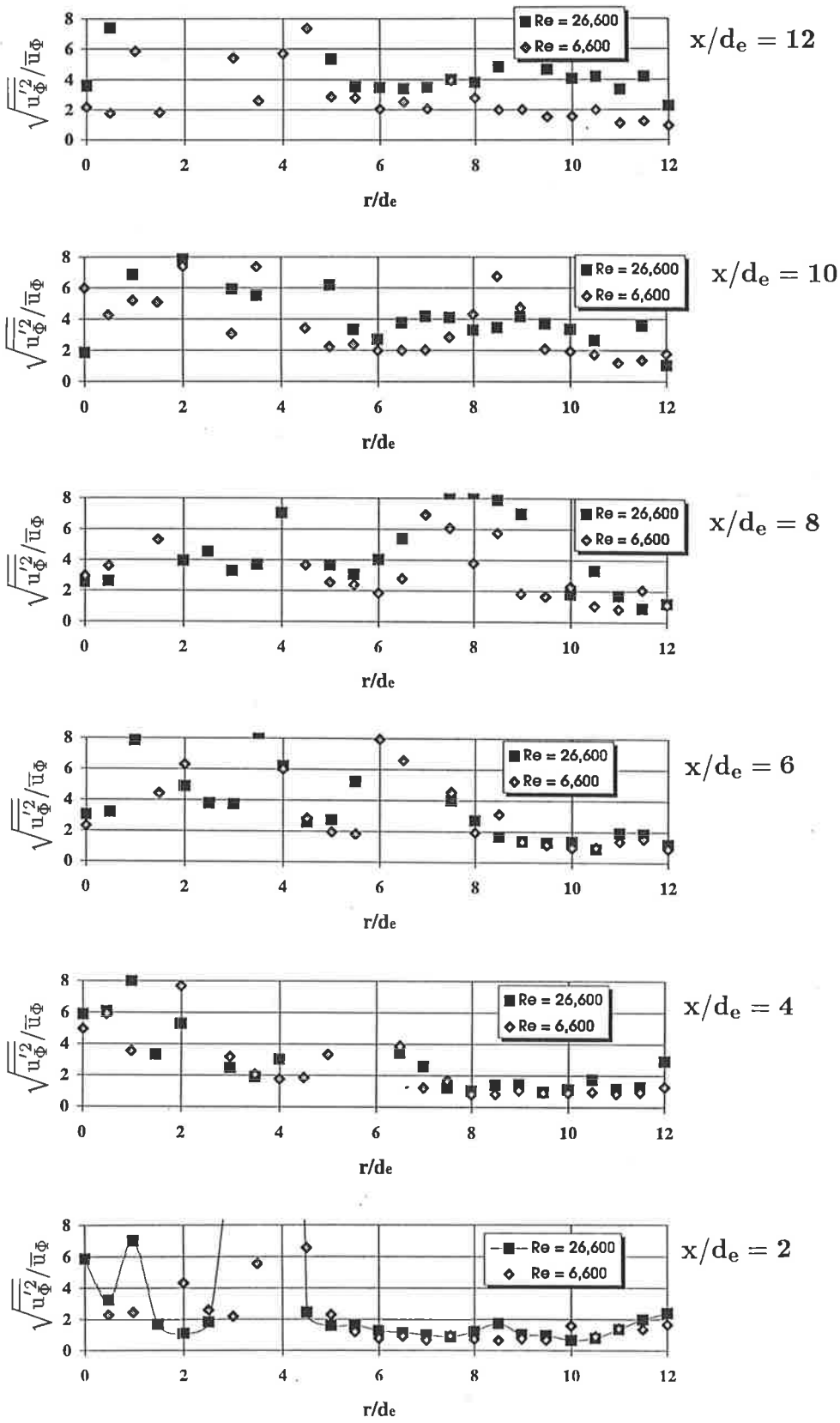

Figure 5.11: **Time-averaged tangential turbulence intensity for Reynolds numbers of 26,600 and 6,600. St_p=0.0098**

5.3 Conclusion

In concluding the present chapter, it can be stated that differences exist in the phase–averaged and the time–averaged velocity and turbulence data in the two Reynolds number cases studied. However, these differences are confined to the region where recirculation of fluid occurs ($x/d_e < 7 \pm 1$ and $r/d_e < 3 - 4$. The main jet characteristics: contours, deflection, velocity decay and spread, as well as the outer regions of the total flow field are almost identical for the two Reynolds number cases. Therefore, it appears that precessing jet flows can be analysed without the viscous terms in the Navier–Stokes equations (e.g. Equations 5.7 to 5.9) can be expected to provide reasonable accuracy. The data suggests that the PJ flow is independent of the (turbulent) Reynolds number, when the Reynolds number is sufficiently high. However, the data shows that the flow is most Reynolds number dependent in the vicinity of the recirculation flow regions. Whether the differences would disappear with still higher Reynolds number cannot be resolved from the present data, which only examined Re=6,600 and Re=26,600.

Chapter 6

Conclusions

To aid the understanding of a naturally occuring but continuously unstable jet which precesses about an axis other than its own, a 'deterministic' analogue, in the form of a mechanically rotated, inclined jet with known initial conditions, has been studied. The 'natural' precessing jet is the result of a fluid mechanical instability which occurs after an abrupt expansion of the flow into an axisymmetric chamber and its subsequent discharge from that chamber over a small step at the exit plane. In the naturally occuring flow the initial diameter of the jet, the angle at which it leaves the nozzle and the frequency with which it precesses about the nozzle axis are all ill–defined and are inconsistent from one cycle to the next. The mechanical analogue studied here has allowed these exit parameters of the jet to be clearly defined and to be made consistent. In the present system reported here the exiting jet is inclined at 45^o to the axis of rotation, has an exit diameter of 10mm and a centreline which intersects the axis of rotation at the exit plane. Influences of the internal and external boundary layer of the spinning mechanical nozzle have been investigated and have been made negligible by means of a thin, non–rotating sheath over most of the nozzle. The integrity of the jet has been

studied when the nozzle is not rotating (St_p=0) by comparison with the established form of a simple turbulent jet and acceptable agreement has been demonstrated. The effect of the Strouhal number of precession on the overall flow field has been examined by several novel means including either phase– or time–averaging of three–dimensional velocity data obtained at a sequence of planes through the jet, and simultaneous time dependent pressure and velocity measurements by means of a recently developed multi–dimensional pressure probe.

Characteristics of precessing jet flows have been found to be strongly dependent on the Strouhal number of precession and only very weakly dependent on the Reynolds number. Two flow regimes have been identified, termed the 'low Strouhal number regime' ($St_p < 0.005 - 0.006$) and the 'high Strouhal number regime' ($St_p > 0.006 - 0.007$), with a smooth transition between the two regimes. In the low Strouhal number flow the precessing jet follows a path which is close to a projected Archimedian spiral and locally is comparable to a simple turbulent jet. In contrast the high Strouhal number flow has dramatically different characteristics and flow patterns.

6.1 Measurements in the Precessing Jet Flow

The measurement techniques used to investigate the precessing jet flows have been:

- laser doppler anemometry (three–dimensional)
- high frequency, pitot type, pressure probe (Cobra probe)
- hot–wire anemometry

The low Strouhal number flows show almost identical values of typical characteristics when compared with a simple turbulent jet. The phase–averaged contours and instantaneous pictures of the jet show that the jet maintains its round shape. A small zone of recirculation is measured in the phase–averaged domain, but it is too weak to be also identified in the time–averaged. The phase–averaged velocity components in the radial and axial directions are almost identical to each other, since the jet continues in its original exit angle of 45^o. Also the turbulence intensities and Reynolds stresses are comparable to each other. The tangential components of velocity and turbulence are negligible in the low Strouhal number flow, since the rate of deflection in the tangential direction is small and the nozzle does not impart a tangential component to the flow since the jet exits on the spinning axis. The rate of decay in the axial velocity and the spreading of the jet are each comparable to that of a simple turbulent jet. Phase– and time–averaged turbulence intensities, phase–averaged Reynolds stresses and time–averaged higher order statistics also show values which are similar to those in a turbulent circular jet.

In the high Strouhal number regime the flow field is dramatically different to the low regime. A region of strong recirculation is established between the precessing jet and the spinning axis, due to the establishment of a low pressure core. This low pressure region is apparent in both the phase– and time–averaged domains. The velocity contours in the phase–averaged jet and the images of the instantaneous jet show a high degree of deformation relative to a non–precessing jet. The precessing jet is deflected towards the spinning axis and backwards so that it lags behind the direction of the precession. A rapid decay of the radial components of velocity and turbulence is observed as the

jet is deflected inwards and significant tangential components are generated. Although the axial and radial components are initially equal, the axial component of velocity and turbulence rapidly becomes the dominant component in the flow field. A 'bifurcation' is detected tangentially in front of the phase–averaged jet, where strong inflow into the recirculation zone, between the jet and the spinning axis, occurs. Also flow into the same recirculation zone is measured in the region not occupied by the phase–averaged jet.

The spreading of the phase–averaged jet is greater in the high Strouhal number flow than in either the low Strouhal number jet or in a simple turbulent jet. This results in an increased decay rate of velocity along the centreline of the precessing jet. Also, phase– and time–averaged turbulence intensities and phase–averaged turbulent shear stresses are high in the region $x/d_e \leq 6$ of the jet, which explains the high entrainment rates of the jet found in earlier investigations. However, none of the preceeding characteristics are evident at distances $x/d_e > 6$. There is no evidence of any precession beyond $x/d_e = 6$ where the phase–averaged and time–averaged results are identical. A ring–like structure, which is many times the scale of the nozzle dimensions and is symmetric about the nozzle axis, is found in both the time–averaged and phase–averaged flow. However, no preferred frequency is measured in this region, neither at the frequency of precession nor at a lower frequency. Nevertheless, the visualisation images identify some structure in the turbulence. This evidence suggests that the flow does not grow by pairing, or amalgating of structures of a characteristic size, as occurs in a non–precessing jet. Rather a wide spectrum of turbulence scales is found. The turbulence intensity and Reynolds stress levels in the region downstream from the recirculation are significantly reduced relative to those in the region of the recirculation zone.

Analytical evaluations of the flow field confirm the dependency of the flow field on the Strouhal number. Appropriate normalisation of the three–dimensional, turbulent Navier–Stokes equations leads to the prominence of a single dimensionless parameter, the Strouhal number of precession, when the viscous terms and the Reynolds number effects respectively are neglected. Measurements of two different Reynolds numbers in the same Strouhal number flow have shown the precessing jet flow to be largely independent of the Reynolds number downstream of x/d_e=6. Only at distances $x/d_e \leq 6$ do the Reynolds number differences appear.

6.2 Identified Flow Structures

Flow structures in the low and high Strouhal number regimes have been been identified visually by the following techniques:

- laser induced fluorescence (LIF) in water flow
- laser sheet using Glycol vapour, Titanium Dioxide and glass beads in air flow
- conditional smoke pulses in air flow

The structures in low Strouhal number PJ flows ($St_p < 0.005 - 0.006$) are closely similar to those in a simple turbulent jet. As the rotational frequency and the Strouhal number are small, the Kelvin–Helmholtz instabilities from which the flow structures (vortex puffs) develop and follow each other at a respectable distance in almost the same way as a simple jet. The jet, as a momentum source, supports the shear between the jet flow and the ambient fluid and the jet structures are not significantly deformed.

These structures are evident even in the far field of the jet. A small low pressure field between the jet and the spinning axis is apparent, but it is weak and does not lead to any significant jet deflection of individual elements of the jet fluid from a straight line path which projects back to the origin at the nozzle exit. The path of the jet centreline, which is not a mean streamline, therefore describes the expected Archimedian spiral.

In high Strouhal number flows significant recirculation of fluid has been observed. The structures in the jet become distorted and begin to interact one with the next in a manner which causes an increase in the curvature of the jet locus. The jet ceases to be an adequate momentum source for the vortices. Expressed alternatively, the ring–like vortices or puffs become highly deformed and the successive puffs are displaced laterally so they no longer follow behind each other at a 'respectable' distance. This results in an asymmetric pressure field across the jet trajectory and a high deflection of the jet from the original 45^{o} exit angle.

Comparing the trajectories of the two precessing jet flow regimes with an Archimedian spiral path emphasises the strong differences between the low and the high Strouhal number regimes. The projected path of the low Strouhal number jet is in good agreement with the path predicted by an Archimedian spiral. But measurements in the high Strouhal number regime have shown that the trajectory follows a much tighter curve than that predicted by the Archmedian spiral, due to the vortex puff interactions and to the recirculation and low pressure core between the jet and its spinning axis.

6.3 Future Work

The precessing jet flow, being a relatively recently identified phenomenon in fluid mechanics, is still poorly understood. The precessing jet flow produced with the mechanically rotated nozzle, as presented here, as well as the flow produced inside and outside the fluidic nozzle need to be investigated further. Some investigations, which appear to have potential to increase understanding of the flow, are suggested below.

6.3.1 Further Research

In the investigation reported in the present thesis it was only possible to explore the Strouhal number and Reynolds number dependencies of the precessing jet flows created by the mechanical nozzle. The influence of the exit angle of the jet in particular requires further research while changes in the exit diameter of the jet are not expected to be significant. An investigation of such changes for the same Reynolds number as in this work, and for the same mass flow rate, would establish limits on the Reynolds number independence found in the present work. In this regard it is interesting to note that for low Reynolds number laminar jets a full Navier–Stokes computation at the Pennsylvania State University (Manohar et al. 1996) has shown strong evidence of the precessional instabilities. Investigations with the mechanical nozzle and combustion are also needed to build a link to the rapidly advancing commercial application of the PJ, that is of the fluidic nozzle, as an industrial burner ('GYRO–THERM'). Parametric studies in flames with the mechanical nozzle will enable comparison with data obtained for the fluidic nozzle and would greatly assist the understanding of the highly successful but very complicated flow and combustion process.

The fluidic nozzle, which is being investigated by Hill (1997), will also need further work to understand the mechanism that intitiates and drives the precession in the axisymmetric cavity. To be able to control and vary the precession for each industrial application enables optimisation of the burner designs. Parametric studies on the fluidic nozzle will be more difficult than the mechanically driven flow addressed in the present thesis, since the precessing jet flow exiting from the cavity involves many more unknowns. Not only do the exit diameter, the exit angle, the exit velocity and the frequency of precession appear as variables, as in the mechanical nozzle, but also the location of the jet exit is not on the spinning axis and the shape of the exiting jet is not well defined.

6.3.2 Existing and Potential Industrial Applications

As described in Section 1, the fluidic nozzle, which produces the continuously unstable precessing jet flow, has been commercialised as the GYRO–THERM burner. To date, the industrial burner has been applied in the cement, lime and alumina industries. Burners in the range of 20MW – 100MW have been installed in Geelong Cement, VIC, Queensland Alumina, Gladstone, and Swan Portland Cement, WA, in Australia, and in Lafarge Cement, Richmond, Canada. Two more burners have recently been commissioned in the USA.

The characteristics of the burner which yield simultaneously both reductions of emissions and of fuel consumption, and the relatively simple design show considerable potential for its adoption in many more sectors of industry which require process heating by means of fossil fuels. Interest from the glass and metals industries is being persued by FCTI (Fuel and Combustion Technology Int., Australia) and several small burners (5MW) have been commissioned. The technology is also relevant in the field of power generation and several tests using a GYRO–THERM burner as a pilot in coal fired boilers have been performed successfully. The precessing jet flow also has application as a simple and efficient mixing device and this could open applications well beyond the combustion field.

To realise all or even some of the above potentials will require many more PhD studies and many years of research to understand and be able to apply the precessing jet over its full range of potential applications !

Bibliography

[1] Abbiss,J.B., Bradbury,L.J.S., Wright,M.P. (1975) *Measurements on an Axi-Symmetric Jet Using a Photon Correlator.* Proc. of the LDA-Symposium, The Accuracy of Flow Measurements by Laser Doppler Methods, Copenhagen, pp 319–335.

[2] Abell,C.J. (1977) *Acoustic Coupling in a Turbulent Flow.* 6th Australasian Conference on Hydraulics and Fluid Mechanics, Adelaide, Australia, pp 41–45.

[3] Abell,C.J., Luxton,R.E. (1979) *Progress Report SENRAC Project P45 to June 1979.* Department of Mechanical Engineering, University of Adelaide, Australia.

[4] Abell,C.J., Luxton,R.E. (1980) *Progress Report NERDDP/SENRAC Grant 79/9174, Mixing Enhancement in Combusting Flows.* Department of Mechanical Engineering, University of Adelaide, Australia.

[5] Abell,C.J., Luxton,R.E. (1981) *Progress Report NERDDP Projects 79/9174, 80/0336, SENRAC Project P45, Mixing Enhancement in Combusting Flows.* Department of Mechanical Engineering, University of Adelaide, Australia.

[6] Abramovich,G.N. (1963) *The theory of turbulent jets.* MIT Press, Cambridge, Massachusetts.

[7] Andreopoulos,J. (1985) *On the Structure of Jets in a Crossflow.* Journal of Fluid Mechanics, v 157, pp 163–197.

[8] Antonia,R.A., Rajagopalan,S. (1990) *Performance of lateral vorticity probe in a turbulent wake.* Experiments in Fluids, v 9, pp 118-120.

[9] Antonia,R.A., Satyaprakash, B.R., Hussain,A.K.M.F. (1982) *Statistics of fine-scale velocity in turbulent plane and circluar jets.* Journal of Fluid Mechanics, v 119, pp 55-89.

[10] Badri Narayanan,M.A., Raghu,S. (1982) *Two Dimensional Jet Subjected to Periodic Oscillations in the Potential Core Region.* Report 82 FM2, Dep. of Aeronautical Eng., Indian Institute of Science, Bangalore-560 012.

[11] Badri Narayanan,M.A., Platzer,M.A. (1987) *Jet Excitation by a Bivane System and its Application to an Ejector for Thrust Augmentation.* Report of Naval Postgraduate School, Monterey, California, NPS-67-87-004.

[12] Balint,J.L., Vukoslavcevic,P., Wallace,J.M. (1987) *A Study of the Vortical Structure of the Turbulent Boundary Layer.* Advances in Turbulence, Bellot+Mathieu, Springer Verlag, pp 456-464.

[13] Balint,J.L., Wallace,J.M., Vukoslavcevic,P.(1991). *The velocity and vorticity vector fields of a turbulent boundary layer. Part 2. Statistical Properties.* Journal of Fluid Mechanics, v 228, pp 53-86.

[14] Barchilon,M., Curtet,R. (1964). *Some details of the Structure of an Axisymmetric Confined Jet With Backflow.* Journal of Basic Engineering, Trans.of the ASME, v 86, pp 777-787.

[15] Batchelor, G.K. (1967). *An Introduction to Fluid Dynamics.* Cambridge University Press.

[16] Battaglia,F., Kulkarni,A.K., Merkle,C.L. (1995). *Numerical simulations of asymmetric channel flows for gas burners.* Fourth Australian Flame Days, Adelaide, Australia.

[17] Battaglia,F. (1997). *Numerical simulations of asymmetric channel flows.* PhD Thesis, Pennsylvania State University.

[18] Bergh,H. and Tijdeman,H. (1965). *Theoretical and experimental results for the dynamic response of pressure measuring systems.* National Aero and Astronautical Research Institute, Amsterdam, Report NLR–TRF.238, 1965

[19] Bernard,P.S., Thomas,J.M., Handler,R.A. (1995). *Vortex Dynamics and the Production of Reynolds stress.* To appear in Journal of Fluid Mechanics.

[20] Birch,A.D., Brown,D.R., Fairweather,M., Hargrave,G.K. (1989) *An experimental study of a turbulent natural gas jet in a cross-flow.* Combustion Science and Technology, pp 217-232.

[21] Bisset,D.K., Antonia,R.A., Britz,D. (1990) *Structure of large-scale vorticity in a turbulent far wake.* Journal of Fluid Mechanics, v 218, pp 463-482.

[22] Bisset,D.K., Antonia,R.A., Browne,L.W.B. (1990) *Spatial organization of large structures in the turbulent far wake of a cylinder.* Journal of Fluid Mechanics v 218, pp 439-461.

[23] Blackwelder,R.F. (1981) *Hot-Wire And Hot-Film Anemometers.* Methods of Experimental Physics: Fluid Dynamics, v 18, part A, pp 259-314.

[24] Bousgarbies,J.L., Brizzi,L.E., Foucault,E., Vigner,A. (1993) *Etude par ADL du champ de vitesse au voisinage d'un jet debouchant perpendiculairement dans une couche limite transversale.* Internal Report, L.E.A., Poitiers, France.

[25] Bousgarbies,J.L., Brizzi,L.E., Foucault,E. (1993) *Visualisation et description des principales structures tourbillomaires engendrees par un jet circulaire debouchant perpendiculairement dans une ecoulement transversale.* Internal Report, L.E.A., Poitiers, France.

[26] Bousgarbies,J.L., Brizzi,L.E., Foucault,E. (1992) *Coherent structures generation from a circular jet issuing into a cross boundary layer. Low Reynolds study.* IUTAM Symposium entitled: Eddy Structures Identification in Free Turbulent Shear Flows, Poitiers, France.

[27] Bradshaw,P. (1968) *Simple wind tunnel design.* NPL Aero Report, v 1258.

[28] Bradshaw,P., Pankhurst,R.C. (1964) *The design of low-speed wind tunnels.* Prog. Aerospace Sci., v 5, No.1.

[29] Braun,M. (1979) *Differentialgleichungen und ihre Anwendungen.* Springer-Verlag.

[30] Bremhorst,K. (1993) *Accuracy of Laser Doppler Anemometry.* Workshop on Laser Diagnostics in Fluid Mechanics and Combustion, Sept./Oct. 1993, Melbourne, Australia, pp 1.1-1.8.

[31] Bremhorst,K., Harch,W.H. (1978) *The mechanism of jet entrainment.* AIAA Journal, v 16, pp 1104-1106.

[32] Bremhorst,K., Hollis,P.G. (1987) *Velocity measurements in a fully pulsed subsonic air jet.* Progress report, March 1987.

[33] Bremhorst,K., Hollis,P.G. (1990) *Velocity field of an axisymmetric pulsed, subsonic air jet.* AIAA Journal, v 28, No.12, pp 2043-2049.

[34] Bremhorst,K., Watson,R.D. (1981) *Velocity field and entrainment of a pulsed core jet.* Journal of Fluids Engineering, v 103, pp 605-608.

[35] Bremhorst,K. (1979) *Unsteady Subsonic Turbulent Jets.* Recent Dev. in Theoretical and Exp. Fluid Mech., Springer-Verlag, Germany, pp 480-500.

[36] British Standards Institution (1946) *Flow Measurements* British Standard Code B.S. 1042:1943.

[37] Bronstein,I.N., Semendjajew,K.A. (1981) *Taschenbuch der Mathematik.* Verlag Harri Deutsch.

[38] Browne,L.W.B., Antonia,R.A., Chambers,A.J. (1983) *Effect of the separation between cold wires on spatial derivatives of temperature in a turbulent flow.* Boundary-Layer Meteorology, v 27, pp 129-139.

[39] Brown,G.L., Roshko,A. (1974) *On Density Effects and Large Structure in Turbulent Mixing.* Journal of Fluid Mechanics, v 644, pp 775–816.

[40] Catalano,G.D.,Chang,K.S., Mathis, J.A. (1989) *Investigation of turbulent jet impingement in a confined crossflow.* AIAA Journal, v 27, pp 1530-1535.

[41] Catalano,G.D.,Mathis,J.A.,Chang,K.S. (1991) *Higher-Order statistics of a turbulent jet in a confined crossflow.* AIAA Journal, v 29, No.12, pp 2124-2131.

[42] Cervantes de Gortari,J., Goldschmidt,V.W. (1981) *The Apparent Flapping Motion of a Turbulent Plane Jet – Further Experimental Results.* Journal of Fluids Engineering, v 103, pp 119–126.

[43] Chandrsuda,C., Bradshaw,P. (1981) *Turbulence structure of a reattaching mixing layer.* Journal of Fluid Mechanics, v 110, pp 171–194.

[44] Champagne,F.H. (1978) *The fine-scale structure of the turbulent velocity field.* Journal of Fluid Mechanics, v 86, part 1, pp 67-108.

[45] Champagne,F.H., Pao,Y.H., Wygnanski,I.J. (1976) *On the two-dimensional mixing region.* Journal of Fluid Mechanics, v 74, part 2, pp 209-250.

[46] Champagne,F.H., Sleicher,C.A., Wehrmann,O.H. (1967) *Turbulence measurements with inclined hot-wires. Part 1: Heat transfer experiments with inclined hot-wire.* Journal of Fluid Mechanics, v 28, part 1, pp 153-175.

[47] Champagne,F.H., Sleicher,C.A. (1967) *Turbulence measurements with inclined hot-wires. Part 2: Hot-wire response equations.* Journal of Fluid Mechanics, v 28, part 1, pp 177-182.

[48] Charbonnier,J.M., Leblanc,R.L. (1994) *Interaction of a perpendicular wall jet with cross flow.* 2nd Int.Conf.Experimental Fluid Mechanics, Torino, Italy, July 1994.

[49] Charbonnier,J.M., Lapostolle,S., Simeonides,G. (1994) *Comparative Application of two infrared scanners to heat transfer measurements in a Mach 6 wind tunnel.* Eurotherm No42, QIRT 94, Sorento, Italy, Aug.1994.

[50] Chen,T.H., Goss,L.P., Talley,D.G., Mikolaitis,D.W. (1992) *Dynamic Stabilization Zone Structure of Jet Diffusion Flames from Liftoff to Blowout.* Journal of Propulsion and Power, v 8, No.3, pp 548-552.

[51] Chevray,R., Tutu,N.K. (1978) *Intermittency and preferential transport of heat in a round jet.* Journal of Fluid Mechanics, v 88, pp 133-160.

[52] Claypole,T.C., Syred,N. (1981) *The Precessing Vortex Core in Swirl Stabilised Combustors.* La Revista di Combustibule, v34, No 7/8, pp 281–291.

[53] Clermont,J.R., Pierrard,J.M., Scrivener,O. (1975) *Evolution of the Velocity Profiles in the Outlet of a Tube and in the Jet of Polymer Solutions.* Proc. of the LDA-Symposium, The Accuracy of Flow Measurements by Laser Doppler Methods, Copenhagen, pp 731–735.

[54] Corrsin,S. (1963) *Turbulence: experimental methods* Handbuch der Physik, v 8, part 2, Springer Verlag, Berlin.

[55] Crabb,D., Durão,D.F.G., Whitelaw,J.H. (1981) *A round jet normal to a crossflow.* Journal of Fluids Engineering, v 103, pp 142-153.

[56] Crow,S.C., Champagne,F.H. (1971) *Orderly structure in jet turbulence.* Journal of Fluid Mechanics, v 48, pp 547-591.

[57] Curtet,R. (1958) *Confined Jets and Recirculation Phenomena with Cold Air.* Combustion and Flame, v 2, no.4, pp 383-411.

[58] De Guzman,M.M., Fletcher,C.A.J. and Hooper,J.D. (1993) *Computational Investigation of Cobra Probe Operation.* Subm. Journal of Methods for Heat and Fluid Flow.

[59] Dimotakis,P.E., Miake-Lye,R.C., Papantoniou,D.A. (1983) *Structure and Dynamics of round turbulent jets.* Journal of Physics of Fluids, v 26(11), pp 3185–3192.

[60] Döbbeling,K., Lenze,B., Leuckel,W. (1990). *Computer-aided calibration and measurements with a quadruple hotwire probe.* Experiments in Fluids, v 8, pp 257-262.

[61] Dracos,T., Giger,M., Jirka,G.H. (1992) *Plane turbulent jets in a bounded fluid layer.* Journal of Fluid Mechanics, v 241, pp 587-614.

[62] Durão,D.F.G., Whitelaw,J.H. (1975) *The Influence of Sampling Procedures on Velocity Bias in Turbulent Flow.* Proc. of the LDA-Symposium, The Accuracy of Flow Measurements by Laser Doppler Methods, Copenhagen, pp 138–149.

[63] Durst,F., Melling,A., Whitelaw,J.H. (1981) *Principles and Practice of Laser Doppler Anemometry.* 2nd Edition, Academic Press London.

[64] Durst,F., Jovanovic,J., Sender,J. (1993) *Detailed measurements of the near wall region of turbulent pipe flow.* FED v 146, Data validation for CFD Codes, ASME, pp 79-87.

[65] Eckelmann,H., Nychas,S.G., Brodkey,R.S., Wallace,J.M.(1977) *Vorticity and turbulence production in pattern recognized turbulent flow structures.* Physics of Fluids, v 20, No.10, part 2, pp 225-231.

[66] Edwards,R.W. (1981) *A new look at particle statistics in laser-anemometry measurements.* Journal of Fluid Mechanics, v 105, pp 317-325.

[67] Eisenlohr,H., Eckelmann,H. (1989) *Vortex splitting and its consequences in the vortex street wake of cylinders at low Reynolds number.* Physics in Fluids A:, v 1, No.2, pp 189-192.

[68] Eivan,S., Avidor,J.M., Gutmark,E. (1987) *Initial Instability in a Freejet Mixing Layer Measured by Laser Doppler Anemometry.* AIAA Journal, v 25, No.4, pp 628-630.

[69] Engineering Science Data Unit (1972) *Pressure drops in ducts across round-wire gauzes normal to the flow.* Fluid Mechanics, Internal Flow, v 3, ESDU 72009.

[70] Engineering Science Data Unit (1972) *Pressure losses in flow through a sudden contraction of duct area.* Fluid Mechanics, Internal Flow, ESDU 78007.

[71] Everett,K.N., Gerner,A.A. and Durston,D.A. (1983) *Seven-Hole Cone Probes for High Angle Flow Measurement: Theory and Calibration.* AIAA Journal, v 21, pp 992-998.

[72] Favre-Marinet,M., Binder,G., Hac,T.V. (1981) *Generation of Oscillating Jets.* Journal of Fluids Engineering, v 103, pp 609–614.

[73] Fornaciari,N.R., Schefer,R.W., Sanford,R., Claytor,R.S. (1994) *Application of laser-based diagnostics to industrial scale burners.* 25th Int.Symposium on Combustion, Irvine, USA, Aug.1994.

[74] Foss,J.F., Ali,S.K., Haw,R.C.(19–) *A Critical Analysis of Transverse Vorticity Measurements in a Large Plane Shear Layer.* pp 446-455.

[75] Freemann,A.R. (1975) *Laser Anemometer Measurements in the Recirculating Region Downstream of a Sudden Pipe Expansion.* Proc. of the LDA-Symposium, The Accuracy of Flow Measurements by Laser Doppler Methods, Copenhagen, pp 704–709.

[76] Fric,T.F., Roshko,A. (1989). *Structure in the Near Field of the Transverse Jet* 7th Symposium on Turbulent Flows, Stanford, August 1989.

[77] Fric,T.F., Roshko,A. (1994). *Vortical structure in the wake transverse jet* Journal of Fluid Mechanics, v 279, pp 1-47.

[78] Froud,D. (1993). *A Study of Flow Patterns in Power Station Boilers.* Master Thesis, University of Wales, Cardiff/UK.

[79] Froud,D., O'Doherty,T., Syred,N. (1994). *Phase Averaging of the PVC in a Swirl Burner under Piloted and Premixed Combustion Conditions.* Combustion and Flame,

[80] Gad-el-Hak,M., Blackwelder,R.F., Riley,J.J. (19–) *Visualization techniques for studying transitional and turbulent flows.* pp 568-575.

[81] Gadgil,S. (1971). *Structure of jets in rotating systems* Journal of Fluid Mechanics, v 47, part 3, pp 417-436.

[82] George,W.K.Jr. (1975) *Limitations to measuring accuracy inherent in the Laser Doppler signal.* Proc. of the LDA-Symposium, The Accuracy of Flow Measurements by Laser Doppler Methods, Copenhagen, pp 20–63.

[83] Gerich,D., Eckelmann,H. (1982) *Influence of end plates and free ends on the shedding frequency of circular cylinders.* Journal of Fluid Mechanics, v 122, pp 109-121.

[84] Gibson,M.M.(1963) *Spectra of turbulence in a round jet.* Journal of Fluid Mechanics, v 15, pp 161-173.

[85] Glezer,A., Coles,D. (1990) *An Experimental Study of a Turbulent Vortex Ring.* Journal of Fluid Mechanics, v 211, pp 243-283.

[86] Graham,L.J.W., Winter,A.R., Bremhorst,K., Daniel,B.C. (1989) *Clock-induced bias errors in laser Doppler counter processors.* Journal of Physics E: Sci.Instrum., v 22, pp 394-397.

[87] Greenspan,H.P. (1968) *The theory of rotating fluids.* Cambridge University Press, London, 1968.

[88] Greenspan,H.P. (1988) *On the vorticity of a rotating mixture.* Journal of Fluid Mechanics, v 191, pp 517-528.

[89] Gupta,A.K., Lilley,D.G. (1994) *Combustion and Environmental Challenges for Gas Turbines in the 1990s.* Journal of Propulsion and Power, v 10, No.2, pp 137-147.

[90] Hammache,M., Gharib,M. (1991) *An experimental study of the parallel and oblique vortex shedding from circular cylinders.* Journal of Fluid Mechanics, v 232, pp 567-590.

[91] Hancock,G.J. (1987) *A review of the aerodynamics of a jet in a cross flow.* Aeronautical Journal, pp 201–213.

[92] Handler,R.A., Bernard,P.S., Rovelstad,A.L., Swearingen,J.D. (1992) *On the role of accelerating fluid particles in the generation of Reynolds stress.* Physics of Fluids A, v 4, No.6, pp 1317–1319.

[93] Heister,S.D., Nguyen,T.T., Karagozian,A.R. (1989) *Modelling of Liquid Jets Injected Transversely into a Supersonic Crossflow.* AIAA Journal. v 27,No.12, pp 1727-1734.

[94] Heitor,M.V., Moreira,A.L.N.(1993) *Thermocouples and sample probes for combustion studies.* Prog.Energy Combust.Sci, v 19,No.12, pp 259-278.

[95] Heard,D.E., Jeffries,J.B., Smith,G.P., Crosley,D.R. (1992) *LIF Measurements in Methane/Air Flames of Radicals Important in Prompt-NO Formation.* Combustion and Flame. v 88, pp 137-148.

[96] Hill,S.J.(1992) *Characterisation of the Flow Fields Produced by the Enhanced Mixing Nozzle: A Development Towards High Temperature and Multi-Phase Applications.* Internal Report, Dep.Mech.Eng, University of Adelaide, Australia.

[97] Hill,S.J., Nathan,G.J., Luxton,R.E. (1992) *Precessing and Axial Flows Following a Sudden Expansion in an Axi-Symmetric Nozzle.* 11th Australasian Fluid Mechanics Conference Hobart, Dec.1992.

[98] Hill,S.J. (1997) *Precessing and Axial Flows Following a Sudden Expansion in an Axi-Symmetric Nozzle.* PhD Thesis, University of Adelaide.

[99] Hinze, J.O. (1959) *Turbulence* McGraw-Hill.

[100] Hirs, G. (1992) *Exergy Loss: A Basis for Energy Taxing.* Int. Conference on Energy Efficiency in Process Technology, Athens, Greece.

[101] Hooper,J.D. (1980) *Fully Developed Turbulent Flow Through A Rod Cluster.* Thesis presented for the Degree of Doctor of Philosophy, University of New South Wales.

[102] Hooper,J.D. and Musgrove,A.R. (1991) *Multi-Hole Pressure Probes for the Determination of the Total Velocity Vector in Turbulent Single-Phase Flow.* 4th Int.Symposium on Transport Phenomena. Sydney, July 1991.

[103] Hooper,J.D., Musgrove,A.R. (1995) *Pressure Probe Measurements of Reynolds Stresses and Static Pressure Fluctuations in Developed Pipe Flow.* Twelth Australian Fluid Mechanics Conference. Sydney, December 1995.

[104] Hooper,C.L., Westphal,R.V. (1991) *Hybrid approach to data reduction for multi-senso hot wires.* Experiments in Fluids, v 11, Technical Notes, pp 398-400.

[105] Hussain, A.K.M.F. (1983) *Coherent structures - reality and myth.* Physics in Fluids, v 26, No.10, pp 2816-2850.

[106] Hussain, A.K.M.F. (1984) *Coherent Structures and Incoherent Turbulence.* Turbulence and Chaotic Phenomena in Fluids, pp 453-460.

[107] Husain, H.S.,Hussain,F. (1993) *Elliptic jets. Part 3. Dynamics of preferred mode coherent structure.* Journal of Fluid Mechanics, v 248, pp 315–361.

[108] Hussain,A.K.M.F., Zaman,K.B.M.Q. (1981) *The 'preferred mode' of the axissymmetric jet.* Journal of Fluid Mechanics, v 110, pp 39-71.

[109] Irwin,A.P.A.H., Cooper,K.R. and Girard,R. (1979). *Correction of Distortion Effects Caused by Tubing Systems in Measurements of Fluctuating Pressures.* Journal of Industrial Aerodynamics. v 5, pp 93-107.

[110] Jenkins,B.G., Nathan,G.J., Manias,C.G. (1995) *Modelling of Precessing Jet Burners and their Application to Rotary Alumina Kilns.* Third International Conference on Combustion Technologies for a Clean Environment, July 1995.

[111] Johnson,R.W. (1993) *Prediction of Turbulent Coaxial Streams of Constant and Variable Density.* Journal of Propulsion and Power, v 9, No.4, pp 588-596.

[112] Johnston,J.P., Nishi,M. (1990) *Vortex Generator Jets – Means for Flow Separation Control.* AIAA Journal, v 28, No.6, pp 989-994.

[113] Judd,A.M. (1975) *Calibration of a five tube probe for measuring wind speed and direction.* Journal of Physics E: Sci.Instrum., v 8, pp 115-116.

[114] Kamotani,Y., Greber,I. (1972) *Experiments on a turbulent jet in a cross flow.* AIAA Journal, v 10, pp 1425-1429.

[115] Karasso,P.S., Mungal,M.G. (1992) *LIF Measurements of Mixing in Turbulent Shear Layers.* 6th Int.Symp.on Appl. of Laser Techniques to Fluid Mech., Lisbon, Portugal, July 1992.

[116] Kavsaoglu,M.S., Schetz,J.A. (1989) *Effects of Swirl and High Turbulence on a Jet in a Cross Flow.* AIAA, v 26, No.6, pp 539–546.

[117] Keffer,J.F., Baines,W.D. (1963) *The round turbulent jet in a cross-wind.* Journal of Fluid Mechanics, v 15, part 4, pp 481-497.

[118] Kelso,R.M. (1991) *A Study of Free Shear Flows near Rigid Boundaries.* PhD Thesis, University of Melbourne, Australia.

[119] Kelso,R.M., Lim,T.T., Perry,A.E. (1996) *An experimental study of round jets in cross–flow.* Journal of Fluid Mechanics, to appear 1996.

[120] Klewicki,J.C. (1989) *Velocity-vorticity correlations related to the gardients of the Reynolds stresses in parallel turbulent wall flows.* Journal of Physics in Fluids A:, v 1, No.7, pp 1285-1288.

[121] Klewicki,J.C., Falco,R.E. (1990) *On accurately measuring statistics associated with small-scale structure in turbulent boundary layers using hot-wire probes.* Journal of Fluid Mechanics, v 219, pp 119-142.

[122] Klewicki,J.C. (1989) *Velocity–Vorticity correlations related to the gradients of the Reynolds stresses in parallel turbulent wall flows.* Physics of Fluids A, v 1, No.7, pp 1285–1288.

[123] Klewicki,J.C., Murray,J.A., Falco,R.E. (1994) *Vortical motion contributing to stress transport in turbulent boundary layers.* Physics of Fluids, v 6, No.1, pp 277–286.

[124] Khodadadi,J.M., Vlachos,N.S. (1989) *Experimental and Numerical Study of Confined Coaxial Turbulent Jets.* AIAA Journal, v 27, No.5, pp 532-541.

[125] Ko,N.W., Lam,K.M. (1989) *Flow Structures of Coaxial Jet of Mean Velocity Ratio 0.5.* AIAA Journal, v 27, No.5, pp 513-514.

[126] Kolmogorov,A.N. (1962) *A refinement of previous hyptheses concerning the local structure of turbulence in a viscous incompressible fluid at high Reynolds number.* Journal of Fluid Mechanics, v 13, pp 82-85.

[127] Komori,S., Ueda,H. (1985) *The large-scale coherent structure in the intermittent region of the self-preserving round free jet.* Journal of Fluid Mechanics, v 152, pp 337-359.

[128] Kotsovinos,N.E., List,E.J. (1975) *Turbulent Measurements in a Two-Dimensional Buoyant Jet Using Laser Doppler Velocimetry.* Proc. of the LDA-Symposium, The Accuracy of Flow Measurements by Laser Doppler Methods, Copenhagen, pp 684–689.

[129] Krogstad,P.A., Antonia,R.A., Browne,L.W.B. (1992) *Structure Investigation in a Turbulent Boundary Layer Using Orthogonal X-Wire Arrays.* 11th Australasian Fluid Mech. Conf., Hobart/Australia, Dec.1992.

[130] Lading,L., Edwards,R.V. (1975) *The Effect of Measurement Volume on Laser Doppler Anemometer Measurements as Measured on Simulated Signals.* Proc. of

the LDA-Symposium, The Accuracy of Flow Measurements by Laser Doppler Methods, Copenhagen, pp 64–80.

[131] Lee,J.H.W, Rodi,W. (1994) *Numerical Simulation of Line Puffs* in: Recent Research Advances in Fluid Mechanics of Turbulent Jets and Puffs, v 255, pp 73–88, Kluwer Academic Publishers.

[132] Lesieur,M. (1990) *Fluid mechanics and its applications: turbulence in fluids.* Kluwer Academic Publishers.

[133] Liepmann,D., Gharib,M. (1992) *The role of streamwise vorticity in the near-field entrainment of round jets.* Journal of Fluid Mechanics, v 245, pp 643-668.

[134] Ligrani,P.M., Singer,B.A., Baun,L.R. (1989) *Miniature five-hole pressure probe for measurement of three mean velocity components in low-speed flow.* Journal of Physics E: Sci.Instrum. v 22, pp 868-876.

[135] Lim,T.T., Kelso,R.M., Perry,A.E. (1992) *A Study of a Round Jet in Cross–Flow at Different Velocity Ratios.* 11th Australasian Fluid Mechanics Conference, Hobart, Australia, December 1992.

[136] Loader,A.J., Thew,M.T. (1975) *Analysis and Characteristics of Turbulence in Confined Swirling Flow Studied with an LDA.* Proc. of the LDA-Symposium, The Accuracy of Flow Measurements by Laser Doppler Methods, Copenhagen, pp 690–703.

[137] Lovett,J.A., Turns,S.R.(1990) *Experiments on Axisymmetrically Pulsed Turbulent Jet Flames.* AIAA Journal, v 28, No.1, pp 38-46.

[138] Lozano,A., Smith,S.H., Mungal,M.G., Hanson,R.K. (1993) *Concentration Measurements in a Transverse Jet by Planar Laser-Induced Fluorescence of Acetone.* AIAA Journal, v 32, No.1, Technical Notes, pp 218-221.

[139] Lu,S.S., Willmarth,W.W. (1973) *Measurements of the structure of the Reynolds stress in a turbulent boundary layer.* Journal of Fluid Mechanics, v 60, part 3, pp 481-511.

[140] Lumley,J.L. (1965) *Interpretation of Time Spectra Measured in High-Intensity Shear Flows.* Physics in Fluids, v 8, No.6, pp 1056-1062.

[141] Luxton,R.E. (1993) *On mixing cement and the hot end of aerodynamics.* Symposium on Developments in Fluid Dynamics and Aerospace Engineering, Bangalore/India.

[142] Luxton,R.E., Nathan,G.J., Luminis Pty.Ltd. (1988) *Mixing of Fluids.* Patent Application No.16235/88, Australian Patent Office, April 1988, International Patent Application No. PCT/AU88/00114, April 1988.

[143] Manias,C.G., Nathan,G.J. (1993) *The precessing jet gas burner – a low NO_x burner providing process efficiency and product quality.* Journal of World Cement.

[144] Manias,C.G., Nathan,G.J. (1994) *Low NO_x clinker Production.* Journal of World Cement.

[145] Manias,C.G., Nathan,G.J. (1995) *Low NO_x clinker Production.* Journal of World Cement, 1995.

[146] Manohar, S.S. (1994) *Large Eddy Simulation of a Precessing Deflected Jet.* PhD proposal, Pennsylvania State University, 1994.

[147] Manohar, S.S., Pauly,L.L., Kulkarni,A.K. (1996) *Three-Dimensional Numerical Analysis of Low Reynolds Number Precessing Jets.* Internal Report, Pennsylvania State University, 1996.

[148] Margason,R.J. (1993) Fifty Years of Jet in Cross Flow Research. AGARD, Computational and Experimental Assessment of Jets in Cross Flow, pp 1-1 – 1-41.

[149] Martens,S., Schulz,R., Spiess,B., Gass,J., Suter,P. (1994) *Comparison of different radiation models for flames applied to a 200kW Methane combustor.* EUROTHERM Seminar, no.37, Heat Transfer in Radiating and Combusting Systems.

[150] Mason,P.J., Morton,B.R. (1987) *Trailing vortices in the wakes of surface-mounted obstacles.* Journal of Fluid Mechanics, v 175, pp 247-293.

[151] Maxworthy,T. (1974) *Turbulent Vortex Rings* Journal of Fluid Mechanics, v 64, pp 227-239.

[152] Maxworthy,T. (1977) *Some experimental studies of vortex rings* Journal of Fluid Mechanics, v 81, part 3, pp 465–495.

[153] McLaughlin,D.K., Tiederman,W.G. (1973) *Biasing correction for individual realization of laser anemometer measurements in turbulent flows.* Physics of Fluids, v 16, pp 2082-2088.

[154] Mehta,R.D. (1977) *The aerodynamic design of blower tunnels with wide-angle diffusers.* Prog. Aerospace Sci., v 18, pp 59-120.

[155] Mehta,R.D., Bradshaw,P. (1978) *Design rules for small low speed wind tunnels.* Aeronautical Journal, Technical Notes, pp 443–449.

[156] Meissner,L.P., Organick,E.I. (1984) *Fortran - Featuring structured programming.* Addison-Wesley 1984.

[157] Melander,M.V., Hussain,F. (1994) *Topological vortex dynamics in viscous flows.* Journal of Fluid Mechanics, v 260, pp 57-80.

[158] Melling,A., Whitelaw,J.H. (1975) *Optical and Flow aspects of particles.* Proc.of the LDA-Symposium, The Accuracy of Flow Measurements by Laser Doppler Methods, Copenhagen, pp 382-402.

[159] Mi,J., Nathan,G.J., Luxton,R.E. (1995) *Dynamic Oscillation of a Quasi–Planar Jet.* 12th Australasian Fluid Mechanics Conference, Sydney, Australia, December 1995.

[160] Miller,I.S., Shah,D.A., Antonia,R.A. (1987) *A constant temperature hot-wire anemometer.* Journal of Physics in Engineering E: Sci.Instrum., v 20, pp 311-314.

[161] Moffat,R.J. (1988) *Describing the Uncertainties in Experimental Results.* Experimental Thermal and Fluid Science, v 3, pp 3-17.

[162] Morton,B.R. (1969) *The strength of vortex and swirling core flows.* Journal of Fluid Mechanics, v 38, pp 315-333.

[163] Morton,B.R. (1984) *The Generation and Decay of Vorticity.* Geophys. Astrophys. Fluid Dynamics, v 28, pp 277-308.

[164] Morton,B.R., Nguyen,K.C., Cresswell,R.W. (1994) *Similarity and Self–Similarity in the Motion of Thermals and Puffs.* Recent Research Advances in Fluid Mechanics of Turbulent Jets and Puffs, v 255, pp 89–115, Kluwer Academic Publishers.

[165] Moustafa,G.H., Rathakrishnan,E. (1993) *Studies on the Flowfield of Multijet with Square Configuration.* AIAA Journal, v 31, No.7, pp 1189-1190.

[166] Mullinger,P.J. (1984) *Burner design for coal fired cement kilns.* Journal of World Cement, December 1984.

[167] Mullinger,P.J. (1986) *Fuel cost reduction by flame control.* Journal of World Cement, March 1986.

[168] Mungal,M.G., Lourenco,L.M., Krothapalli,A. (1994) *Instantaneous Velocity Measurements in Laminar and Turbulent Premixed Flames Using On-Line PIV.* Int.Symposium on Appl. of Lasers to Fluid Mechanics, Lisbon, Portugal, July 11-14 1994.

[169] Mungal,M.G., Lozano,A., Nguyen,S.A. (1992) *Large-Scale Structure of High Reynolds Number Jets and Jet Flames.* 2nd Caribbean Conf.on Fluid Dynamics, St.Augustine, Trinidad, Jan.5-8 1992.

[170] Musgrove,A.R., Hooper,J.D. (1993) *Pressure Probe Measurements of the the Turbulent Stress Distribution in a Swirling Jet.* 3rd World Conf. on Experimental Heat Transfer, Fluid Mechanics and Thermodynamics. Hawaii, USA, Oct./Nov. 1993.

[171] Musgrove,A.R., Hooper,J.D. (1995) *Pressure–Velocity Correlations in Swirling Jet Flow.* 6th Asian Congress of Fluid Mechanics, Singapore, May 1995.

[172] Musgrove,A.R., Hooper,J.D., Rainey,S., Maher,M.T. (1995) *The Calibration and Use of a Water-Based Version of the Cobra Probe.* 6th Asian Congress of Fluid Mechanics, Singapore, May 1995.

[173] Nathan,G.J. (1988) *The Enhanced Mixing Burner.* PhD Thesis, University of Adelaide, Australia.

[174] Nathan,G.J. (1992) *The Radiation Characteristics of the . Precessing Jet Burner firing Natural Gas in a 50kW Furnace.* Internal Report to Gladstone Power Station, Queensland Electricity Commission, Dept.Mech.Eng, University of Adelaide, Australia.

[175] Nathan,G.J., Brumale,S., Proctor,D., Luxton,R.E. (1993) *NO_x reduction in flames by modification of turbulence with jet precession.* Combustion and Emission Control, ISBN 0902597434, pp 213–230.

[176] Nathan,G.J., Luxton,R.E. (1988) *A Stable, Un-Premixed Gas Burner with Infinite Turn-Down Ratio.* 1st European Conf. Industrial Furnaces and Boilers, Lisbon/Portugal, March 1988.

[177] Nathan,G.J., Luxton,R.E. (1989) *The combustion characteristics of an enhanced mixing nozzle.* The Combustion Institute, Joint Int.Conf., Sydney, Australia, Sep.1989, pp 248-251.

[178] Nathan,G.J., Luxton,R.E. (1989) *A Precessing Asymmetric Flow Field in an Abruptly Expanding Axi-Symmetric Duct.* 10th Australasian Fluid Mechanics Conf., Melbourne, Australia, December 1989.

[179] Nathan,G.J., Luxton,R.E., Balendra,S.A., Williams,G.H., Manias,C.G. (1990) *A Preliminary assessment of the Enhanced Mixing Burner in a cement kiln.* Internal Report, Dep.Mech.Eng, University of Adelaide, Australia.

[180] Nathan,G.J., Luxton,R.E. (1991) *The Stability and Emission Characteristics of the Enhanced Mixing Burner in a 50kW Furnace.* Final Report to the State Energy Research Advisory Committee for the Period 1989/90, Dep. Mech.Eng., University of Adelaide, Australia.

[181] Nathan,G.J., Luxton,R.E. (1991) *The entrainment and combustion characteristics of an axi-symmetric, self exciting, enhanced mixing nozzle.* ASME/JSME Thermal Engineering Proceedings, v 5, pp 145-152.

[182] Nathan,G.J., Luxton,R.E. (1991) *Flame Stability and Emission Characteristics of the Enhanced Mixing Burner.* 2nd European Conf. on Industrial Furnaces and Boilers, Algarve, Portugal, April 1991.

[183] Nathan,G.J., Luxton,R.E. (1991) *Mixing enhancement by a self-exciting, asymmetric precessing flow-field.* Fourth International Symposium of Transport Phenomena, Sydney, Australia, July 1991.

[184] Nathan,G.J., Luxton,R.E. (1991) *A low NO_x gas burner with a radiant flame.* Energy Efficiency in Process Technology - Comm.of the European Communities. Vouliagmeni/Greece, Oct. 1992.

[185] Nathan,G.J., Luxton,R.E. (1992) *A three dimensional instability behind a large axisymmetric sudden expansion.* Submitted to Journal of Fluid Mechanics.

[186] Nathan,G.J., Luxton,R.E. (1992) *The flow field within an axi-symmetric nozzle utilising a large abrupt expansion.* Recent Advances in Experimental Fluid Mechanics, pp 527-532.

[187] Nathan,G.J., Luxton,R.E. (1992) *Large Scale Turbulence Generated by a Precessing Free Jet.* Internal Report, University of Adelaide, Australia.

[188] Nathan,G.J., Luxton,R.E. (1992) *Results from Full-Scale Trials Firing the Precessing Jet Burner with Natural Gas in QEC Gladstone Boiler No.6.* Internal Report, Dept.Mech.Eng., University of Adelaide, Australia, Sept.1992.

[189] Nathan,G.J., Luxton,R.E. (1992) *The enhanced mixing burner: a technical brief.* Internal Report, Dept.Mech.Eng., University of Adelaide, Australia.

[190] Nathan,G.J., Luxton,R.E., Smart,J.P. (1992) *Reduced* NO_x *Emissions and Enhanced Large Scale Turbulence from a Precessing Jet Burner.* 24th Symposium of Combustion, Sydney, Australia, July 1992.

[191] Nathan,G.J., Manias,C.G, Luxton,R.E. (1991) *Potential Increases in the Efficiency of a Rotary Kiln using an Enhanced Mixing Burner.* IEAust International Mech Eng Congress, Sydney, Australia, July 1991, pp 58-61.

[192] Nathan,G.J., Manias,C.G. (1992) *The precessing jet gas burner - a low* No_x *burner providing process efficiency and product quality improvements.* Int.Kiln Assoc.Conf., Toronto, Canada, Oct.1992.

[193] Nathan,G.J., Smart,J.P. (1991) *A Simple, Unswirled Low* No_x *Gas Burner.* 2nd Austr.Flame Days, IFRF, Sydney, Australia, Oct.1991.

[194] Nathan,G.J., Smart,J.P. (1991) *An Investigation of the Combustion Characteristics of the Enhanced Mixing Burner firing Natural Gas at 2MW.* IFRF Doc. No. F90/y/9, Int. Flame Research Foundation, Ijmuiden, Netherlands.

[195] Nathan,G.J., Turns,S.R., Bandaru,R.V. (1996) *The Influence on NO_x Emissions and Radiation from Turbulent Flames.* Journal of Combustion Science and Technology, v 112, p 213.

[196] Neill,T., Kennedy,,I.M. (1990) *Soot Formation in Ducted Turbulent Diffusion Flames.* AIAA Journal, v 29, No.6, pp 932-935.

[197] Needham,D.J., Riley,N., Smith,J.H.B. (1988) *A jet in a crossflow.* Journal of Fluid Mechanics, v 188, pp 159-184.

[198] Newbold,G.J.R. (1997) *Mixing and Combustion Characteristics of the Precessing Jet Burner.* PhD Thesis, University of Adelaide.

[199] National Inst. of Economic and Industry Research (1994) *Measuring the Economic Impact of Reducing Greenhouse Gas Emissions.* Report for the Electricity Supply Ass. of Australia.

[200] Nishiyama,H., Ota,T., Hamada,M., Takahashi,Y. (1991) *Temperature Fluctuations of a Two-Dimensional Slightly Heated Jet Issuing into a Cross Flow.* Experimental Heat Transfer, Fluid Mechanics and Thermodynamics, pp 436-442.

[201] Owen,J.M., Rogers,R.H. (1975) *Velocity Biasing in Laser Doppler Anemometers.* Proc. of the LDA-Symposium, The Accuracy of Flow Measurements by Laser Doppler Methods, Copenhagen, pp 89–114.

[202] Page,M.A., Earbry,M.D. (1990) *The breakdown of jet flows in a low-Rossby-number rotating fluid.* Journal of Engineering Mathematics, v 24, pp 287-310.

[203] Paleokrassas,I.A. (1992) *Energy Efficiency in Process Technology.* Energy Efficiency in Process Technology - Comm.of the European Communities. Vouliagmeni/Greece, Oct. 1992.

[204] Pankhurst,R.C., Holder,D.W. (1952) *Wind tunnel technique.* Pitman.

[205] Papangelou,A.(1992) *A "robust" vortex-shedding anemometer.* Experiments in Fluids, v 14, Technical Notes, pp 208-210.

[206] Paschereit,C.O., Oster,D., Long,T.A., Fiedler,H.E., Wygnanski,I. (1992) *Flow visualization of interaction among large coherent structure in an axisymmetric jet.* Experiments in Fluids, v 12, pp 189-199.

[207] Patankar,S.V., Basu,D.K., Alpay,S.A. (1977) *Prediction of the Three-Dimensional Velocity Field of a Deflected Turbulent Jet.* Journal of Fluids in Engineering, pp 758-762.

[208] Perry,A.E. (1982) *Hot-wire anemometry.* Clarendon Press Oxford.

[209] Perry,A.E. (1986) *A Descripton of Eddying Motions and Turbulence.* 9th Australasian Fluid Mechanics Conference, Auckland, December 1986.

[210] Piatt,M., Viets,H. (1979) *Conditional Sampling in an Unsteady Jet* AIAA Aircraft systems and Technology Meeting, New York, August 1979.

[211] Piomelli,U., Balint,J.L., Wallace,M. (1989) *On the validity of Taylor's hypothesis for wall-bounded flow.* Physics in Fluids A: v 1, No.3, pp 609-611.

[212] Presser,C., Gupta,A.K., Avedisian,C.T., Semerjian,H.G.(1992) *Combustion of Methanol and Methanol/Dodecanol Spray Flames.* Journal of Propulsion and Power, v 8, No.3, pp 553-559.

[213] Presser,C., Gupta,A.K., Semerjian,H.G., Avedisian,C.T. (1994) *Droplet Transport in a Swirl-Stabilized Spray Flame.* Journal of Propulsion and Power, v 10, No.5, pp 631-638.

[214] Press,W.H., Flannery,B.P., Teukolsky,S.A., Vetterling,W.T. (1987) *Numerical Recipes: The Art of Scientific Computing* Cambridge University Press.

[215] Pratte,B.D., Baines,W.D. (1967) *Profiles of the round turbulent jet in a cross flow.* ASCE, Journal of the Hydraulics Division, HY 6, pp 53-64.

[216] Prandtl,L., Oswatitsch,K., Wieghardt,K. (1984) *Führer durch die Strömungslehre* 8.Auflage, Vieweg Verlag, Braunschweig.

[217] Proctor,D., Nathan,G.J., Luxton,R.E., Pearson,I.G., Brumale,S.A., Mann,B.A., Schneider,G.M. and Newbold,G.J.R. (1993) *The Efficient Low NO_x Burning of Gas for Large Scale Industrial Applications.* 2nd International Conference on Combustion Technologies for a Clean Environment. v II, paper 26.1, pp 1-8. Lisbon, Portugal, Sep.1993.

[218] Proctor,D., Nathan,G.J., Pearson,I.G., Mann,B.A., Schneider,G.M. and Luxton,R.E. (1993) *The Turbulence and Combustion Interaction in a Free Precessing Jet Flame.* The Australian Symposium on Combustion incl. The Third Australian Flame Days, Newcastle, Australia, Nov.1993.

[219] Rajagopalan,S., Antonia,R.A. (1992) *Structure of Spanwise Vorticity in a low Reynolds Number Turbulent Boundary Layer.* 11th Australasian Fluid Mech. Conf., Hobart/Australia, December 1992, pp 243-246.

[220] Rajaratnam,N. (1976) *Turbulent jets.* Elsevier Scientific Publishing Company.

[221] Rhode,D.L., Lilley,D.G. (1983) *Mean Flowfields in Axisymmetric Combustor Geometries with Swirl.* AIAA Journal, v 21, No.4, pp 593-600.

[222] Richards,J.M. (1965) *Puff motions in unstratified surroundings.* Journal of Fluid Mechanics, v 21, pp 97-106.

[223] Ricou,F.P., Spalding,D.B. (1961) *Measurements of entrainment by axisymmetrical turbulent jets.* Journal of Fluid Mechanics, v 11, pp 21-32.

[224] Roberts,J.B.(1973) *On the correction of hot wire turbulence measurements for spatial resolution errors.* Aeronautical Journal, Technical Notes, pp 406-412.

[225] Rogers,M.M., Moin,P. (1987) *The structure of the vorticity field in homogeneous turbulent flows.* Journal of Fluid Mechanics, v 176, pp 33-66.

[226] Røkke,N.A., Hustad,J.E., Sonju,O.K. (1994) *A Study of Partially Premixed Unconfined Propane Flames.* Combustion and Flame, v 97, pp 88-106.

[227] Røkke,N.A., Hustad,J.E., Sonju,O.K., Williams,F.A. (1992) *Scaling of Nitric Oxide Emissions from Buoyancy-Dominated Hydrocarbon Turbulent-Jet Diffusion Flames.* 24th Int.Symp.on Combustion/The Comb.Inst., Sydney, Australia, pp 385-393.

[228] Rosenhead,L. (1963) *Laminar Boundary Layers.* Oxford at the Clarendon Press.

[229] Roshko,A. (1991) *Uses of flow visualization in research.* Int. Conference on Exp. Fluid Mechanics, pp 3-11.

[230] Roshko,A. (1954) *On the development of turbulent wakes from vortex streets.* NACA Rep. 1191, pp 801-825.

[231] Rouse,H., Ince,S. (1957) *History of Hydraulics (rev.ed.).* Iowa Institute of Hydraulic Research.

[232] Sallam,T.M., Kaji,M., Nakanishi,S., Ishigai,S. (1980) *Visualisation of Recirculating Flows in Reversed-Flow Furnace Models.* Technology reports of the Osaka University, Mechanical Engineering, Osaka, Japan, pp 57-61.

[233] Sallam,T.M., Kaji,M., Nakanishi,S., Ishigai,S, Matsumoto,S. (1980) *Characteristics of Reversed Flow Due to Jet Issuing to Dead-End channel.* Technology reports of the Osaka University, v 30, No.1539, pp 217-224.

[234] Salter,C. (1966) *Low-speed wind tunnels for special purposes.* NPL Aero Report 1218 (revised).

[235] Saunders,C., Rickards,J., Swales,C., Barrett,R.V. (1994) *The application of 3D Laser Doppler Anemometry to Large Scale Flow Measurements on a Formula 1 Racing Car.* 7th Int.Symposium on Applications of lasers to fluid mechanics, Lisbon, Portugal, July 1994.

[236] Savage,S.B., Sobey,R.J. (1975) *Horizontal momentum jets in rotating basins.* Journal of Fluid Mechanics. v 71, part 4, pp 755-768.

[237] Schlichting,H., Truckenbrodt,E. (1967). *Aerodynamik des Flugzeugs. Band 1: Grundlagen der Strömungsmechanik, Aerodynamik des Tragflügels.* Springer-Verlag 1967.

[238] Schlichting,H. (1960). *Boundary Layer Theory* McGraw-Hill, New York, 4th edition, pp 747.

[239] Schneider,W. (1985). *Decay of Momentum Flux in Submerged Jets* Journal of Fluid Mechanics, v 154, pp 91–110.

[240] Schneider,G.M., Nathan,G.J. and Luxton,R.E. (1992). *An Experimental Study of a Precessing, Deflected Jet.* 11th Australasian Fluid Mechanics Conference Hobart, Dec.1992.

[241] Schneider,G.M., Vidakovic,S.S., Hooper,J.D., Musgrove,A.R., Nathan,G.J. and Luxton,R.E. (1993) *Theoretical and Experimental Pressure Field Evaluation Downstream of a Mechanically Precessing Jet.* 4th Heat and Mass Transfer Conference. Brisbane, Australia, Dec.1992.

[242] Schneider,G.M., Nathan,G.J., Luxton,R.E., Hooper,J.D., Musgrove,A.R. (1994) *Velocity and Reynolds Stresses in a Precessing, Deflected Jet.* 2nd Int.Conf. on Experimental Fluid Mechanics, Torino, Italy, July 1994.

[243] Schneider,G.M., Nathan,G.J. and Luxton,R.E. (1994). *Velocity Contours in a Precessing, Deflected Jet.* 1st International Conference on Flow Interaction. Hong Kong, Sep.1994.

[244] Schneider,G.M., Froud,D., Syred,N., Nathan,G.J., Luxton,R.E. (1996) *Velocity Measurements in a Precessing Jet Flow Using a Three Dimensional LDA System.* Journal of Experiments in Fluids, to appear in 1996.

[245] Schneider,G.M., Nathan,G.J., Luxton,R.E., Hooper,J.D., Musgrove,A.R. (1996) *Velocity and Reynolds Stresses in a Precessing Jet* Journal of Experiments in Fluids, to appear in 1996.

[246] Schetz,J.A. (1992). *Hydrodynamics of Jets in Crossflow.* Encyclopedia of Fluid Mechanics, v 2, Dynamics of Single-Fluid Flows and Mixing, ed.Cheremisinoff.

[247] Scott,K.D. (1986) *The turbulent boundary layer on a long slender cylinder in axial flow effects of yaw.* Final Report on a Research Project for the Honours Degree, Dep.Mech.Eng., University of Adelaide, Australia.

[248] Shepherd,I.C. (1981) *A Four Hole Pressure Probe for Fluid Flow Measurements in Three Dimensions.* Journal of Fluids Engineering, v 103, pp 590-594.

[249] Shlien,D.J. (1987) *Observation of dispersion of entrained fluid in the self-preserving region of a turbulent jet.* Journal of Fluid Mechanics, v 183, pp 163-173.

[250] Simmons,J.M., Lai,J.C.S., Platzer,M.F. (1981) *Jet Excitation by an Oscillating Vane.* AIAA Journal, v 19, No.6, pp 673-676.

[251] Simmons,J.M., Platzer,M.F., Smith,T.C. (1978) *Velocity Measurements in an oscillating plane jet issuing into a moving air stream.* Journal of Fluid Mechanics, v 84, part 1, pp 33-53.

[252] Smith,S.H., Lozano,A., Mungal,M.G., Hanson,R.K. (1993) *Scalar Mixing in the Subsonic Jet in Crossflow.* AGRAD's Jet in Cross Flow Symposium. Winchester, UK, April 1993.

[253] Spliethoff,H., Maier,M., Hein,K.R.G. (1994) *Low NO_x-Firing and the Requirements for the Coal Size* Summary of the poster, 25th Int.Symposium on Combustion, Irvine, USA, Aug.1994.

[254] Sreenivasan,K.R., Antonia,R.A. (1978) *Joint Probability Densities and Quadrant Contributions in a Heated Turbulent Round Jet.* AIAA Journal, v 16, No.6, pp 867-868.

[255] StGeorges,M., Buchlin,J.M., Riethmuller,M.L., Lopez,J.P., Lieto,J., Griolet,F. (1992) *Fundamental multidisciplinary study of liquid sprays for absorption of pollutant or toxic clouds.* 7th Int.Symp.on Loss Prevention and Safety Prom. in the Proc.Ind., Taormina, Italy, May 1992.

[256] StGeorges,M., Griolet,F., Buchlin,J.M., Riethmuller,M.L., Lieto,J. (1993) *Modelling of the mitigation of hazardous releases by diluting and absorbing fluid curtains.* European Meet. on Chem. Industry and Environment, Girona, Spain, June 1993.

[257] Stocker,D.P., Sheu,J.C., Chen,L.D.(1993) *Preliminary observations of the effect of microgravity on a pulsed jet diffusion flame.* Western States Sect./Combustion Institute, Fall Meeting, pp 93-065.

[258] Sykes,R.I., Lewellen,W.S., Parker,S.F. (1986) *On the Vorticity Dynamics of a Trubulent Jet in a Crossflow.* Journal of Fluid Mechanics, v 168, pp 393–413.

[259] Syred,N., Beer,J.M. (1974) *Swirling Flows – A Review.* Journal of Combustion and Flame, v 23, pp 143–201.

[260] Syred,N., O'Doherty,T. (1992) *An Overview of Flame Driven Emission Work at Cardiff.* Internal Report, University of Wales, Cardiff, UK.

[261] Syred,N., O'Doherty,T. (1992) *The Interaction of the Precessing Vortex Core and Reverse Flow Zone in the Exhaust of a Swirl Burner.* Institute of Energy.

[262] Syred,N., Sidnu,B.S, Styles,A.C. (1984) *Characteristics of Swirling Flow Exhausting from Nozzles with Curved Walls.* Laser Anemometry in Fluid Mechanics, ed.Durao, pp 241–252.

[263] Syred,N., Hanby,V.I., Gupta,A.K. (1973) *Resonant instabilities generated by swirl burners.* Journal of the Institute of Fuel, pp 402–407.

[264] Tansley,G.D. (1994) *CFD Through PHOENICS.* Lecture Notes and introductory course in PHOENICS, Dep.Mech.Eng., University of Adelaide, Australia.

[265] Taylor,G.I. (1937) *The spectrum of turbulence* Proceedings Of the Royal Society, A 164, pp 477-490.

[266] Taylor,G.I. (1938) *Production and Dissipation of Vorticity in a Turbulent Fluid.* Proceedings Of the Royal Society, A 164, 476, pp 15-23.

[267] Tennekes,H., Lumley,J.L. (1973) *A First Course in Turbulence.* 2nd edition, MIT Press.

[268] Tollmien,W. (1926) *Berechnungen turbulenter Ausbreitungsvorgänge* Z.A.M.M., v 6, pp 468–478. (english translation, N.A.C.A. TM 1085, 1945).

[269] Tonouchi,J.H., Pratt,D.T., Steele,R.C. (1994) *The Effects of Macro-and Micro-mixing on Lean Premixed Combustion.* Work-in-Progress-Poster, 25th Int.Symp. on Combustion, Irvine, USA, July/Aug.1994.

[270] Townsend,A.A. (1966) *The mechanism of entrainment in free turbulent flows.* Journal of Fluid Mechanics, v 26, pp 689–715.

[271] Townsend,A.A. (1976) *The Structure of Turbulent Flow.* 2nd edition, Cambridge University Press.

[272] Tritton,D.J. (1977) *Physical Fluid Dynamics* van Nostrand Reinhold Company.

[273] Turner,J.S. (1964) *The flow into an expanding spherical vortex* Journal of Fluid Mechanics, v 18, pp 195–208.

[274] Turner,J.S. (1986) *Turbulent entrainment: the development of the entrainment assumption, and its application to geophysical flows.* Journal of Fluid Mechanics, v 173, pp 431-471.

[275] Valenti,M. (1993) *Retrofitting Plants with Low-NO_x Burners.* Mechanical Engineering, May 1993.

[276] van de Loo,P. (1985) *The turbulent boundary layer on a long slender cylinder aligned with the flow.* Final Report on a Research Project for the Honours Degree, Dep.Mech.Eng., University of Adelaide, Australia.

[277] Vidakovic,S.S., Luxton,R.E. (1992) *Fluid Mechanics of Deflected Jets: Evaluation of Nozzle Thrust Vectors.* 11th Australasian Fluid Mechanics Conference, Hobart, Australia, Dec.1992.

[278] Vidakovic,S.S. (1995) *Fluid Dynamic Means of Varying the Thrust Vector from an Axisymmetric Nozzle.* PhD Thesis, University of Adelaide, Australia.

[279] Viets,H. (1975) *Flip–Flop Jet Nozzle* AIAA Journal, v 13, No.10, pp 1375–1379.

[280] Vukoslavcevic,P., Wallace,J.M. (1981) *Influence of velocity gradients on measurements of velocity and streamwise vorticity with hot-wire X-array probes.* Rev.Sci.Instrum., v 52, No.6, pp 869-879.

[281] Vukoslavcevic,P., Wallace,J.M., Balint,J.L. (1991) *The velocity and vorticity vector fields of a turbulent boundary layer. Part 1. Simultaneous measurement by hot-wire anemometry.* Journal of Fluid Mechanics, v 228, pp 25-51.

[282] Wallace,J.M. (1986) *A review: Methods of measuring vorticity in turbulent flows.* Experiments in Fluids. v 4, pp 61-71.

[283] Ward,D.E., Nathan,G.J. (1990) *The feasibility of applying Enhanced Mixing Techniques to the Swanbank-A pulverised fuel burners.* Internal Report to the Queensland Electricity Commission, Dept. Mech.Eng, University of Adelaide, Australia.

[284] Ward,D.E., Nathan,G.J., Luxton,R.E., Truce,R.J. (1990) *An Enhanced Mixing PF Burner for the QEC Swanbank-A Power Station.* 1st Australian Flame Days, IFRF, Brisbane, Australia, Dec.1990.

[285] Watt,D.W., Vest,C.M. (1990) *Turbulent flow visualization by interferometric integral imaging and computed tomography.* Experiments in Fluids, v 8, pp 301-311.

[286] Weber,R., Dugué,J. (1992) *Combustion Accelerated Swirling Flows in High Confinements.* Prog.Energy Combust.Sci., v 18, pp 349-367.

[287] Wieghardt,K.E.G. (1953) *On resistance of screens.* Aero Quarterly, v 4, p 186.

[288] Wigeland,R.A., Ahmed,M., Nagib,H.M. (1978) *Vorticity Measurements Using Calibrated Vane-Vorticity Indicators and Cross-Wires.* AIAA Journal, v 16, No.12, pp 1229-1234.

[289] Williamson,C.H.K (1989) *Oblique and parallel modes of vortex shedding in the wake of a circular cylinder at low Reynolds numbers.* Journal of Fluid Mechanics, v 206, pp 579-627.

[290] Willmarth,W.W., Bogar,T.J. (1977) *Survey and new measurements of turbulent structure near the wall.* Physics of Fluids, v 20, No.10, part 2, pp S9-S21.

[291] Winter,A.R., Graham,L.J.W., Bremhorst,K. (1991). *Velocity Bias Associated With Laser Doppler Anemometer Controlled Processors.* J.Fluids Eng., Trans, ASME, v 113, pp 250-255.

[292] Winter,A.R., Graham,L.J.W., Bremhorst,K. (1991). *Effects of time scales on velocity bias in LDA measurements using sample and hold processing.* Experiments in Fluids, v 11, pp 147-152.

[293] Wright,M.A. (1970) *The evaluation of a simplified form of presentation for five-hole spherical and hemispherical pitometer calibration data.* Journal of Physics E: Sci.Instrum., v 3, pp 356-362.

[294] Wu,J.M., Vakili,A.D., Yu,.F.M. (1988) *Investigation of the interacting flow of nonsymmetric jets in crossflow.* AIAA Journal, v 26, pp 940-947.

[295] Wygnanski,I., Fiedler,H. (1969) *Some measurements in the self-preserving jet.* Journal of Fluid Mechanics, v 38, pp 577-612.

[296] Wyngaard,J.C. (1968) *Measurement of small-scale turbulence structure with hot wires.* Journal of Physics E: Sci.Instr., v 1, Series 2, pp 1105-1108.

[297] Wyngaard,J.C. (1969) *Spatial resolution of the vorticity meter and other hot-wire arrays.* Journal of Physics E: Sci.Instr., v 2, Series 2, pp 983-987.

Appendix A

Further Visualisation: St_p=0.002 and Re=26,600

Figure A.1: **Conditional smoke visualisation. St_p=0.002, Re=26,600.**

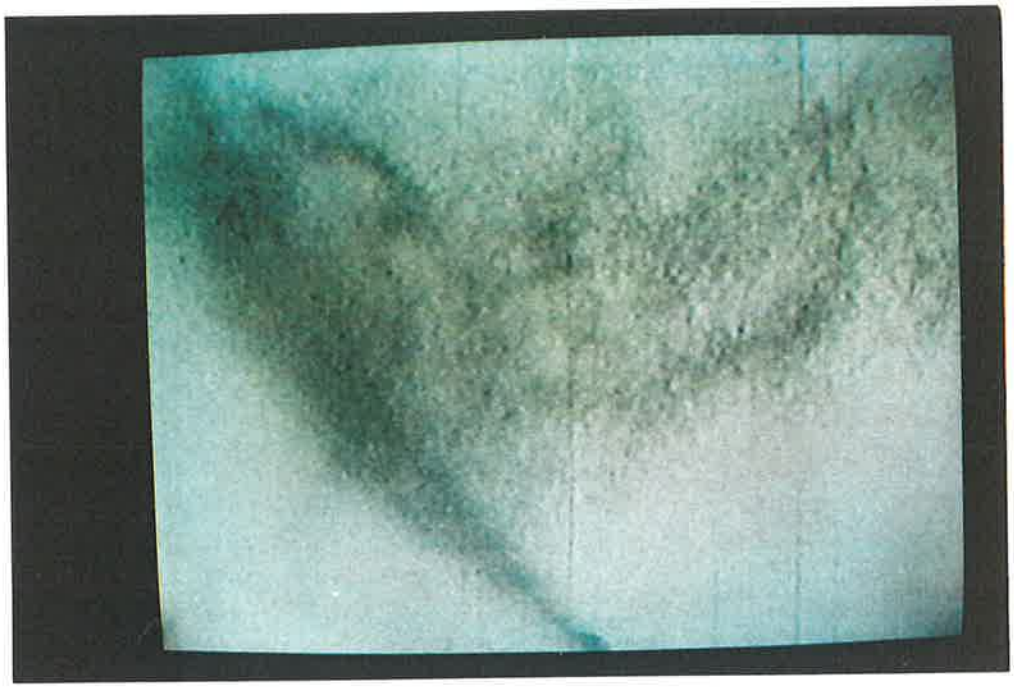

Figure A.2: **Laser illuminated flow field of the precessing jet. St_p=0.002, Re=26,600.**

Appendix B

Further Visualisation: St_p=0.015 and Re=26,600

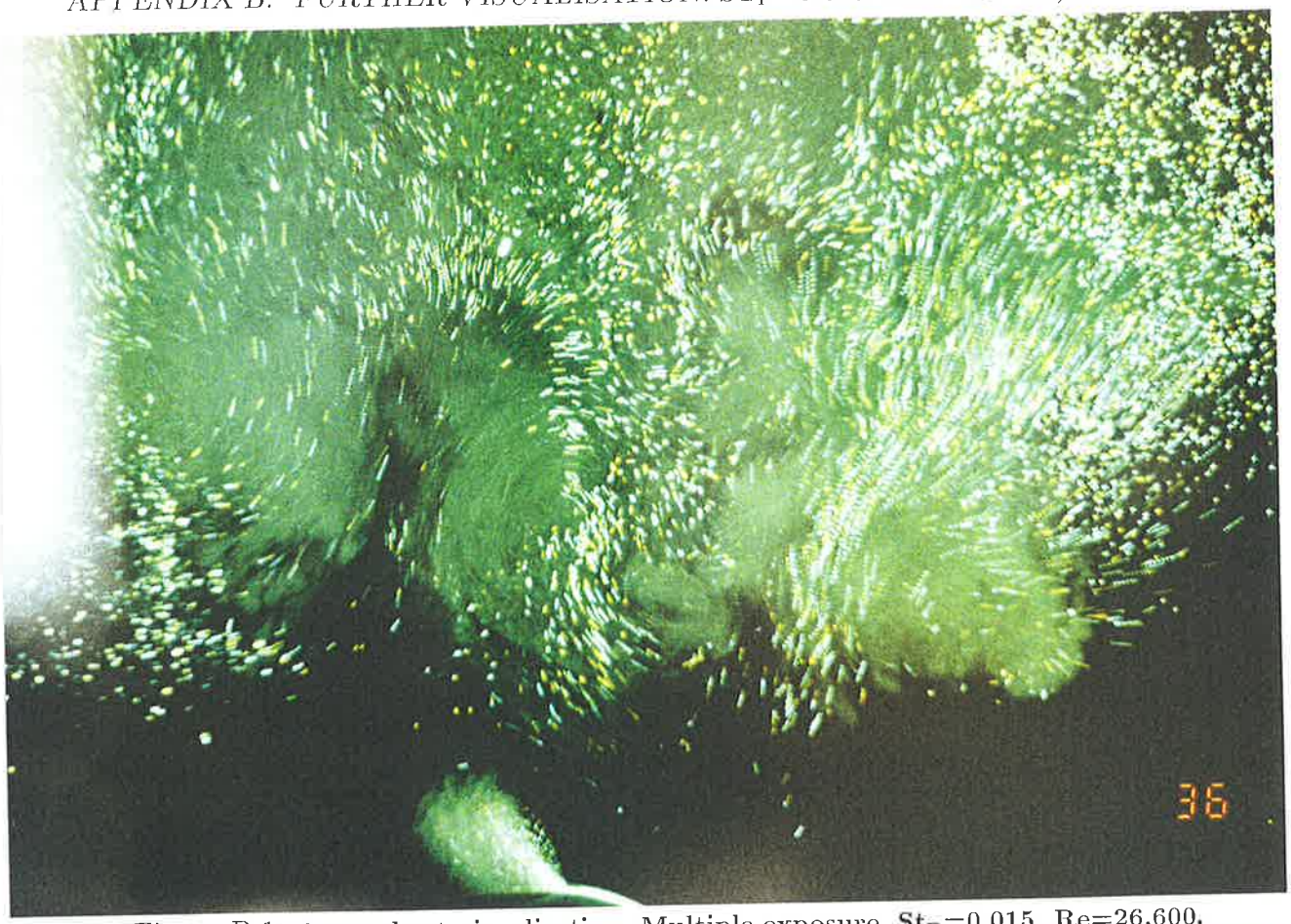

Figure B.1: **Laser sheet visualisation. Multiple exposure, St_p=0.015, Re=26,600.**

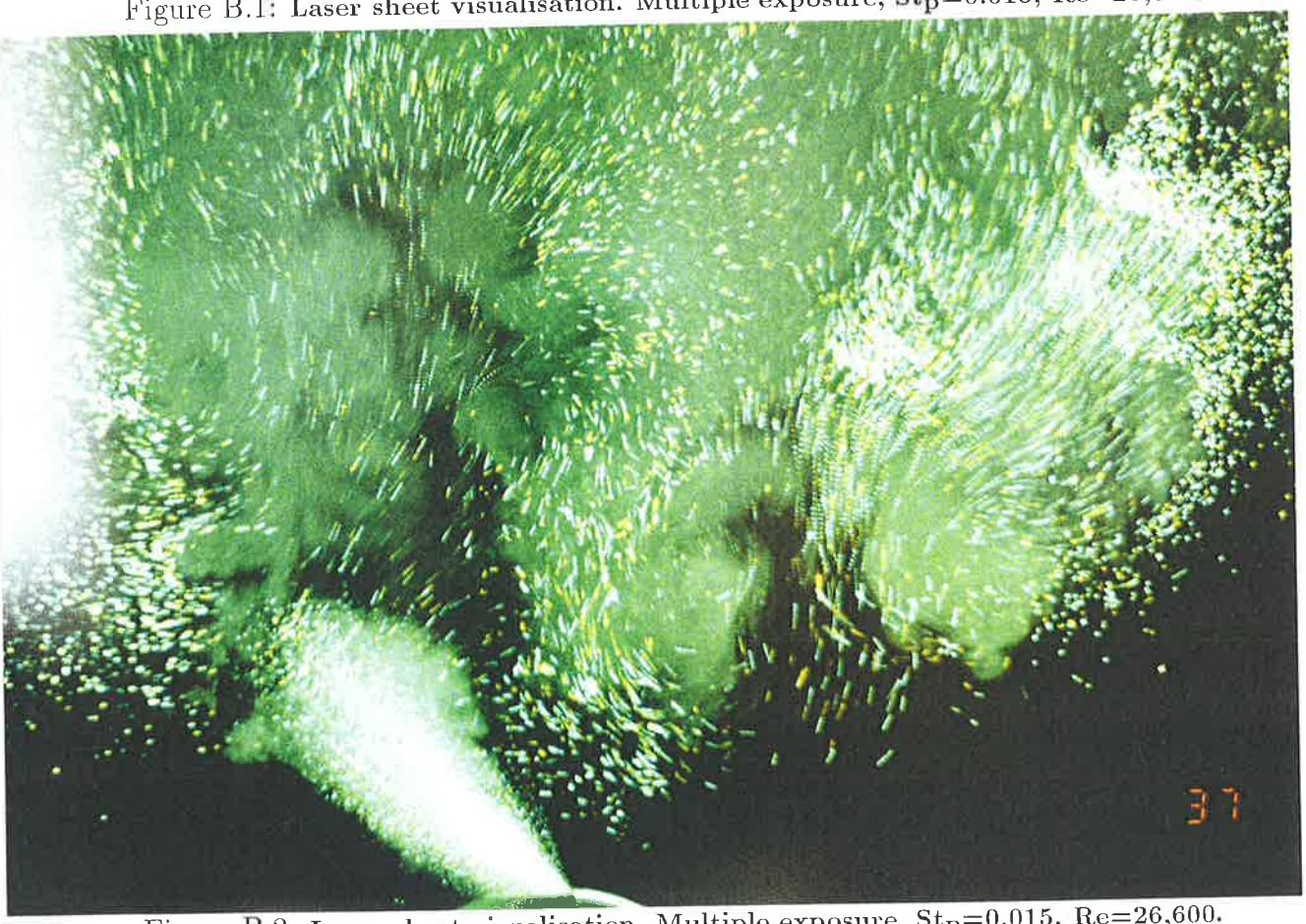

Figure B.2: **Laser sheet visualisation. Multiple exposure, St_p=0.015, Re=26,600.**

Appendix C

Further Results: St_p=0.0058, Re=26,600

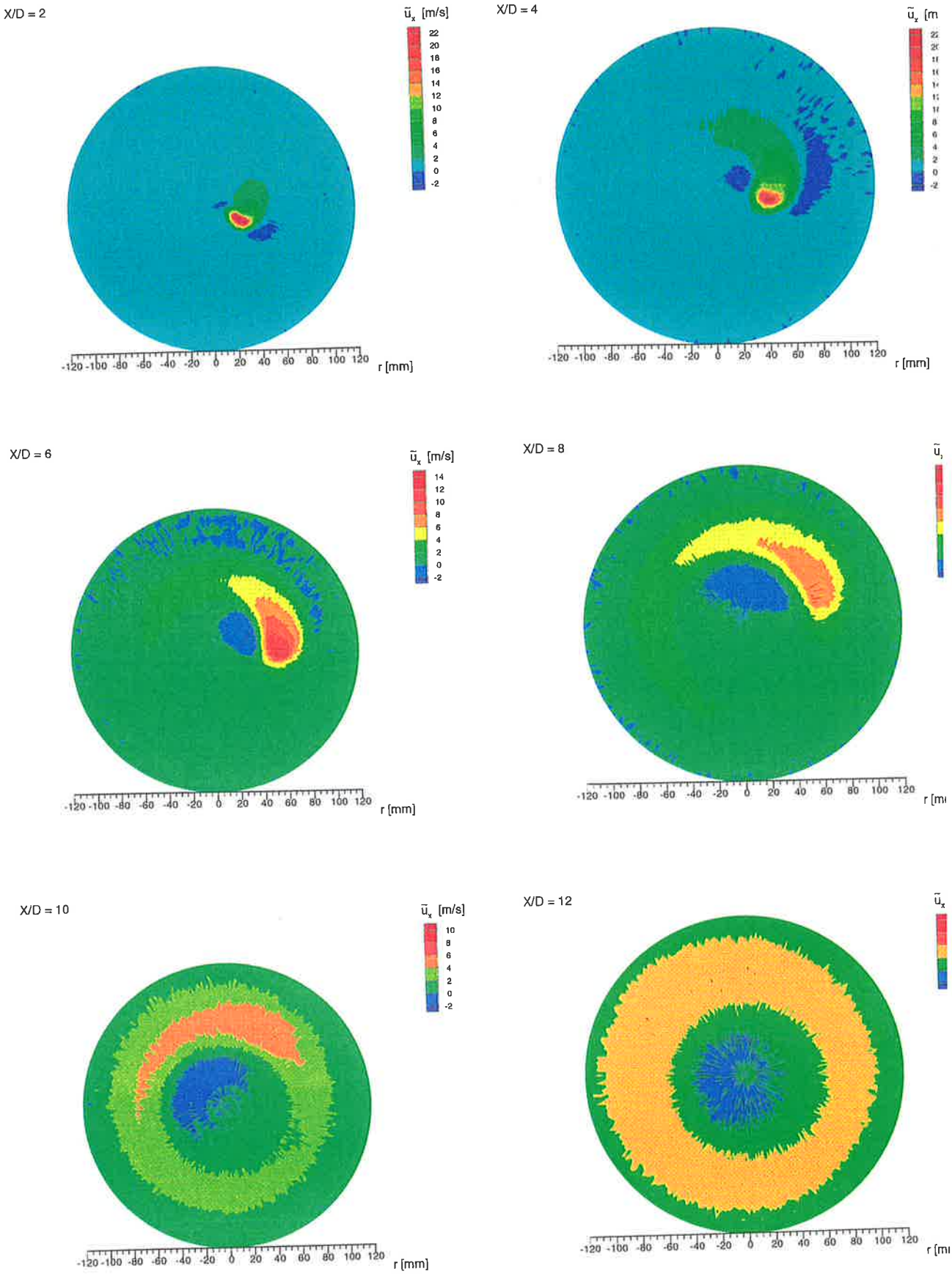

Figure C.1: **Phase-averaged axial velocity $\tilde{u}_x$ contour at x/d_e=2, 4, 6, 8, 10, 12**

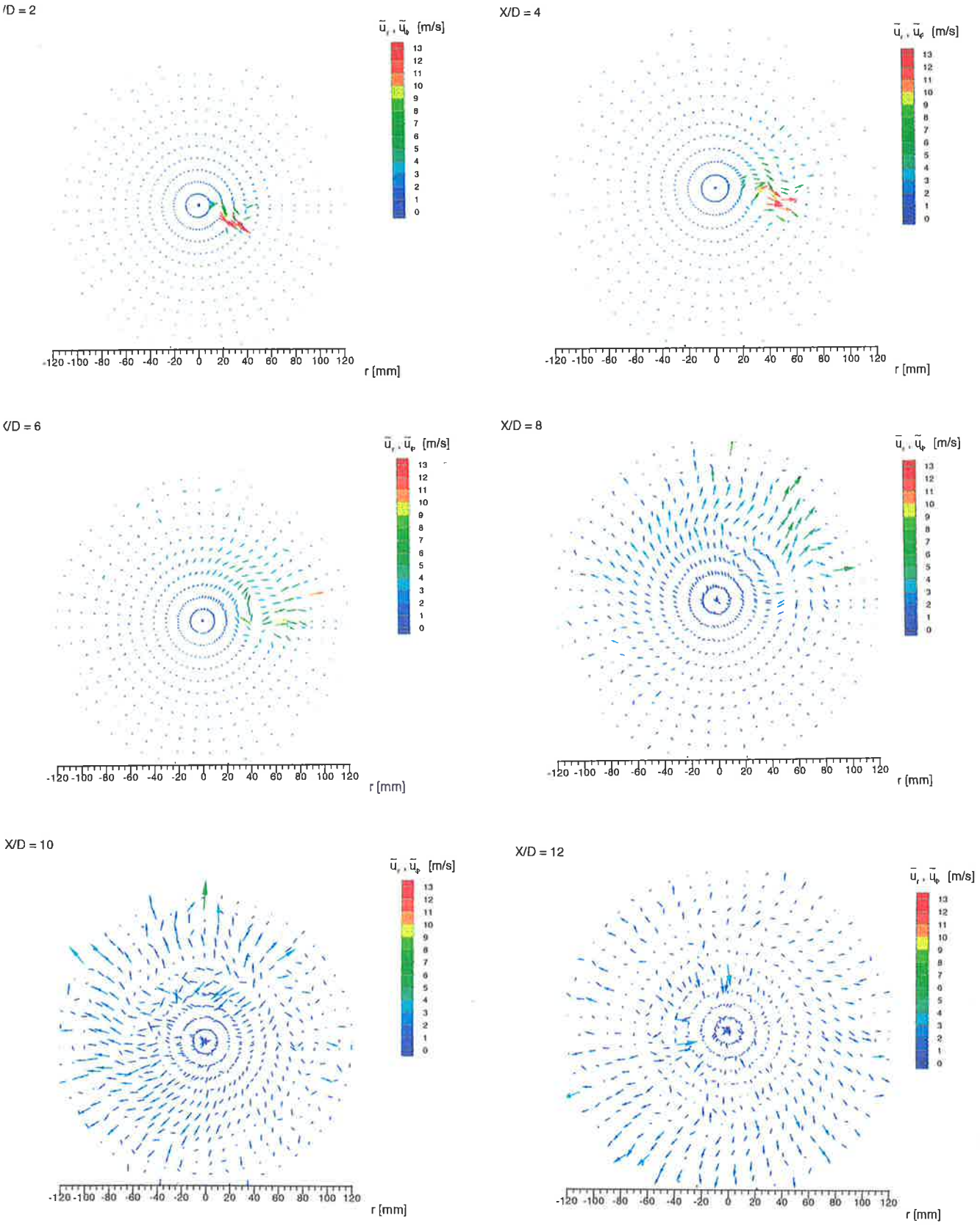

Figure C.2: **Phase-averaged radial–tangential velocity $\tilde{u}_r - \tilde{u}_\Phi$ at x/d_e=2, 4, 6, 8, 10, 12**

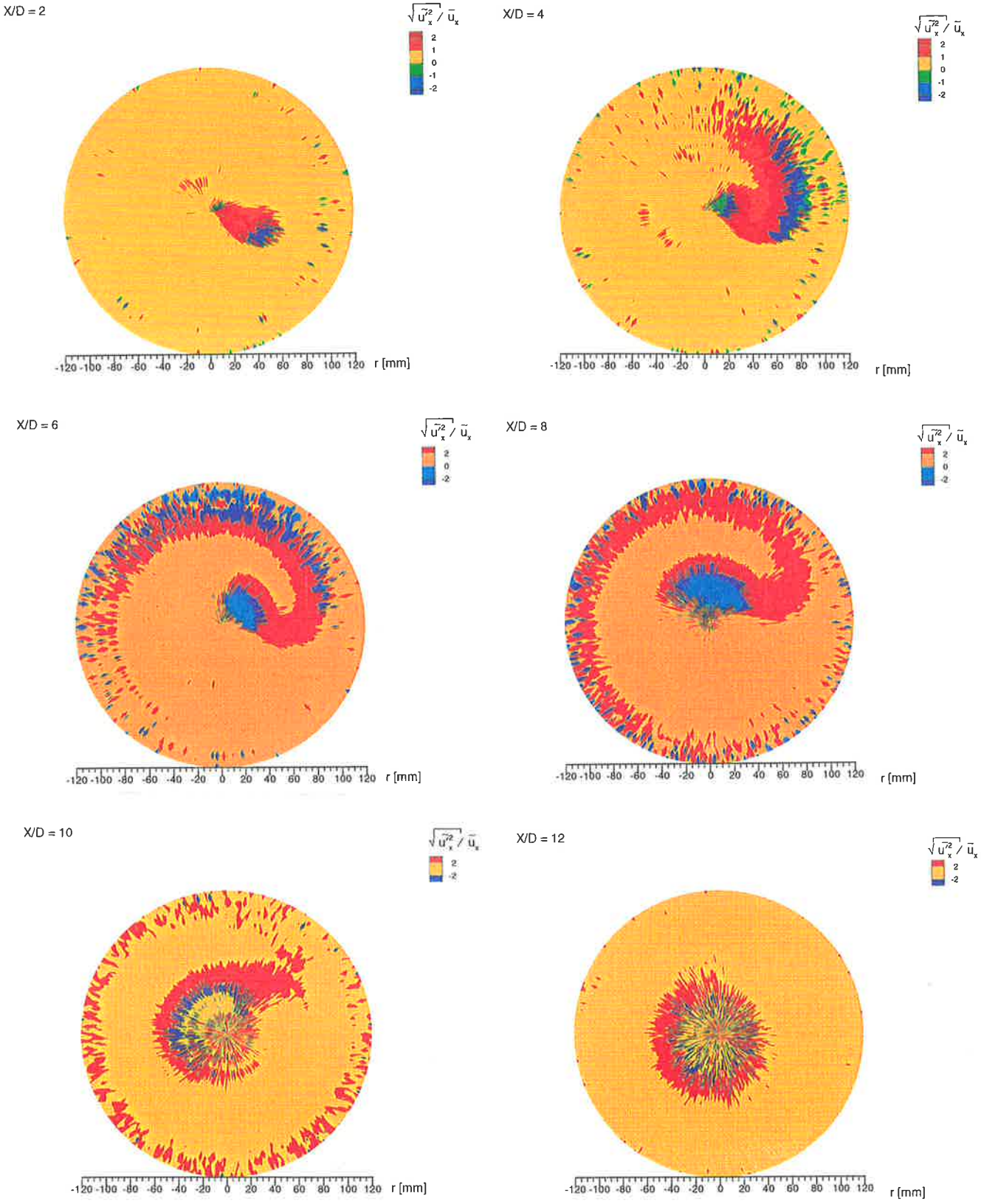

Figure C.3: **Phase-Averaged Axial Turbulence Intensity at x/d_e=2, 4, 6, 8, 10, 12**

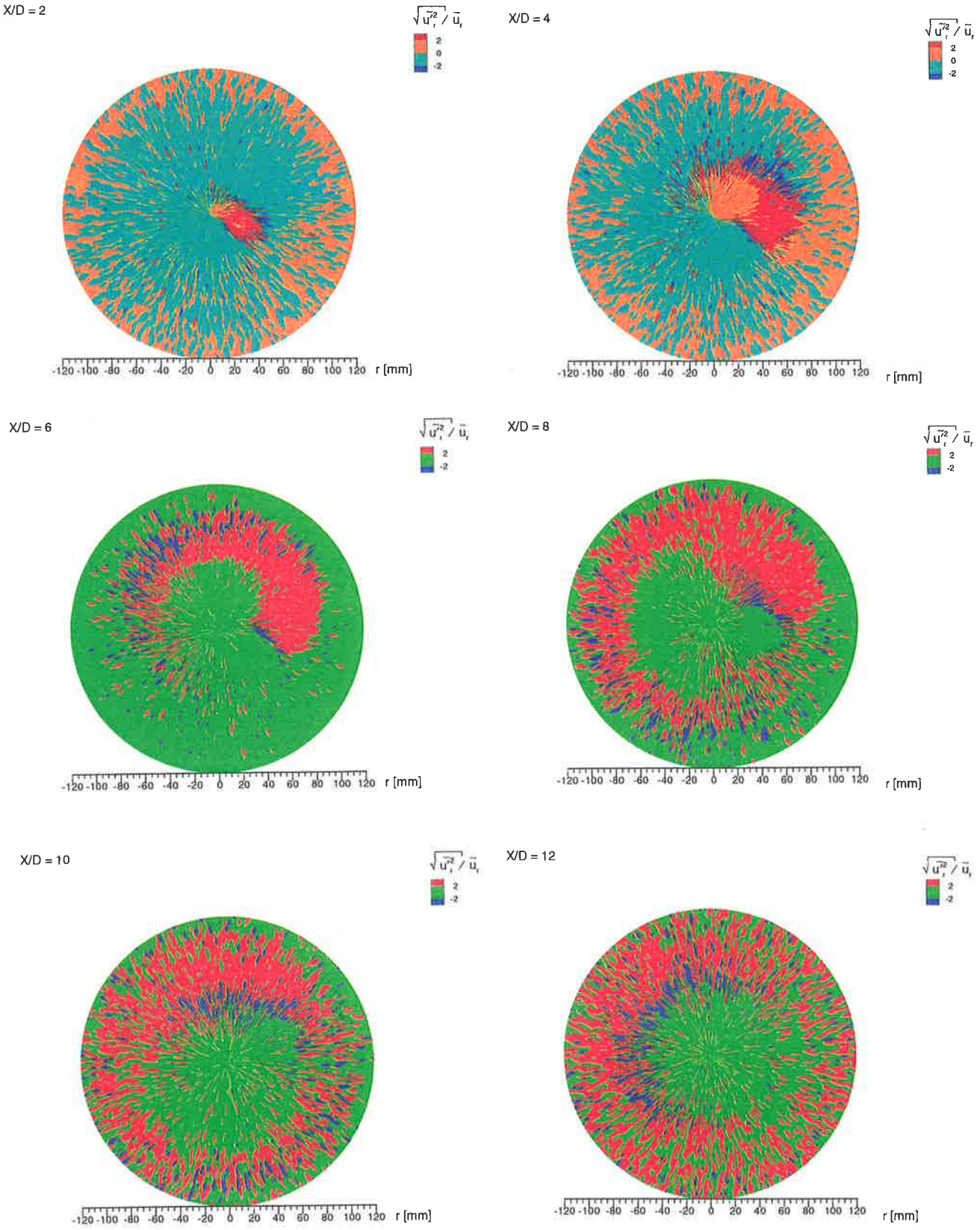

Figure C.4: **Phase-Averaged Radial Turbulence Intensity at x/d_e=2, 4, 6, 8, 10, 12**

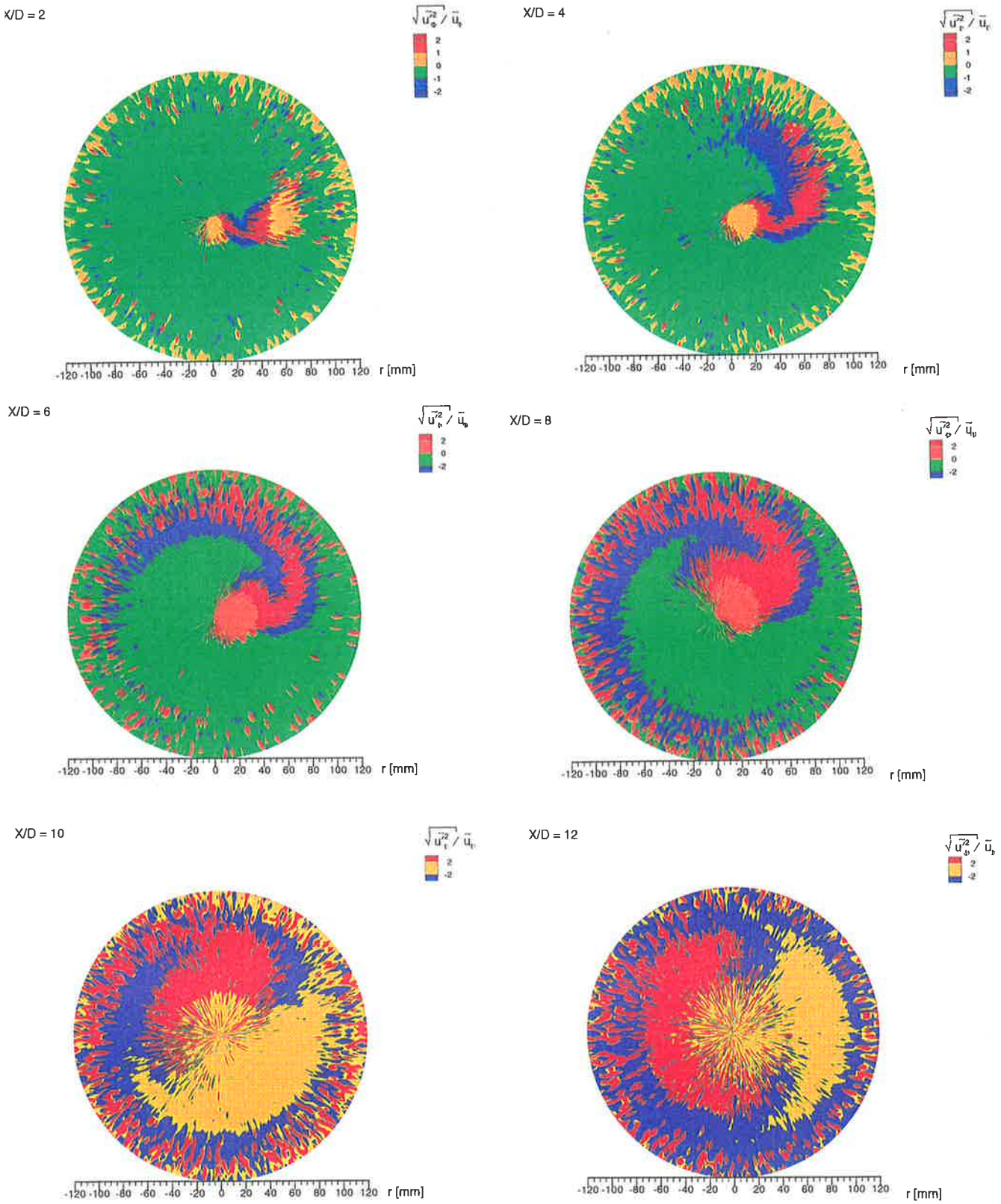

Figure C.5: **Phase-Averaged Tangential Turbulence Intensity at x/d_e=2, 4, 6, 8, 10, 12**

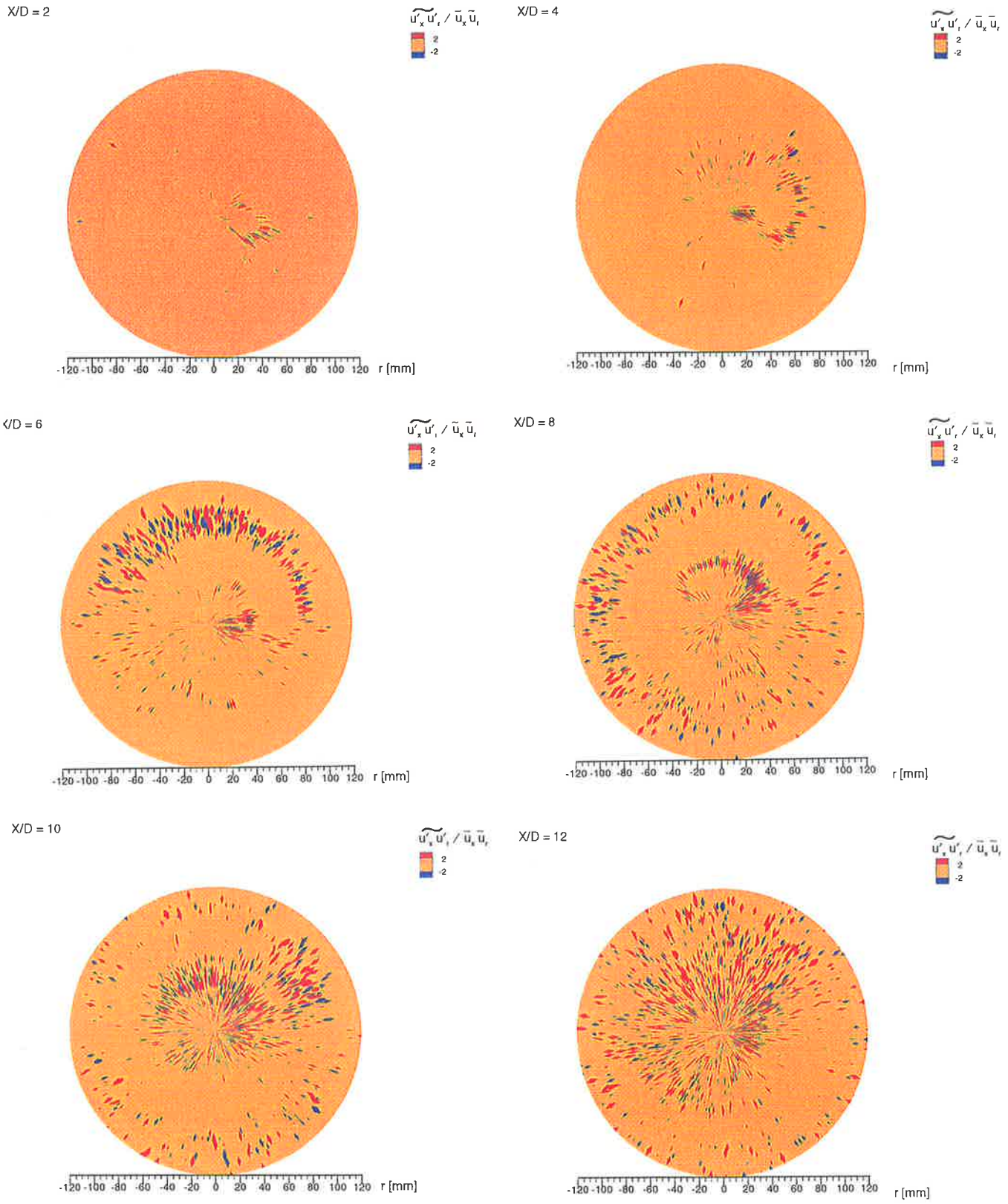

Figure C.6: **Phase-Averaged Reynolds stress $\frac{\widetilde{u'_x \cdot u'_r}}{u_x \cdot u_r}$ at x/d_e=2, 4, 6, 8, 10, 12**

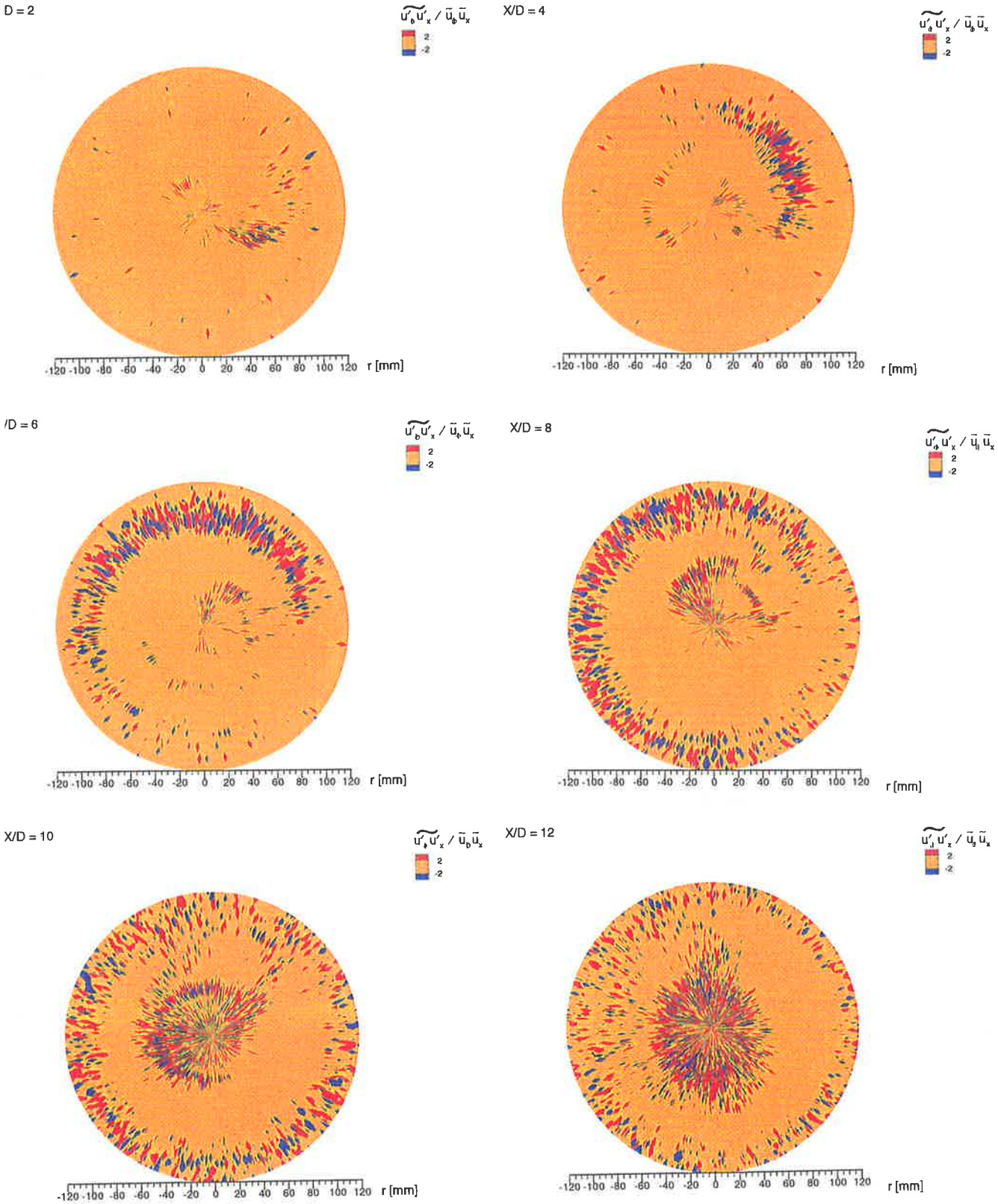

Figure C.7: **Phase-Averaged Reynolds stress $\frac{\widetilde{u_X \cdot u_\Phi}}{u_X \cdot u_\Phi}$ at x/d_e=2, 4, 6, 8, 10, 12**

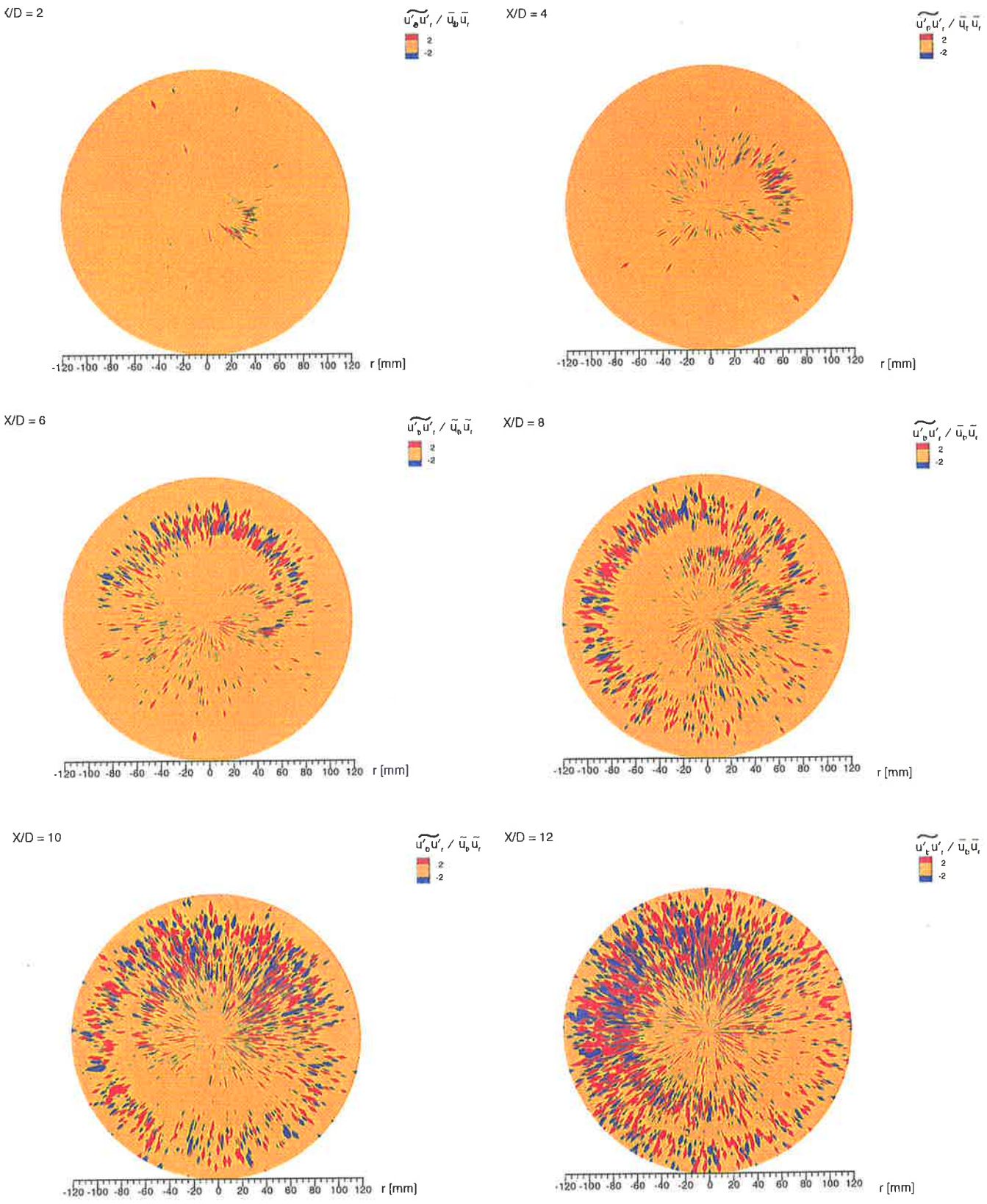

Figure C.8: **Phase-Averaged Reynolds stress $\frac{\widetilde{u'_\Phi \cdot u'_r}}{u_\Phi \cdot u_r}$ at x/d_e=2, 4, 6, 8, 10, 12**

Appendix D

Further Results: St_p=0.0098, Re=26,600

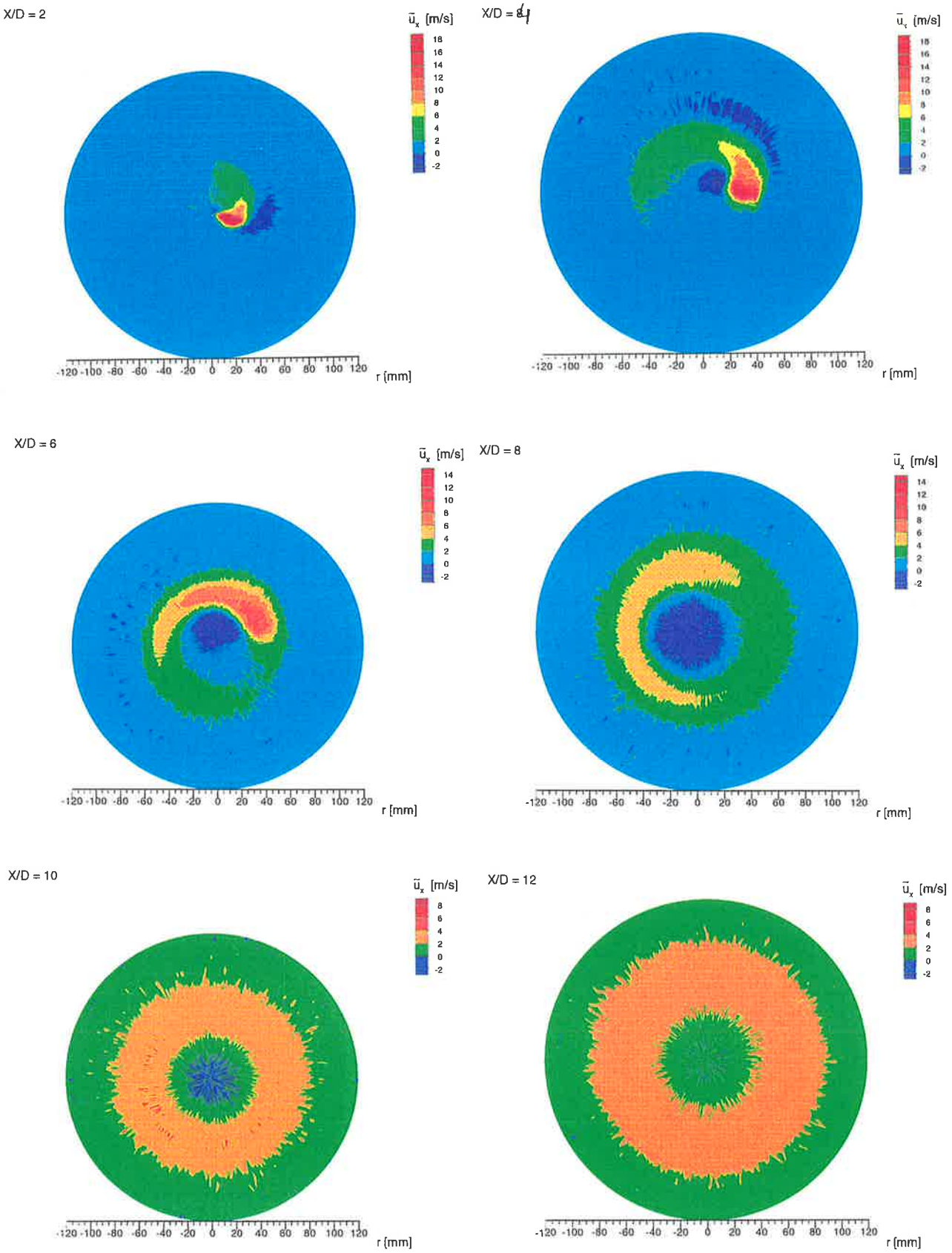

Figure D.1: **Phase-averaged axial velocity $\tilde{u}_x$ contour at x/d_e=2, 4, 6, 8, 10, 12**

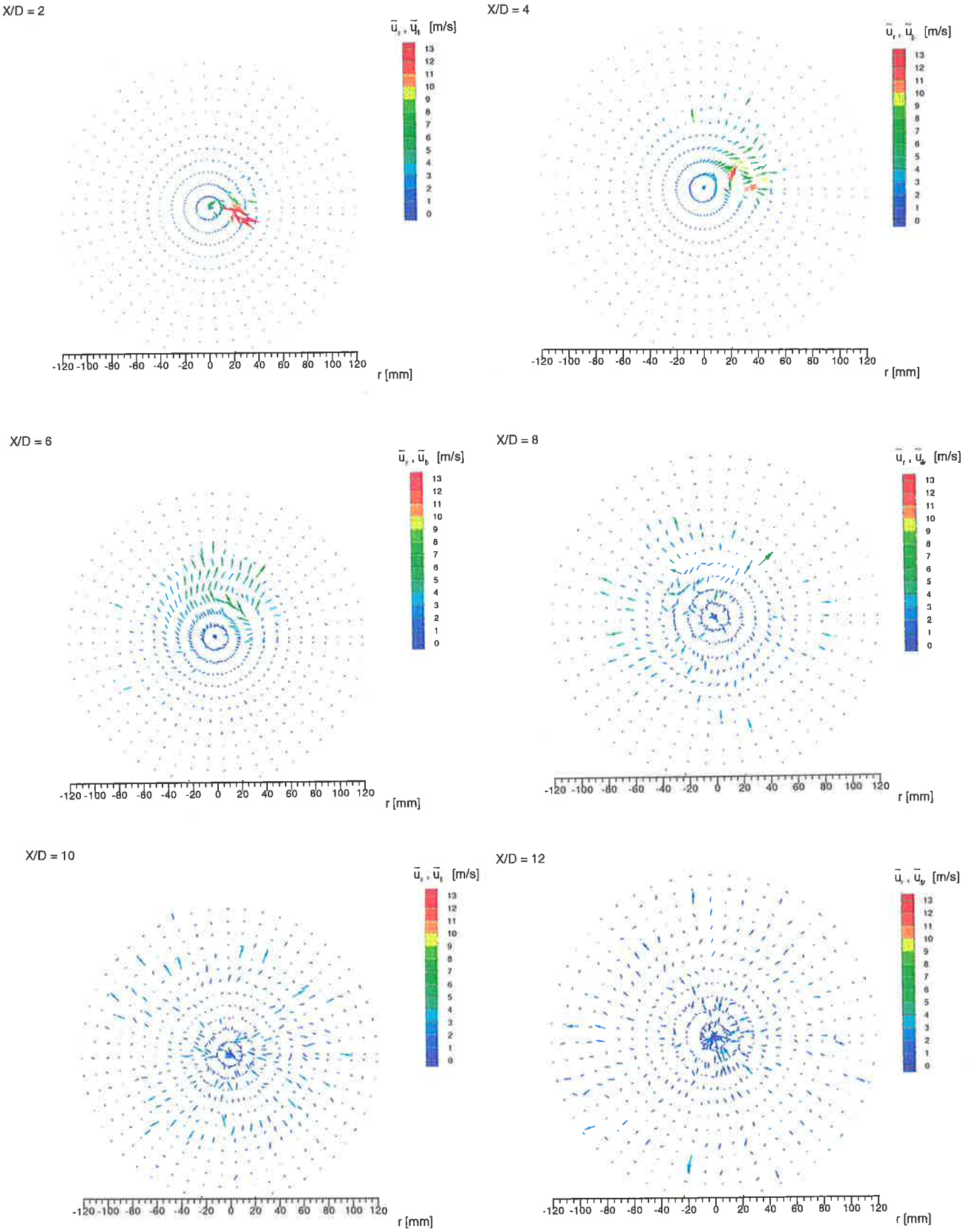

Figure D.2: **Radial-Tangential Velocity $\tilde{u}_r - \tilde{u}_\Phi$ vectors at x/d_e=2, 4, 6, 8, 10, 12**

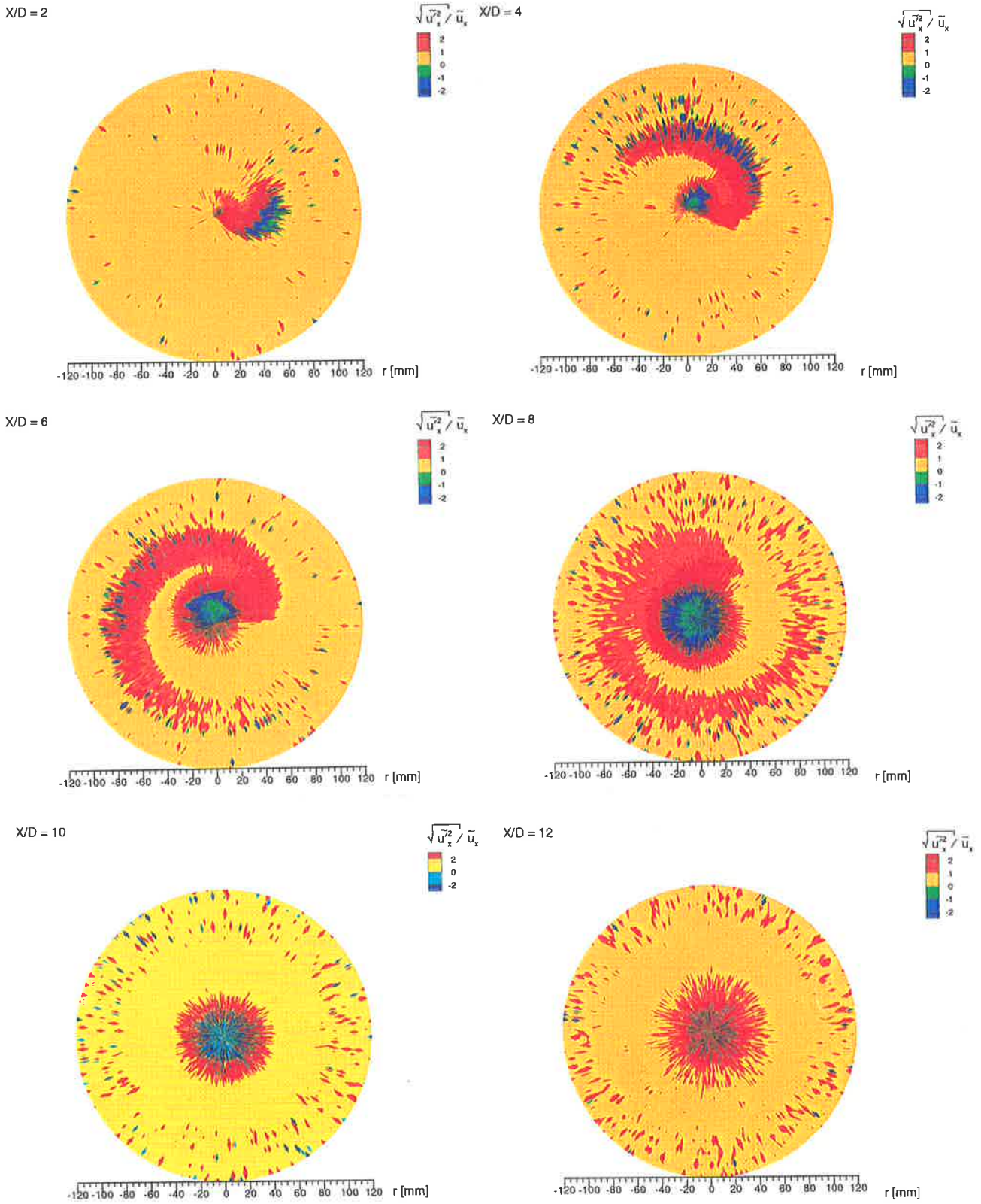

Figure D.3: **Phase-Averaged Axial Turbulence Intensity at x/d_e=2, 4, 6, 8, 10, 12**

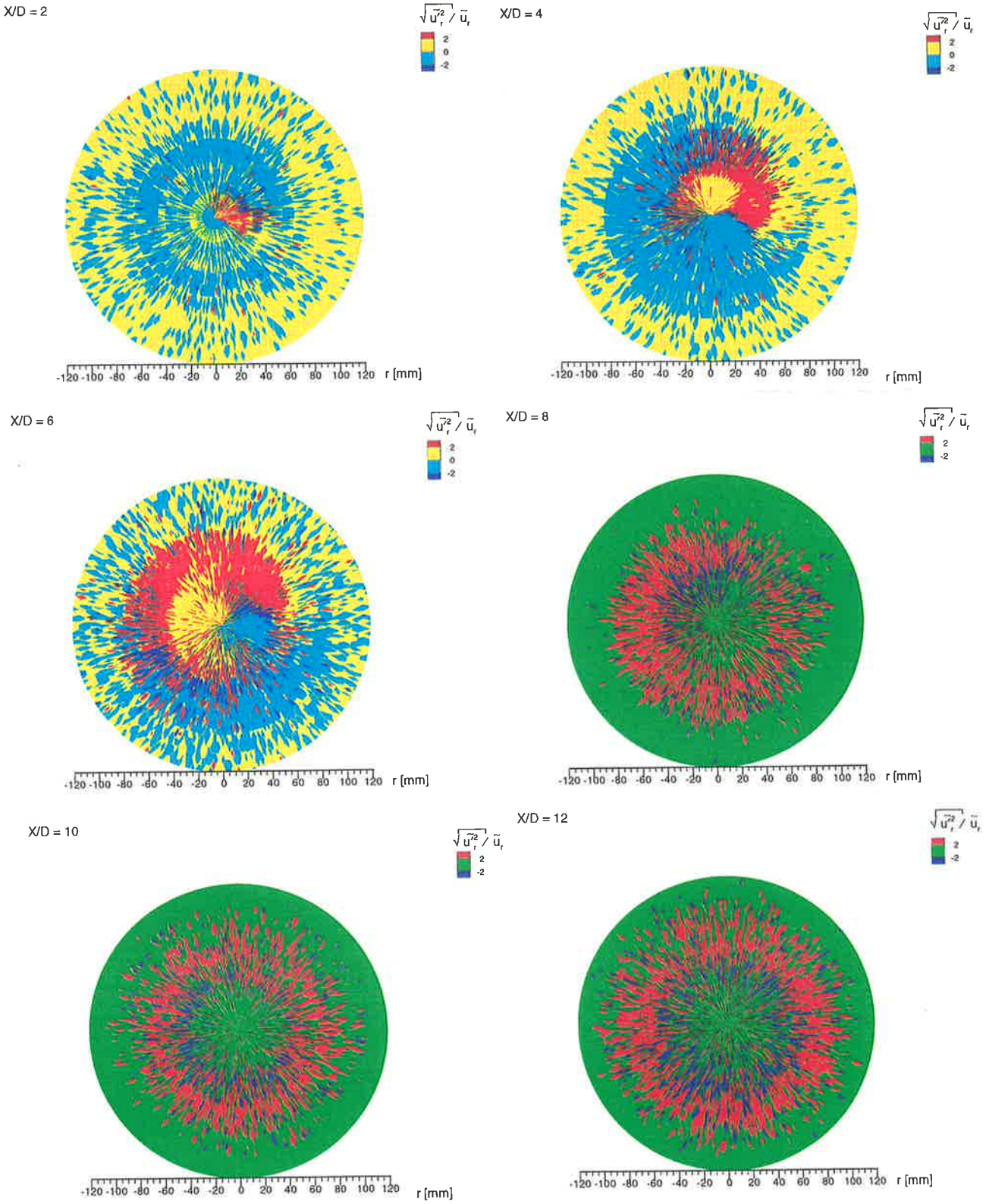

Figure D.4: **Phase-Averaged Radial Turbulence Intensity at x/d_e=2, 4, 6, 8, 10, 12**

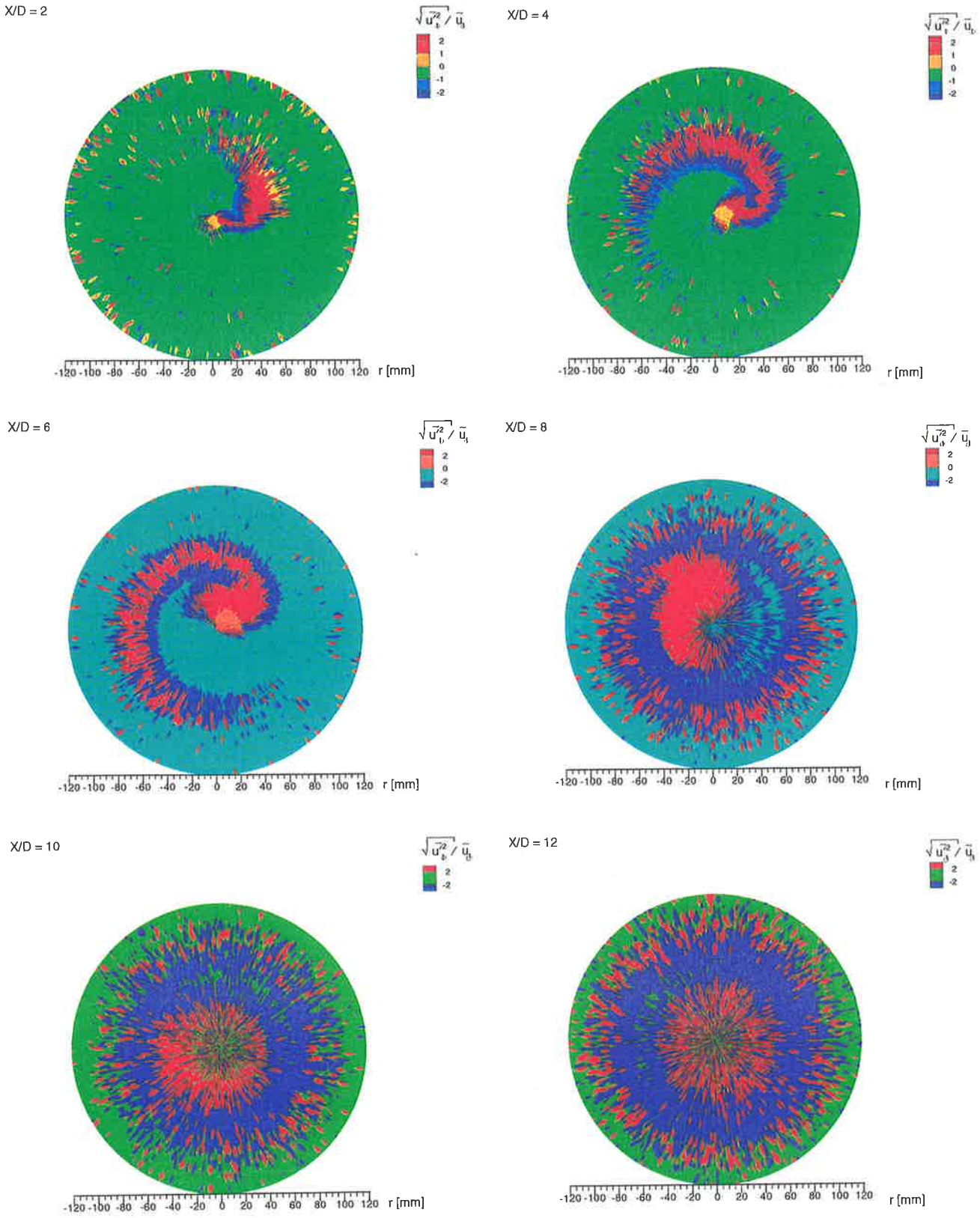

Figure D.5: **Phase-Averaged Tangential Turbulence Intensity at x/d_e=2, 4, 6, 8, 10, 12**

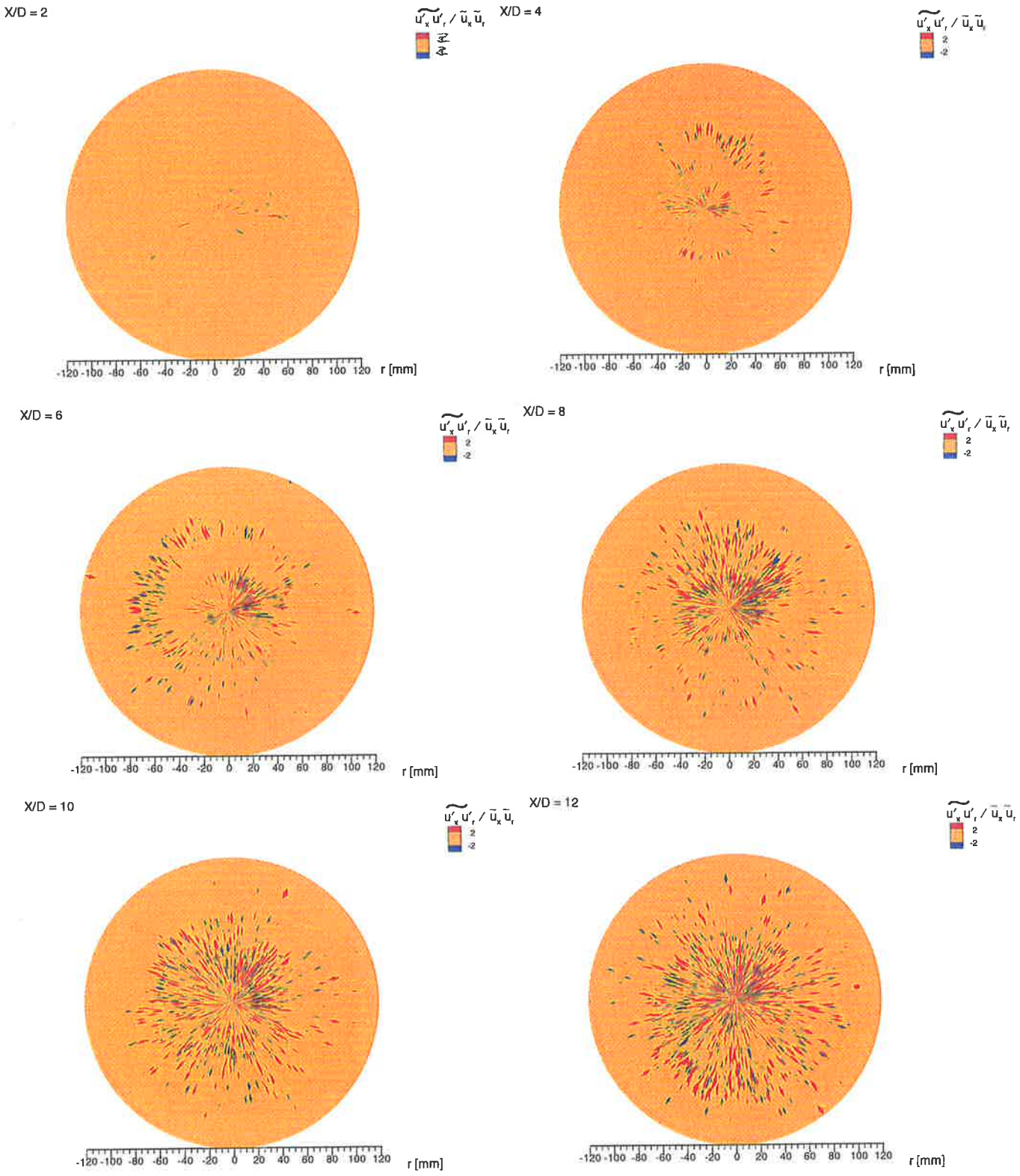

Figure D.6: **Phase-Averaged Reynolds stress $\frac{\widetilde{u_x \cdot u_r}}{u_x \cdot u_r}$ at x/d_e=2, 4, 6, 8, 10, 12**

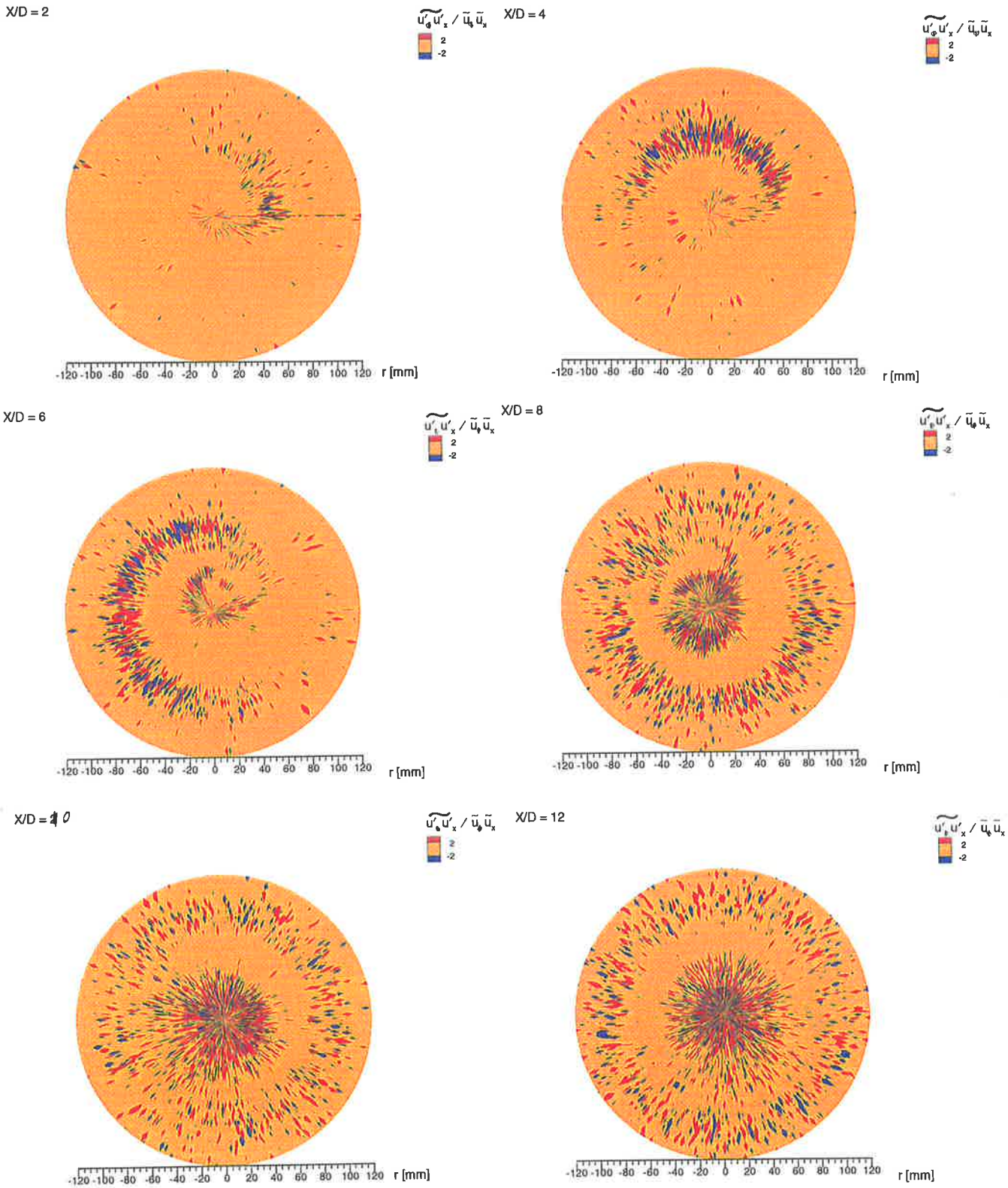

Figure D.7: **Phase-Averaged Reynolds stress $\frac{\widetilde{u_x \cdot u_\Phi}}{u_x \cdot u_\Phi}$ at x/d_e=2, 4, 6, 8, 10, 12**

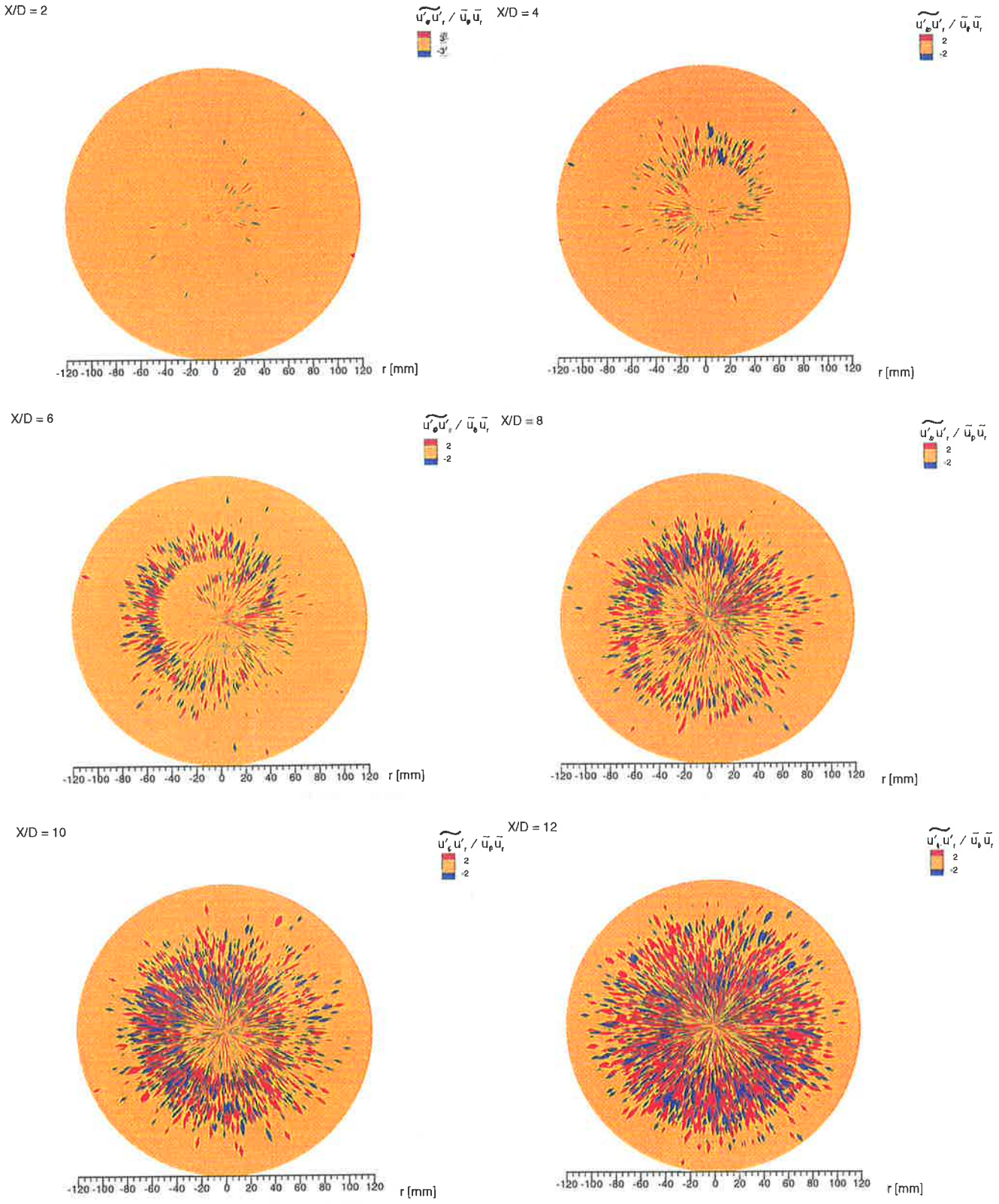

Figure D.8: **Phase-Averaged Reynolds stress $\frac{\widetilde{u_\Phi \cdot u_r}}{u_\Phi \cdot u_r}$ at x/d_e=2, 4, 6, 8, 10, 12**

Appendix E

Further Results: St_p=0.0098, Re=6,600

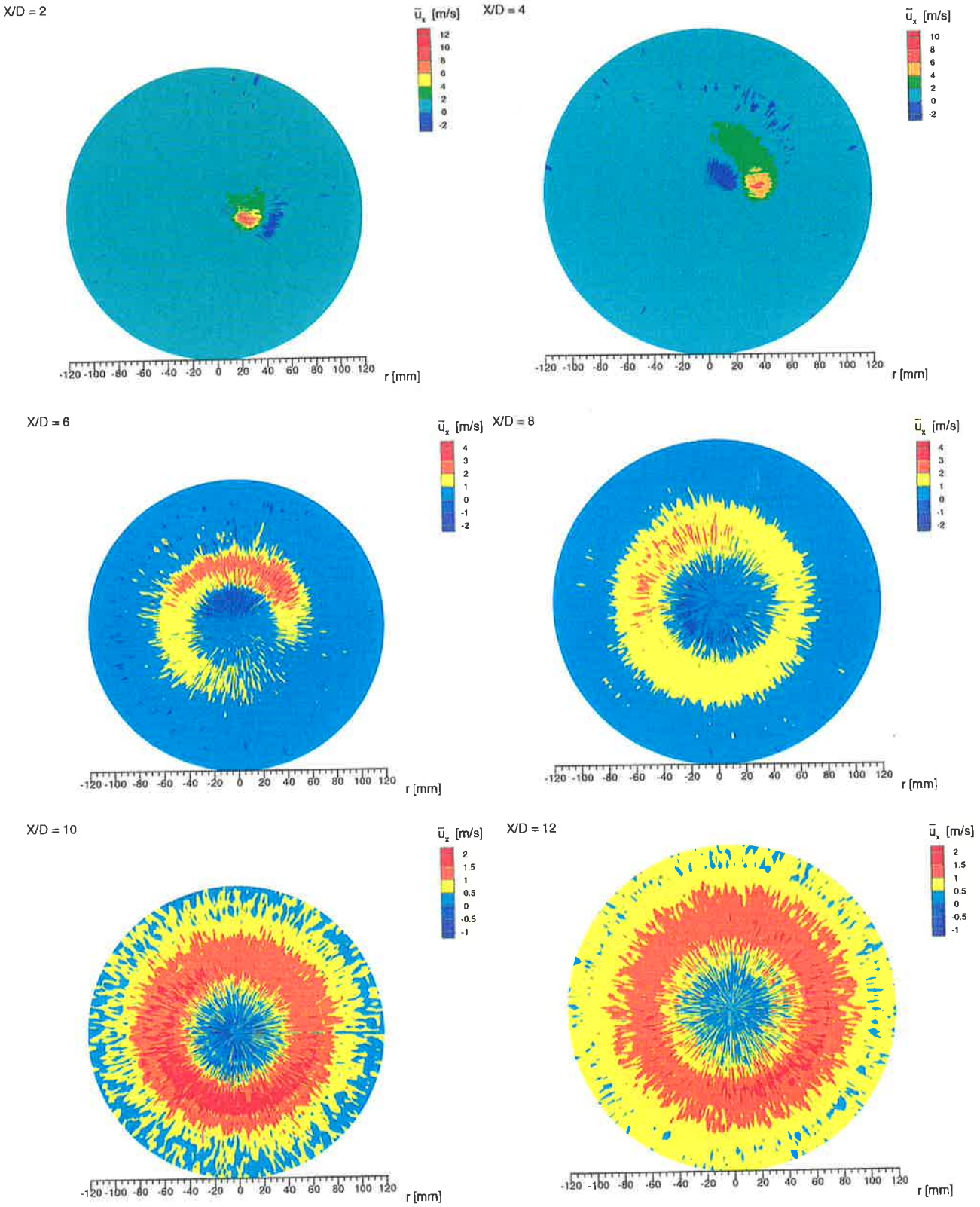

Figure E.1: **Phase-averaged axial velocity $\tilde{u}_x$ contour at x/d_e=2, 4, 6, 8, 10, 12**

Appendix F

Technical Drawings of the Mechanical Nozzle

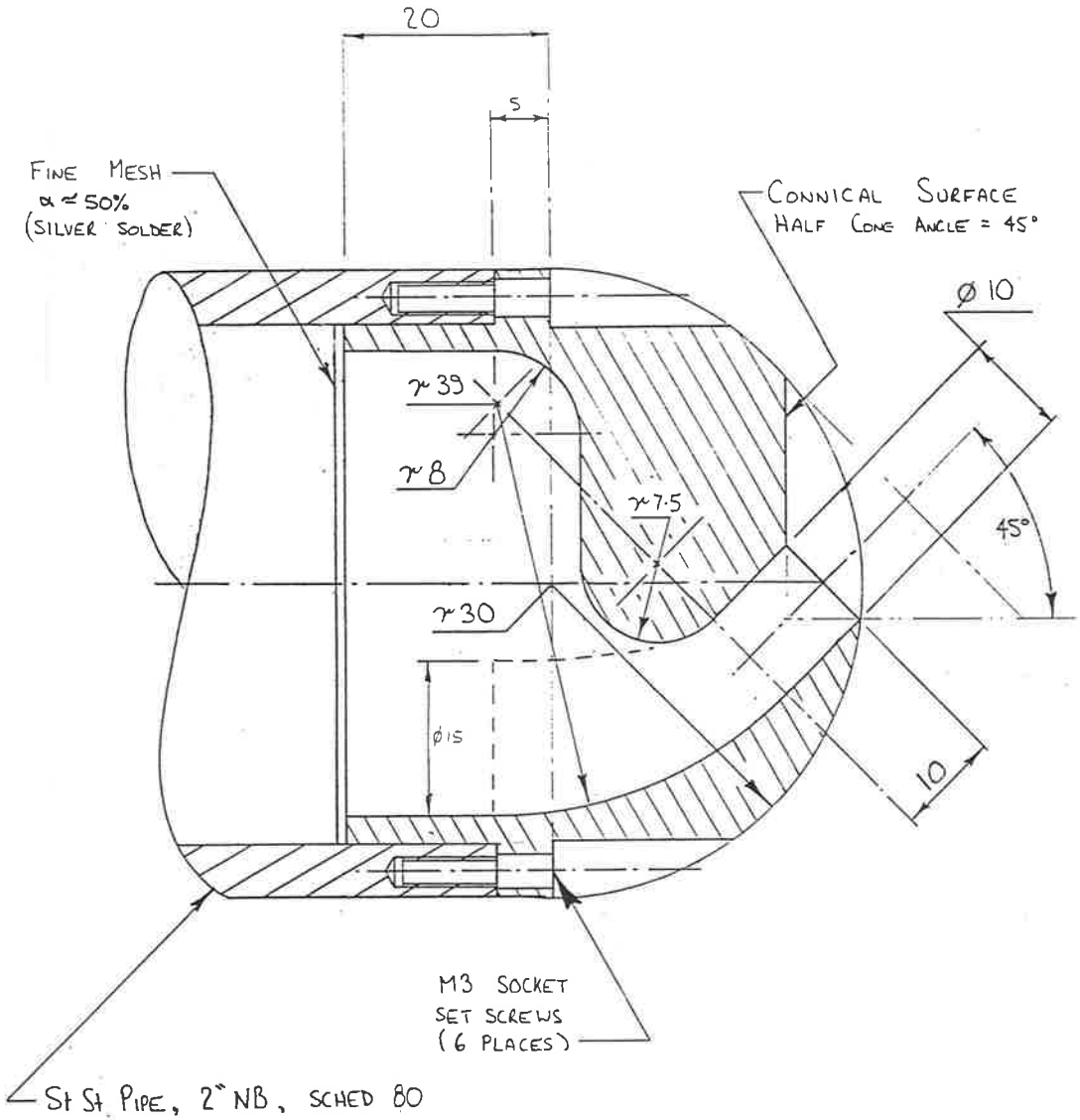

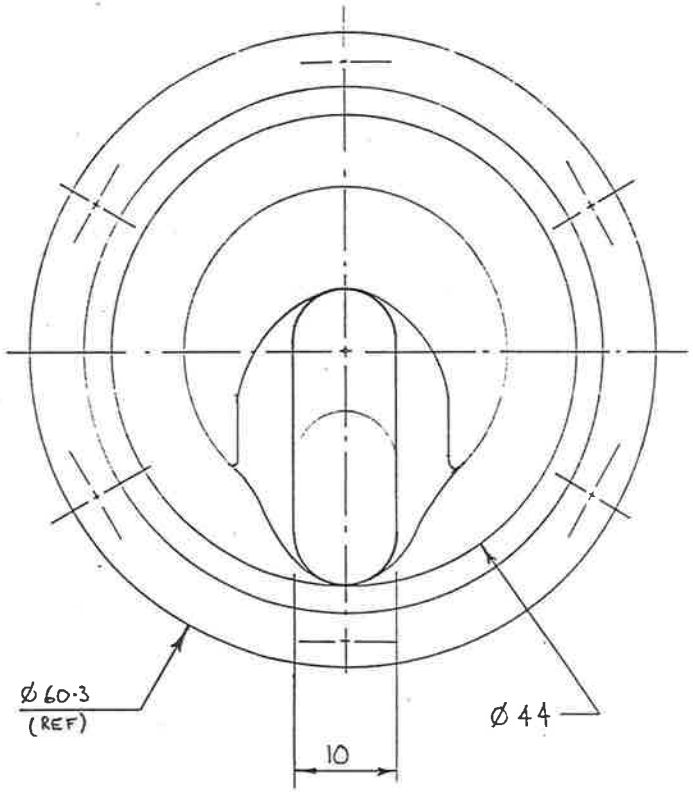

UNIVERSITY OF ADELAIDE - DEPT. MECH. ENG.		
TITLE : MECHANICALLY PRECESSING DEFLECTED JET		
SCALE 2:1	1ST ANGLE OF PROJECTION	DATE : 30/7/91
DRAWN: G I. NATHAN	CHECKED :	SHT

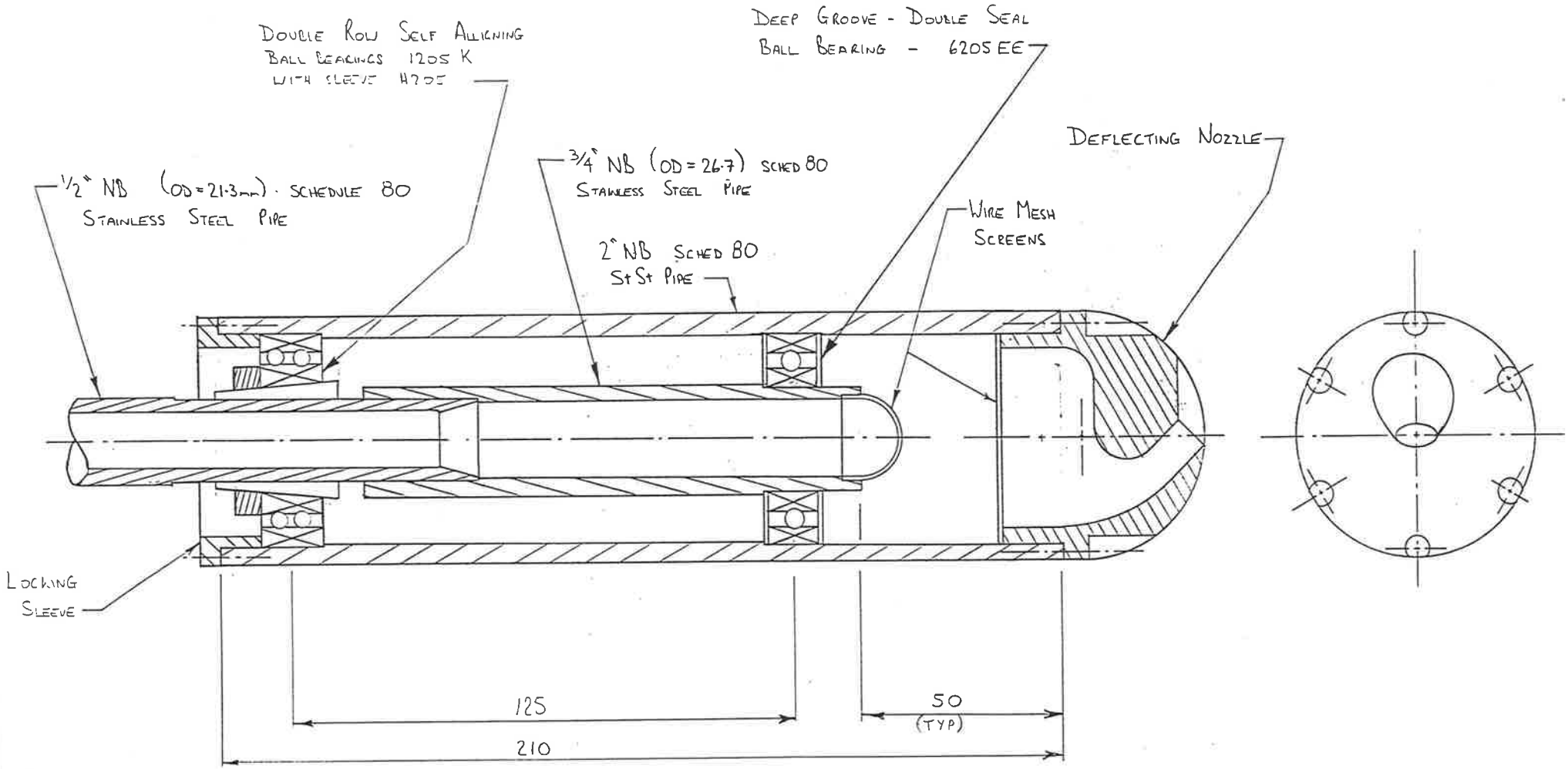

University of Adelaide - Dept Mechanical Engineering		
Titile: Mechanically Precessing Deflected Jet Assy Dwg		
Scale 1:1	3rd Angle of Proj	Date 30-7-91
Drawn: G.J. Nathan	Checked:	Sht 1/